

Interferometric Synthetic Aperture Radar for remote satellite monitoring of bridges



Sivasakthy Selvakumaran

Supervisor: Prof C.R. Middleton

Department of Engineering
University of Cambridge

This dissertation is submitted for the degree of
Doctor of Philosophy

Newnham College

August 2019

Declaration

This thesis is the result of my own work and includes nothing which is the outcome of work done in collaboration except as declared in the Preface and specified in the text. It is not substantially the same as any that I have submitted, or, is being concurrently submitted for a degree or diploma or other qualification at the University of Cambridge or any other University or similar institution except as declared in the Preface and specified in the text. I further state that no substantial part of my thesis has already been submitted, or, is being concurrently submitted for any such degree, diploma or other qualification at the University of Cambridge or any other University or similar institution except as declared in the Preface and specified in the text. It does not exceed the prescribed word limit for the relevant Degree Committee

Sivasakthy Selvakumaran
August 2019

Interferometric Synthetic Aperture Radar for remote satellite monitoring of bridges

Sivasakthy Selvakumaran

Abstract

The structural health of critical infrastructure is difficult to assess and monitor with existing methods of evaluation which rely predominantly on visual inspection and/or the installation of sensors to measure the in-situ performance of structures. There are vast numbers of critical structures that need to be monitored and these are often located in diverse geographical locations which are difficult and costly to access. Recent advances in satellite technologies provide the opportunity for global coverage of assets and the measurement of displacement to sub-centimetre accuracy. Such measurements could supplement existing monitoring techniques and provide asset owners with additional insights which could inform operational and maintenance decisions.

Most past research within the field of Interferometric Synthetic Aperture Radar (InSAR) monitoring using satellite radar imagery focusses on widespread measurement of land areas, although there have been some case studies using InSAR to assess movements of individual structures such as dams. However, there is limited published research into the use of these techniques for accurately monitoring the displacements of individual civil engineering structures over time and relating these measurements to structural performance. This research focusses on bridges as a specific example of critical infrastructure to establish whether remote satellite monitoring can be used to measure displacements at a resolution that is sufficiently accurate for use in monitoring of performance, and examines the relevance and limitations of satellite monitoring to civil engineering applications in general.

In order to assess the millimetre-scale performance of InSAR, an initial evaluation was undertaken in controlled conditions on a purpose-built test bed fitted with satellite reflectors at the National Physical Laboratory in Teddington to validate InSAR displacement measurements against traditional terrestrial in-situ displacement measurements. Subsequently, traditional sensor and surveying measurements of displacements were compared with InSAR displacement measurements at key points of interest on Waterloo Bridge and the Hammer-smith Flyover. A further case study on Tadcaster Bridge was undertaken to demonstrate the potential applicability of InSAR displacement measuring techniques for monitoring bridges at risk of scour failure. Scour is the most common form of bridge collapse around the

world and to date no cost-effective and widely applicable method for providing advanced warning of impending failure due to scour has been developed. Methodologies for integrating digital, structural and signal processing models for the identification and mapping of InSAR measurement points on bridge structures from SAR imagery were developed, as well as methodologies for combining satellite data with traditional surveying methods

An important outcome of this research was that through comparison of independent measurements, InSAR measurements are of a scale that is applicable to bridge monitoring. Remote sensing can therefore reach global coverage, with unsupervised readings over an interval of days, and as such supplement traditional inspection regimes. However, this outcome must be presented with several limitations. Practical implications of applying InSAR to real bridges are discussed, including imaging effects and the suitability of monitoring different forms of bridge deformation.

The key to successful implementation of InSAR monitoring of bridges lies in understanding the limitations and opportunities of InSAR, and making a clear case to satellite data providers on what specifications (resolution, frequency, processing assumptions) would unlock using such datasets for wider use in monitoring of infrastructure. InSAR can provide measurements and useful insights for bridge monitoring but it is limited to specific cases and, at this stage of technological development, it should be considered as a tool for specific bridges and failure mechanisms rather than a full bridge monitoring solution.

Acknowledgements

Firstly, I would like to thank my PhD supervisor, Professor Cam Middleton, who persuaded me that returning to academia from industry for this would be a worthwhile experience! His guidance and support has been invaluable, and opened up a great number of opportunities for me.

This work was made possible by EPSRC (UK) Award 1636878, with iCase sponsorship from the National Physical Laboratory (NPL) and additional funding from Laing O'Rourke. Thank you to Elena Barton from NPL who has provided great insights from the field of measurement and uncertainty and Peter Hewitt from Laing O'Rourke who has supported this work not only with structural monitoring data, but also his professional insights and expertise in instrumentation and monitoring.

Thank you to the German Aerospace Center (Deutsches Zentrum für Luft- und Raumfahrt, DLR) for welcoming me as a guest researcher, for teaching me about the wonderful world of remote sensing, and for giving me the capability to do image processing of SAR data. I would particularly like to thank Simon Plank, Christian Geiß and Hannes Taubenböck for their time, support and enthusiasm.

I would also like to thank the Satellite Applications Catapult who have supported with staff time and technical advice in setting up a number of experiments. Particular thanks to Richard Hilton for supporting this work and providing a platform for it to reach maximum practical impact, for Terri Freemantle and Louise Hetherton in helping the experiments run smoothly and Cristian Rossi, who has acted as an additional academic supervisor, providing InSAR technical guidance and helping me connect into the earth observation community.

I would particularly like to thank Mark Bew who has supported this work from the early stages, from bringing organisations together, all the way to reviewing methodologies with useful comments and insights. Thank you also to Andrea Marinoni for his signal processing

and mathematical insights, as well as general encouragement. I would also like to thank Stephen Pottle, John Longley, Graham Webb and Paul Fidler for their support throughout the PhD journey.

There are many organisations who have devoted time and effort in providing me with data and insights for various case studies during the PhD journey. These include the UK Bridge Owners Forum, Transport for London, Westminster City Council, North Yorkshire County Council, London Underground, WSP and Ramboll UK.

TerraSAR-X data for Tadcaster Bridge study and additional preliminary studies was provided by the German Aerospace Centre (DLR) under proposal MTH3513. TerraSAR-X and Cosmo SkyMed-X data tasked for this study was funded by Innovate UK via the Satellite Applications Catapult, who provided additional Cosmo SkyMed-X archive data. Processed data over Hammersmith Flyover was provided by Telespazio VEGA UK.

The colleagues and networks within Cambridge University Engineering Department, the Laing O'Rourke Centre for Construction Engineering and Technology, the Centre for Smart Infrastructure and Construction (CSIC) and Newnham College have been invaluable support. Thank you to the US Alumna of Newnham College who funded a summer study in the United States, supporting me not just with funding but with contacts, their network and their friendship. Thanks also go to the Institution of Engineering and Technology (IET) who supported my time in Munich through funding from the Leslie H Paddle Scholarship Award for Postgraduate Studies. The results of this thesis were also recognised by an award from the Cambridge Society for Applied Research (CSAR).

The final thank you goes to my parents and sister, Mathy. Thank you for your patience and support.

Table of contents

List of figures	xv
List of tables	xix
Nomenclature	xxi
1 Introduction	1
1.1 Motivations	1
1.2 Research aims and objectives	3
1.3 Research philosophy	4
1.4 Research approach	5
1.4.1 Research phases	5
1.4.2 Methodology	6
1.4.3 Scope	7
1.5 Outline of thesis	8
2 InSAR Theory	11
2.1 Introduction to Synthetic Aperture Radar	11
2.2 Basic SAR principles	12
2.2.1 SAR imaging	14
2.2.2 Speckle	15
2.2.3 Interpretation of SAR images	17
2.3 Interferometric SAR	19
2.3.1 Across-track interferometry	21
2.3.2 Differential interferometry	22
2.4 InSAR processing methodologies	26
2.4.1 Persistent Scatterer Interferometry (PSI)	26
2.4.2 Small Baselines Subsets (SBAS)	27
2.5 PSI Processing Methodology	27

2.5.1	Coherence	27
2.5.2	Connection graph	28
2.5.3	Coregistration	29
2.5.4	Interferogram Generation	29
2.5.5	Flattening and topical phase removal	31
2.5.6	Atmospheric phase removal	31
2.5.7	Geocoding	32
2.6	Available data	32
3	Literature Review	35
3.1	Structural health monitoring	35
3.2	Applications of InSAR	39
3.3	Application of InSAR to bridge monitoring	40
3.3.1	Image interpretation	41
3.3.2	Persistent Scatterer three-dimensional positioning	42
3.3.3	Accuracy and reliability of InSAR measurements	43
3.3.4	InSAR Line of Sight measurements	45
3.3.5	Thermal expansion	46
3.3.6	Motivations for research	48
4	NPL Measurement Experiment	51
4.1	Introduction	51
4.2	Design of the radar reflector	52
4.3	Experiment Site	54
4.4	Equipment	56
4.4.1	Installation and orientation of corner reflectors	57
4.4.2	Installation of GNSS stations	59
4.5	Data collection methodology	62
4.6	Processing methodology	64
4.6.1	SAR processing	64
4.6.2	GNSS processing method	65
4.6.3	Reference systems	66
4.7	Results	68
4.7.1	The effect of multilooking	73
4.7.2	Trends within the data	73
4.7.3	Error sources in differential InSAR	77
4.7.4	Error sources in GNSS readings	78

4.8	Discussion	79
4.8.1	Understanding InSAR quality	79
4.8.2	Measurement of uncertainty	82
4.8.3	Uncertainty associated from taking vertical component of LOS measurement	83
4.9	Conclusions	85
5	Waterloo Bridge	87
5.1	Introduction	87
5.2	Bridge structure	88
5.3	Experimental set up	89
5.3.1	Traditional monitoring	89
5.3.2	Satellite data sets	89
5.3.3	Corner reflectors	90
5.4	Method	93
5.4.1	Data processing of in-situ data	93
5.4.2	Data processing of SAR data	94
5.5	Results	94
5.5.1	Resolving in one direction of movement	95
5.5.2	Using multiple look directions	99
5.6	Multidimensional analysis	101
5.6.1	Measure of fit	102
5.6.2	Mapping of SAR and ATS functions	103
5.7	Method to combine terrestrial and SAR	105
5.8	Discussion	111
5.8.1	Understanding InSAR quality	111
5.8.2	InSAR data sparsity	112
5.8.3	Use of corner reflectors	113
5.9	Conclusions	113
6	Hammersmith Flyover	115
6.1	Introduction	115
6.2	Bridge structure	115
6.3	Background to monitoring work	116
6.4	Deployed monitoring systems	118
6.4.1	Deployed traditional monitoring systems	118
6.4.2	InSAR data analysis	119

6.5	Results	121
6.6	Methods for interpreting InSAR outputs	122
6.6.1	Digital modelling	122
6.6.2	Method for the identification of target points	125
6.7	Bridge behaviour anomaly detection	130
6.8	Discussion	133
6.8.1	Augmenting a wider digital network	133
6.8.2	Understanding the suitability of InSAR to a specific bridge	134
6.8.3	Understanding InSAR data quality	134
6.8.4	InSAR data sparsity	135
6.9	Conclusions	136
7	Tadcaster Bridge	137
7.1	Introduction	137
7.2	Scour failure in bridges	137
7.3	Using InSAR for monitoring deformations due to scour	139
7.4	Study area	140
7.5	Method	142
7.5.1	Data sets	142
7.5.2	Processing Methods	142
7.6	Results	144
7.6.1	Deformation map	145
7.7	Discussion	148
7.7.1	Precursors to failure	148
7.7.2	Identification of outliers	149
7.7.3	Application to early warning systems	151
7.7.4	Mapping movement behaviour against environmental data	152
7.7.5	InSAR processing considerations	153
7.8	Conclusions	154
8	InSAR for Bridge Structural Monitoring: Conclusions	157
	References	165
	Appendix A TerraSAR-X London SAR acquisitions	177
	Appendix B Cosmo SkyMed-X London SAR acquisitions	179

Table of contents	xiii
<hr/>	
Appendix C Tadcaster site SAR acquisitions	181

List of figures

1.1	Phases of research	5
1.2	Summary of research methods.	6
1.3	Phases of research aligned with thesis structure	9
2.1	Synthetic aperture radar imaging geometry	12
2.2	Radar wave characteristics.	13
2.3	Chirped signal	14
2.4	SAR image of bridges crossing the River Thames	15
2.5	Multiple scatterers within a single SAR resolution cell	16
2.6	Projection of SAR radar.	17
2.7	SAR radar foreshortening effect.	18
2.8	SAR radar layover effect.	18
2.9	SAR radar shadow effect.	19
2.10	Interferogram of the London area created with Envisat satellite data	20
2.11	Satellite geometry for interferogram imaging.	21
2.12	Image of digital elevation model (DEM) from the Shuttle Radar Topography Mission (SRTM).	22
2.13	Satellite geometry for along-track (differential) imaging.	23
2.14	Differential interferogram using TerraSAR-X London SAR images.	25
2.15	Simplified PSI processing chain	27
2.16	Example connection graphs	30
2.17	Interferogram using section of TerraSAR-X London data with topographic component included.	31
3.1	Bridge over water multi-bounce effects.	42
4.1	Graphical representation of SAR point target response	52
4.2	Trihedral corner reflector shape	53
4.3	Site layout for corner reflector experiment	55

4.4	Photo of installed corner reflectors mounted on concrete base at NPL site . . .	56
4.5	Photos of corner reflector stages to control movement	57
4.6	Corner reflector geometry	58
4.7	SAR image before corner reflector installation	58
4.8	SAR image after corner reflector installation	59
4.9	Point target analysis example	60
4.10	GNSS layout at corner experiment test site	61
4.11	Photo of GNSS device set up at 'building' location of test site	62
4.12	Site and corner reflector layout	63
4.13	Vertical movements imposed over time for Corners A and C	63
4.14	Time-Position plot for acquisitions used in corner reflector experiment . . .	66
4.15	Example differential interferogram used in corner reflector experiment . . .	67
4.16	GNSS recorded vertical movement over time for all sites	69
4.17	GNSS recorded vertical movement over time for 'Corner' site	69
4.18	Plot of movement of Corner A as wrapped results	70
4.19	Plot of movement of Corner C as wrapped results	70
4.20	Principle of phase unwrapping	71
4.21	SAR incidence angle.	72
4.22	Plot of Corner A movement over time	72
4.23	Plot of Corner C movement over time	73
4.24	Monthly rainfall during SAR readings	74
4.25	Temperature on dates of SAR readings	76
4.26	Temperature, SAR and displacement gauge readings	76
4.27	Statistical information for Corner C vertical displacement SAR measurements.	80
4.28	Principle of Spectral Angle Mapping	81
4.29	Vertical component of line of sight (LOS) measurement.	83
4.30	Calculated uncertainty values for each graph region of Corner C.	84
5.1	Elevation of Waterloo Bridge.	88
5.2	ATS and target prism locations on the bridge and embankments	90
5.3	Photo of corner reflector installed on site	91
5.4	Annotated SAR amplitude image with corner installation	92
5.5	Plot of distance across river between north and south river walls over time .	94
5.6	Persistent scatterers monitored on Waterloo Bridge	95
5.7	Bridge orientation in relation to satellite imaging geometry	96
5.8	Incidence angle in relation to bridge and satellite imaging geometry	97

5.9	Graph of average bridge deck temperature and InSAR-measured longitudinal movement	98
5.10	Plot of relative ATS and SAR movements	98
5.11	Comparison between relative ATS and SAR longitudinal measurements . .	100
5.12	Graph of possible Reconstruction Error (RE) values	104
5.13	ATS viewing geometry as used to define equations	105
5.14	Plotting various functions for the combination of ATS and SAR equations .	108
5.15	Misplacement of ATS on the vertical direction $\Delta z_{ATS} = Az^t - Az^{t-1}$	109
6.1	Photo of Hammersmith Flyover	116
6.2	Temperature sensor locations.	118
6.3	LVDT installation for bearing movement measurement	119
6.4	Time-position plot for 2015 to 2018 images processed	120
6.5	PS points on Hammersmith Flyover and surrounding area	121
6.6	SAR imaging effects impacting Hammersmith imagery	123
6.7	Three-dimensional interpretation of PS points on Hammersmith Flyover . .	124
6.8	Points representing persistent scatterers associated to the bridge overlaid onto a map of the bridge.	126
6.9	Temperature data for span BC	128
6.10	Temperature data passed through FFT	128
6.11	Examples of oscillating InSAR point passed through a FFT.	129
6.12	Selected non-oscillating InSAR point passed through a FFT.	129
6.13	Movement and temperature of Pier B over time.	130
6.14	Movement and temperature of Pier N over time with all InSAR PS.	131
6.15	Movement and temperature of Pier N over time with selected InSAR PS. . .	132
7.1	Scour of bridge piers.	138
7.2	Tadcaster Bridge schematic and extent of collapse	141
7.3	Stages before scour collapse of Tadcaster Bridge.	143
7.4	Temporal - perpendicular baseline for interferometric stack	144
7.5	SBAS velocity results over Tadcaster SAR image	145
7.6	SBAS results over Tadcaster Bridge	146
7.7	Movement of scatterers attributed to the bridge plotted over time	147
7.8	Adaptive threshold for bridge movement	150
7.9	River flow rate alongside the progression of scatterer 'b' on Tadcaster Bridge.	152
A.1	Footprint of TerraSAR-X imagery over London	177

B.1	Footprint of Cosmo SkyMed-X imagery over London	180
C.1	Footprint of TerraSAR-X imagery over Tadcaster	181

List of tables

2.1	SAR Satellite launch information	34
2.2	SAR Satellite resolution information	34
4.1	RCS values for different trihedral corner reflector sizes for X-band and C-band satellites	54
4.2	List of TerraSAR-X ascending acquisitions used in corner reflector experiment	65
4.3	Pearson correlation coefficients	80
4.4	Spectral Angle Mapper (SAM) values	81
6.1	Timeline of events for Hammersmith Flyover	117
A.1	TerraSAR-X acquisition list for Waterloo Bridge study	178
B.1	Cosmo SkyMed-X acquisition list provided by Telespazio	179
B.2	Cosmo SkyMed-X acquisition list processed by author	180
C.1	TerraSAR-X acquisition list for Tadcaster Bridge study	182

Nomenclature

Acronyms / Abbreviations

ASI Agenzia Spaziale Italiana (Italian Space Agency)

ATS Automated Total Station

DEM Digital Elevation Model

dInSAR Differential Interferometric Synthetic Aperture Radar

DLR Deutsches Zentrum für Luft- und Raumfahrt (German Aerospace Center)

DSM Digital Surface Model

ESA European Space Agency

ETRS European Terrestrial Reference System

FBM Fundamental Bench Mark

GCP Ground Control Point

GNSS Global Navigation Satellite System

GPS Global Positioning System

InSAR Interferometric Synthetic Aperture Radar

ITRF International Terrestrial Reference Frame

ITRS International Terrestrial Reference System

LOS Line of Sight

LVDT Linear Variable Differential Transformers

NPL	National Physical Laboratory
PSI	Persistent Scatterer Interferometry
PS	Persistent Scatterer
RADAR	RADio Detection And Ranging
SAR	Synthetic Aperture Radar
SBAS	Small Baseline Subsets Algorithm
SCR	Signal-to-Clutter Ratio
SHM	Structural Health Monitoring
SLC	Single Look Complex
SNR	Signal-to-Noise Ratio
SRTM	Shuttle Radar Topography Mission
TRS	Terrestrial Reference System
UTM	Universal Transverse Mercator
WGS	World Geodetic System

Chapter 1

Introduction

1.1 Motivations

Our cities are a complex mix of diverse ecosystems, institutions, assets and infrastructure. The rapid expansion of cities as the global population grows is exposing more people and economies to the risk of disasters and the effects of climate change. Disruption to one part of the city ecosystem, such as transport networks, water supply, drainage or energy systems, affects both urban management, local economies and the delivery of key services, as well as the lives and livelihoods of the people within these cities. The widespread deterioration and recent collapses of bridges, dams, tunnels and other key services have highlighted the importance of structural health monitoring (SHM) in supporting maintenance decisions and preventing collapses. A study by the RAC Foundation [1] found that within the UK alone, 71,652 bridges were managed by local authorities in 2018, of which 3,177 (4.4% of the total) are categorised as ‘substandard’ (meaning that they are unable to carry the heaviest vehicles now seen on roads, including lorries of up to the legal load limit of 44 tonnes) and will require weight restrictions, increased monitoring or even managed decline. The different regional Highway authorities were found to have 1 to 8% of their bridge stock as ‘substandard’. Within the United States, the American Society of Civil Engineers found 9.1% of bridges to be structurally deficient in 2016, and in that year on average there were 188 million trips across a structurally deficient bridge each day [2]. The implications of bridge asset failure can be profound in terms of safety, economic prosperity and social well-being of communities. Given the impact of this issue, and the fact that bridge ageing and deterioration presents a global problem, the topic of bridge monitoring will be the focus of this research.

Current standard practice for the monitoring of bridges in most countries is to periodically schedule visual inspections, relying on inspectors to be able to spot signs of problems or unusual behaviours before they reach a catastrophic stage. The subjective nature of human

judgement is useful to identify non-standard behaviours and to apply a case-specific approach, but previous studies [3, 4] highlight that this does not necessarily provide reliable results. For example, a study by Moore et al. [3] published by the Federal Highways Authority in the USA points out some of the weaknesses in the current approach in the United States where there was a significant amount of variation in assigned Condition Rating (scaled numerically from 0 to 9) during visual inspection. This variation was found to be in thoroughness of inspection records as well as variation on which sections of the bridge were inspected. The study found that the data collected depended on factors such as the level of training obtained by the inspector, whether the inspector was colour-blind, whether the inspector had a fear of traffic or heights, or the weather on the day of inspection. This would suggest a need to supplement visual inspections with less subjective insights.

A balance also needs to be struck between having regular asset monitoring and the cost of doing so, financially as well as with regard to the disruption caused to the network (e.g. by bridge closure). Consequently, inspections are typically carried out every few years. Using Highways England bridge inspections as an example, the regulation for bridges is to have a General Inspection every two years, with a Principal Inspection taking place every six years. A General Inspection relies on a person looking at a bridge from some distance as a “*visual inspection of all parts of the structure that can be inspected without special access equipment or traffic management arrangements*”, whilst a Principal Inspection is the “*close examination, within touching distance, of all inspectable parts of a structure*” [5]. It has been suggested that structural health monitoring, leveraging technology to take more frequent readings, could provide more objective and repeatable data to supplement visual inspections and manage risk [6, 7].

Earth observation data from satellites is becoming more accessible, and at improving spatial and time resolutions. This data can provide a means of remote monitoring which covers large geographical regions and provide insights into infrastructure assets that are difficult to access or regularly monitor with conventional approaches. Within the asset management context outlined, satellite monitoring provides the opportunity to remotely collect information related to an asset in an interval period of days. Thus, there are opportunities in being able to monitor for signs of unusual behaviour that develop in the periods between inspections or are not picked up visually. Remote satellite monitoring offers a further advantage over traditional in-situ sensor monitoring in that it does not require an electrical connection or power source at site or closure and physical access to the bridge.

There are many different forms of satellite data, from optical images taking photographs, to sensors which can monitor forms of air pollution, to communications which facilitate navigation. Notably, radar imagery taken by satellites can be used to monitor millimetre-

scale movements of built environment assets over time by exploiting the principles of radar interferometry. Using radar monitoring is well established for investigating large earth movements and monitoring of city scale deformation, but there has been limited research investigation on use of radar to monitor single infrastructure assets, which is now becoming feasible with improvements to the achievable resolution. This research was based on Interferometric Synthetic Aperture Radar (InSAR) techniques, which have the capability to provide wide-area, high density, remote measurements of displacement at millimetre-scale [8, 9]. Optical satellite images were also used to support the interpretation of the information derived from InSAR data.

The research first focussed on determining the precision, repeatability and uncertainty of measurements with respect to displacement sensors, terrestrial surveying and other methods traditionally employed to study structural behaviour. The research then focussed on the use InSAR techniques to investigate bridge problems, specifically failures and collapse, to understand whether InSAR can be used to pick up precursors to failure, and thus forecast and diagnose loss of service and potentially dangerous situations.

1.2 Research aims and objectives

This research aims to investigate InSAR satellite measurement technologies and understand their relevance, utilisation, opportunities and limitations for civil engineering applications of bridge monitoring. The key research objectives are to address the following research questions:

- 1. Can InSAR satellite measurement technology provide remote measurement at the necessary level of accuracy, reliability and resolution such that it is able to replace or complement traditional forms of physical measurement and monitoring of bridge assets?*
- 2. Can InSAR satellite measurement technology be used to identify signs or precursors of failure in bridge assets?*

The primary method of satellite measurement used in this research is Interferometric Synthetic Aperture Radar (InSAR), which is now becoming available at a resolution which has the potential to be of use to monitor the condition and in service performance of bridge assets. In light of the significant implications of bridge asset failure and with a number of very recent failures, this research sets out to establish if InSAR data is of a suitable quality to provide reliable readings of bridge performance and if this data can be processed to establish new insights, diagnostics and failure prediction.

Given the backlog of structurally deficient assets and limited funding, there is a need to consider the ‘value’ of the big datasets generated through such techniques (financially and otherwise) to make the best use of them in line with other traditional forms of monitoring, and therefore deliver value to asset owners [10]. Civil engineers stand to gain from this research through developing methods by which they can be better equipped to predict and prevent structural failure, and better understand how to operate and maintain large infrastructure assets. In addition to supplementing current asset management practice with complementary data about assets and their surroundings, scenarios for which satellite measurement technology could potentially be useful include:

- predicting impending structural failures through detection of small but changing movements prior to collapse;
- identifying anomalous bridge movements that would indicate signs of potential problems (e.g. seized bridge bearings); and,
- reviewing performances of bridges before and after significant events (e.g. flooding).

1.3 Research philosophy

The research strategy (and subsequent methodology developed) is a means of systematically solving a research problem and understanding the logic and reasoning behind the various steps that are formulated. For this research, considering the purpose and strategy behind the research informed the selection of the specific investigations and experiments undertaken to answer the research questions. The research philosophy can be considered by help of established research ‘paradigms’. The research paradigm can be defined as “the broad framework, which comprises perception, beliefs and understanding of several theories and practices that are used to conduct a research” [11]. The philosophical domain of this work falls largely within the paradigm of pragmatism. To a pragmatist, “the mandate of science is not to find truth or reality, the existence of which are perpetually in dispute, but to facilitate human problem-solving” [12].

This research stems from the consideration of problems faced by infrastructure asset owners in providing effective structural monitoring systems, initially through interviews and discussion with asset owner and manager groups (such as the Bridge Owners Forum, Transport for London and Network Rail based in the UK, and the US Army Corps of Engineers) to identify key concerns and problems faced, and where the most severe concerns lie. The primary goal was to take the science and algorithms developed for use in the earth observation sector and understand how they were constructed and how they can be applied (or

modified) such that they provide useful insights for the purpose of monitoring infrastructure. The research was not undertaken to dispute the basis on which these interferometry methods were derived, but to facilitate and push forward our understanding as it applies to the behaviour of infrastructure assets.

1.4 Research approach

1.4.1 Research phases

The research approach used can be described in three phases (Figure 1.1) as outlined below.

(1) The Preparatory Stage investigated the context and motivations for the research through interviews with asset owners and a literature review of current asset monitoring practice and use of InSAR satellites for remote monitoring of assets. This first phase aggregated knowledge about the problem, and critically assessed work done in this field to date such that a path to suitable hypotheses and research questions were formed. As part of this first stage, a preliminary piece of work was undertaken, processing sample satellite data to create a data acquisition strategy and to place orders for satellite acquisitions for the main experimental phase. This piece of work also facilitated detailed planning of the experimental deployment, selection of suitable test sites and discussions with infrastructure owners to understand access requirements, design test apparatus, and work out instrumentation strategies.

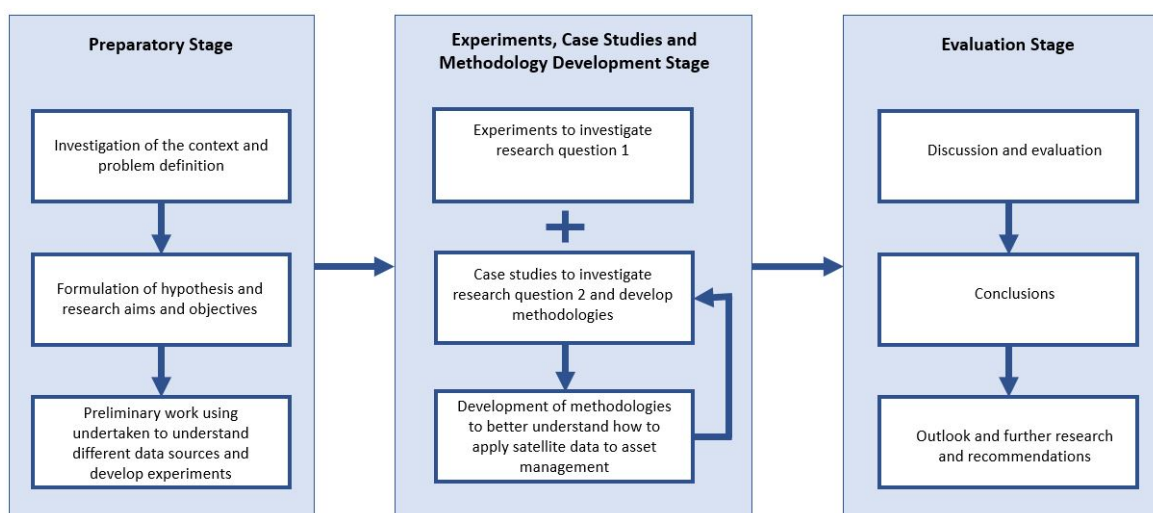


Fig. 1.1 Phases of research.

(2) In the Experiments and Methodology Development Stage, experiments to test the research hypotheses were developed and implemented, and case studies were identified and

examined. This research required mixed methods, employing both experimental and case study methods.

To verify the accuracy of InSAR measurements to investigate the first research question, a classic Experiment strategy provided an appropriate approach, as it is rigid and scientific in structure to enable the research to be replicated. The purpose of an experiment is to test the causal effects of a specified behaviour or phenomena on a group compared to a control set which is not subjected to any phenomena.

The research task to address the second research question considered a collapse which has already occurred in a real-world context (rather than a collapse controlled in laboratory conditions) and problems with bearings, and used satellite imagery from a data archive to analyse the events retrospectively. This was an empirical inquiry investigating a contemporary behaviour or phenomenon within its real-world context, and the boundaries between the behaviour and context were not clearly evident. For this reason, a Case Study is the most appropriate strategy.

(3) In the final Evaluation Stage, the research questions have been answered, with new methodologies developed in the previous stage having been evaluated. This set the scene for a discussion on the lessons learned through this process, and conclusions and outlook for further research are presented.

1.4.2 Methodology

As outlined in the previous section, the research was undertaken using Experiment and Case Study methodologies. Figure 1.2 summarises how these methods are used to address each research question.

	Research Question 1	Research Question 2	Experiments	Case Studies
NPL Corner Experiment	X		X	
Waterloo Bridge	X	X	X	X
Hammersmith Flyover		X		X
Tadcaster Bridge		X		X

Fig. 1.2 Summary of research methods.

The first experiment was a controlled experiment, where known points were moved in controlled quantities, and measured using InSAR measurements and in-situ conventional displacement measurements. An experiment was undertaken to impose and measure movement at the ground surface at two distinct points, relative to a third such that the accuracy and reliability of the data could be assessed. To create known points on the earth's surface to monitor, three radar reflectors and a test rig were designed, constructed and installed on an outdoor site at the National Physical Laboratory. Three additional points near the site were measured using Global Navigation Satellite System (GNSS) devices for comparison. The experimental set up, processing methodology and results are presented in Chapter 4.

The second experiment on Waterloo Bridge in Chapter 5 was designed to similarly assess accuracy, reliability and resolution of the satellite monitoring techniques, but in the context of a real life bridge asset. This was not designed as a controlled experiment in the same manner that the corner experiment was, as the bridge movements were not known or imposed in a controlled manner, but rather measured with an in-situ monitoring system (Automated Total Station measurements) and compared with InSAR measurements at known locations. Within this work, the uncertainty and relationship of these datasets were examined to understand the application of satellite data in bridge monitoring contexts.

A 'Case Study' is defined by Yin [13] as "an empirical inquiry that investigates a contemporary phenomenon (the 'case') in depth and within its real-world context". Employing this method, highlighted in a pragmatic manner not only what InSAR measurement can provide under theoretical or controlled environmental settings, but also the practicalities of using such measurements as it relates to structures in the real world (where the boundaries between the behaviour and context are not clearly evident as they are with a controlled experiment). To address the second research question, Chapter 6 on Hammersmith Flyover considered a bridge with known bearing and movement problems and Chapter 7 on Tadcaster Bridge considered the collapse of a bridge that had already occurred, in a real-world context (rather than a failure or collapse controlled in laboratory conditions). Waterloo Bridge in Chapter 5 is also used as a case study to understand how InSAR can monitor a number of different loading and bridge movement effects in the context of its environmental surroundings.

1.4.3 Scope

'Remote sensing' or 'remote monitoring' has a number of definitions, but in essence it is the acquisition of data about an object without contact or physical touch. Satellite monitoring is considered for this research as it provides a means of remote monitoring without having to be physically present at the asset of interest. Within the broad field of satellite monitoring, InSAR technologies are considered as they provide a means of measuring small-scale

movement. Other data collected on various bands of the electromagnetic spectrum (such as optical or hyperspectral imagery) provide insights into environmental surroundings, but measuring movement is a more useful form of quantitative data which more clearly quantifies bridge behaviour. An alternative technology which makes use of satellites to measure movement are Global Navigation Satellite Systems (GNSS), such as the commonly known American-owned Global Positioning System (GPS). This form of measurement requires the installation of an on-the-ground receiver at each point of interest on the asset to take measurements using navigation satellites and is better suited to fulfilling high-frequency monitoring and rapid/near-real-time delivery of contemporary measurement data. InSAR provides an attractive option by using the structural asset itself without a receiver (or with the option of enhancing asset reflectivity through low-cost reflectors, discussed later in this work).

There are various asset-monitoring situations in which InSAR can be deployed, and these are discussed in more detail in Chapter 3. The focus of this research was specifically limited to bridge structures, building on existing work within the field of InSAR monitoring of bridges and working towards addressing gaps identified within the literature (as outlined in Chapter 3). Within this scope, there existed the opportunity to integrate civil engineering structural knowledge and monitoring methods with the advancements progressed by the satellite monitoring sector to derive value from InSAR satellite data for bridge asset owners.

1.5 Outline of thesis

This thesis is structured as eight Chapters which work through the research phases (Figure 1.3). It begins with this Chapter, which introduces the research, the motivations behind why it was undertaken, and describes the aims and objectives that it seeks to address. The research philosophy and broad methodology of the research set up and experimental design are also discussed.

Chapter 2 describes Interferometric Synthetic Aperture Radar (InSAR) and provides an introduction to the basic theory behind the production of SAR images acquisitions and the image processing methodologies used to employ InSAR techniques for the purpose of infrastructure monitoring.

Chapter 3 is a literature review plus evidence from interviews which first explores current approaches to bridge inspection and management. A critical review of the effectiveness of different solutions currently employed is presented in order to provide an understanding of

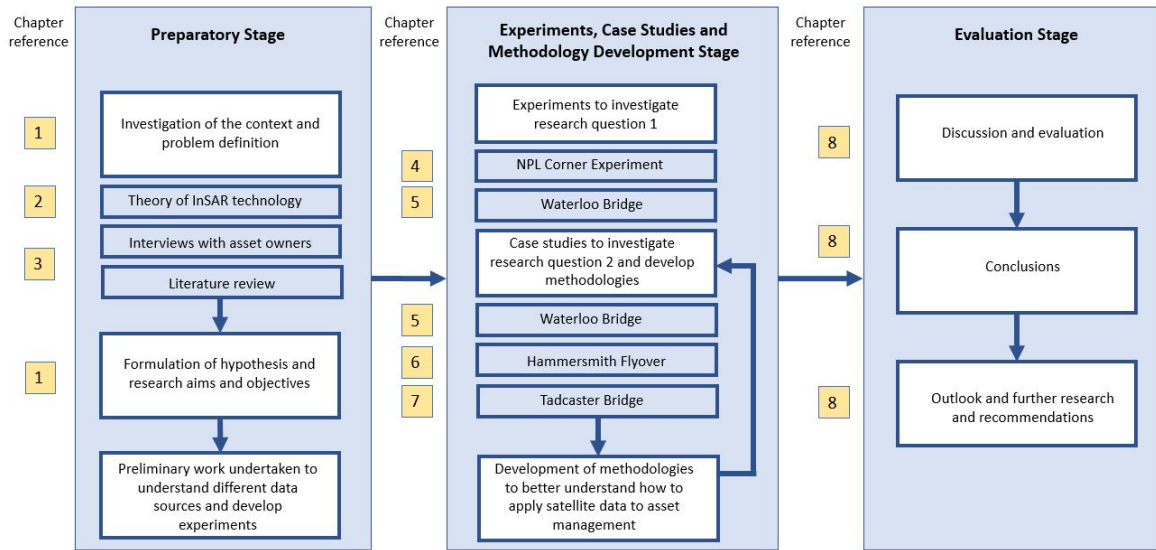


Fig. 1.3 Phases of research aligned with thesis structure.

how technologies, such as InSAR, can provide clearly demonstrable value to asset owners. A review of the current state-of-the-art in InSAR monitoring is then presented. This includes a review of research into InSAR for bridge monitoring and was undertaken to assess what research has already been undertaken and critically evaluate where there are gaps in the current body of knowledge.

Chapter 4 describes a controlled experiment undertaken to assess the uncertainty of the InSAR measurement data being analysed, using known imposed movements and measuring response using conventional ground-based and InSAR measurements.

Chapters 5 presents an experiment on Waterloo Bridge in London, which compares InSAR measurements against traditional surveying measurements. The use case investigates the uncertainty of measurement data (in both SAR and ground-based measurement) and highlights the importance of incorporating environmental data into bridge management, modelling and assessment. The Chapter also explores how InSAR data sets can be combined with traditional surveying techniques to unlock additional insights.

Chapter 6 is a case study which looks at Hammersmith Flyover in London. In-situ displacement sensors are used to provide measurement data against which the InSAR data can be compared. The focus of this Chapter is on the development of methodologies for which InSAR measurements can make use of current digital environments used in the civil engineering field, and also presents a method developed to select data points of interest

within the InSAR data. The methods introduced are then applied to show how InSAR can be used to identify anomalies in bridge behaviour, and thus has potential for use as a system to warn of potential bridge deficiencies.

Chapter 7 presents evidence of how InSAR techniques can be used to monitor bridges at risk of scour, using Tadcaster Bridge, England, as a case study. The study highlights how precursors to failure can be observed in InSAR data well before actual collapse of the bridge. The chapter also discusses how InSAR monitoring could, in some instances, be developed as an early warning system for the structural health monitoring of bridges.

Finally, Chapter 8 reviews the research and discusses the work undertaken with respect to answering the research questions, commenting on the use of InSAR for bridge monitoring in everyday asset management. It then provides some concluding remarks and recommendations for areas of future research.

Chapter 2

InSAR Theory

2.1 Introduction to Synthetic Aperture Radar

Synthetic Aperture Radar (SAR) has been used for remote sensing of the earth for over 30 years to monitor various phenomena, such as monitoring earthquakes, flood mapping, and sea and ice classification [14]. It is an active remote sensing system which acquires data by sending and receiving radiowaves or microwaves (both in the invisible part of the electromagnetic spectrum with wavelengths in the millimetre to metre range). Unlike optical imaging systems (which use light waves) SAR is able to penetrate through clouds and precipitation, and can also be used both day and night irrespective of sun illumination of the ground. Thus, SAR provides a technology which can provide high-resolution, all-weather imaging with global coverage.

Satellites with the objective of SAR data collection are designed to follow a near-polar orbit (i.e. they travel in a north-south direction from pole to pole) around the earth. The satellites travel northwards on one side of the Earth (the ascending pass) and then towards the south pole on the second half of their orbit (the descending pass). In conjunction with the earth's own rotation (east-west) this orbit allows the satellite to cover all of the earth's surface over about 10 days.

The following Chapter provides an overview of the relevant theory leading to the formation of SAR images and the processing undertaken for this research. The intention is to provide an understanding of the key elements related to the application of InSAR for bridge monitoring but avoid detailed descriptions and derivations for which there are a number of suitable reference books. For further information on SAR image formation, books by Bamler and Schättler [15] or Cumming and Wong [16] provide useful descriptions. Bamler and Hartl [8] and Hanssen [17] are key literature references on Interferometric SAR (InSAR) process-

ing. There are also various other tutorial papers and guides available on SAR principles and theory [18–21].

2.2 Basic SAR principles

SAR systems have a side-looking imaging geometry which takes images by means of radar pulses installed on a forward moving satellite. Figure 2.1 illustrates the typical SAR imaging geometry, where the satellite moves in an along-track, or *azimuth*, direction. The direction perpendicular to the flight path is known as the *slant range*. The *nadir* is the point on the earth surface directly below the satellite sensor as it progresses along its line of flight. The width of the acquired image is the *swath width*, but the length of the image is dependent on how long the radar is turned on for. The angle between the radar slant range and the vertical (z) is called the *incidence angle*.

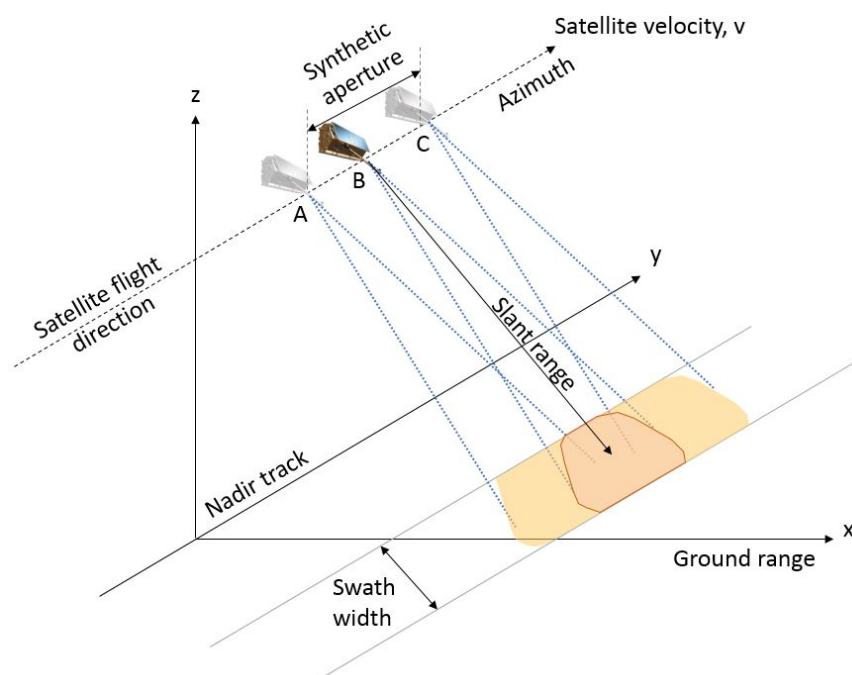


Fig. 2.1 Synthetic aperture radar imaging geometry and key terminology.

This system makes use of the flight path of the satellite to electronically simulate a much larger antenna (or aperture) than the satellite actually carries. This attribute is the basis of the name "synthetic aperture radar" or "SAR". This synthetic aperture concept exploits the fact that different targets falling within the antenna footprint display different Doppler frequency shifts in their reflected radar signals. The SAR processor on the satellite stores returned radar

signals for the time period, say T , from position A to C in Figure 2.1. An appropriate coherent combination of the received signals (taking into account their Doppler history) allows the reconstruction of a signal which would have been obtained by a virtual aperture (of length $v \cdot T$, where v is the satellite speed) that is much longer than the physical antenna length. This makes the "synthetic aperture" large and hence a higher resolution can be achieved for a smaller antenna length.

A SAR signal is a wave that is almost purely sinusoidal in nature, $\sin\phi$, with a period of 2π radians, which contains amplitude and phase information and has a specific wavelength (Figure 2.2). When features on the ground move, the distance between the sensor on the satellite and the earth's surface changes, thereby producing a corresponding change in measured signal phase. The changes in measured phase values that occur between repeat passes (and therefore image acquisitions) of the satellite are used to quantify ground movement in the direction of the line of sight of the satellite. As the signal is periodic, travel distances that differ by an integer multiple of the wavelength result in exactly the same phase change. Therefore, the phase of the SAR signal indicates the fraction of the wavelength of the last wave cycle. The number of 2π cycles that the wave has travelled is not counted, but will this unknown number of 2π cycles need to be considered when working with SAR measurement data (as explained later in this chapter).

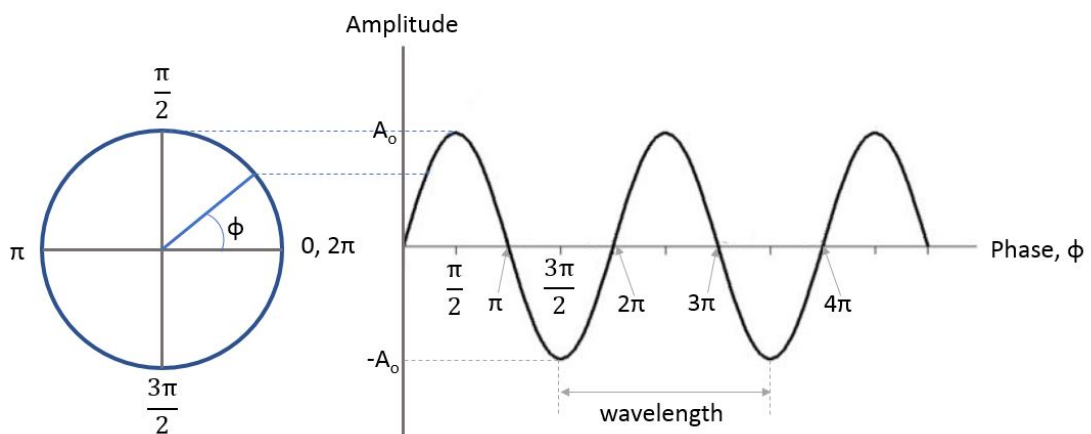


Fig. 2.2 Radar wave characteristics.

The SAR satellite system transmits these sinusoidal signals as electromagnetic pulses and receives the echoes of the back-scattered signal. To do this, the SAR sensor on these satellites commonly uses frequency modulated pulsed wave-forms in the form of "chirped" signals for transmission of the sinusoidal wave. A linear "chirped" signal is a sinusoidal wave

that increases in frequency linearly over time (Figure 2.3). The amplitude of the transmitted sinusoidal waveform is constant during the pulse time. The reason the sinusoidal pulse is transmitted as a "chirp" is that in these "chirped" signals the pulse is allowed to be much longer, and therefore allows more energy to be emitted and received. The SAR sensor on the satellite emits the pulse, and after it is emitted there is an "echo window" period where the SAR sensor collects the back-scattered echoes and stores the received signals.

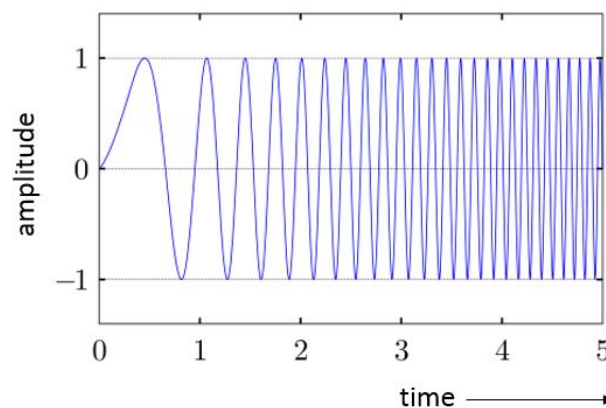


Fig. 2.3 Chirped signal containing the sinusoidal waveform.

2.2.1 SAR imaging

The components of the reflected and received signal must then be assigned to the correct position within the spatial representation of the imaged area on the SAR image. Objects within the imaged area experience different Doppler frequency shifts in relation to their distances from the satellite track (the SAR sensor is moving between emitting and receiving radar) due to the Doppler effect. This is analogous to the perception in sound of an ambulance moving towards or away from a person - the pitch appears higher than that of a stationary alarm due to the increase in frequency of sound waves, and as it passes away, the pitch appears lower due to the decrease in frequency. At the front (or leading) edge of the beam ahead of the SAR sensor, objects reflect the radar with an increased frequency. Those at the back end of the beam are reflected with a decrease in frequency, and the radar is actively operated such that the frequency and delivery of signals are knowingly sent and received. Thus, the frequencies of transmitted and reflected signals can be compared to understand the frequency shift and the reflections can be assigned to their correct positions within the image.

SAR imaging is the production of a digital SAR image that is made up of a two-dimensional matrix formed by columns and rows of ‘pixels’. The two dimensions of the matrix correspond to the range direction and the azimuth direction. The pixels are also known as ‘resolution cells’ and are associated with an area on the earth’s surface (the size of the resolution cell varies with each satellite). The value in each pixel comes from the received radar reflections and is complex in nature, with the real and imaginary parts of this complex value representing amplitude and phase values respectively.



Fig. 2.4 SAR image of bridges crossing the River Thames, London, United Kingdom. The River Thames can be seen as a dark (black) feature within the SAR image, with the bridges spanning the river reflecting to different extents due to individual bridge properties.

2.2.2 Speckle

A SAR image of distributed targets contains noise in the form of *speckle*. With a pulse radar system such as SAR, coherence describes the phase relationships between the transmitted and the received pulses. SAR is a coherent system, and as such speckle noise is inherent. Speckle noise from SAR results from the coherent processing of back-scattered signals from

multiple distributed targets within a SAR resolution cell. Any objects causing a scattering of a SAR signal are called *scatterers*. The total reflection response of the cell is coherent superposition of each scatterer's reflection, and the final imaging result of the cell reflects the vector sum of the scatterers (Figure 2.5). The visible effect of speckle in the image is a seemingly random placement of conspicuously bright or dark pixels.

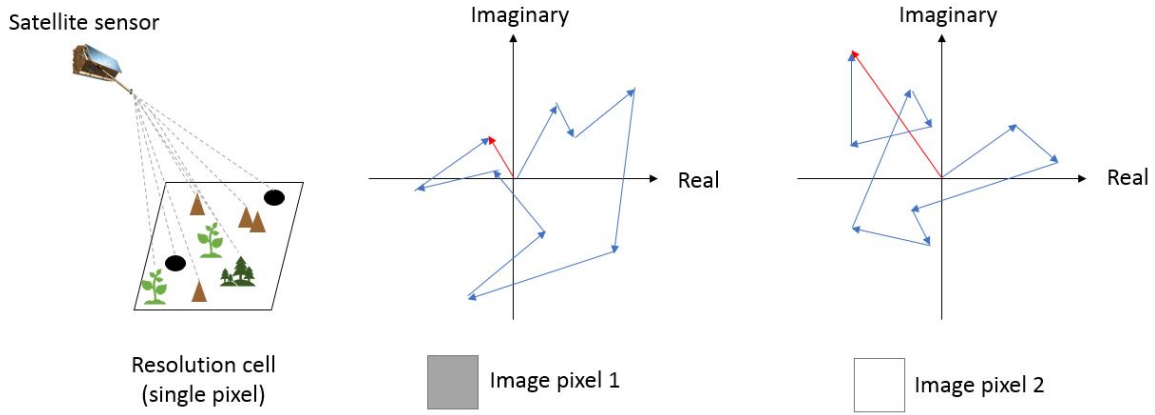


Fig. 2.5 Multiple scatterers within a single SAR resolution cell.

For each resolution cell the total scattered field is the coherent sum of the contributions given by each elementary scatterer, given by Equation 2.1:

$$Ae^{j\psi} = \sum_{k=1}^N A_k e^{j\psi_k} \quad (2.1)$$

where A and ψ represent the amplitude and the phase, respectively, of a certain resolution cell, A_k and ψ_k are the amplitude and the phase of the individual elementary scatterers respectively, and N is the total number of elementary scatterers in the resolution cell.

The noise caused by this effect can impact the ability to identify ground objects (especially point targets) and increase uncertainty of SAR image classification, making it very difficult for edge abstraction (extracting information at the edge of pairwise pixels), image segmentation (the process of partitioning a digital image into multiple segments, typically for identifying objects and boundaries in images), target recognition and classification [22]. It is therefore important to apply methods which reduce the speckle noise, whilst retaining as much detail as possible. There are two broad strategies to achieve this. Non-adaptive filters apply a single filter to the entire image uniformly, whereas adaptive filters are more complex filters which adjust to match local properties within the image, which are computationally more intensive but preserve natural edges and boundaries.

Multi-looking processes are an example of an averaging process that reduces the spatial resolution to improve the radiometric resolution. These processes are efficient but lose a lot

of detail and edge resolution. Over the years, numerous adaptive speckle filter techniques have been developed, each of which have different classes and distributions and have been outlined and compared for performance by de Leeuw and de Carvalho [23].

2.2.3 Interpretation of SAR images

Sometimes SAR data is converted from the slant range projection (the original SAR geometry previously outlined in Figure 2.1) into a ground range projection (Figure 2.6) but it is important to note that data in ground range projection is neither in a cartographic reference system, nor is it geometrically corrected. A more involved geocoding process is required to convert the SAR data into a map projection so that each pixel in the SAR image is directly associated to the position on the ground. Geocoding considers the Doppler frequency shift in the azimuth direction and the non-linear compression of the imaged surface information in the range direction.

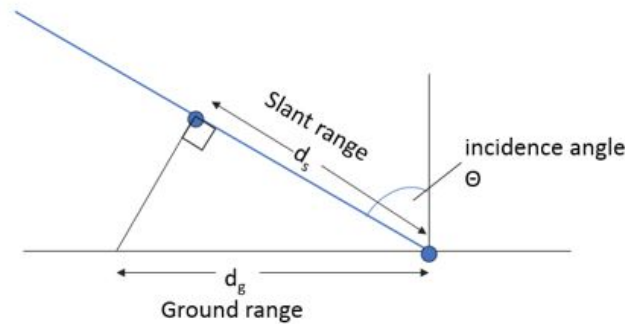


Fig. 2.6 Projection of SAR radar.

SAR images typically appear geometrically distorted. In a radar image, the three-dimensional objects of the scene are mapped to a two-dimensional image in slant-range and azimuth. This results in effects such as the following:

Foreshortening occurs when the SAR radar reaches the base of a tall object tilted towards the radar (e.g. a mountain) before it reaches the top of the object. As the radar measures LOS distance in slant-range, the slope (A to B) in Figure 2.7 appears compressed and its length will be represented incorrectly (a to b) in the image plane.

Layover occurs when the radar beam reaches the top of a tall object (B) before it reaches the base (A) (Figure 2.8). The return signal from the top of the feature will be received before

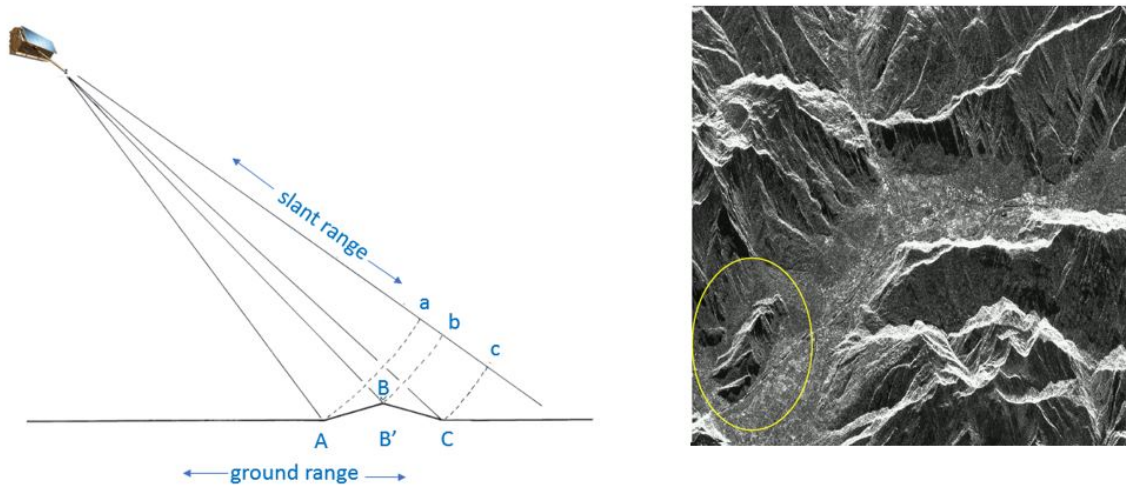


Fig. 2.7 SAR radar foreshortening effect. SAR image provided by Deutsches Zentrum für Luft- und Raumfahrt (DLR).

the signal from the bottom. The end result is that the top of the object is displaced towards the radar from its true position on the ground, and the bottom and the top of such slopes are reverse imaged (b to a). Both layover and foreshortening result in similar visual effects in the imagery, and are both more severe for small incidence angles.

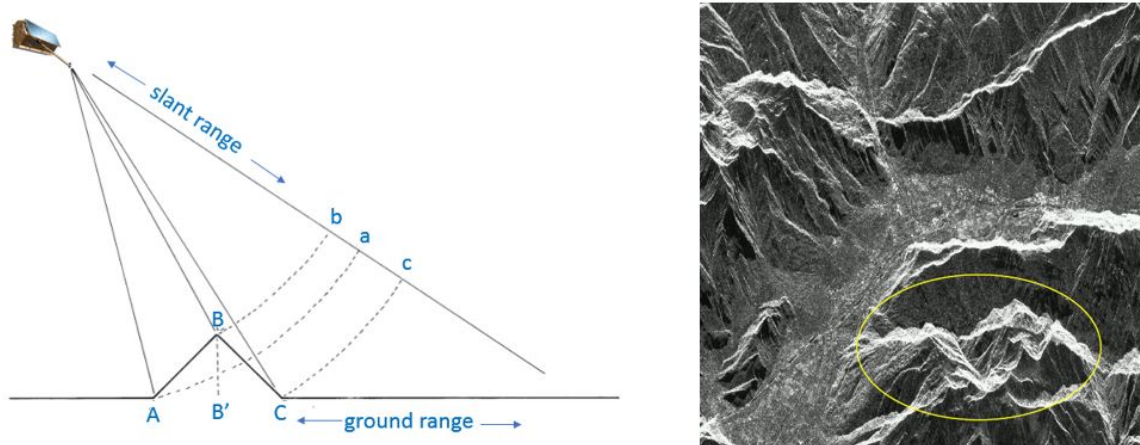


Fig. 2.8 SAR radar layover effect. SAR image provided by Deutsches Zentrum für Luft- und Raumfahrt (DLR).

Foreshortening and layover result in **radar shadows**. Shadow occurs when the radar beam is not able to illuminate the ground because this ground is in the shadow of another feature (Figure 2.9). In the case of bridges in urban scenarios (such as Hammersmith Flyover presented in Chapter 6), the presence of tall buildings adjacent to the bridge put parts of the bridge in shadow, and so parts of the bridge are not imaged by the SAR radar. The effects of

shadows increasing with SAR incidence angle (and so a steeper imaging angle will "see" more of the bridge in this particular instance).

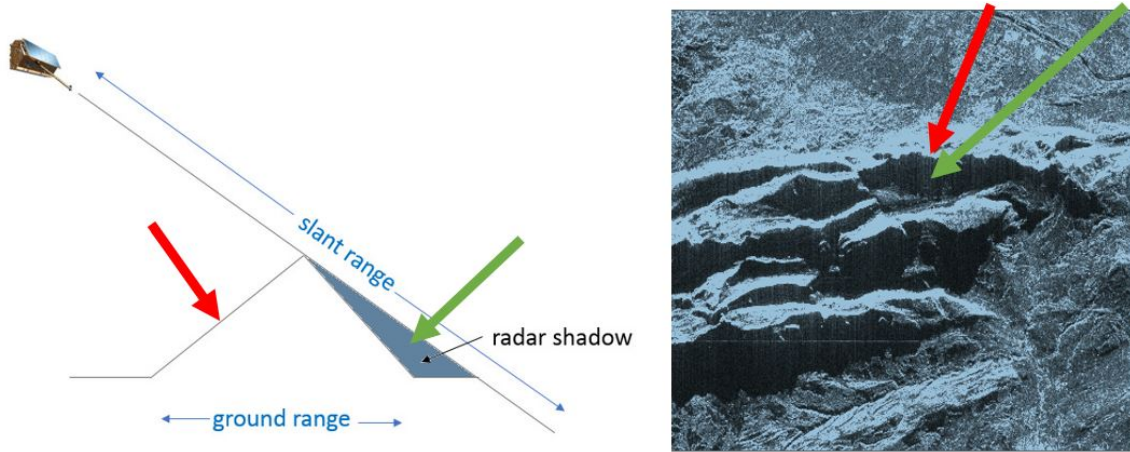


Fig. 2.9 SAR radar shadow effect. Red and green arrows on diagram correspond to the red and green arrows on the SAR image, illustrating these corresponding regions. SAR image provided by Deutsches Zentrum für Luft- und Raumfahrt (DLR).

2.3 Interferometric SAR

In this Chapter so far, the basic principles of SAR signals have been introduced, and the formation and interpretation of single SAR images have been discussed. The strength of SAR techniques lies in combining multiple images through exploiting the physics of interferometry, which is discussed in this section.

The principle of SAR interferometry is to compare the phase of two or more complex radar images for a given scene that have been acquired from slightly different positions or at different times. Interferometry is described by Simons and Rosen [30] as relying on “*the constructive and destructive interference of electromagnetic waves from sources at two or more vantage points to infer something about the sources or the relative path length of the interferometer*”. The satellite generates the outgoing SAR signal (with known phase) which can then be compared to the phase of the return signal which is dependent on the distance to the ground. The complex phase vector information of one image is multiplied by the complex conjugate phase vector information of another image to form an “interferogram”. This results in the common backscatter phase in each resolution element being cancelled whilst leaving a phase term proportional to the differential path delay. Thus, an “interferogram” (such as the example in Figure 2.10) is a complex image with each pixel comprising a phase difference (from 0 to 2π radians) between two distinct SAR snapshots of a given horizontal resolution.

The 0 to 2π radians difference is seen in the image as interferometric fringes (shown in Figure 2.10 as repeating cycles through a rainbow of colours).

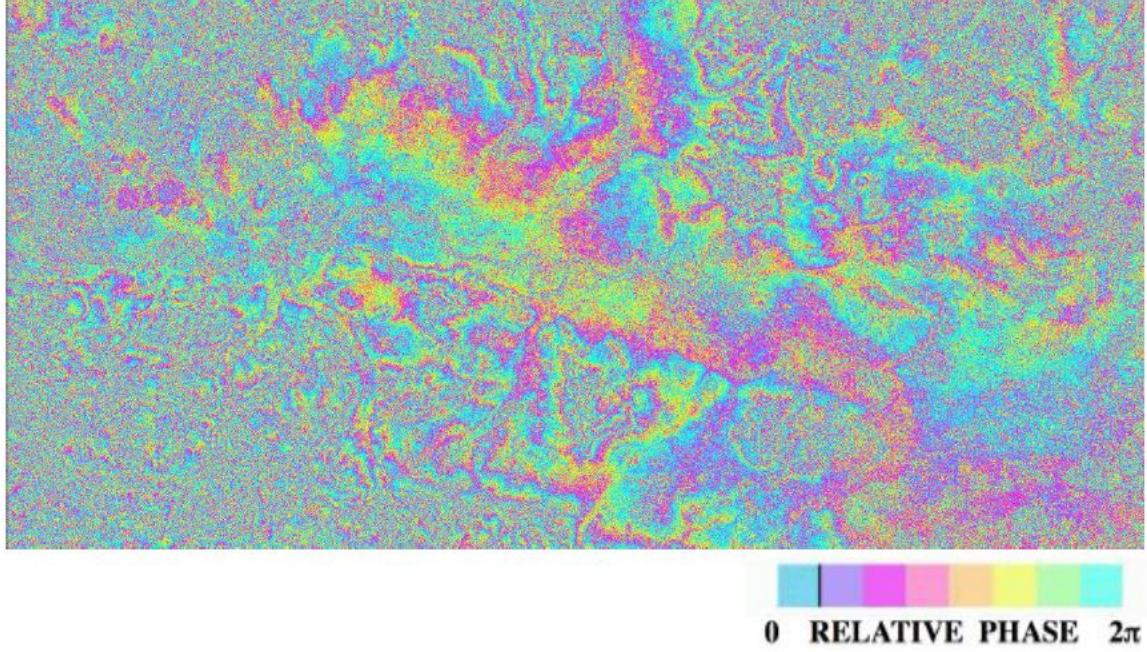


Fig. 2.10 Interferogram of the London area created with Envisat satellite data; this is a phase map proportional to the relative terrain altitude, where the phase discontinuities resemble the contour lines.

The interferometric phase map in Figure 2.10, ϕ_{int} , is composed of the following components (Equation 2.2):

$$\Delta\phi_{int} = \Delta\phi_{defo} + \Delta\phi_{topo} + \Delta\phi_{atm} + \Delta\phi_{orb} + \Delta\phi_{noise} \quad (2.2)$$

where $\Delta\phi_{defo}$ represents the phase due to deformation of the target in the time between the acquisitions, $\Delta\phi_{topo}$ refers to the residual topographic component after removing the external DEM, $\Delta\phi_{atm}$ corresponds to the difference in atmospheric propagation times between the two acquisitions used to form the interferogram, $\Delta\phi_{orb}$ refers to the error introduced due to the use of imprecise orbits in mapping the contributions of Earth's ellipsoidal surface, and $\Delta\phi_{noise}$ represents the phase noise due to the scattering background and other uncorrelated noise terms.

The removal of some of these terms is discussed within the processing methodologies outlined in section 2.4. The interferogram is defined through phase principal values, with values ranging into the interval $(-\pi, +\pi)$. An important challenge which still remains is the presence of a phase 'unwrapping' process which is required to estimate the 2π -multiple

integers, and thus makes the problem non-linear. For every interferogram pixel, there is an estimation of the number of phase cycles to be added to the ‘wrapped’ value. This ‘unwrapping’ issue and its limitations for bridge monitoring is described in further detail by way of examples in Chapters 4 and 5.

Acquiring images from different positions is done from mutually displaced flight tracks and is known as *across-track interferometry* and is used for precise measurement of surface topography (and production of Digital Elevation Models). Images taken from the same flight track, but at different times are used for *along-track interferometry*, which is used for *differential interferometry (dInSAR)*. More advanced techniques based on the stacking of many images allow for the extraction of non-linear subsidence and other slow motion deformation rates through methods such as Persistent Scatterer Interferometry (PSI) [24] explained below in Section 2.4.

2.3.1 Across-track interferometry

A single SAR image does not contain information about the elevation angle and therefore the height of the imaged scene. However, by using the principles of across-track interferometry the elevation angle can be determined. This mode of imaging, which uses two SAR sensors moving with laterally displaced flight paths, results in each scatterer of the imaged scene having a characteristic range difference that can be evaluated to retrieve the surface height. These type of SAR missions can be used to produce a Digital Elevation Model (DEM). Note that ‘ B ’ in Figure 2.11 is the *baseline* (distance between the two satellites), and ‘ B_{\perp} ’ is the *perpendicular or interferometric baseline* (as marked in Figure 2.11).

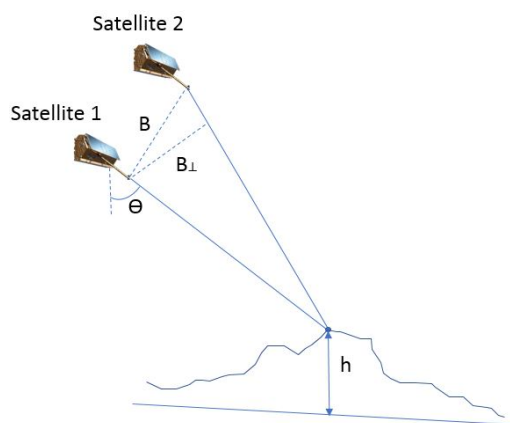


Fig. 2.11 Satellite geometry for interferogram imaging in the plane normal to the flight direction. ‘ B ’ is the baseline, ‘ B_{\perp} ’ is the perpendicular or interferometric baseline, and ‘ h ’ is the height above a selected reference datum.

This research is focussed on movement of structures, rather than generating elevation models (although DEMs are used as input during the processing, as explained later), and will focus on use of along-track interferometry, used in differential interferometry and multi-temporal InSAR, rather than across-track interferometry. Further information regarding the methodology and application of across-track interferometry can be found in the literature, for example in works produced by Bamler and Hartl [8] and Rosen et al. [25].

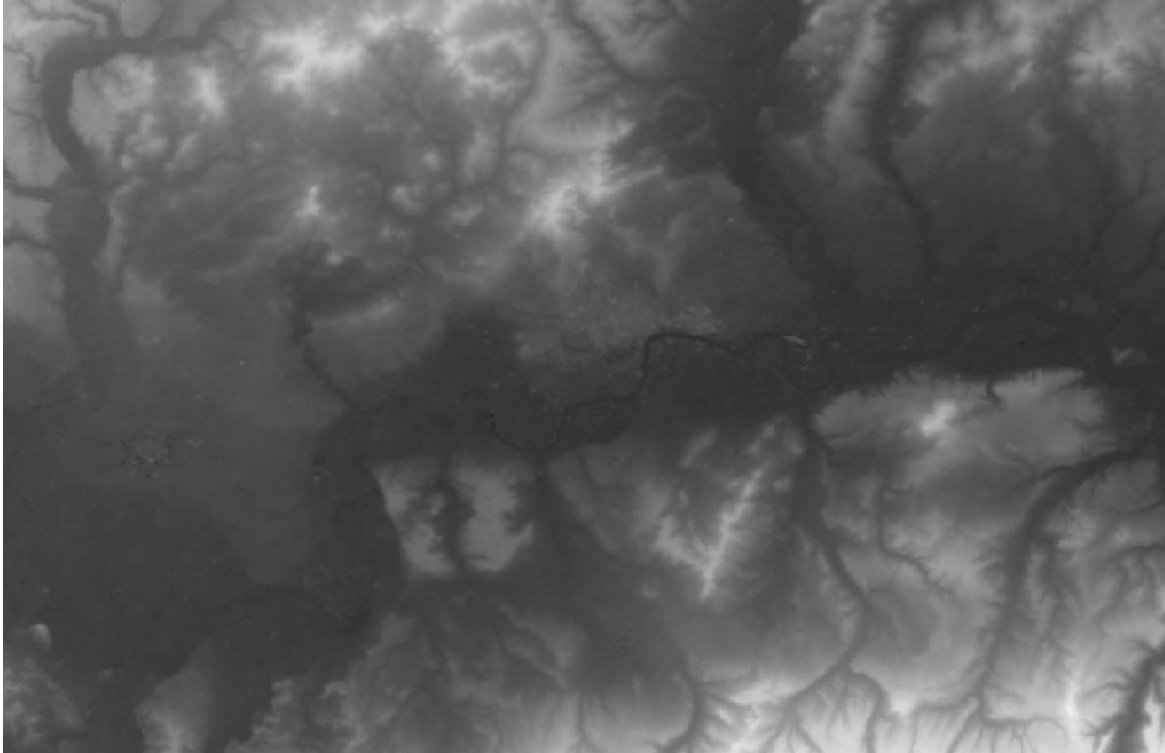


Fig. 2.12 Image of digital elevation model (DEM) from the Shuttle Radar Topography Mission (SRTM) over part of London.

2.3.2 Differential interferometry

Differential InSAR, or dInSAR, was first described by Gabriel et al. [26] and makes use of differential interferograms (two interferograms or an interferogram and a DEM) relevant to the area of interest, to compute the deformation of the observed area. The principle of dInSAR will be briefly summarised below.

As previously depicted in Figure 2.11, the distance between the two satellites in the plane perpendicular to the orbit is called the interferometer baseline, ' B ', and its projection perpendicular to the slant range is the perpendicular baseline, ' B_{\perp} '. Considering two images taken from the same flight track, but at different times to form an interferogram, the phase

information would only be related to the LOS displacement in the scene between the two images provided there was zero baseline (i.e. ‘ $B = 0$ ’) between the satellite positions (something closer to the scenario depicted in Figure 2.13). In reality, there is always some baseline, and the slightly different imaging geometries produce a slight parallax when the area has topography, making the interferogram sensitive to the topography in the scene.

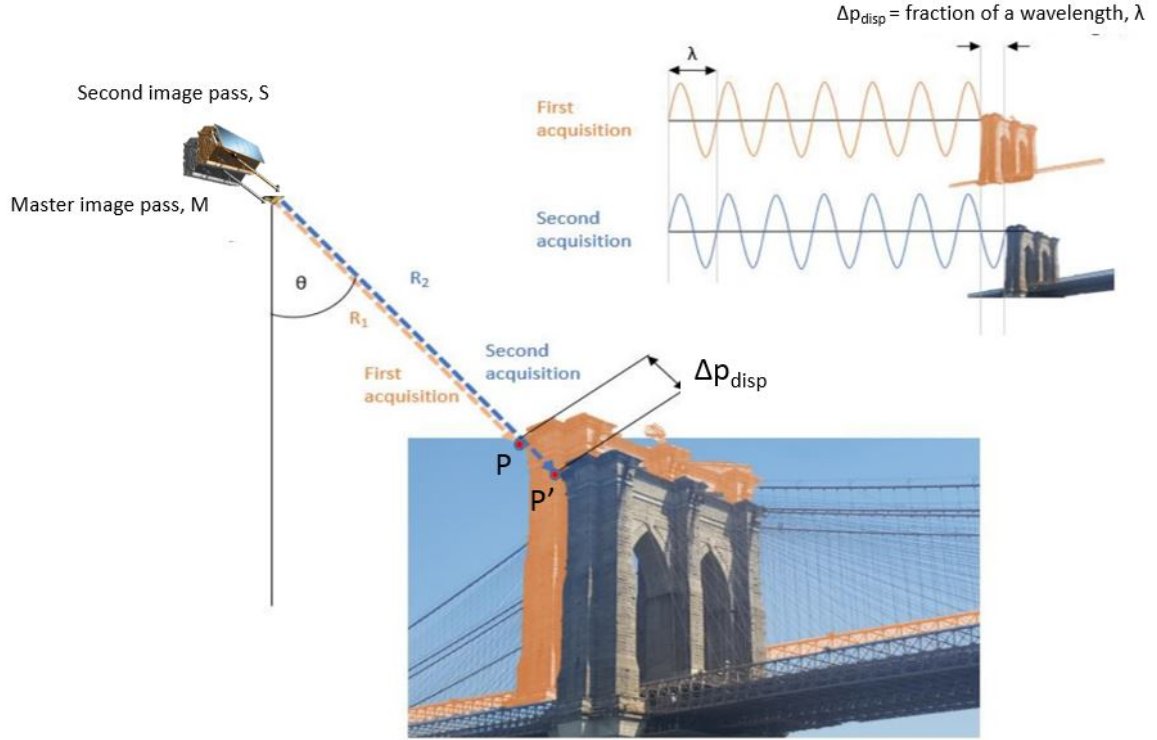


Fig. 2.13 Satellite geometry for along-track (differential) imaging.

Before this consideration, let us consider the general geometry of along-track interferometry (images taken in the same satellite flight track) using Figure 2.13. The change in phase due to the displacement is given by Equation 2.3:

$$\phi_{disp} = \frac{2\pi}{\lambda} \Delta p_{disp} \quad (2.3)$$

where Δp_{disp} is the scatterer change in displacement in the slant-range direction.

To explain the process of differential interferometry, Crosetto et al. [27] considers a single pixel location, P, in Figure 2.13 which is acquired in a SAR image by satellite M measuring a phase ϕ_M :

$$\phi_M = \phi_{geometry-M} + \phi_{scatter-M} = \frac{2 \cdot 2\pi \cdot MP}{\lambda} + \phi_{scatter-M} \quad (2.4)$$

MP is the sensor to target distance, $\phi_{scatter-M}$ is the phase shift generated during the interaction between the SAR waves and the target P, λ is the radar wavelength, and $2 \cdot 2\pi = 4\pi$ accounts for two way path of the radar from the satellite to the ground and back. The same equation holds true for a satellite S passing over this track at a later point, when the target has moved from P to P' and satellite S acquires a second image. The interferometric phase is the difference between these two values:

$$\Delta\phi_{int} = \phi_S - \phi_M = \frac{4 \cdot \pi \cdot (SP' - MP)}{\lambda} + \phi_{scatter-s} - \phi_{scatter-M} \quad (2.5)$$

By adding and subtracting $\frac{4 \cdot \pi \cdot SP}{\lambda}$ to equation 2.5, the following equation is obtained:

$$\Delta\phi_{int} = \phi_S - \phi_M = \frac{4 \cdot \pi \cdot (SP - MP)}{\lambda} + \frac{4 \cdot \pi \cdot (SP' - SP)}{\lambda} + \phi_{scatter-s} - \phi_{scatter-M} \quad (2.6)$$

As the waves are interacting with the same object, the $\phi_{scatter-s}$ and $\phi_{scatter-M}$ term will cancel out and the two remaining terms relate to the topographic phase component, ϕ_{topo} (which includes the reference ellipsoidal phase component due to the assumption of the surface of the Earth being curved as an ellipsoid) and the line of sight (LOS) deformation, ϕ_{def} :

$$\Delta\phi_{int} = \frac{4 \cdot \pi \cdot (SP - MP)}{\lambda} + \frac{4 \cdot \pi \cdot (SP' - SP)}{\lambda} = \phi_{topo} + \phi_{def} \quad (2.7)$$

To find the differential SAR interferometric measurement, this topographic component must be removed. This can be done using an external DEM to remove the topographic phase, leaving the subtle changes in the range distance. It should be noted that for this to work, the external DEM must be of the same order of magnitude or better than the phase sensitivity of the interferometric baseline. Using a DEM model input and subtracting it from Equation 2.7 would leave the differential InSAR phase, i.e. the LOS deformation. An example of a differential interferogram produced for the processing of SAR images taken over the London area for this research is shown in Figure 2.14. The deformation pattern shown in Figure 2.14 are linked to atmospheric disturbances.

However, in reality other considerations must also be taken into account, such as the effects introduced by atmospheric delay and variations in water vapour content in the earth's troposphere. These limitations can be overcome by using a large stack of images in a time series. It is also important to remember, as previously mentioned, that interferometric phase values are known only with modulo 2π (the wrapped phase), and it is therefore not possible to measure phase differences greater than π unambiguously. The limit of π on the differential

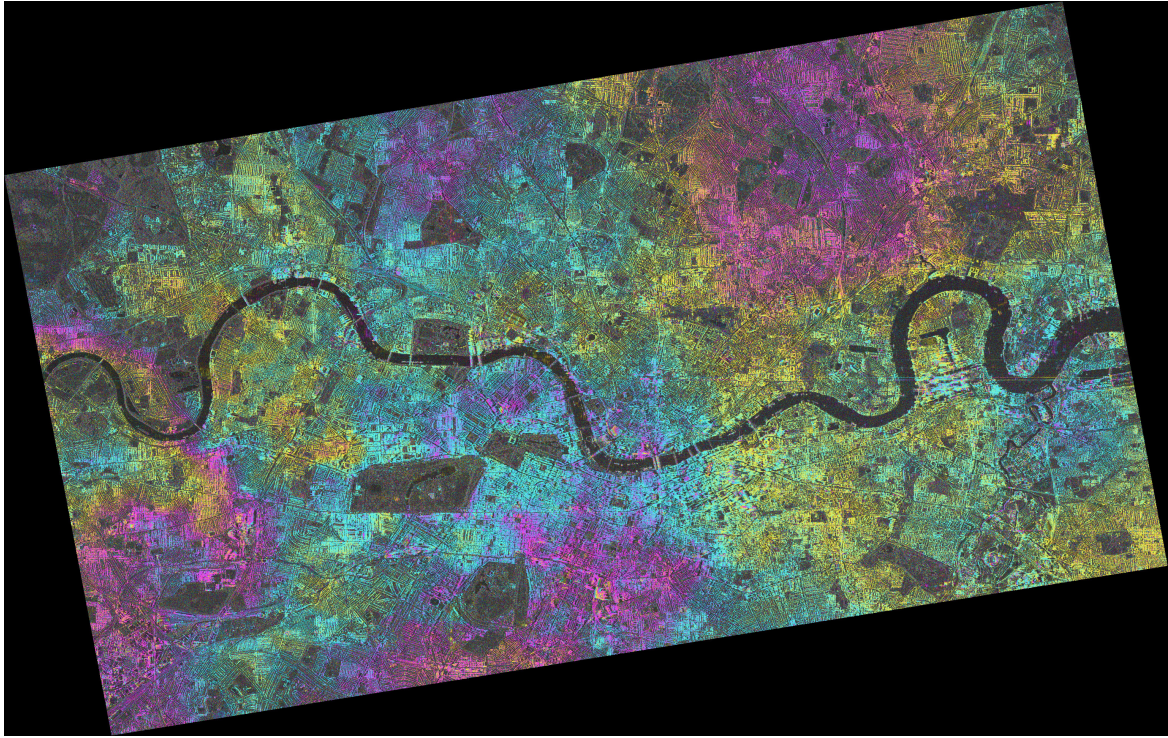


Fig. 2.14 Differential interferogram using TerraSAR-X London SAR images.

phases corresponds to a maximum differential deformation of $\lambda/4$ over two consecutive SAR acquisitions.

Within the context of this research, this limits the bridge monitoring end use cases that can employ InSAR monitoring. For example, using a X-band SAR sensor with a wavelength of 31mm limits the movements that can be unambiguously defined to measurements of 7.75mm or less between acquisitions. To monitor deformation rates of ground surrounding bridge structures, the maximum detectable velocity depends on [28]:

- the spatial gradient of the deformation;
- the spatial density of scatterers;
- the radar wavelength;
- the temporal sampling of the acquisitions defined by the revisit time of the SAR satellite.

Considering the wavelength and revisit time of the TerraSAR-X and Sentinel-1 satellites as an example, the maximum differential deformation rate measurable is 25.7cm/year and 42.6cm/year respectively [27]. These values are theoretical and in practice also depend on

the noise level of the data and the specific phase unwrapping technique used to resolve phase ambiguities.

2.4 InSAR processing methodologies

Multi-temporal InSAR techniques are extensions of the conventional InSAR techniques noted above, aimed at addressing the problems caused by decorrelation (degradation of the quality of interferometric phase) and atmospheric effects. These techniques involve the processing of multiple SAR acquisitions over the same area to allow for the correction of phase noise terms and therefore reduce the errors associated with the deformation estimates.

Several approaches have been described in the literature in order to extract the different contributions of interest, and two of the most established algorithms (which are used in this research) are outlined below. The choice between these two methods is based on the scattering mechanism of the target being studied. The *Persistent Scatterer Interferometry* approach outlined below is for single or dominant point scatterers, whilst the *Small Baselines Subsets* approach (also outlined below) is used for distributed targets. There are a number of other algorithms which develop and vary these methods, and a review and comparison of different methods in the literature is presented by Crosetto et al. [27].

2.4.1 Persistent Scatterer Interferometry (PSI)

The Persistent Scatterer Interferometry (PSI) technique, also known as Permanent Scatterer Interferometry, is the approach proposed by Ferretti et al. [24, 9] and further developed by Hooper et al. [29]. The technique extends the dInSAR principle by using many SAR acquisitions. In this way, it is possible to analyse the temporal dimension in addition to the spatial evaluation and thus to separate the movement from the atmospheric disturbance and the orbital error. In most cases, a linear model of ground motion is assumed for the time series analysis. The potential for this technique to provide movement measurement accuracy of 1mm/year has previously been demonstrated [24, 30]. The experiments showing the potential accuracy are carefully set up with radar reflectors on the top of a carefully selected building and measures line of sight measurement. This research investigates the application of this accuracy in real life scenarios related to infrastructure monitoring and the uncertainty of the data in being resolved into a component of movement (e.g. measuring vertical movement as derived from InSAR line of sight measurement).

2.4.2 Small Baselines Subsets (SBAS)

The Small Baseline Subset (SBAS) technique by Berardino et al., [31] is another extensively used algorithm. SBAS techniques, in contrast to PSI techniques, create differential interferograms based on using SAR image pairs characterised by a small orbital separation (baseline), and allows for the analysis of distributed targets. The SBAS methods involve stacks of low-resolution, multi-looked interferograms which are individually unwrapped. The unwrapped points are selected based on the average coherence which falls above a defined threshold value across all interferograms.

2.5 PSI Processing Methodology

This research primarily makes use of the PSI technique as the majority of case studies concern objects which have strongly coherent points which are used as persistent scatterers (PS). Dense urban areas provide large numbers of suitable PS candidates due to the materials and geometries of the scene. Most of the studies in this research are based in the urban setting of the city of London, UK and as such PSI was the predominant processing technique used. Hammersmith Flyover in Chapter 6 was found to have natural PS along the deck and was processed using PSI. In the case of Waterloo Bridge in Chapter 5, the bridge was enhanced with reflectors which then made it ideal for PSI analysis. In the study of Tadcaster Bridge in Chapter 7, the site did not provide suitable PS candidates and so an SBAS approach was adopted. For this particular case, the processing involved in SBAS analysis is outlined in that case study (Chapter 7). For PSI analysis used in the rest of the studies, an overview of the processing chain is summarised in Figure 2.15 and outlined in the subsections below.

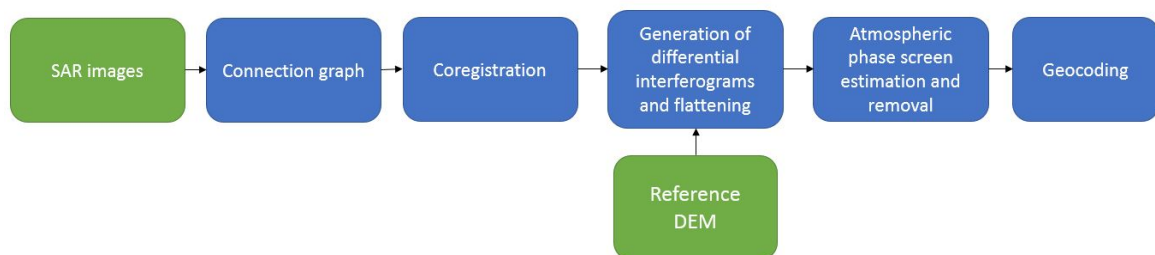


Fig. 2.15 Simplified PSI processing chain.

2.5.1 Coherence

When employing such measurement techniques, it is important to understand the expected progressive movement or behaviour such that a point out of line in a trend can be recognised.

If the movement jumps up and down in an unpredictable way between readings, it is difficult to identify what results are reliable and what is noise or an error. The signal to noise ratio (SNR) is therefore a useful measure of the interferogram quality [32]. Decorrelation creates areas that are spatially disjointed and irregular over time, leading to difficulties in interpreting the geodetic movements.

Coherence (or correlation, as the two terms are often used synonymously) is a measure of how much two "pixels" look alike, and is an estimate of phase noise, taking a value between zero and one. Coherence will comprise contributions from a number of effects, which can be summarised by Equation 1 below (where the magnitude $|\gamma|$ is the coherence and $\gamma = 1$ signifying completely coherent scatterers with an absence of phase noise), as defined by Simons and Rosen [33]:

$$\gamma = \gamma_N \cdot \gamma_G \cdot \gamma_Z \cdot \gamma_T \quad (2.8)$$

where:

γ_N is the correlation influenced by noise in the radar system and processing approach.

γ_G the correlation influenced by the different observing geometries, or look angle of the satellite. This is also known as baseline or speckle correlation. The key consequence to note is that there exists a critical perpendicular baseline of the satellite positions, over which the interferometric phase becomes pure noise.

γ_Z the volumetric correlation influenced by the vertical extent of scatterers. e.g. due to vegetation. The critical baseline reduces in the case of volume scattering when the scatterers are not present on a plane surface, but instead are present within a volume (for example, the branches on a tree). For such examples, the speckle change also depends on the depth of the volume occupied by the scatterers.

γ_T the temporal correlation which depends on the time between image acquisitions and is influenced by repositioning of scatterers within a resolution element over time. The longer the temporal resolution, the more likely that the surface changes between image acquisitions.

2.5.2 Connection graph

At this stage the combination pairs of SAR images used to generate differential interferograms is defined. The differential interferograms to be generated are based on the relationships established in this stage and depicted in the connection graphs. In PSI processing, these interferogram pairs all have one image in common, a Master image, which is selected as the reference image for the processing for which all the processed slant range pairs will be co-registered (the image denoted by a yellow markers in each of the graphs in Figure 2.16).

The points and pairs are plotted as the normal distance (perpendicular baseline, ' B_{\perp} ', of the satellite positions) of the satellite from the Master acquisition satellite location (vertical axis) and the input acquisition dates (horizontal axis) as shown in Figure 2.16. The Master acquisition is selected such that it is approximately in the centre of these two parameters and filters can be applied so that certain acquisitions are discarded based on certain parameters. For example, those which have too large a spatial baseline (increasing the likelihood low coherence) can be discarded.

2.5.3 Coregistration

The SAR images are coregistered, meaning that they are spatially aligned using the amplitude values within the SAR image pixel. Precise coregistration is required before interferograms are generated to increase the coherence of the interferogram, to improve the quality of the phase unwrapping procedure, and to lead to a more accurate phase in the final interferogram [34].

The conventional process of coregistration was based on iterative techniques, cross correlation of the detected amplitude images and the concept that the quality of the interference fringes between images is highest when the images are correctly aligned [35]. Other methods evaluate the phase information of different spectral properties of the SAR signal to evaluate incorrect coregistration information on a pixel by pixel basis [34]. Li and Bethel [36] summarise the commonly used SAR image coregistration algorithms and evaluate these methods with SAR data.

2.5.4 Interferogram Generation

As previously outlined, interferograms are formed to measure the phase difference between two complex SAR images. This is done by multiplying one image by the complex conjugate of the other. To explain this, and using the notation set out by Bamler Hartl [8], let the single complex-valued SAR image be $u_i = |u_i| e^{j\phi_i}$, where $|u_i|$ is the amplitude, ϕ_i is the phase and the subscript i indicates the master ($i = 1$) or the slave image ($i = 2$). After coregistration of the two images, the interferogram, v , is formed by:

$$v = u_1 u_2^* = |u_1| |u_2| e^{j(\phi_1 - \phi_2)} = |u_1| |u_2| e^{j\phi} \quad (2.9)$$

where $*$ indicates the complex conjugate operator.

The end result is a pattern of fringes containing all of the information on the relative geometry between the two images. Each cycle of colour represents a cycle (modulo 2π)

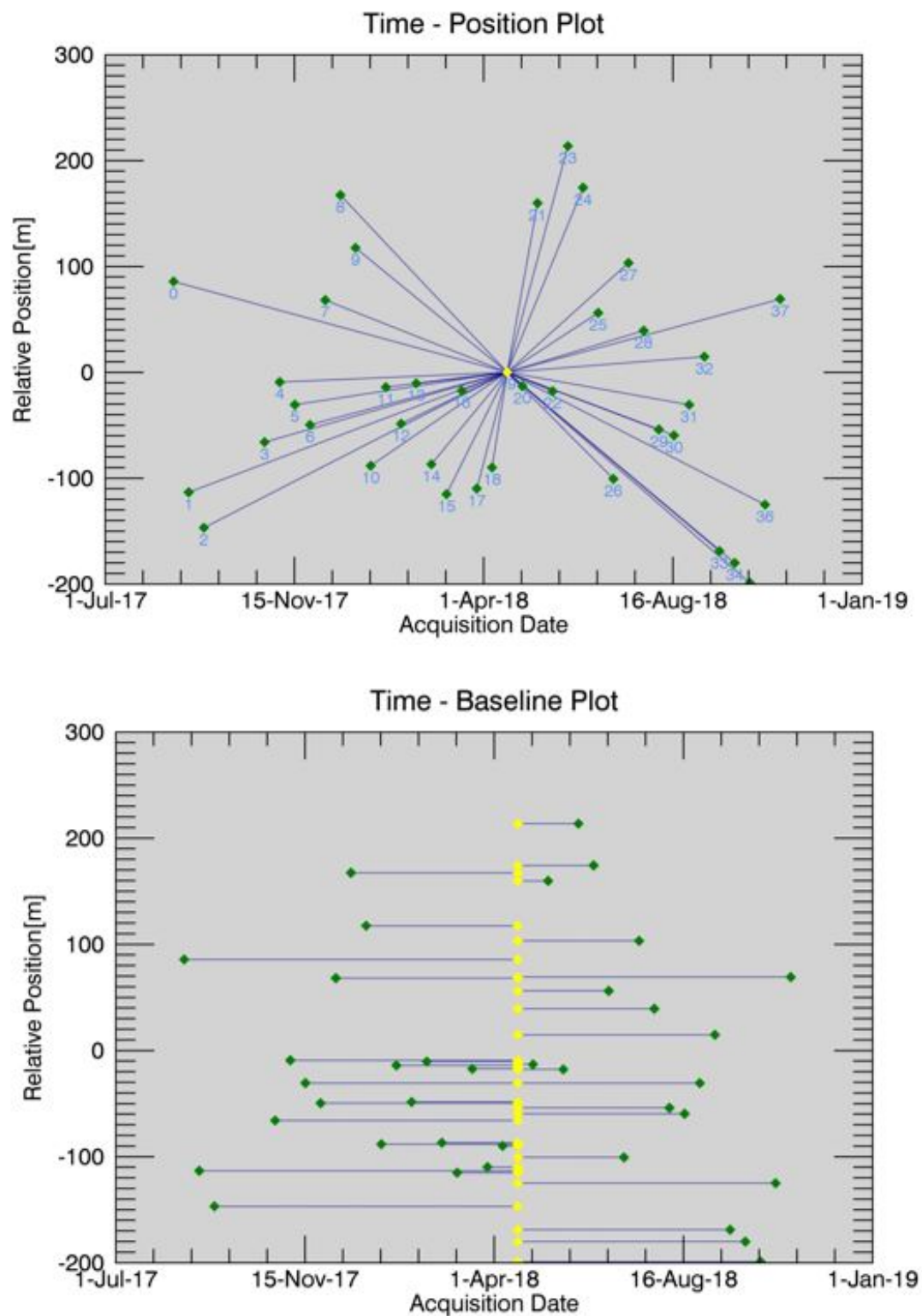


Fig. 2.16 Example connection graphs used for data processing in this research. The Master acquisition is marked as a yellow point with other acquisitions marked as green points. The connections are the pairs of interferograms generated during the processing. Figure produced using ENVI SARscape software.

of the interferometric phase. An example of an interferogram was previously depicted in Figure 2.10. For PSI, a ‘differential interferogram’ is required. Differential interferograms are generated by subtracting pairs of interferograms from one another (or a DEM from an interferogram).

2.5.5 Flattening and topical phase removal

The topographic phase (ϕ_{topo}) term in the interferometric (ϕ_{int}) Equation 2.2, is not of interest for displacement mapping and must be removed (topographic fringes visible in Figure 2.17). Several techniques have been developed to do this. They all essentially derive the topographic phase from another data source, either a DEM or another set of interferometric data. The Interferogram Flattening method adopted for this research is performed using an input reference Digital Elevation Model.

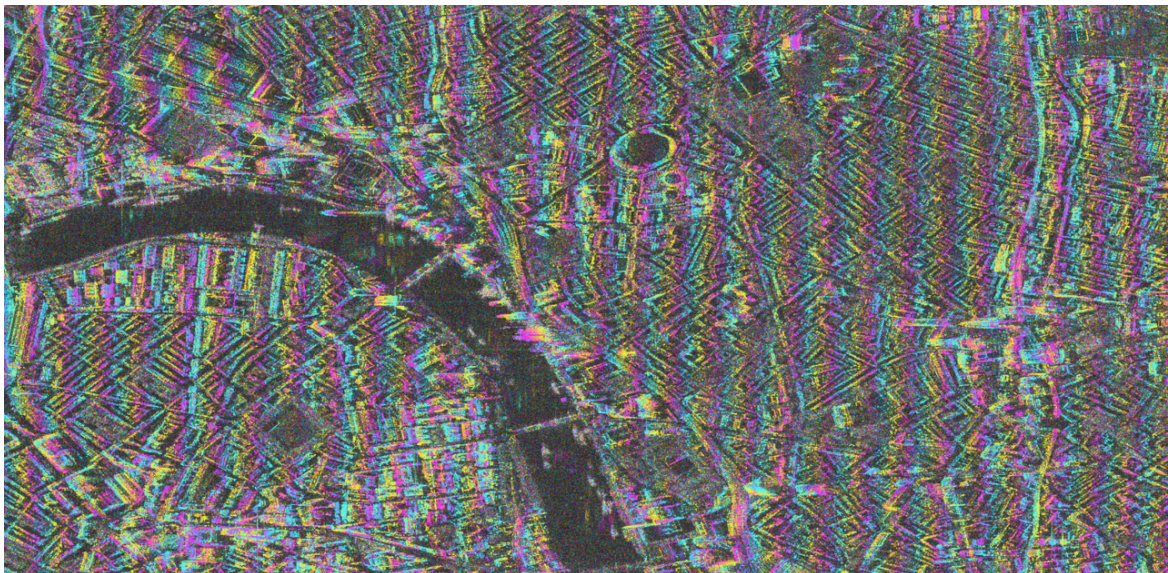


Fig. 2.17 Interferogram using section of TerraSAR-X London data for two images taken with an 11-day interval, before the topographic component is removed using DEM.

2.5.6 Atmospheric phase removal

The atmospheric phase component of each image is primarily due to the water vapor content in the troposphere which the SAR has to pass through and varies from image to image (and also within a single image). This contribution is sometimes referred to as the Atmospheric Phase Screen, or APS. In the previous steps, the ϕ_{topo} from Equation 2.2 has been estimated, and after removing this component from the image stack, a new set of residual differential

interferograms is created. This residual information contains the APS and the phase noise. The APS component can be estimated by applying spatial and temporal filters, exploiting the frequency response of the APS both in time (high-pass) and space (low-pass), and can then be removed. After the removal of the APS component, the remaining residual motion is added to the previously estimated deformation, thus estimating the deformation over time for each pixel.

2.5.7 Geocoding

In practical applications, decorrelation occurs in cases such as open water where the surface is constantly turbulent. Complete decorrelation, $\gamma=0$, occurs even with very short satellite re-visit periods. Snow can affect correlation in winter months, with correlation returning after the snow has gone. In the context of this research, construction sites, with ground profiles constantly changing or objects frequently moving around, will result in decorrelation, and therefore a lack of PS candidates. During the PSI processing the correlation values are calculated for each PS, and PS points above a selected threshold are selected.

The selected PS points are then mapped onto commonly used earth coordinates such that they can be interpreted on maps we use everyday. The process of geocoding SAR interferograms is defined by Schwäbisch [37] as "the conversion of the unwrapped interferometric phase into a terrain map in an earth-related coordinate frame". The height and deformation estimates of all PS points are made relative to a reference, or Ground Control Point (GCP), which can be selected based on a PS at a point known to be stable or at a point where the displacement is known (and can be input into the processing). If a known GCP is not input, the PSI process can assume a height value, which is extracted from the external Digital Elevation Model (DEM) supplied during processing, for this GCP. If the reference point is not stable in time or its true absolute height value is not equal to the corresponding DEM height, the resulting height and deformation estimates will be biased by these effects. For the geocoding of PSI results for the United Kingdom employed in this research, the results have been projected onto the geographic coordinate system World Geodetic System 1984 (WGS84) with the Universal Transverse Mercator projected coordinate system for the 30 North region (UTM30N).

2.6 Available data

The SAR satellites operate at designated frequencies with L-band, C-band, and X-band being the predominate wavelengths. This research makes use of X-band data (approximately

3cm in wavelength) as these satellites collect SAR images with a higher resolution (and relatively narrow swath width) than L-band or C-band satellites. There are a number of systems currently providing SAR data, including historical satellites that are no longer in service but from which data from past missions is available to access. These satellites differ not only in radar frequency and wavelength, but also in polarisation, temporal resolution, spatial resolution, swath, availability of data and cost [18].

Civilian SAR satellites have been available as data sources since the early 1990s. The radar satellite ERS-1 (European Remote Sensing Satellite) was launched on in July 1991 by the European Space Agency (ESA). Together with the identical satellite ERS-2, which was launched in April 1995, this satellite system provided a database for SAR interferometry applications in the period from 1992 to 2001. These sensors orbited the earth at an altitude of around 780km and acquired over the same area of Earth every 35 days (repeat cycle). The spatial resolution of this radar data is 4m by 8m. Only one acquisition mode was available, which facilitated a continuous and comprehensive Earth observation. The ESA successor Envisat / ASAR (Environmental Satellite / Advanced SAR) had a different mission concept. It was more flexible in the acquisition process (i.e., it had a configurable radar beam in elevation) and was therefore not used for continuous area monitoring. Its spatial resolution and the repeat cycle of the SAR images acquired were similar to those of the previous ERS satellites. It was launched in March 2002 and could be used interferometrically until 2011. Sentinel-1 is the successor to Envisat and is currently operational. It was launched in April 2014 and provides images over every 6 days (the mission currently comprises two satellites). This satellite provides a frequent repeat cycle, and ESA provides this SAR imagery free of charge. However, the spatial resolution is approximately 20m by 5m. This strongly limits applications such bridge and infrastructure monitoring unless the structure is very large. For this reason Sentinel-1 imagery was not used in this research.

There are a number of SAR satellites that provide a finer pixel resolution. Bovenga et al. [28] summarise many of the current SAR satellite missions and some key details related to each constellation. Two of the current SAR satellite constellations were used in this research (Table 2.1). TerraSAR-X and TanDEM-X are two German SAR missions operated by the German Aerospace Center (DLR). TerraSAR-X was launched in June 2007 and its twin satellite, TanDEM-X, was launched in June 2010. These two satellites travel close to one another (so even with two satellites in orbit, the repeat cycle over a selected area of the earth is 11 days). The reason for having two satellites travelling close to one another is to facilitate simultaneous across-track interferometry from two slightly different angles to derive a world-wide digital elevation model (DEM) of the earth's surface. Cosmo SkyMed-X is a SAR mission operated by the Italian Space Agency (ASI). It has similar specifications

of TerraSAR-X but it is based on a constellation of 4 satellites, providing interferometric acquisitions on the same area every 4 days (the repeat cycle of a single sensor is 16 days). The first satellite of this constellation was launched in December 2007 and it is still active today. Both of these satellite constellations are commercial satellite constellations, and so imagery must be either purchased from the provider or granted for academic research use.

Table 2.1 SAR Satellite launch information

Satellite Constellation	Operating Agency	Launch Date
COSMO-SkyMed-X	ASI (Italian Space Agency)	1 - June 2007 2 - December 2007 3 - October 2008 4 - November 2010
TerraSAR-X and TanDEM-X	DLR (German Aerospace Centre)	1- June 2007 2 - June 2010

These satellites have different acquisition modes which result in different pixel resolutions and different overall image size (and swath width). Some of these options and modes are presented in Table 2.2 for illustrative purposes. In general, the finer the pixel resolution, the smaller the area imaged and the higher the cost. This research uses data from TerraSAR-X, TanDEM-X, and Cosmo SkyMed-X satellites, both new acquisitions tasked specifically for this research, as well as making use of the archive of data. A compromise was made with available budget, area of interest, time period of investigation and number of images that could be purchased or acquired for this research, and all images used in this research were taken in 'Stripmap' mode (rather than wider modes, or finer 'Spotlight' resolutions).

Table 2.2 SAR Satellite resolution information

Satellite Constellation	Wavelength (mm)	Resolution Azimuth/Range (m)
COSMO-SkyMed-X	31	1.0 / 1.0 (Spotlight) 3.0 / 3.0 (Stripmap) 30 / 30 (ScanSAR)
TerraSAR-X and TanDEM-X	31	0.24 / 0.6 (Staring Spotlight) 1.0 / 1.0 (Spotlight) 3.3 / 2.8 (Stripmap) 20 / 20 (ScanSAR)

Chapter 3

Literature Review

This Chapter begins by reviewing the literature on current bridge structural health monitoring practice, in order to understand how to assess new monitoring technologies (such as InSAR) for value to asset owners making asset maintenance decisions. It then provides a brief overview of the development of InSAR applications, before focusing on InSAR for bridge monitoring and topics which are related to the application of InSAR to this purpose.

3.1 Structural health monitoring

Regular inspections of infrastructure assets are required to understand levels of deterioration and prevent failures and other potentially serious consequences. Current infrastructure asset maintenance practice in many countries (including the UK) tends to be based primarily on periodically scheduled visual inspections to assess condition and performance. As previously mentioned, Highways England's bridge inspection regime comprises a General Inspection every two years, with a more detailed Principal Inspection taking place every six years. Where specific issues have been identified, a "special inspection" strategy is implemented using appropriate non-destructive testing or monitoring (which may include, for example, fibre optic sensors, wireless sensor networks, micro-electro-mechanical systems (MEMS) sensors, traditional surveying techniques etc.). The frequency of inspections may also be increased where problems have been identified.

Visual inspections are reliant upon a subjective human element to assess risks and deterioration. On the one hand, this is invaluable, but on the other hand it introduces a question of reliability (as outlined with reference to the study by Moore et al. [3] in Chapter 1). Structural Health Monitoring (SHM) is seen as a means of complementing these visual inspections with more objective data, collected in set time periods between inspections, and providing supplementary data which would not traditionally be collected

by visual inspection (such as traffic or train loading cycles, which can be compared against design and assessment predictions and assumptions).

In more recent years, several large bridges across the world have been fitted with extensive SHM systems. These systems comprise an integrated system of sensors to monitor the performance of a structure. The intention is to collect data from these sensors and combine them in a meaningful way to compare measurements of the bridge in service against the predicted movements and behaviour based on the design conditions. In some systems, the data is intended to update deterioration models to better predict deterioration and warn of failure, as well as to convert this data into information to support the design of future bridges as part of a continuous improvement process. Bridges are often designed with certain assumed environmental parameters, but these are rarely evaluated against the changing natural environment conditions to check the validity of these assumptions. New sensor technologies are increasingly being deployed on bridges, in order to collect both environmental measurements (wind speeds, temperature, humidity, etc.) as well as direct measurements of the performance of the asset [38, 39]. For this research there is a similar hypothesis that the use of InSAR to provide contextual information on the ground, assets and environment around the asset could also bring added value to bridge monitoring. However, it is important to bear in mind the lessons learned through review of current SHM schemes.

The use of SHM systems, which are created as collection of sensors, to measure as many parameters and environmental conditions as possible in the hope of capturing behaviour of interest may not make best use of limited funds and is not likely to generate best value to asset owners [40]. A paper by Wong [41] outlined the data collection and evaluation architecture behind the large-scale, global bridge SHM system installed on Tsing Ma suspension bridge in Hong Kong. The SHM system was broken down into defined modules (sensory system, data acquisition and transmission system, data processing and control system, structural health evaluation system, structural health data management system, and inspection and maintenance system) which had multiple sensor inputs in key locations in order to compare and validate measurements. These measurements were then intended to be used to update or calibrate finite element models of the bridge and to evaluate the performance of the global bridge structural system and its local structural components using measured data conditions. The paper concluded that SHM systems for long span bridges should be able “to facilitate the planning of bridge inspection activities, and be able to determine not only the cause of damage, but also the extent of remedial work, once the damage is identified”. However, there were no specific examples providing evidence of the system being utilised convert the captured data into information to be used for detecting damage or deterioration of the bridge and plan for remedial work. The paper was written to indicate what “should” be done to

design and install a bridge SHM system, and although logical and well thought through, the paper provided little evidence of an evaluation of the system in use other than that the system facilitates the preparation of “Monthly Bridge Health Monitoring Reports” and “the Annual Bridge Health Evaluation Reports”. The content of these reports and resulting impact on maintenance regimes or predictive maintenance work was not discussed.

In interviews conducted with bridge asset owners for this research on InSAR bridge monitoring, some questioned the value provided by global SHM systems, but many agreed that a well thought out system that derives a practical output can provide a financial benefit if sensors and instrumentation are utilised to address specific concerns or issues. One such discussion on both the value and the shortcomings of SHM was with the Chief Bridge Engineer for Transport Scotland, and by way of example, is outlined below.

The Forth Road Bridge is an important long span suspension bridge, significant both for its engineering history and keeping the local Scottish economy moving. It has a main span of 1,006 metres between the two main towers and an overall length of 2.5km. Like many similar bridges, it is a very flexible structure, subject to high winds, significant differential and diurnal temperature ranges, large movements, and other adverse environmental effects. Traffic loading on the bridge is now double the magnitude and over twice the volume per day than that which was expected by the engineers who designed the structure in the late 1950's, with a significant increase in the weight, size and volume of all vehicles, especially heavy goods vehicles, on UK roads [9]. Also, the effects of temperature and wind are now better understood and together with traffic loading are the three main transient loads that affect the bridge.

“As the structure ages and materials deteriorate, maintaining and operating the bridge to cope with increasing demands and expectation, in an ever more stringent financial environment, becomes more challenging. A large capital programme of maintenance and improvement works on the bridge is continuing and structural health monitoring has a crucial role to play.” – Chief Bridge Engineer, Transport for Scotland, June 2016

The Forth Road Bridge SHM system brings together a number of monitoring methods, including remote satellite monitoring. It includes GNSS antennae, and a number of inertial sensors and communications systems that aim to provide a greater understanding about the bridge's movements. This was stated by the Chief Bridge Engineer as being extremely valuable during an enforced closure of the bridge during December 2015 when a truss end link failure was found on the bridge steelwork. During the subsequent repair period with storms Eva, Frank, Gertrude and Henry, as well as during the post-repair, pre-opening load

testing period, he stated that Transport Scotland were able to use the SHM system to obtain and interpret the actual deflections of the main suspended span and compare these with those predicted using their analysis model. However, conversely, the bridge was heavily instrumented and inspected prior to the failure of the truss end link, but the system did not pick up this failure (noticed during a visual inspection) which resulted in the bridge being closed during December, a period of heavy use due to Christmas holidays.

These examples show that the generation of large quantities of data through extensive SHM with the aim of providing new insights and real time behaviour of assets does not necessarily mean that useful information is provided to asset owners, designers and developers. Thus the data generated does not necessarily provide sufficient value to justify the cost of installing such systems using the asset life cycle budget [10]. The limited budget of asset owners means that an owner's decisions for when maintenance should be undertaken and on which assets (or parts of assets) the budget should be spent within a portfolio of assets is important.

Webb et al. [40] investigated a number of monitoring schemes and discuss the reasons for which one would want to install a SHM system, as well as who benefits from the monitoring. Asset owners want information for operation and maintenance planning; designers stand to gain an advantage from monitoring actual asset behaviour against design assumptions to better understand structural behaviour for future design; and contractors could make use of information during the construction period to reduce cost, resources or time, or increase safety during construction. From the review of SHM bridge systems, Webb et al. were able to develop a classification system of five categories for SHM deployments: anomaly detection, sensor deployment studies, model validation, threshold check and damage detection. A paper by Middleton et al. [10] also reviewed case studies of SHM deployments and questions the value behind the installation of some of these systems (condemning some systems as failing to deliver on promises of reliable, objective, real-time information which were sold to asset owners, designers and contractors). It concludes that a clear framework behind the motivations of a SHM system is required in order for the system to be effective and meet expectations.

Based on this review, this research has been designed to place an importance on not simply executing a 'sensor deployment study' of remote satellite monitoring to see whether satellites can be utilised to measure various parameters, but rather on demonstrating value to asset owners by determining how satellite remote monitoring sits within the current monitoring landscape, and how it can complement existing systems and sensors to provide clearly demonstrable value to asset owners.

3.2 Applications of InSAR

The advantages of remote sensing over traditional ground-based SHM systems include global coverage and the ability to monitor remote or difficult to access structures (or those in dangerous locations). Although the application of InSAR to structural asset monitoring is a newly emerging field, the technology has historical success within other domains.

InSAR has been successfully used to measure earth surface displacements for a number of applications. There are numerous studies published in the last couple of decades that illustrate the contribution of InSAR techniques to the Earth Sciences field, including research into the deformation of the earth's crust, tectonic deformation and volcanic deformation. The possibilities of deformation measurement using InSAR have been demonstrated as early as the late 1980s [26] using Seasat satellite data to detect vertical motions caused by soil swelling of irrigated fields in the Imperial Valley, California. The technique became more widely accepted following the measurement of deformation associated with the 1992 Landers earthquake in California, which used interferometric images of ERS-1 satellite radar data collected before and after the earthquake to form images of the deformation surrounding the rupture [42, 43]. Since this period, InSAR measurement techniques have continued to provide insights into post-earthquake deformation and an understanding of crustal deformation processes, fault interactions and the rheology of the earth's lithosphere [44]. Understanding movement and slips of fault lines through combining InSAR measurements with precise GPS point measurements has made steps towards providing substantially improved determinations of interseismic strain accumulation along active faults, enabling earthquake potential to be better determined and classified [45]. These techniques have also been successfully used to measure displacements to monitor volcano deformation [46].

Monitoring using InSAR has also been proven to be useful in a number of applications related to subsidence and slope movement. In the last few decades, monitoring of ground subsidence over city-scale areas [47] has highlighted the effects of anthropogenic actions. These include movements due to ground water exploitation [48], mining and tunnelling activities [49] and oil and gas extraction [50]. In the case of Mexico City, InSAR monitoring revealed certain places within the city with subsidence rates of up to 300mm/year due to extraction of ground water in excess of natural recharge and consequent compaction of clay-rich lacustrine sediment which makes up the ground [47]. As an example of slope failure monitoring, the Geological Survey of Norway is currently using InSAR to model slope movements in mountainous areas to track motion and predict landslides, so that areas can be evacuated and relevant authorities given adequate warning. They have installed a network of corner reflectors as artificial targets to stand above the snow, in order to collect InSAR data even during winter months [51].

Satellite technology related to InSAR is a field that is evolving rapidly [52]. As shown above, early InSAR systems have been used to study large scale deformations (such as earthquakes or volcanoes) but coarse spatial resolutions meant that the imagery was not fine enough to collect sufficient information on single buildings or infrastructure assets to undertake useful structural monitoring. However, recently deployed SAR sensors in the X-band wavelength range are able to collect imagery with a metre, or even sub-metre, spatial pixel resolution and a frequency of every few days. This spatial resolution allows for a number of pixels to cover a single asset and enables the gathering of information about certain types of asset behaviour [53, 54].

There are a number of different infrastructure application examples in the literature, which use cases for both single asset as well as larger scale linear assets. One such example of the latter is the use of InSAR monitoring for railway assets at a national scale [55]. Such examples highlight the opportunity to monitor not only individual assets themselves, but also the surrounding region that could impact them through embankment failure or landslides. There is a significant amount of literature around the monitoring of dams and the land adjacent to them [56–58]. Although InSAR is limited to the monitoring of surface level deformations, the technique can make use of surface level deformations to understand subterranean infrastructure activities such as tunnelling by measuring settlement resulting from the tunnelling process [59, 60].

Remote monitoring also provides invaluable opportunities for monitoring safety critical infrastructure that cannot be accessed easily. Mosul Dam faced a growing concern of failure (which would have resulted in catastrophic flooding affecting over a million people) when it was captured by the Islamic State (IS) group. The maintenance and cement grouting that was taking place prior to the capture had ceased, raising concerns about potential dam failure. InSAR was used to remotely monitor the asset, generating a deformation map to understand regions of subsidence and better understand destabilisation processes [61].

3.3 Application of InSAR to bridge monitoring

Considering bridge assets, InSAR has the potential to monitor assets which are difficult to access more frequently for inspection, as well as monitor those in hazardous areas or after disasters when access is cut off (providing that the asset itself has not been significantly impacted to the point where visual imagery would confirm this anyway). Bridges could be monitored after severe floods, or other significant events to ensure the bridge and surrounding ground is not moving excessively or sinking.

A review of the literature reveals that the potential for smaller scale, single asset monitoring using InSAR is growing, but bridges in particular have been developing as a topic of interest within the InSAR research field in recent years. The sections below cover some of the most relevant literature on applications of SAR to bridge monitoring contexts, as well as other topics of relevance that are important to consider when undertaking bridge monitoring

3.3.1 Image interpretation

A common theme mentioned across the majority of papers specifically dedicated to InSAR for bridge monitoring is the challenge of interpreting SAR imagery for bridges and how the side-looking sensor principle of SAR creates a high level of difficulty in understanding where reflections are coming from and how the processed data relates to the real-life scenario. Some of the effects mentioned in the theory in Chapter 2 include shadow effects, layover effects and height fit. Shadow effects occur when parts of the superstructure physically higher up create a shadow and prevent the SAR signal from reaching lower regions, the net result of which is that there are no persistent scatterers (PS) from PSI processing on the part of the bridge in the ‘shadow’. Layover effects are also due to the relative positioning of different components of the bridge. In the case of layover, the upper part of the bridge can appear to be on the opposite side of the lower bridge in the SAR image, depending on the viewing angle and the relative slant range of the bridge from the satellite. Multiple-bounce effects are also important to consider and occur when the SAR signal bounces off more than one physical object or entity before returning to the SAR sensor. This is a common issue with bridges spanning water bodies (Figure 3.1).

Qin et al. [62] works on understanding how different PSs correspond to different components of the bridge (e.g. PS attributed to the railing on the mid-span of a deck or those which relate to a tower or arch) to better understand and interpret the InSAR time series measurement of the PSs identified. One other field of imagery interpretation work is the use of high resolution SAR and optical imagery for feature extraction and the automated detection of bridges (primarily over bodies of water) [63]. An extension of this work by Soergel et al. [64] used InSAR to estimate the height of a bridge above the water that the bridge was spanning by making use of the multiple-bounce effects. The application of such analysis could potentially prove useful in understanding water levels to monitor for flooding and scour-inducing effects. However, the results of the proposed technique reported in this paper revealed a large variation in estimated measurement (in the order of metres), was only applicable for limited cases (based on bridge type and geometry) and was valid for only one particular instance in time (without evolution of change in river level over time).

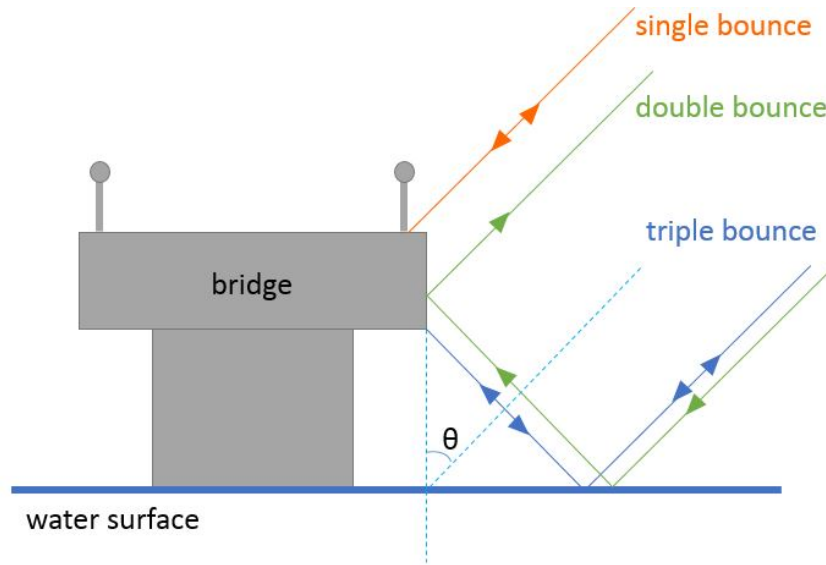


Fig. 3.1 Bridge over water multi-bounce effects.

3.3.2 Persistent Scatterer three-dimensional positioning

In terms of three-dimensional (3-D) positioning, the absolute position accuracy of synthetic aperture radar (SAR) scatterers has been demonstrated to be in the centimetre scale for two-dimensional (2-D) radar coordinate positional accuracy. For example, Eineder et al. [65] conducted experiments using TerraSAR-X to measure large-scale Earth surface displacements, such as those caused by solid Earth tides, achieving relative accuracies of between 2.6 and 5.9cm. Dheenathayalan et al. [66] and Dheenathayalan et al. [67] developed a procedure to fix positioning errors in radar coordinates (before the geocoding stage of the processing in order to avoid non-linear distortions in mapping the 2-D processed data in radar coordinates into 3-D terrestrial coordinates) and achieved an accuracy of absolute positioning in 2-D radar coordinates of about 7cm (and up to approximately 66cm in 3-D). More recent work by Dheenathayalan et al. [68] reported a 3-D positioning error of 28cm. Better 3-D positioning accuracy has been achieved using ‘stereo SAR’ (using acquisitions from multiple satellite tracks over the same area of interest) with Zhu et al. [69] reporting a positioning accuracy of around 20cm and Ginsinger et al. [70] reporting the location of PSs in 3-D with a precision better than 4cm. However, this stereo SAR approach is often not possible in practice as it requires multiple satellite tracks over the same area, and for same physical scatterer to be visible in both geometries. This lack of common points viewed by multiple satellite viewing geometries is the case for the bridges studied in Chapters 5 and 6, where each satellite imaging track only images one side of the bridge or the other, but does not result in common PSs.

There are works which make use of digital models to better interpret and classify PSs. Auer et al. [71] employed ray-tracing to simulate geometric scattering for the interpretation of high resolution TerraSAR-X images and from this, related PSs to different parts of the buildings being studied. The approach of using of geometrical models for interpretation was used for localising PSs and for aiding in the interpretation for this research on InSAR monitoring of Hammersmith Flyover, as described in Chapter 6. The other bridge studies used the 3-D positioning accuracy generated by the InSAR processing, but employed manual interpretation to understand where the PSs were being reflected from.

3.3.3 Accuracy and reliability of InSAR measurements

To investigate the research question relating to accuracy and reliability of InSAR for the purposes of bridge monitoring, it is important to consider the scale of measurement accuracy that InSAR can provide. There are a number of studies which deploy reflectors to create SAR reflection points (SAR reflectors are described in further detail in Chapter 4). Ferretti et al. [30] proved that measuring movements to sub-millimetre accuracy was possible through an experiment using two dihedral reflectors (two-plane metal piece, the design of which is detailed within the paper) which were moved a few millimetres between SAR acquisitions. Although this showed that this level of measurement precision was possible, it is worth noting that this test was performed in ideal conditions, for example, by having perfectly identifiable point targets in the SAR image, minimised atmospheric effects, slow and controlled deformation, etc. The PSI process is complex and dependent on a number of different factors. Some examples include the SAR sensor used, the number of acquisitions processed, density of PSs, quality (coherence) of PSs, the quality and distance of the reference point used in processing, and the specific type and rate of deformation being monitored. The performance reported in this paper cannot therefore be extended to every possible practical application of InSAR measurement. Looking at the aim and results of the paper, the experiment was designed with the aim being “to demonstrate that Interferometric Synthetic Aperture Radar (InSAR) measurements can indeed allow a displacement time series estimation with sub-millimeter accuracy (both in horizontal and vertical directions)” and found that the standard deviation of the error between InSAR measurements and ground truth was 0.75mm in the vertical direction, and 0.58mm in the horizontal direction - specifically in the east-west direction. As explained in the theory, SAR satellites currently fly in the near-polar orbit and as such (in the non-polar regions) the north-south surface displacements have little contributions to the line of sight (LOS) measurements, but this measurement technique is ideally suited to measurement of displacements in the east-west direction perpendicular to the SAR satellite flight direction. Therefore the study looked at vertical and one particular direction of horizontal movement,

which cannot be applied to all instances of horizontal movement. Marinkovic et al. [72] also conducted an experiment comparing corner reflectors with leveling observations, reporting vertical differences of 2.8mm for Envisat data and 1.6mm for ERS-2 data. Quin et al. [73] deployed a network of specially developed reflectors which were moved using micrometric vernier controls, and reported that the relative displacements between the reflectors had a standard deviation of 0.48mm along the line of sight direction using TerraSAR-X satellite data.

PSI and SBAS InSAR processing involves a complex estimation process in which the selection of different processing parameters and processing algorithms can result in different errors even when studying the same stack of data. The validation of InSAR measurements, and particularly PSI and combined PSI-SBAS methods have been the focus of a large number of studies. The majority of these studies are based on comparing InSAR deformation time series readings (or deformation velocities calculated from these results) with independent estimations of the same quantities acquired by other measurement techniques (such as levelling). One notable example described by Raucoules et al. [74] was a project run by the European Space Agency (ESA) entitled Persistent Scatterer Interferometry Codes Cross Comparison and Certification (PSIC4). In this project eight different teams processed SAR data over the same geographical area in France (which was known to be experiencing subsidence due to mining activities) using InSAR PSI and without any a priori information about the site. Comparison of the subsidence velocity calculated by each of the teams showed a standard deviation of between 0.6 and 1.9mm/year. Validation of these velocity rates against rates measured on the ground showed a variation of between 5 and 7mm/year. It is also noted within the study that the levelling data on the ground was collected using automated electronic levels, which themselves had a specified precision performance of up to 1.5mm, and comparing PSI points with levelling data was undertaken had to include some interpolation of levelling data points to coincide the PSs with the levelling measurements. These considerations could affect the final measurement validation results.

Another notable large-scale study around the same period in time was the TerraFirma Validation project (also run by ESA, and summarised by Crosetto et al. [75] and Adam et al. [76]) which also compared the PSI results for two geographical sites from different teams. The aims of this study included the comparison of outputs from different PSI processing algorithms to certify that the operational service providers participating in the study produced consistent results. In this instance, the first comparison of processing algorithms was performed in the 2-D SAR coordinate system (rather than geocoded products given to end users in everyday 3-D map coordinates) to more easily understand the cause of any differences in the results. The second comparison was a comparison against ground truth information.

The comparison between teams was based on sets of common PSs found by at least two teams. The standard deviation of the deformation velocity calculated by each of the teams in this instance was between 0.4 and 0.5mm/year. If looking at these results for the time series as individual measurement readings (rather than a best fit of points to calculate velocity) the standard deviation was found to be between 1.1 and 4.0mm. Validation of these velocity rates against rates measured on the ground in this study was found to be between 1.0 and 1.8mm/year (and for time series measurements was between 4.2 to 6.1mm).

This list of validation studies is by no means exhaustive. There is a large volume of work and case studies comparing InSAR measurements with data collected on the ground by other surveying and measurement tools.

3.3.4 InSAR Line of Sight measurements

As outlined in the theory in Chapter 2, PSI measurements refer to one-dimensional measurements in the line of sight (LOS) of the satellite. Bridges deform in three dimensions. InSAR provides the estimate of one component of bridge deformation which is obtained by projecting the three dimensional deformation into the LOS direction. This one-dimensional measurement is a significant limitation for bridge monitoring, but there are a number of works in the literature dedicated to the attempt to resolve two- and three-dimensional measurements from InSAR sources. Hu et al. [77] provide a useful review of the different methods proposed in the literature. The first collection of methods in this field comprise methods to derive two-dimensional displacement maps (displacement in the range and azimuth directions of SAR geometry) from a single interferometric pair [78, 79]. These displacement maps are not useful in bridge monitoring as they provide a snapshot in time, and furthermore, bridge engineers are interested in movements in particular directions as set by the bridge co-ordinate system (i.e. longitudinal, transverse and vertical directions). Even if such methods could be extended to a time series, measurements in the range and azimuth directions are not particularly useful for bridge monitoring. The second collection of methods propose to derive three-dimensional displacement. These methods include combining different satellite passes with different viewing geometries, integrating InSAR and GPS data (such as the method proposed by Gudmundsson et al. [80]), and making assumptions on the direction of the deformation being studied (for example, Wright et al. [81] used knowledge of earthquake orientation being in an east-west direction to consider north-south displacements as insignificant and therefore negligible). The possibility of applying some of these methods into working out InSAR-measured bridge displacement in three-dimensions is investigated and discussed in Chapter 5.

3.3.5 Thermal expansion

Studies have also shown that InSAR can pick up movements that capture structural movements due to thermal expansion in buildings and bridges. There are a few approaches in the literature regarding displacements due to thermal changes. Studies on thermal expansion of bridges have been undertaken as a proof that measured displacements of PSs on bridges correlate with temperature. This was done in some cases to estimate the thermal coefficient of the bridge material (steel or concrete), or in other cases to removed the temperature component of the movement and study the residual movement for other effects (such as settlement). Goel et al. [82] model thermal component as a sum of cosine functions used to describe the motion of the movements attributed to temperature, and by correlating the thermal component of the movement with the air temperature history at the acquisition times.

Lazecky et al. [83] broke down SAR phase contributions into elevation changes, linear deformation trend and thermal dilation, to estimate the thermal component (assuming a linear relation between the temperature and the SAR phase for the thermal expansion coefficient). This work was later expanded in a paper by Lazecky et al. [84], which considered the difference between measured bridge temperature and general air temperature and also developed a thermal expansion model based simple thermal expansion models used for bridge modelling which is described as follows:

$$t_l = c \cdot l \cdot \Delta t \quad (3.1)$$

where t_l is the thermal expansion of a bridge segment between expansion joints, c is the thermal expansion coefficient for the material (e.g. $10 \times 10^{-6}/\text{C}$ as a possible value for concrete), l is the length of the expanding structure, and Δt is the change in temperature causing expansion.

Monserat et al. [85] and Crosetto et al. [86] provided a method to create maps of an estimated thermal expansion parameter, called ‘thermal maps’. This was done by connecting the persistent scatterers together and computing the phase difference of each connection. The method consisted of estimating three unknowns in an equation which describes the components of the measured phase shift: an assumed linear deformation velocity, the residual topographic error (related to the perpendicular baselines of the interferograms) and the thermal dilation parameter (which in this instance was related to the average temperature differences between the acquisitions of the images). The thermal dilation parameter was estimated using the measured displacements, assumptions on motion, parameters related to the SAR imaging, and the temperature difference between the acquisitions of each of the two images of a given interferogram. This temperature difference was presumably an

air temperature collected from weather data, but this was not stated. The thermal map was formed by integrating the the differential thermal dilation parameter associated with each PS connection.

Fornaro et al. [87] outlined an approach to approximating the thermal component of a SAR signal also by forming an equation based on the linear deformation of a persistent scatterer, a component associated with temperature and the remaining nonlinear component of the deformation. This equation was rearranged with some approximations to create an equation for γ , a parameter that connected the deformation (function of temperature) and the SAR signal. This was then converted from a continuous function to discrete function to make an approximation for each pixel, and then work out a means of finding this γ value. The paper described this as solving a matrix, and this matrix was then extended into a tensor with some assumptions put in place to create a mathematical estimation. Some of these assumptions are not explicitly clarified, such as the reason for selecting maximum values within the defined system matrix.

The literature also highlights the limitations of linear deformation models often used in PSI analysis, which may not be suitable when considering movement due to thermal effects and monitoring the non-linear behaviour of infrastructure [88, 83]. It should be noted that there are several InSAR processing software packages which provide the option to download air temperature from a region (from weather data) to estimate and remove thermal components of InSAR-measured displacements, through some of the methods outlined above. A key problem in employing these standard approaches is that the product becomes a 'black box tool' and it is not clear what estimations are made.

The first research question to be addressed within this thesis relates to investigating whether InSAR measurements show sufficient accuracy, reliability and resolution to be on the same level as traditional methods (such as surveying and sensor monitoring). To investigate this question, separating the thermal component of the displacement would not serve a purpose. The second research question relates to practical application in spotting problems or precursors to failure. Approaching this problem from a bridge engineer's perspective, displacements due to thermal expansion are an important consideration. Although there is some merit in removing this component to understand if there are other factors affecting the bridge (for example, ground movement) understanding the total movement is vital in assessing the functionality of bridge components such as bearings and expansion joints. To apply the InSAR measurements into a practical scenario, it is important to understand all bridge motion to quantify the effect of the full envelope of applied loads when considering the impact on, say, bridge bearings. For these reasons the thermal component of the displacement was assessed and considered in terms of understanding the overall bridge behaviour, but

these specific methods outlined in the literature were not employed to remove a proportion of the measured displacement.

3.3.6 Motivations for research

A key point noted by several validation studies is the importance of not working in ‘blind conditions’ when processing InSAR data, but instead understanding the context of the displacements being studied. An article by Crosetto et al. [75] on validation studies stated that PSI deformation measurements “should include the user validation, where the suitability (fit-to-purpose) of PSI to monitor deformation in a given type of application has to be proved” and includes other considerations apart from precision and accuracy. The body of work on InSAR monitoring for bridges is relatively small, and fewer where bridge-specific characteristics and behaviours are considered.

The literature on using InSAR for bridge monitoring starts with applying InSAR measurement techniques (which have established use in ground settlement monitoring) to monitoring settlement bridge components or settlement of the land on which bridge piers are founded [89, 90] but has developed into more detailed studies on identifying specific components of bridges, attempting to understand bridge behaviour in response to temperature, and determining bridge movement in three dimensions.

There appears very little literature in relation to monitoring for precursors to failure, apart from Sousa and Bastos [91] who monitored the steady linear deformation of points on a bridge in the years preceding its collapse and a very recent study by Milillo et al. [92] on the collapse of the Morandi Bridge. Within the InSAR community there is an understanding that settlement, and notably differential settlement, are signs of alarm that asset owners would want to be made aware of. However, there is a lack awareness or understanding about different bridge failure mechanisms, what signs of behaviour would be worth monitoring, and if/how InSAR would be a suitable tool to do so. The closest work in this regard would be the work presented by Cusson et al. [93] which compared InSAR measurements with numerical modelling data and noted that line of sight displacement from InSAR used to pick up the thermal sensitivity of the bridge should be able to identify issues such as frozen or damaged bearings, pier flexibility issues or structural numerical modelling issues, but without any evidence or case studies of the technique being employed in such a way.

In addition to temperature, other environmental effects (such as vehicle loading, wind, or tide for bridges in certain water bodies) can affect bridge movement, but research on InSAR satellite monitoring of bridges to date has not considered the impact of these other effects. There are a number of reasons to explain this, such as the spatial resolution of satellite SAR data and frequency of readings, but the understanding the impact of these loads

being neglected by InSAR monitoring (such as the effect of tidal loading not being accounted for by InSAR monitoring in the study on Waterloo Bridge, detailed later in Chapter 5), is important in understanding the full picture of bridge structural health.

Another observation from reading studies from the literature is that much of the work within InSAR for infrastructure monitoring has relied on processing SAR data, and then trying to explain strange behaviours shown within that data. With regard to bridge monitoring, there is a lack of research which evaluates InSAR measurements against in-situ ground data as to validate the measurements or provide an understanding in the uncertainty of the measurement data. As far as the author is aware, there is no direct comparison of satellite InSAR bridge measurement validated by in-situ sensors or ground monitoring. There are only experiments in the literature which are similar in nature involve sensors and ground-based radar, such as the work by Gentile and Bernardini [94] which compared accelerometer data with data from a ground-based radar interferometer to study traffic-induced dynamic responses of a road bridge.

Chapter 4

NPL Measurement Experiment

4.1 Introduction

The suitability of using InSAR for bridge monitoring relies on the precision and reliability of the measurements, as defined in the first research question. This experiment was designed to investigate the accuracy, reliability and resolution of measurements, so to identify whether these would be suitable for bridge monitoring applications, and to better understand uncertainties within the measurement data.

The processing and interpretation of a series of SAR images for infrastructure monitoring requires the identification of pixels which contain the response of stable natural reflectors (persistent scatterers) which are then associated to physical objects on the ground. In this experiment, known points were displaced by a fixed amount in a vertical direction of movement. To create the known points within the SAR image, three corner reflectors were mounted on a test rig specifically designed for this experiment. The imposed displacements were measured on the ground using conventional displacement sensors to compare with InSAR satellite measurements. Three additional points near the test rig were measured using Global Navigation Satellite System (GNSS) devices for comparison, and to understand ground movement in the region around the test rig.

In this Chapter, Sections 4.2 and 4.3 explain how the corner radar reflectors were designed and how a suitable site was chosen. Section 4.4 outlines the experimental set up, including the test rig, the method for installing and orientating the corner reflectors, and the installation of the GNSS measurement stations. Section 4.5 explains how the reflectors were moved and then Section 4.6 explains how the InSAR and GNSS data were processed. The results of the experiment are presented in Section 4.7 and a discussion is presented in Section 4.8 which includes sources of error (and how they were minimised in the experiment), observations

made from the data and quantification of measurement uncertainty, before finally presenting conclusions in Section 4.9.

4.2 Design of the radar reflector

The type of radar reflector to be used was selected and a suitable site to conduct the experiment was first identified. There are different types of radar reflectors, such as a flat plate, a dihedral made of two plates forming a corner, or corners in various shapes. A trihedral radar reflector, commonly known as a “corner reflector”, was selected for use in this study. This type of reflector facilitates a triple-bounce of the incident radar energy from three mutually orthogonal plates such that the incoming radar wave emitted from the satellite is reflected back to the satellite receiver. Corner reflectors are the most commonly used type of radar target deployed for Persistent Scatterer Interferometry (PSI) [95]. The corner reflector becomes the dominant scatterer in a resolution pixel and is much stronger than echoes from dimmer distributed scatterers within the pixel, often referred to as “clutter”. The literature identifies a number of theoretical and experimental studies on corner reflectors [96, 97, 30, 98–100].

The Radar Cross Section (RCS) is a measure of the reflectivity (i.e. brightness) of a point-like target in a SAR image. The RCS of the Corner Reflector needs to be significantly higher than the background clutter (known as the signal to clutter ratio, SCR, or as the signal-to-noise ratio, SNR). In SAR images, the 3dB beamwidth (the width between the two points on the main lobe peak where the intensities are 3 dB below the maximum intensity in the azimuth and range directions) is a useful measure of signal response (Figure 4.1). The 3dB level is considered as a useful measure as above the 3dB level, the amplitude falls to $1/\sqrt{2}$ and the power of the output falls to half the power of the input.

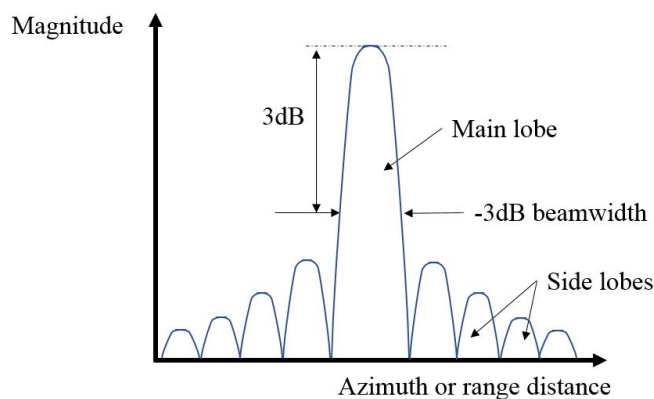


Fig. 4.1 Graphical representation of SAR point target response.

The RCS of a trihedral corner reflector has a 3dB beamwidth of approximately 40° about the symmetry axis of the reflector (the peak boresight direction) [101]. This means that a trihedral design is much more forgiving of field alignment errors when compared to other reflector designs [98]. The corner reflector was selected for this study, using a triangular plate shape (rather than square and quarter-circle shaped plates), even though it has the lowest RCS of the three forms for a given size, because it is more rigid, robust and easy to manufacture (Figure 4.2). One study by Sarabandi and Tsen-Chieh Chiu [100] described ‘optimum’ corner reflectors as having hexagonal-shaped plates, created by trimming the ineffective part of a trihedral corner reflector that does not contribute to the RCS pattern. In practice, manufacturing complexity and the reduction in overall rigidity of the corner reflector mean that they do not offer significant performance benefits over a trihedral corner reflector.

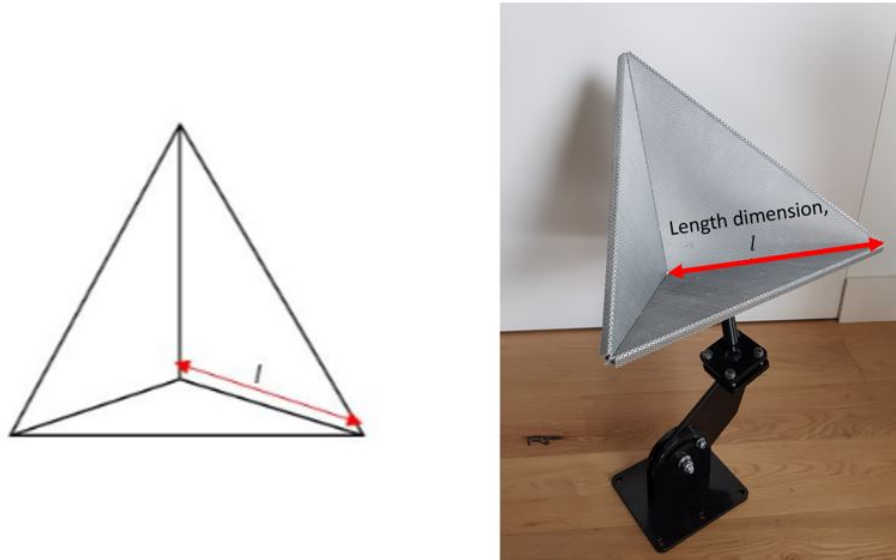


Fig. 4.2 Trihedral corner reflector shape where ‘ l ’ is the length dimension of the interior edge used in the RCS calculation

The theoretical peak RCS value for the trihedral corner reflector is given by the following equation (in m^2) [101]:

$$RCS = \frac{4\pi l^4}{3\lambda^2} \quad (4.1)$$

where: l is the length of the non-hypotenuse sides of the right-angled isosceles triangular plate, and λ is the radar wave length (for TerraSAR-X X-band = 0.031 m)

The RCS values for different trihedral corner reflector sizes for X-band satellites (TerraSAR-X and CosmoSkyMed-X) and C-band satellite (Sentinel 1) were calculated as shown below in Table 4.1. Studies in the literature have deployed much large corner reflectors, from corner lengths of 50cm up to a couple of metres, in various studies and calibration exercises

[102, 96, 103]. However, the purpose of this measurement study is to identify the application of InSAR in infrastructure monitoring, and whilst large reflectors can be installed in remote fields or potentially on some flat building tops, this size cannot feasibly be installed on structures such as bridges. For this reason, a smaller reflector with $l = 0.35m$ was selected here as this was a size permitted for installation on bridges by bridge owners (detailed later, in Chapter 5 on Waterloo Bridge). Calculations comparing corner reflectivity with background clutter at this site suggested that the signal from this corner reflector should be detected.

Table 4.1 RCS values for different trihedral corner reflector sizes for X-band and C-band satellites

Corner Length, l (m)	RCS (m^2)		RCS (dBm^2)	
	X-Band	C-Band	X-Band	C-Band
0.35	65.4	11.2	18.2	10.5
0.50	272.4	46.5	24.4	16.7
0.75	1379.1	235.6	31.4	23.7
1.00	4358.8	744.7	36.4	28.7

The corner reflector material was also considered for this study. Aluminium was commonly used by studies in the literature for the construction of the plates making up the corners, given that is light weight and does not suffer from corrosion as badly when compared to steel. A thermoplastic powder coat (sometimes applied to increase longevity of the corner in field usage) was not applied, given that the experiment would be installed for a relatively short period and such an additive may introduce RCS losses [98]. Pre-fabricated perforated sheeting also reduces RCS [104] but facilitates drainage (water accumulation within the reflector would have a greater reduction in RCS than the introduction of holes), reduces wind load, reduces overall weight and promotes self-cleaning of dirt and other deposits. A previous study by Qin et al. [103] was used to identify that the hole size and spacing of the perforated aluminium sheeting used to fabricate the reflectors in this study was well within acceptable thresholds for reflection effectiveness.

4.3 Experiment Site

Effective deployment of a corner reflector includes the consideration of the background clutter from other reflectors in the vicinity of the deployment location. This requirement would suggest a site which has a clear space - either a clear roof area with sufficient space around the reflector so that there is no interference with the pixels corresponding to the radar



Fig. 4.3 National Physical Laboratory (NPL) and surrounding area as viewed by optical satellite imagery (image from Google Maps, 2018). The boundary of the grass field test site is marked with a dashed red line, and the main NPL building and test site are indicated by arrows.

signal reflection from the corner reflector, or an open field site. Point target analysis (based on the SAR target response discussed in section 4.2) was used to check the suitability of the chosen site by calculating the signal to clutter ratio and working out whether the installed corner reflector would be significantly brighter than the surrounding clutter, such that it is clearly identifiable and the most prominent scatterer within a given pixel. The National Physical Laboratory (NPL) site, pictured in Figure 4.3, contains a small grass field next to the staff car parking area. This area is within a site boundary controlled by security to prevent accidental or intentional damage to the corner reflectors.

To consider the atmospheric component of displacement readings as negligible, the distance between neighbouring corner reflectors must be minimised (as there is less likely to be different atmospheric conditions in closely adjacent areas). In the study by Crosetto et al. [105], a set of interferograms produced from C-band ERS satellite data was analysed over an urban area known to be stable, thus enabling the atmospheric signal between pairs of points as a function of the distance to be estimated. It was found that the standard deviation of the atmospheric component ranges, in terms of line of sight (LOS) displacement, from

0.7 to 1.8mm at 100m; from 0.8 to 3.1mm at 200m; and from 0.9 to 3.6mm at 300m. In this study, installation of the corners anywhere within the NPL test site (in this case at distances only a few metres apart) would permit this negligible atmospheric effect assumption to be considered valid.

4.4 Equipment

The experiment was set up so that the three corner reflectors (A, B and C) would be mounted on a rig (Figure 4.4). The rig comprised concrete highway road barriers joined by a rigid connection. The concrete barriers were installed at the site on top of a geomembrane and road mat to provide a solid foundation and minimise local deformation of the ground or differential settlements between the adjacent reflectors. Within this research, this test was conducted to:

- a) test the effectiveness of the corner reflectors as these would then be deployed on other structures;
- b) validate the accuracy of the deformations measured by SAR readings;
- c) provide a control measurement, to use in estimating the uncertainty of measured values.

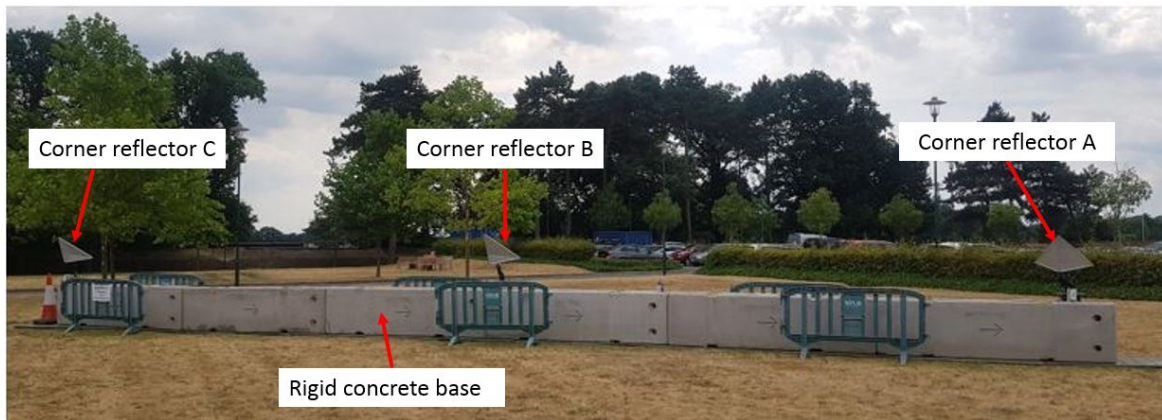


Fig. 4.4 Installed corner reflectors mounted on concrete base at NPL site

A stage platform base was developed to allow two of the corner reflectors (A and C in Figure 4.4) to be raised or lowered by a measured distance vertically up and down by manual control of a dial (Figure 4.5). The stage platform at corner reflector B was locked in a fixed position. The corner reflectors were mounted onto a bracket permitting movement in the arm, as well as via a ball and socket joint, such that the corner reflectors could be positioned so that they faced the line of sight of the satellite before being locked off and held in position for the duration of the experiment.



Fig. 4.5 (left) Stage platform at Corner A with turn dial to control vertical movement; (middle) Corner reflector A on top of stage platform and concrete test rig; (right) Corner reflector A as viewed from other side, with Moniteye displacement gauge visible.

4.4.1 Installation and orientation of corner reflectors

When deployed, the corner reflector geometry (Figure 4.6) must be orientated such that the azimuth and elevation of the boresight vector (originating from the intersection of the three triangular plates, as marked by the blue arrow in Figure 4.6) is directed in the SAR satellite's line of sight (LOS) to maximise the strength of the reflected signal. This orientation was estimated using the Systems Tool Kit (STK) modelling environment [106] by inputting the corner locations and modelling of the TerraSAR-X satellite position the site during each acquisition period, using the method described by Garthwaite et al. [102] to account for the orbit and look angle of the SAR sensor (Figure 4.6). These calculations were then confirmed by the data provider (Airbus) as a secondary check, which was useful given the limited number of acquisitions available in this study, with minimal room for installation mistakes.

Once the three corner reflectors were installed, the first TerraSAR-X acquisition taken after installation was compared to the image before installation commenced. This comparison is seen in Figures 4.7 and 4.8 below and shows the corner reflectors being picked up within the SAR image as three distinct bright point targets.

On installation these point targets identified in the imagery were analysed using point target analysis to assess whether the selected pixels behaved sufficiently like point targets (described previously in Section 4.2) to be suitable targets within the imagery. Figure 4.9 shows an example of some of these results. The Integrated Side Lobe Ratio (ISLR) is the ratio of the energy in the side lobes of the signal response to the energy contained in the

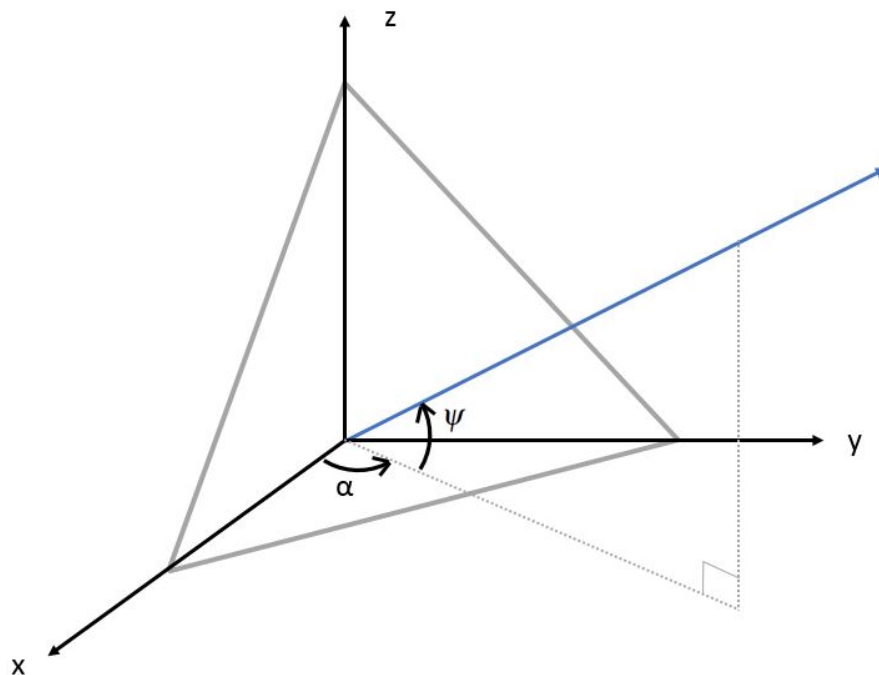


Fig. 4.6 Azimuth angle α and off-nadir angle ψ defined for a corner reflector and used during installation to direct the corner in the LOS. The blue arrow marks the boresight vector.



Fig. 4.7 SAR image of NPL site prior to corner reflector installation (test site circled in red, with the brightest cluster of pixels in the proximity of the test site coming from reflections from the nearby NPL building).



Fig. 4.8 SAR image of NPL site after corner reflector installation (test site circled in red) where the three corner reflectors can be clearly seen as three bright points.

main lobe of the signal response. The Peak Side Lobe Ratio (PSLR) is the ratio between the returned signal of the main lobe and that of the first side lobe of the point signal. The corners were found to be being picked up clearly and consistently in the radar imagery, and the study proceeded with the corner reflectors in this configuration for the remainder of the experiment.

4.4.2 Installation of GNSS stations

GNSS readings were also taken in three locations on site on the dates that the corners were moved. One location was on the ground next to Corner A (labelled "Corner"), a second was on the ground next to Corner C (labelled "End Corner"), and a third reading taken at a location immediately adjacent to the NPL main building (labelled "Building"), as shown in Figures 4.10 and 4.11. The "Corner" location was used as the reference base station to which the other locations would be tied to. The "Building" location was selected even though it was not in the location of the measurement points on the test rig. As NPL is a measurement laboratory facility, it was assumed that the specification and piling of the building would be such that settlement and other movement of the building would be designed to be strictly limited. Therefore, this would be a suitable site to consider as a point that was relatively 'fixed' with minimal ground movement at the surface.

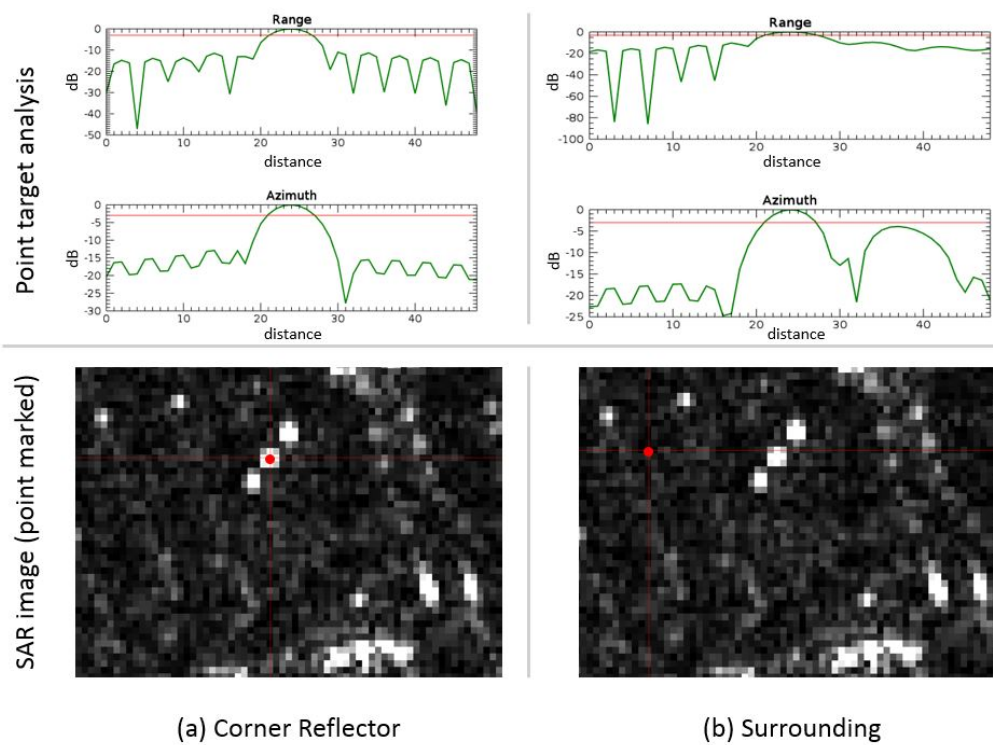


Fig. 4.9 Point target analysis example (a) at the location of a corner reflector, with values of $ISLR = 1.5$ and $PSLR = -10.9$; and (b) in the field area surrounding the test rig, with values of $ISLR = 5.5$ and $PSLR = -1.1$.

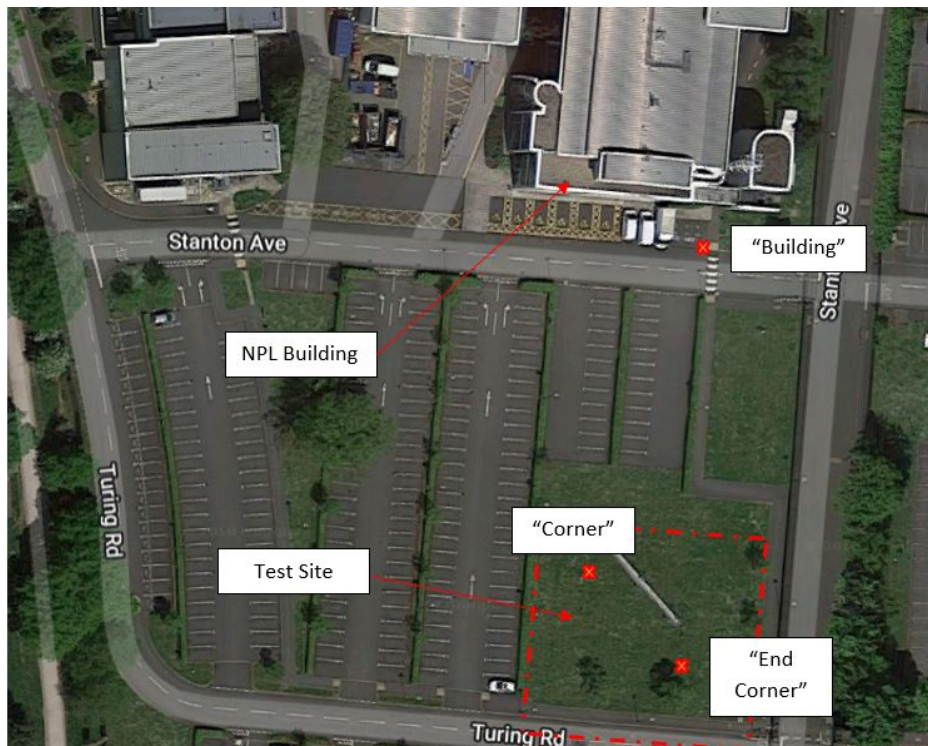


Fig. 4.10 Test site at NPL with locations of GNSS survey locations marked by red crosses. Optical image as base map is from Google optical satellite imagery (imagery and map data property of Google, 2019).

One of the requirements for accurate computation of a GNSS difference vector is that the absolute geographical position of the base station is known to within about 1 metre before further calculations are done. To work out this location, ‘*active*’ base stations can be used. Several UK organisations maintain active base stations. These continuously record GNSS data at the active base station locations, which can be downloaded for post-processing in conjunction with data from GNSS sites in temporary locations. Ideally, the active stations should form a ‘ring’ around the site being measured [107]. As well as detecting systematic errors in the test site readings (for example, errors in different antenna offsets in equipment sets), it would help account for atmospheric effects. The NPL experiment site was within 5 Ordnance Survey Active stations which formed a suitable ‘ring formation’ around the test site, and data from these active stations was downloaded for each of the periods the experiment when GNSS measurements were being collected.



Fig. 4.11 GNSS device set up adjacent to NPL main building (site labelled as “Building” in results).

4.5 Data collection methodology

The layout and labelling of the three corners are shown in Figure 4.12. Corner A was moved in downward steps of approximately 2mm prior to each acquisition (generally taken in 11-day intervals) for the first half of the experiment, and then upward steps over longer intervals for the second part of the experiment. This was primarily due to the stage platform equipment (used to move the corner reflector vertically downward) getting jammed and preventing further downward movement. Corner B, in the middle, was not adjusted and left in place as a “fixed” reference reflector. Corner C was moved downwards in a step of approximately 7mm after 5 acquisitions.

These measurements imposed were done manually, to the nearest visible millimetre using a ruler benchmark post, but a displacement gauge provided by the company Moniteye (a type known as ‘MCS V1’ used for crack monitoring) was used to measure the displacement imposed. These measurements, indicating the movement regime imposed can be seen in Figure 4.13.

On the dates when the NPL site was visited to change the heights of the stage platforms, two Leica GNSS stations and tripods were brought to the site. One station was positioned over the marker point installed at “Corner” and run for a minimum period of 4 or 5 hours. This was done so that it allowed for the passing of multiple GNSS satellites such that this

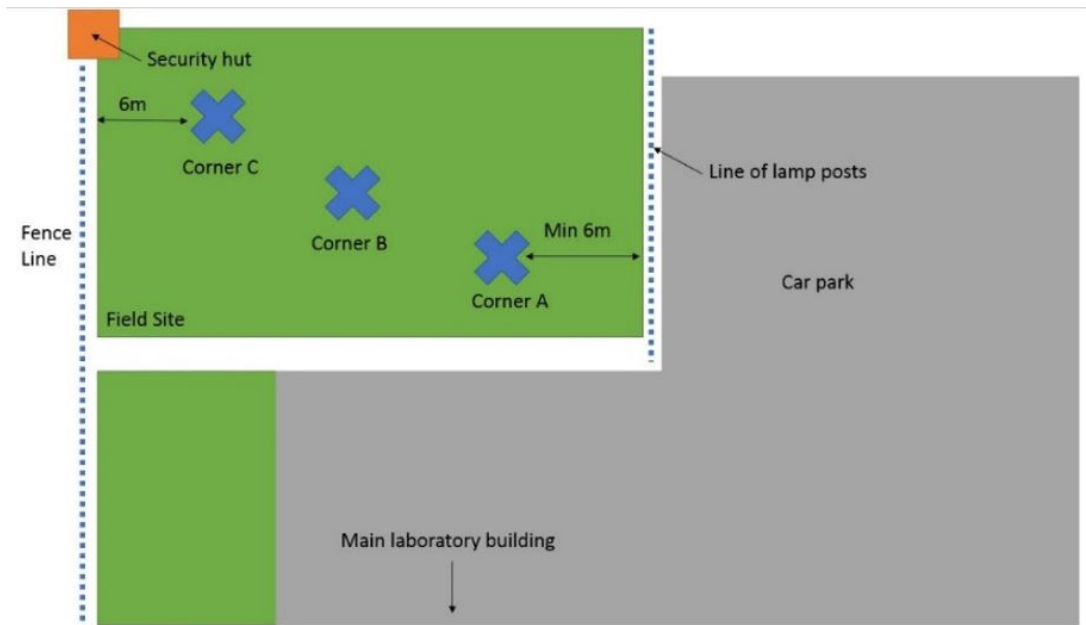


Fig. 4.12 Site and corner reflector layout in direction as viewed from NPL building.

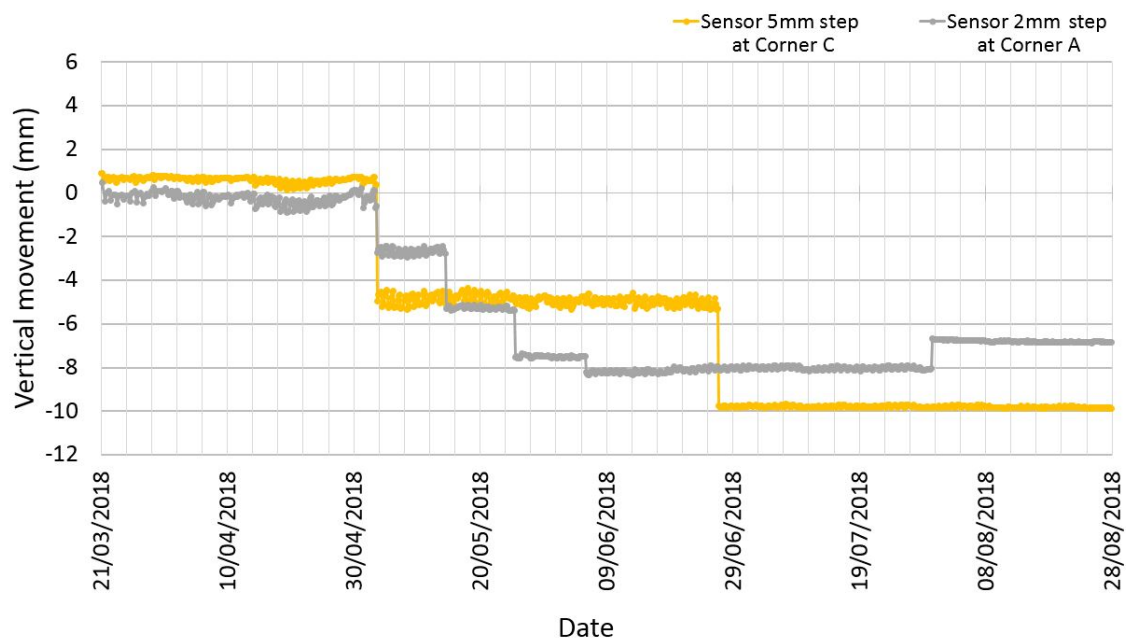


Fig. 4.13 Vertical movements imposed over time for Corners A and C.

station could be tied to the reference stations during the processing, and become the base station to which the other two “rover” station points (at “End Corner” and “Building”) could be tied. The other GNSS station was set up to take readings at the “End Corner” and “Building” points for a minimum of two hours each.

4.6 Processing methodology

4.6.1 SAR processing

The TerraSAR-X ascending acquisitions listed in Table 4.2 were used in the SAR processing with the interferograms between pairs of images each being formed with respect to the Master image, taken on 16th March 2018 (Figure 4.14). An example of one such interferogram is shown in Figure 4.15. This SAR processing uses a very similar approach as the SAR processing methodology proposed by Ferretti et al. [30] for experiments conducted to show the potential of SAR to provide measurements to submillimetre accuracy. The set up, corner reflectors, test rig equipment and SAR data were different to this experiment conducted at NPL, which forms the context against which the other studies forming this research were conducted.

The line of sight (LOS) displacement corresponding to the i th acquisition was computed through a phase difference between the reference reflector (suffix REF) and one of the test reflectors (suffix TEST) as shown in Equation 4.2:

$$\Delta\phi^i = (\phi_{TEST}^i - \phi_{REF}^i) - (\phi_{TEST}^M - \phi_{REF}^M) \quad (4.2)$$

where the superscript M indicates the master acquisition (i.e., the temporal reference) and i is the slave image under study. The estimations derived are therefore relative to the reference reflector (B). These values are extracted from the differential interferograms (Figure 4.15) formed from taking the difference between pairs of images (master image and each slave image).

This difference between two single-look complex SAR images is referred to as the ‘raw interferogram’, as its phase is quite noisy (in the case of repeat-pass acquisitions that are strongly affected by temporal decorrelation). It is common practice to reduce the noise by averaging adjacent pixels in the complex interferogram. This processing, defined as ‘complex multi-looking’ [32] (an extension of the ‘multi-looking’ processing explained in Chapter 2 section 2.2.2), trades geometric resolution for phase accuracy (or altimetric resolution when the interferogram is exploited for DEM generation). Such averaging is quite effective with respect to any uncorrelated noise sources due to temporal, baseline, volume etc.

Table 4.2 List of TerraSAR-X ascending acquisitions used in this study

Image	Date	Perpendicular Baseline (m)
Master M	16-MAR-2018	-
Slave $i = 1$	27-MAR-2018	-93.3868
Slave $i = 2$	07-APR-2018	-73.3421 m
Slave $i = 3$	18-APR-2018	18.1099 m
Slave $i = 4$	29-APR-2018	21.0088 m
Slave $i = 5$	10-MAY-2018	180.581 m
Slave $i = 6$	21-MAY-2018	6.71567 m
Slave $i = 7$	01-JUN-2018	235.617 m
Slave $i = 8$	12-JUN-2018	195.783 m
Slave $i = 9$	23-JUN-2018	75.9386 m
Slave $i = 10$	04-JUL-2018	-83.8636 m
Slave $i = 11$	15-JUL-2018	123.557 m
Slave $i = 12$	26-JUL-2018	57.9672 m
Slave $i = 13$	06-AUG-2018	-36.3224 m
Slave $i = 14$	17-AUG-2018	-42.405 m

[30]. However, it is not able to remove space-correlated artefacts, e.g. due to atmospheric turbulence, errors in flattening, or DEM removal etc. The cost of multi-look processing is the degradation of spatial resolution in the interferometric image.

In this exercise, the images were multi-looked by a factor of 3 in the range and azimuth directions, with the intention of clearly defining the point target within the imagery. The same images were also processed without multi-looking for comparison.

4.6.2 GNSS processing method

RINEX (Receiver INdependent EXchange Format) Data from Ordnance Survey active stations (a network of permanently installed geodetic GNSS receivers throughout Great Britain) was downloaded for the 5 closest active station sites to the NPL experiment site. The RINEX data was downloaded from the Ordnance Survey website for the periods covering the GNSS readings. Leica Geo Office software was used to download the Leica GNSS readings. The RINEX data was then imported into Leica Geo Office and the RINEX data was used to estimate the position of each stationed point for each reading period. The RINEX data was used to tie the “Corner” GNSS reading location to active stations, and then this “Corner”

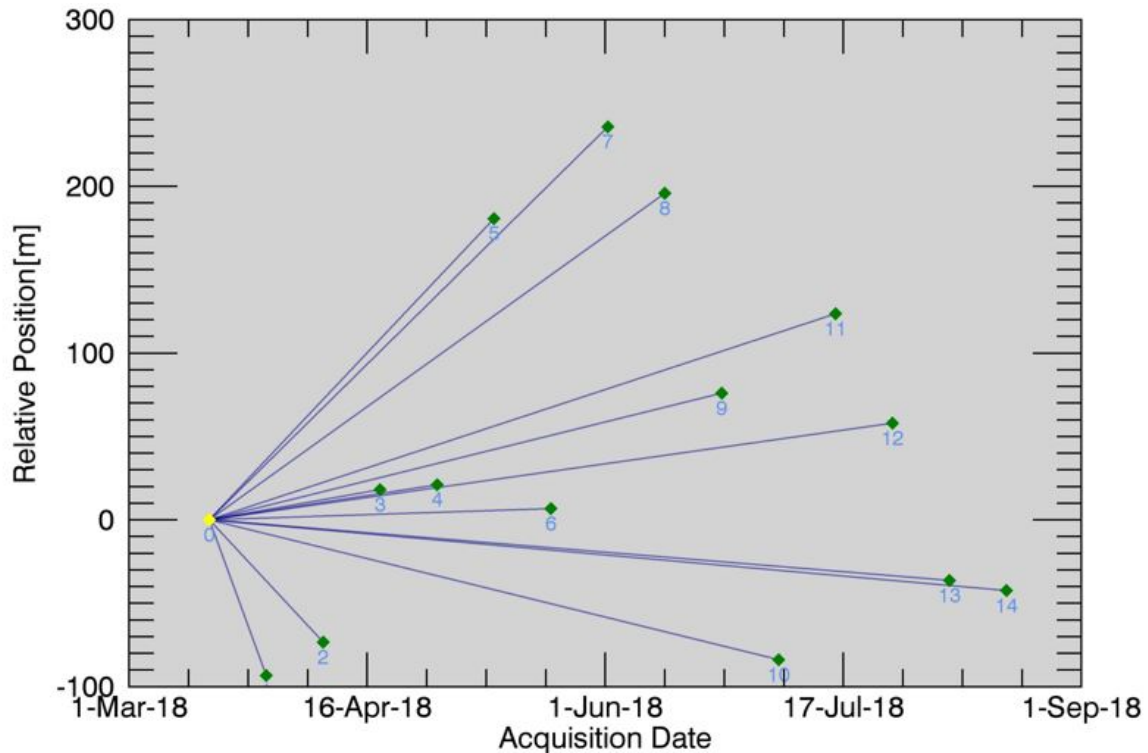


Fig. 4.14 Time-Position plot for the acquisitions used in this study. The Relative Position marks the perpendicular baseline distance of the satellite in space, relative to the first acquisition. As shown, all interferograms (indicated lines connecting the acquisition points marked in green and numbered) were made relative to the first (Master) acquisition on 16/03/2018. Figure produced using ENVI SARscape software.

location was used as the base station (control point) to tie “Corner End” and “Building” to the “Corner” point.

4.6.3 Reference systems

The Earth is an irregular shape and dynamic in nature, but a ‘position’ means a set of coordinates in a clearly defined reference system as well as an understanding of potential positioning error. The reference system used is a critical aspect in terms of tying InSAR measurements to a real-world frame that can be used in practical application for bridge monitoring. Irrespective of the type of coordinates used, a suitable origin (with respect to which the coordinates are stated) is required. The general name for this concept is the Terrestrial Reference System (TRS) or geodetic datum. Using this in practice requires an network of ‘known points’ that makes the coordinate system accessible to users. This network

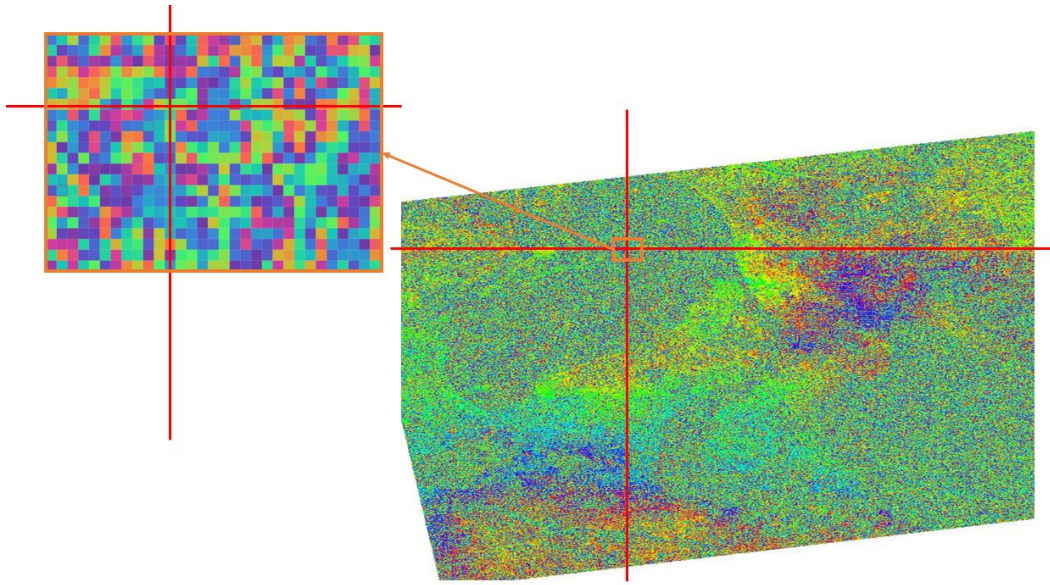


Fig. 4.15 Section from an example differential interferogram used in this study, with the pixel corresponding to Corner Reflector A identified. The image on the left shows a closer view of a section of the interferogram on the right.

of reference points with known coordinates used to realise the TRS is called the coordinate Terrestrial Reference Frame (TRF).

The commonly used World Geodetic System 1984, or WGS84 (used within this research for mapping InSAR results from SAR geometry to real-world frame), consists of a three-dimensional Cartesian coordinate system and an associated ellipsoid so that WGS84 positions can be described as either Cartesian coordinates or latitude, longitude and ellipsoid height coordinates. The origin of the datum is the Geocentre (the centre of mass of the Earth) and it is designed for positioning anywhere on Earth. However, the problem with trying to use a global coordinate system for land surveying in a specific region is that the continents are constantly in motion with respect to each other, at rates of up to 12 centimetres per year [108]. London and Great Britain, like the rest of the European continent, is in motion with respect to the WGS84 coordinate system at a rate of about 2.5 centimetres per year. Over a decade, the WGS84 coordinates of any survey station in Britain change by a quarter of a metre due to this effect, which is unacceptable for precise survey purposes [108].

There are a number of different Terrestrial Reference Frames which realise the WGS84 Geodetic System. This includes the WGS84 broadcast TRF, which is the primary means of navigating in the WGS84 coordinate system via the WGS84 positions of the GPS satellites. A high-accuracy alternative realisation of WGS84 known as ITRS (International Terrestrial Reference System) has been created in a number of versions since 1989, and this is suitable

for international high-accuracy applications. There used to be a difference between the two, but they have been progressively brought together and are now so similar that they can be assumed identical for almost all purposes [108] - the as the International Terrestrial Frame (ITRF) is of higher quality than the broadcast WGS84 TRF, the WGS84 datum now effectively takes its definition from ITRS (coming from the most accurate global TRF ever constructed).

One further realisation, which comes from ITRS is the European Terrestrial Reference System 1989 (ETRS89) [108]. ETRS89 is based on ITRS, except that it is tied to the European continent, and hence it is steadily moving away from the WGS84 coordinate system. The relationship between ITRS and ETRS89 can be precisely defined at any point in time by a simple transformation published by the International Earth Rotation Service. Using ETRS89 the effects of continental motion can be ignored, and the coordinates of a survey station stay fixed apart from any local movement at the location of the survey station. For these reasons, ETRS89 has been officially adopted as a standard coordinate system for precise GNSS surveying by most national mapping agencies in Europe, and was employed in this NPL study using GNSS measurements to provide a frame of reference for the GNSS base station as a stable control point.

The use of this frame also has relevance with regards to the location of the initial persistent scatterer (PS) locations in InSAR processing. InSAR measures the movement of specific points relative to its location at an initial moment in time. Using readings from GNSS enables the initial points to be tied to a suitable Terrestrial Frame.

4.7 Results

The processed GNSS data (Figures 4.16 and 4.17) shows some vertical movement in this region, which would have to be considered with the imposed movement. However, the point plotted for the region next to the NPL main building (which in theory should be reasonably stable due to the foundation arrangements required for the high stability specification of the NPL laboratory building) also shows some movement. This could then suggest that there is some noise within the readings or more large-scale earth effects [65]. When the three GNSS location readings are plotted alongside each other (as shown in Figure 4.16), these movements look insignificant, but the variation is highlighted when plotted separately.

In terms of the SAR data collected, the extracted phase values from the generated interferograms were collated and the difference in values associated with Corners A, B and C (A-B and C-B) were plotted against the imposed vertical movement measured, as shown in Figures 4.18 and 4.19.

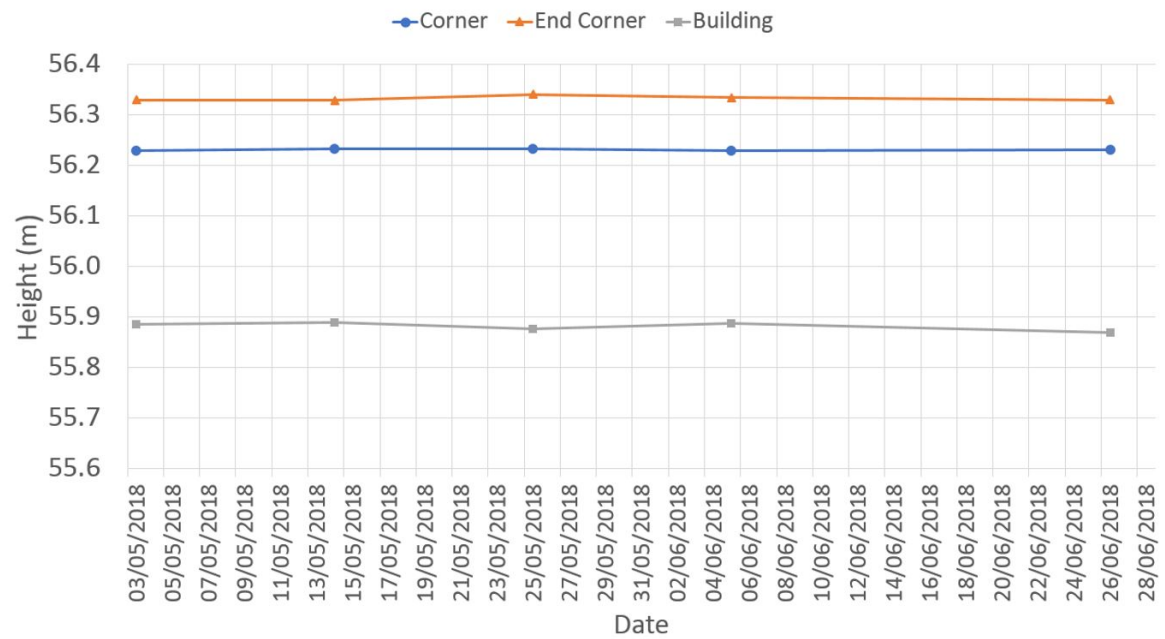


Fig. 4.16 GNNS recorded vertical movement over time for all sites.

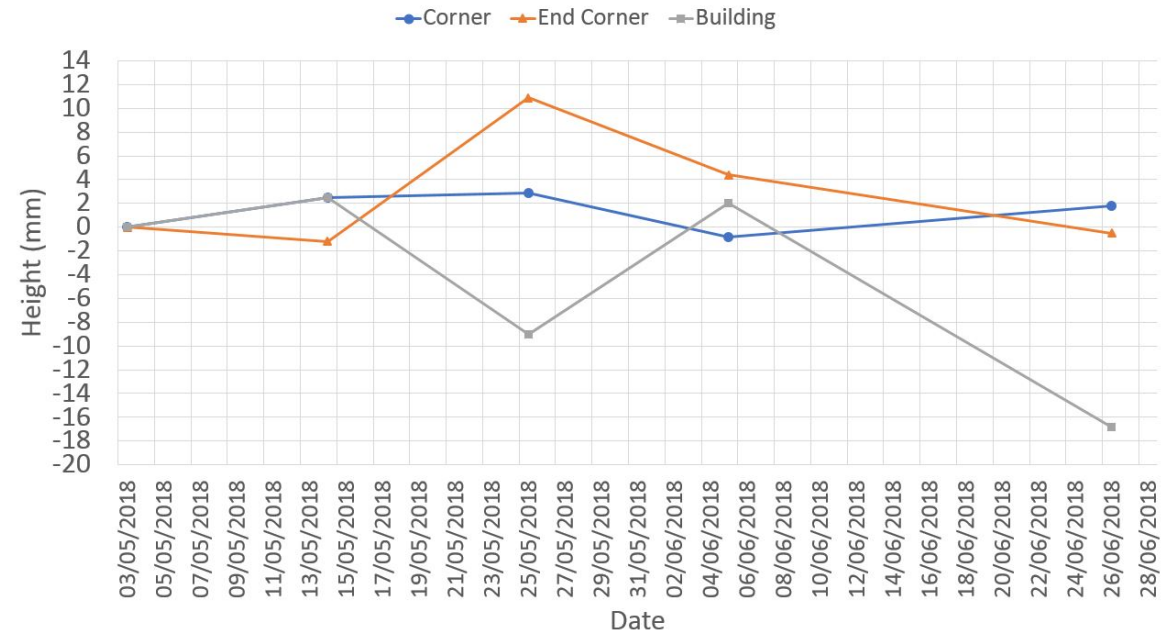


Fig. 4.17 GNNS recorded vertical movement over time for 'Corner' site.

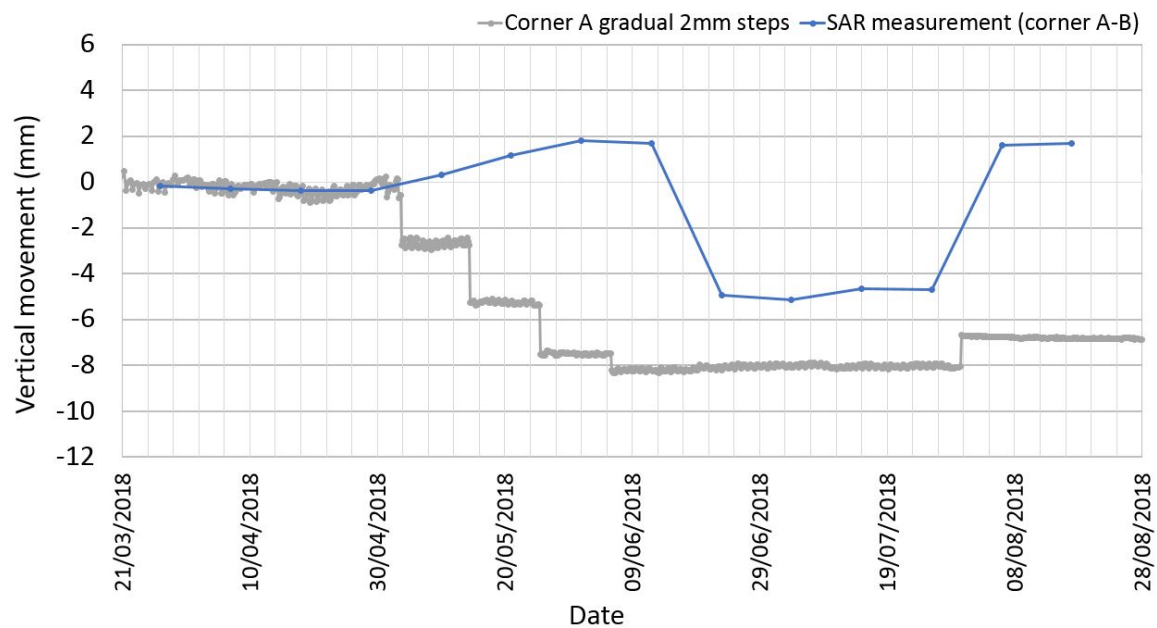


Fig. 4.18 Corner A SAR measurement (phase values for A-B, using multilooking) of vertical deformation plotted against imposed vertical movement without unwrapping.

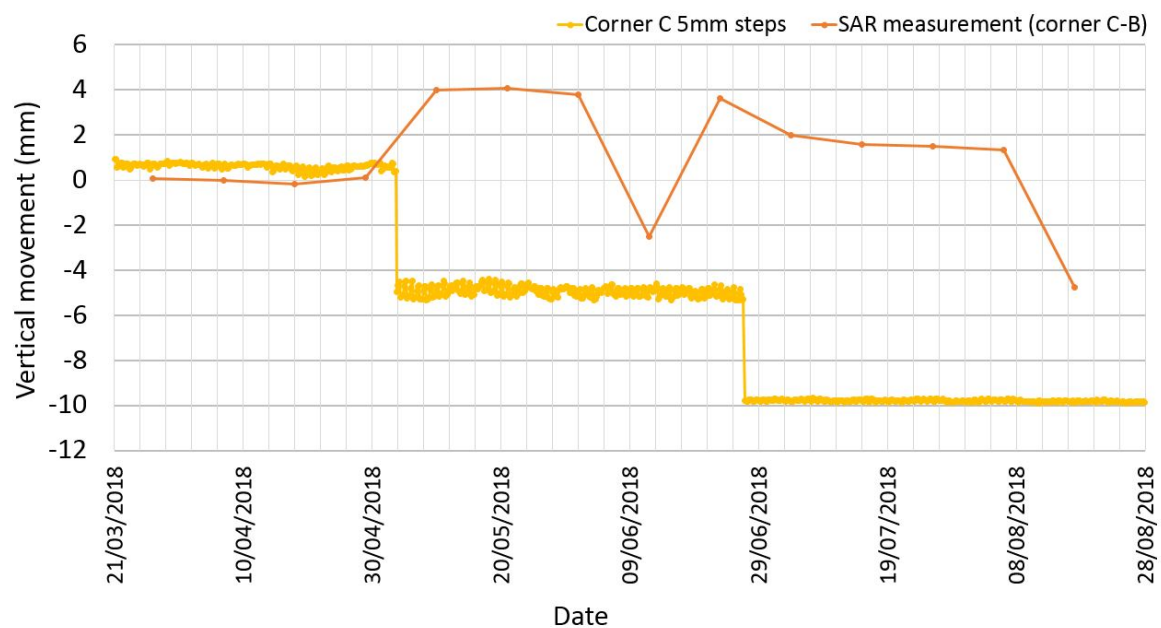


Fig. 4.19 Corner C SAR measurement (phase values for C-B, using multilooking) of vertical deformation plotted against imposed vertical movement without unwrapping.

This method calculates the change in phase value, but without direction. From inspection, it can be seen that each value should be multiplied by -1 to show movement in the downwards vertical direction. The next correction to be applied relates to ambiguities associated with using a sine wave for measurement. All of the phase values extracted (for 'Pixel A', 'Pixel B' and 'Pixel C', relating to the location of Corners A, B, and C respectively) were less than π radians. However, when the values for Pixel A and C are each subtracted from "fixed" corner reflector location, B, some of the resultant values are greater than π .

The phase values from a SAR signal are constrained to a $+\pi$ and $-\pi$ interval. In cases where the phase exceeds this range of values, it will be 'wrapped' so that the phase measurements stay within the range $(-\pi, +\pi)$. Figure 4.20 illustrates this principle. The left-hand graph shows the original signal which has a phase that lies between $+2\pi$ and -2π , and on the right-hand graph, the signal has been restricted to a $+\pi$ and $-\pi$ limit. Once the phase value reaches the upper limit, there is a $+2\pi$ discontinuity (jump) in the graph and the signal carries on from the lower limit.

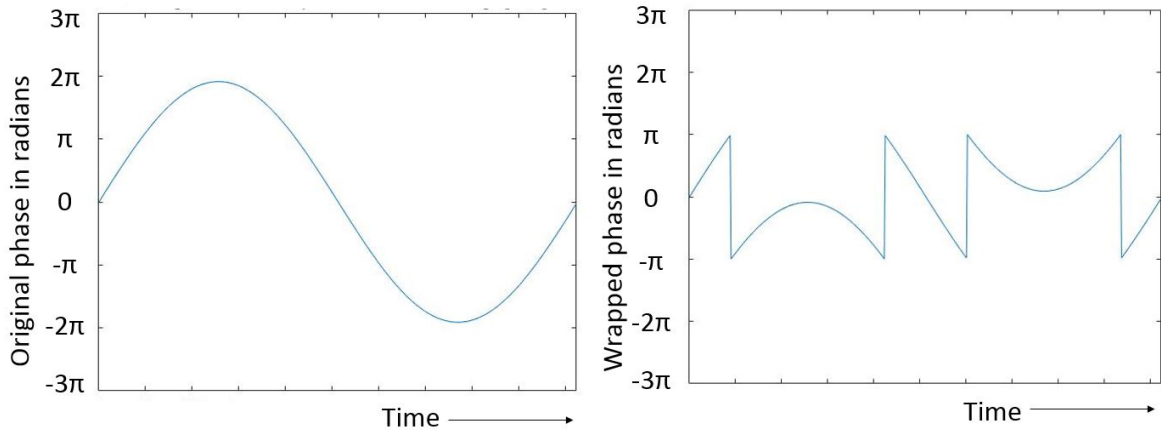


Fig. 4.20 Principle of phase unwrapping, with left hand graph (a) depicting the original signal whose amplitude exceeds the $+\pi$ and $-\pi$ range and the right hand graph (b) showing the wrapped signal when restricted to a $+\pi$ and $-\pi$ limit

The 2π jumps that are present in the wrapped phase signal that is shown in Figure 4.20 (b) must be removed in order to return the phase signal to its continuous form (which is required to make the phase usable in understanding the actual deformation behaviour). This process of determining the 2π ambiguity in measurement to return the signal to its original continuous form is known as 'unwrapping'.

In the particular results considered here for the NPL experiment SAR readings, π was subtracted from the values outside of the π and 2π range. Once the change in phase was determined and unwrapped, the results were converted to a LOS distance by multiplying by wavelength $/2\pi$. From the SAR LOS measurement, the vertical component of that measured

movement was calculated by multiplying the LOS value by the cosine of the incidence angle (the SAR LOS angle to the vertical, Figure 4.21).

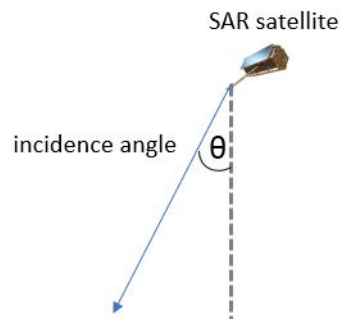


Fig. 4.21 SAR incidence angle.

These vertical measurement results were then plotted and are depicted in Figures 4.22 and 4.23 below.

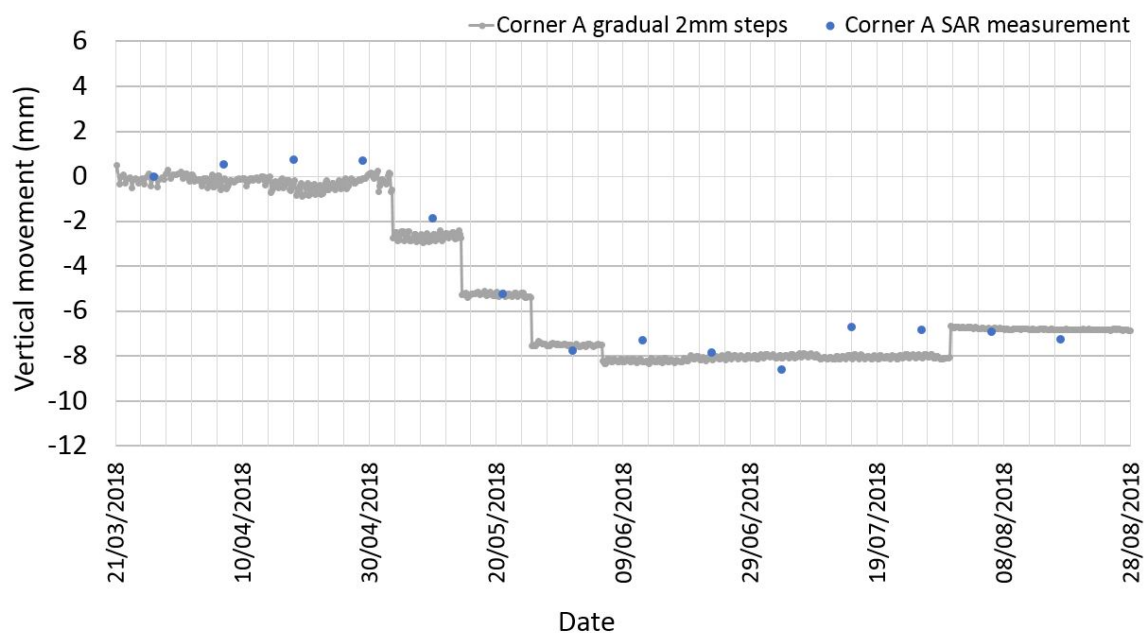


Fig. 4.22 Corner A SAR measurement with unwrapping against imposed vertical movement.

The SAR readings for Corner A generally follow the profile of the steady stepped changes imposed on the corner reflector, but the SAR readings for Corner C (which should have readings at the measurement values held at a steady position) show some drift in what should be a steady reading. This set of results for Corner C is useful in understanding how repeatable the readings are and how much variation exists within the results.

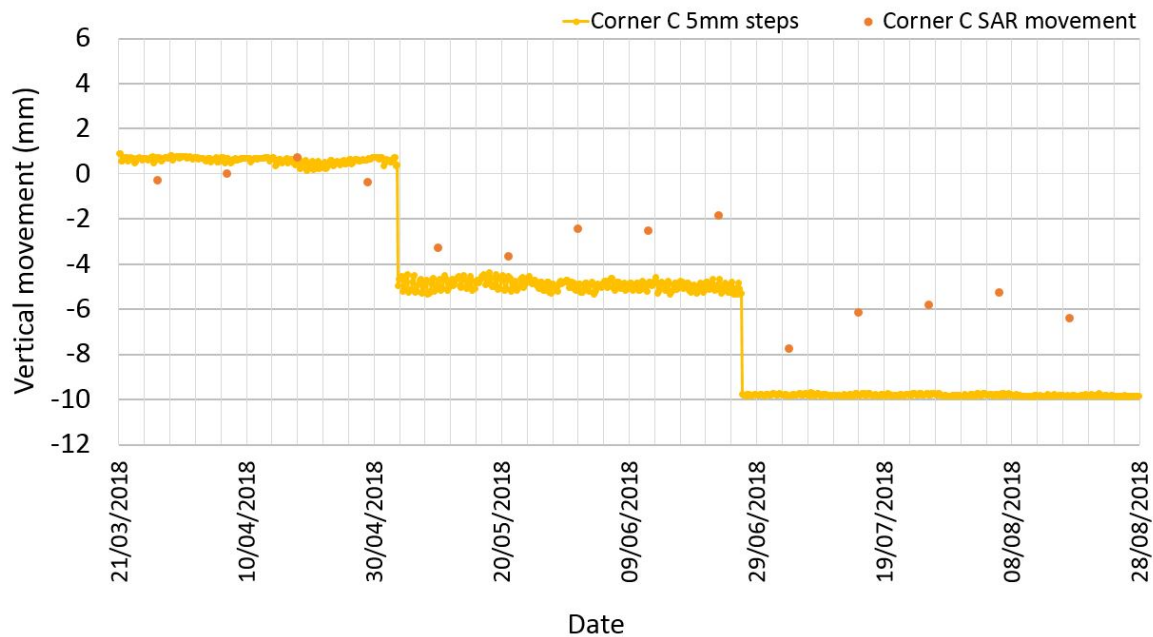


Fig. 4.23 Corner C SAR measurement with unwrapping against imposed vertical movement.

4.7.1 The effect of multilooking

The nature of this experiment means that the anticipated points of interest within the SAR image were designed to be very bright points. The dominant scatterers (the corner reflectors) each create a bright spot that biases the filtering operation, as it saturates the brightness of that pixel and the surrounding pixels. Thus, when a 3-pixel by 3-pixel multilooking filter is applied during the processing, the filtering does not have a strong effect in that it is still picking up the strong signal of the intended pixel.

4.7.2 Trends within the data

For the results for Corner C, the SAR-measured points tended to drift upwards after each imposed step displacement rather than remaining steady as measured on the ground. Rather than a measurement of uncertainty attributed to random error, this suggests a more systematic error. One possible reason for this effect could be local ground deformation. The SAR measurements were taken with respect to the middle reflector, whilst the ground measurements at site were taken at Corners A and C, without measurement at B (which was assumed to be a “fixed” reflector). If the ground in the location of Corner B (in the middle of the test rig) sank more than ends of the concrete block test rig, this could explain the drift as a change in relative movement.

To investigate possible causes of this effect, rainfall data from a gauge based a few miles away from the NPL site in Heathrow (Figure 4.24) and temperature data collected at the NPL experiment site were plotted against the vertical component of the SAR measurements (Figure 4.25).

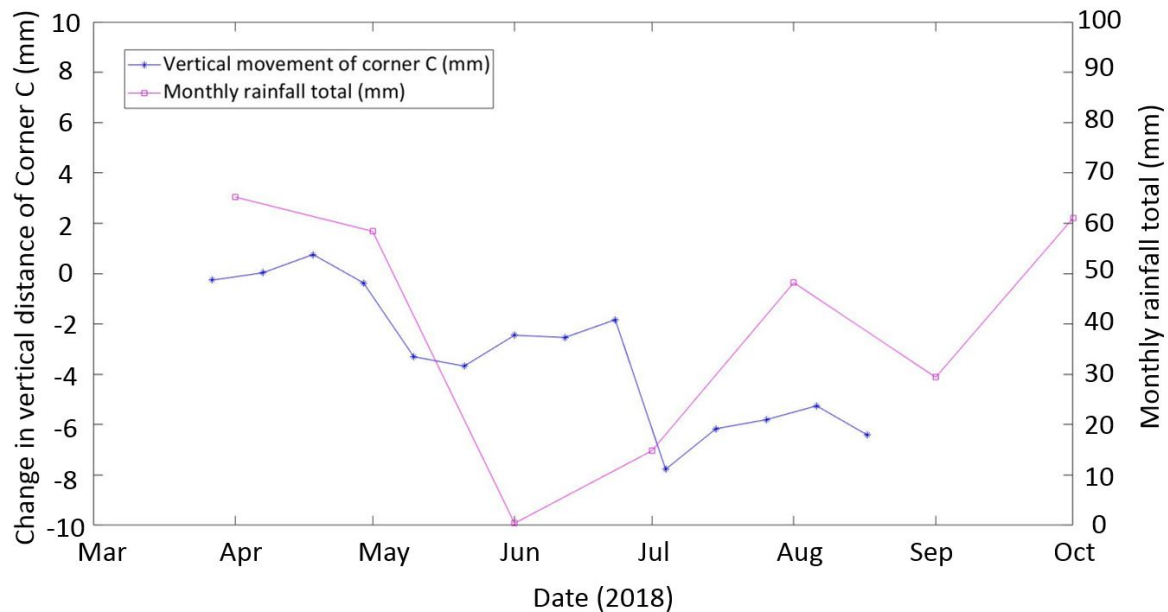


Fig. 4.24 Monthly rainfall during SAR readings. Vertical movement of Corner C is plotted in blue and total rainfall for each month is plotted on the first of each month in magenta.

It is difficult to draw any obvious conclusion using the rainfall data in Figure 4.24. The plot shows the total rainfall for each month plotted at the start of each month. Considering June and July as an example, there was very little rainfall for June, and some rainfall in July. However the data for both months shows a rising drift in the measured values. If the rainfall does not correlate with the measurement drift, this would suggest that there less likely to be an issue with ground shrinking and swelling, and this effect being transferred through the test rig. This conclusion is not, however, robust given the sparsity of the rain data and broad assumptions made.

The temperature data (Figure 4.25) was collected using temperature gauges that were included with the Moniteye displacement gauge unit and therefore collected the temperature as measured on the corner reflector base unit (rather than ambient temperature of the Teddington area). This data does show a steady rise in temperature that generally agrees with the profile of movement (discounting the imposed step changes made by moving the corner reflector vertically). Adding the measured corner reflector vertical movement as recorded by the displacement gauge on site (Figure 4.26) shows that it is not the metal corner base

stand expanding with temperature. A possible explanation is that the low rainfall and higher temperatures drying out the ground might cause the test rig to sink slightly in one section of the rig relative to another, thus resulting in a drift in measurement readings if Corner B is moving relative to Corner C.

Reflecting on the experimental set up and the behaviour of the test rig and ground conditions provides a number of thoughts to consider. The experimental test rig consisted of a concrete block array installed on the ground. The blocks were installed over a geotextile and left for several weeks to allow for initial settlement. From a geotechnical perspective, the concrete blocks would cause some settlement over a period of several months, considering that they were installed on made ground and top soil in the site next to the NPL building. If the concrete blocks settled due to consolidation of the ground material, the InSAR measurements would be expected to yield higher vertical measurements (higher settlements) than the conventional displacement sensors, which are referenced to the top of the concrete block. On the other hand, if the ground beneath the foundation swelled, the InSAR measurements reveal smaller measurements in comparison to the sensor measurements. Referring back to Figure 4.23, this latter explanation could offer some explanation as to why the InSAR measurements continue to show decreasing settlement over time whilst the sensors suggest that the movements of the reflectors are being held steady (the entire rig is moving and the conventional sensors reference point at the top of the wall means that it is not being picked up). This is also based on the assumption that the concrete blocks act as one unit. The concrete base was made up of several units that were connected together such that they were assumed to be acting as a single rigid unit. If the blocks were moving independently to one another to some degree, there may be different effects at different points on the test rig, and this view of settlement effects on the measurements would change.

One further reflection on the experimental for future work would be to set up GNSS devices for the purpose of providing ‘ground-truth’ measurement points such that the InSAR measurements could be tied into a suitable reference system, as described in Section 4.6.3. If this experiment were to be repeated, it would be worth taking GNSS readings at the location of the corner reflectors themselves. This would ideally be achieved by setting up a GNSS measurement station on top of the test rig (rather than points measured on the ground at some distance from the corner reflectors on the ground next to the rig, as was done here). Newer more portable GNSS devices coming into the market could possibly be installed and left on site for the duration on the experiment.

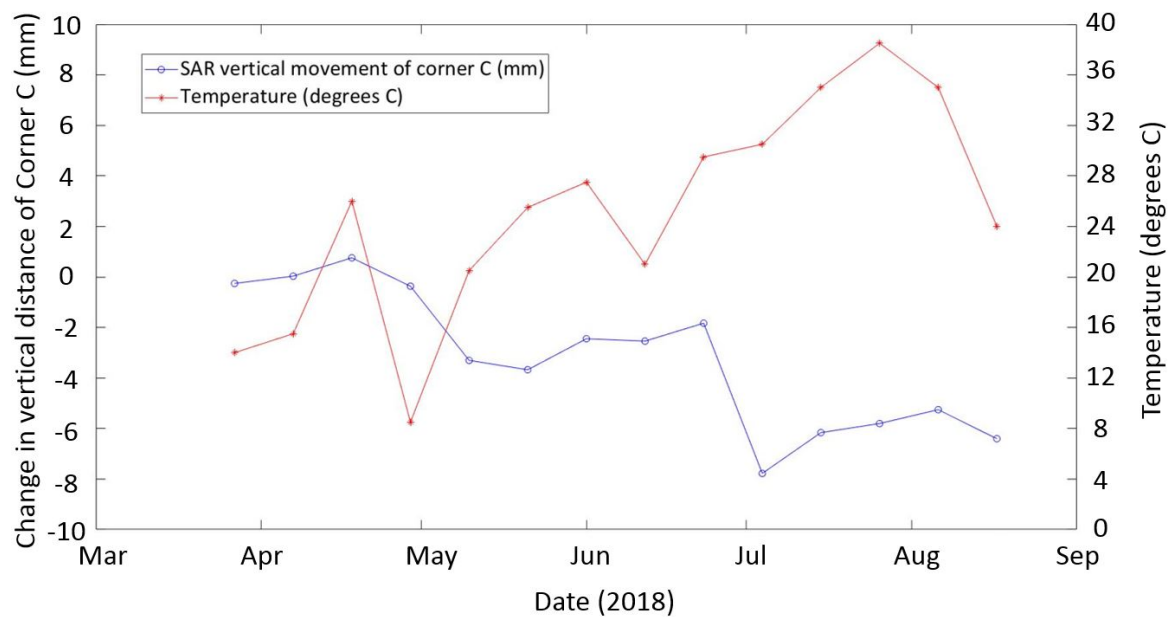


Fig. 4.25 Temperature on dates of SAR readings. Vertical movement of Corner C is plotted in blue and temperature as recorded on site at Corner C at the time of SAR acquisition in red.

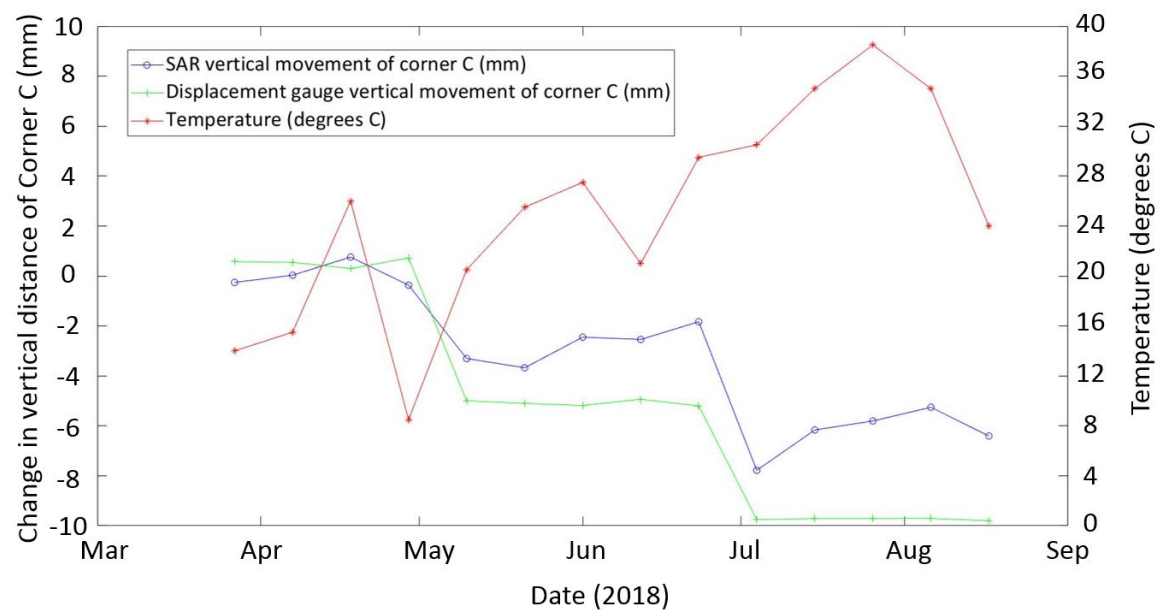


Fig. 4.26 Temperature, SAR and displacement gauge readings. Vertical movement of Corner C as measured by SAR is plotted in blue, vertical movement of Corner C as measured by displacement gauge is plotted in green and temperature as recorded on site at Corner C at the time of SAR acquisition in red.

4.7.3 Error sources in differential InSAR

As outlined in the theory in Chapter 2, the interferometric phase of a pixel ($\Delta\phi_{int}$) in a multi-temporal differential interferogram formed from processing a series of images over time can be represented by a number of components. For ease of reference, this equation is quoted again as Equation 4.3 below:

$$\Delta\phi_{int} = \Delta\phi_{defo} + \Delta\phi_{topo} + \Delta\phi_{atm} + \Delta\phi_{orb} + \Delta\phi_{noise} \quad (4.3)$$

where $\Delta\phi_{defo}$ represents the phase due to deformation, $\Delta\phi_{topo}$ refers to the error introduced by using imprecise topographic information, $\Delta\phi_{atm}$ corresponds to the difference in atmospheric propagation times between the two acquisition used to form the interferogram, $\Delta\phi_{orb}$ refers to the error introduced due to the use of imprecise orbits in mapping the contributions of Earth's ellipsoidal surface, and $\Delta\phi_{noise}$ represents the phase noise due to the scattering background and other uncorrelated noise terms.

The $\Delta\phi_{defo}$ is the component of interest for this experiment. In a perfect experiment, the SAR measurement would only pick up measurements associated with this term, and all other terms in Equation 4.3 would be zero. In reality, the other terms may not be zero, but additionally some measurement uncertainty is introduced through the experimental set up, such as the influence of temperature and true ground movement, as previously discussed.

The spatial heterogeneity of the wet component of atmospheric refractivity (which affects the radar signal propagating through the the atmosphere) is considered a dominant error source, $\Delta\phi_{atm}$, in InSAR methods [109]. However within this experimental set up, the corner reflectors were installed in close proximity. Having deployed the reflectors very close to each other, this phase disturbance was considered negligible, as the spatial behaviour of the atmosphere above each corner location can be considered as the same. This meant that the impact of the atmospheric effects could be reasonably neglected by the double phase difference (subtracting each of Corners A and C from Corner B would remove this component from consideration if $\Delta\phi_{atm}$ was the same for Corners A, B and C). The $\Delta\phi_{orb}$ and $\Delta\phi_{topo}$ could also be considered negligible through similar arguments.

The noise term, $\Delta\phi_{noise}$, remains. In order to limit excessive additions to the noise term, an attempt was made to clean the reflectors periodically. On each site visit, a number of bird droppings on the reflector faces were noted, which may have affected the quality of the returned signal if present during an acquisition.

4.7.4 Error sources in GNSS readings

The main factors affecting accuracy of a single high quality GNSS receiver are errors in satellite positioning, the satellite clocks and the effects of the Earth's atmosphere on the signal's travelling speed [107]. In this experiment the satellite clock and position errors are eliminated by leaving a GNSS base station (in this case the receiver position at the "Corner" location) to collect data for an extended period of time. The Leica Geo Office software corrects for the positions of the satellites using the data recorded by that GNSS receiver and applies those corrections to the other GNSS measurement locations. Similar to the atmospheric component considered in the SAR measurements, the proximity in location of the receivers helps to reduce the atmospheric errors. One final source of error would be a multiple-bounce effect. This would occur if the GNSS receiver was positioned close to the NPL building such that the signal received did not come directly from the satellite, but instead bounced off the nearby building or other surfaces before being received by the GNSS receiver. Overall the experimental set up can consider the lower values of relative positional accuracy, which is about 2mm (this value can be as large as 2 decimetres in certain conditions) [107].

One key question in considering error sources in the GNSS readings is the geological stability of Ordnance Survey Active station sites. The GNSS readings are based on the assumption that these points are fixed, and so the RINEX data provides accurate positioning. On discussion with Ordnance Survey, it was confirmed that OS Net stations were selected to be on stable sites and mostly on buildings, but there is no specific geological investigation prior to choosing a site. The main requirement for OS selection was that the point was considered to be on a "stable structure" such as a substantial building. For the purpose of this study in calibrating GNSS receiver positioning, this is not a suitable "fixed point". OS also have a subset of sites (called GeoNet) that were chosen for maximum long-term stability, where sites were either pile driven helical pier monuments (driven to refusal) or solid metal pins driven directly into exposed bedrock. There are 12 GeoNets sites within the UK, however none of which are in or near the Greater London area (the closest to the NPL site being HERO at Herstmonceux).

Another possibility would be to use Fundamental Bench Marks (FBMs) and tie the Active Station locations to one or more of these sites. The locations of FBMs for the UK are published by Ordnance Survey [110]. FBMs were reference levelling points, primarily installed in the first half of the twentieth century, at sites carefully selected to provide an anchor to bedrock. The nearest FBMs to the NPL location at Teddington are listed as Windsor, H1SU9777 (although in this case this is actually an Auxiliary Berntsen marker installed close to the actual FBM) and at Croydon, H2TQ3260.

Given that the precision of the data collected for the SAR readings was in the order of a few millimetres (on the same scale as the differential GNSS readings), this further measurement refinement using FBMs was not undertaken.

4.8 Discussion

In terms of application to bridge monitoring, the motivations of the research established that one of the goals of this research was to determine the precision, repeatability and uncertainty of measurements with respect to displacement sensors, terrestrial surveying and other methods traditionally employed to study structural behaviour. The NPL experiment allows exploration into the reliability of the results through assessment of how repeatable the data is and how well correlated the measured InSAR data is to conventional sensor measurements. This is first discussed below before moving onto an assessment of uncertainty of the measurement data, which is valuable in structural measurements by providing an understanding about degree of precision of the measurement data.

4.8.1 Understanding InSAR quality

Some basic statistical information is presented in Figure 4.27. In terms of reliability and repeatability of results, this basic statistical information shows that the measurement values for steady readings (no vertical movement imposed) have a range of 1.1mm to 2.5mm. Two further statistical measures are presented below to evaluate the data measured by InSAR against the data measured by in-situ sensors. These are the Pearson correlation coefficient, commonly used in statistics, and the Spectral Angle Mapper which was developed within the remote sensing community to evaluate how similar different spectra are, but has been employed in this instance as an alternative measure to assess the coherent content between two multidimensional signals.

Pearson correlation coefficient

The Pearson correlation coefficient is a statistical measure to understand how well two quantities relate, and quantifies the linear correlation between our two variables, in this case SAR-measured values and ground-measured values. These results are presented below in Table 4.3. Correlation values lie between -1 and +1. The closer the correlation is to -1 the more negatively correlated the variables, and the closer to +1 the more positively correlated. A value close to zero indicates little or no correlation. The results above show

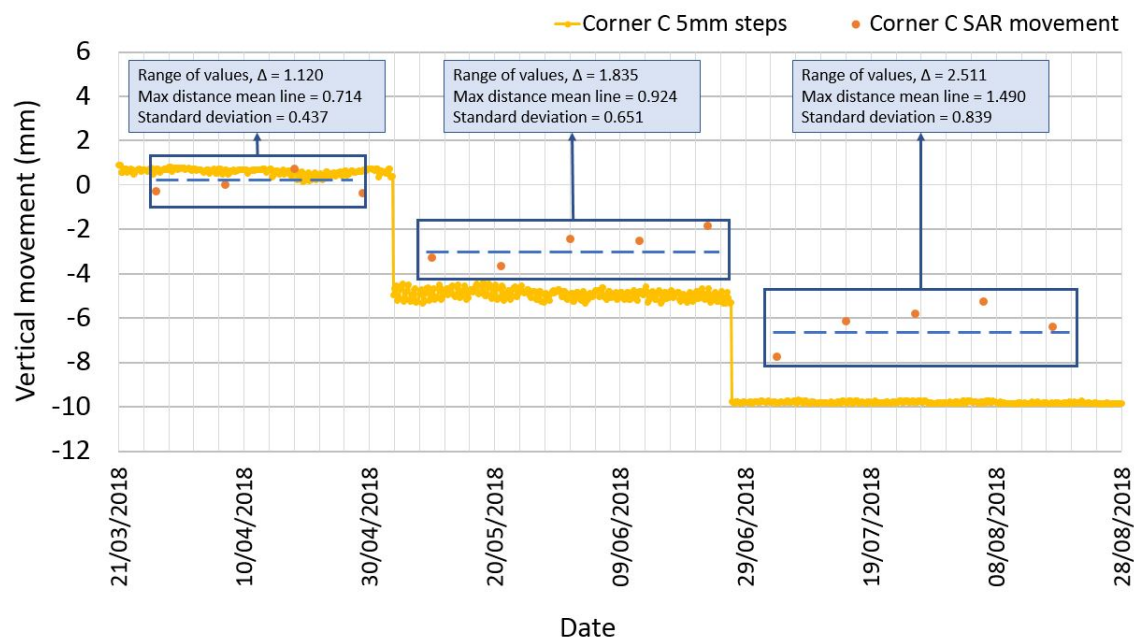


Fig. 4.27 Statistical information for Corner C vertical displacement SAR measurements.

that the correlation of the SAR-measured values and ground-measured values lies close to +1, indicating high correlation.

Table 4.3 Pearson correlation coefficients

Corner	3 x 3 Multilooking	No Multilooking
A	0.986	0.972
C	0.957	0.959

Spectral Angle Mapper

Within the remote sensing field, the Spectral Angle Mapper tool [111] permits rapid mapping of the spectral similarity of image spectra to reference spectra. The tool is used to establish the spectral similarity between two spectra by calculating the "angle" between the two spectra by treating them as vectors in a space with dimensionality equal to the number of bands (nb), as illustrated by a simplified example in Figure 4.28 below.

In this experiment, the movement measured by the displacement gauge on the ground was considered as the reference spectrum and the SAR-measured movement as the test spectrum. This was calculated over 14 bands (a band for each SAR measurement point). Using Spectral Analysis Mapping generalises the geometric interpretation shown in Figure 4.28 to a nb-

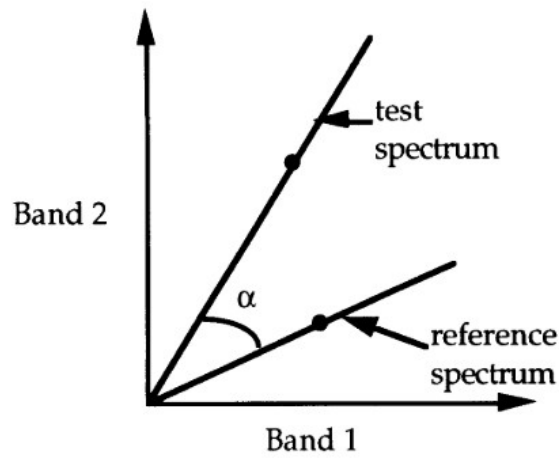


Fig. 4.28 A simplified explanation of this can be given by considering a reference spectrum and a test spectrum from two-band data represented on a two-dimensional plot as two points. This Figure is from a paper by Kruse et al. [111].

dimensional space (where nb is the number of bands). The calculation consists of taking the arccosine of the dot product of the spectra by the following equation:

$$SAM = \arccos \frac{\sum_{i=1}^{nb} t_i r_i}{(\sum_{i=1}^{nb} t_i^2)^{\frac{1}{2}} (\sum_{i=1}^{nb} r_i^2)^{\frac{1}{2}}} \quad (4.4)$$

where nb is the number of bands, r_i is the i th reading for the reference spectrum and t_i is the i th reading for the test spectrum.

Table 4.4 Spectral Angle Mapper (SAM) values

Corner	3 x 3 Multilooking	No Multilooking
A	0.1997	0.2178
C	0.1858	0.1766

The Spectral Angle Mapper calculation was undertaken for each of the corners and was found to have a very small angle value (noted in radians in Table 4.4) which would indicate a very strong correlation between the two sets of measurements. Further discussion on the measurement uncertainty of the data is presented in the discussion below.

4.8.2 Measurement of uncertainty

The measurement of a quantity, especially in the application of infrastructure movement, is not valuable unless the uncertainty of the measurement is also known. The measurement of a bridge cited moving to the nearest hundredth of a millimetre is meaningless if the measurement tolerance is certain only to the nearest 5mm. A measurement of uncertainty is, as stated by the Joint Committee for Guides in Metrology [112], “indispensable in judging the fitness for purpose of a measured quantity value” and is defined as the “non-negative parameter characterizing the dispersion of the quantity values being attributed to a measurand, based on the information used”.

There are a number of means by which uncertainty can be estimated. The US National Institute of Standards and Technology [113] grouped methods into one of two broad categories: Type A) those which are evaluated by statistical methods, and Type B) those which are evaluated by other means (noting that these can also be considered as components “arising from a random effect” and those “arising from a systematic effect”). The latter (systematic) error is usually based on scientific judgement and previous measurements and specifications. In this case, there is an understanding of measurement errors based on the literature, but the primary focus is on using valid statistical methods to determine a value of uncertainty.

Individual standard uncertainties calculated by Type A or Type B evaluations can be combined using the ‘law of propagation of uncertainty’ (also known as the ‘root sum of the squares’ method). The result of this is called the combined standard uncertainty, u_c . For the measurement result y , $u_c(y)$ (taken to represent the estimated standard deviation of the result) is the positive square root of the estimated variance $u_c^2(y)$ obtained from Equation 4.5 provided by Taylor and Kuyatt [113].

$$u_c^2(y) = \sum_{i=1}^N \left(\frac{\partial f}{\partial x_i} \right)^2 u^2(x_i) + 2 \sum_{i=1}^{N-1} \sum_{j=i+1}^N \frac{\partial f}{\partial x_i} \frac{\partial f}{\partial x_j} u(x_i, x_j) \quad (4.5)$$

Equation 4.5 is based on a first-order Taylor series approximation of $Y = f(X_1, X_2, \dots, X_N)$ and is the mathematical expression of the ‘law of propagation of uncertainty’. The partial derivatives $\frac{\partial f}{\partial x_i}$ are referred to as ‘sensitivity coefficients’ and are equal to $\frac{\partial f}{\partial X_i}$ evaluated at $X_i = x_i$. The $u^2(x_i)$ term is the standard uncertainty associated with the input estimate x_i , and $u(x_i, x_j)$ is the estimated covariance associated with x_i and x_j .

Covariance

Within the field of statistics, the standard deviation can be calculated as a standard measure for uncertainty within a single variable data set (quantifying the amount of variation within

the set of values). However, in the context of this experiment, there are two variables for which the uncertainty of SAR measurement data is being assessed by its relationship to the in-situ ground measurement. For this purpose, the covariance can be employed. The covariance is a measure of the joint variability of two random variables. A positive covariance means the variables are positively related, while a negative covariance means the variables are inversely related.

The covariance for Corner A is 11.4 for multilooked results and 10.7 for non-multilooked data. The calculated covariance for Corner C is 10.2 for multilooked results and 9.9 for non-multilooked data. These large positive covariance values indicate that the SAR data is strongly and positively related with the measured data on ground.

4.8.3 Uncertainty associated from taking vertical component of LOS measurement

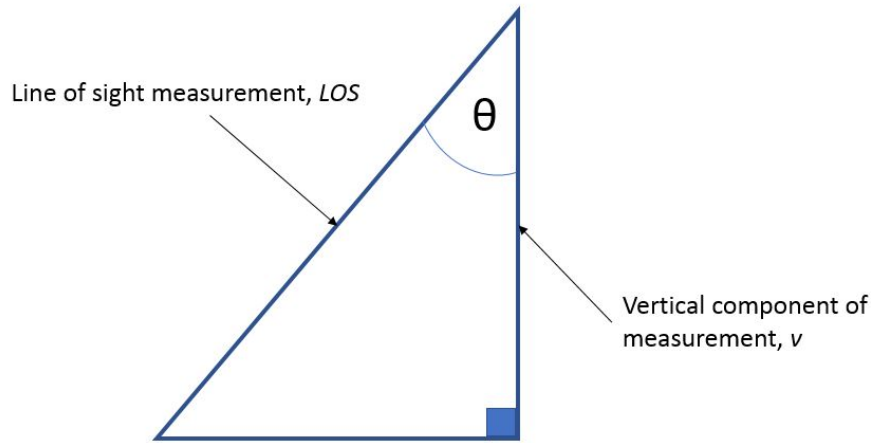


Fig. 4.29 Vertical component of line of sight (LOS) measurement.

The vertical component of the LOS measurement (illustrated using Figure 4.29) was calculated using Equation 4.6.

$$v = LOS \cos \theta \quad (4.6)$$

In this case, v is found by multiplying the line of sight measurement obtained, LOS , by the cosine of the incidence angle set by the SAR satellite, θ . The relative or fractional uncertainty in the value of v can be found from the fractional uncertainties in the LOS and $\cos \theta$ values. The estimated variance σ_v^2 is given by Equation 4.7, where σ_{LOS}^2 and σ_θ^2 are the variance of the LOS and θ values respectively.

$$\sigma_v^2 = \frac{dv^2}{d_{LOS}^2} \sigma_{LOS}^2 + \frac{dv^2}{d\theta^2} \sigma_\theta^2 \quad (4.7)$$

This can then be written as:

$$\sigma_v^2 = \cos^2 \theta \sigma_{LOS}^2 + LOS^2 \sigma_\theta^2 \quad (4.8)$$

Therefore the uncertainty, $u_c(v)$, can be written as Equation 4.9:

$$u_c(v) = \sqrt{\cos^2 \theta \sigma_{LOS}^2 + LOS^2 \sigma_\theta^2} \quad (4.9)$$

All acquisitions were taken with incidence angle range of 36.11 - 38.5 degrees (converted into radians for these calculations), which provides a value for θ and σ_θ . The values of σ_{LOS} and LOS were calculated using the SAR data values. These $u_c(v)$ values were calculated for each of the three regions marked in Figure 4.30.

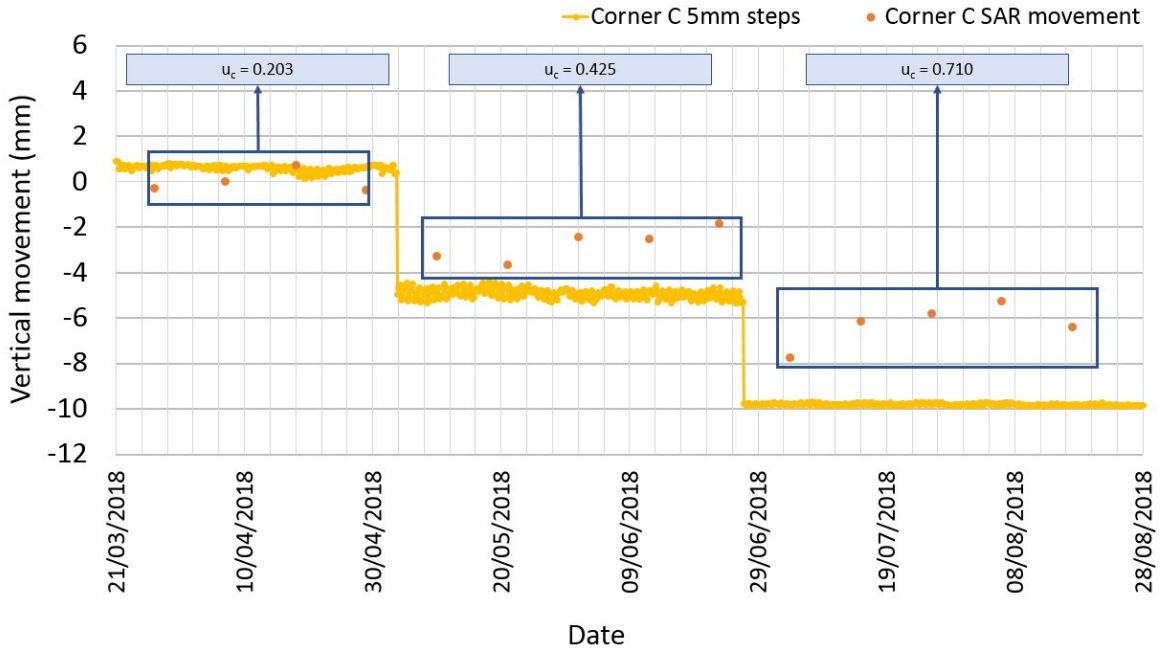


Fig. 4.30 Calculated uncertainty values for each graph region of Corner C.

The uncertainty associated with taking the vertical component of the LOS SAR measurements taken during this experiment ranged from 0.20 to 0.71mm. In a measurement of only a few millimetres, this would significantly impact the measurement result.

4.9 Conclusions

This experiment was designed to investigate the reliability and uncertainty of InSAR measurements to identify whether such measurement techniques are suitable for bridge monitoring applications. The experiment found that there was some variation in repeat readings, giving a range of up to 1.5mm between readings and the mean line around which they were centred. An assessment of uncertainty in deriving the vertical component of these readings was undertaken and found to have an uncertainty of vertical measurement $\pm 0.7\text{mm}$ or better. It can be additionally noted that the SAR measurement readings are of a comparable scale of millimetre-scale measurement as GNSS measurements.

From this experiment, it was determined that the relative displacement measurements obtained from SAR acquisitions were of millimetre-scale in precision, of up to 2mm. This confirmed that InSAR measurements were of the right scale to be considered for use in bridge monitoring and other civil engineering applications.

Chapter 5

Waterloo Bridge

5.1 Introduction

In this Chapter Waterloo Bridge, over the River Thames in London, is presented as an experiment to investigate the potential for using InSAR satellite monitoring data to measure movements of the bridge and hence supplement bridge management activities. The previous Chapter sets out a controlled experiment to assess resolution, sensitivity and uncertainty of InSAR measurement data, whilst this Chapter is aimed at understanding these measurement uncertainties and quality of measurement data within an applied context. As part of working in an applied bridge engineering context, a key goal of this work was to try and measure vertical and horizontal displacements of the bridge deck with time, in particular with respect to temperature expansion and other loads. Furthermore this Chapter aims to highlight that the interpretation and integration of InSAR datasets with conventional civil infrastructure surveying data is more than a trivial task, and a strategy for combining and interpreting varied data from multiple sources to provide useful insights and data analysis to support wider monitoring strategies is presented.

Section 5.2 introduces Waterloo Bridge and provides some context on the structure and monitoring requirements. Corner reflectors for InSAR readings and target prisms for automated total station (ATS) measurements were installed at key points of interest as part of a wider structural monitoring system, as outlined in Section 5.3, and the methods used for data processing are presented in Section 5.4. Section 5.5 presents the results of this processing and the displacement data from the SAR and ATS systems are compared to gain a better understanding of the uncertainty in the measurements and the relationship between the datasets. Section 5.7 investigates how the two methods of measurement could be combined to enhance the robustness of the measurements before presenting some points for consideration

in the practical application of such systems by industry in Section 5.8, with conclusions presented in Section 5.9.

5.2 Bridge structure

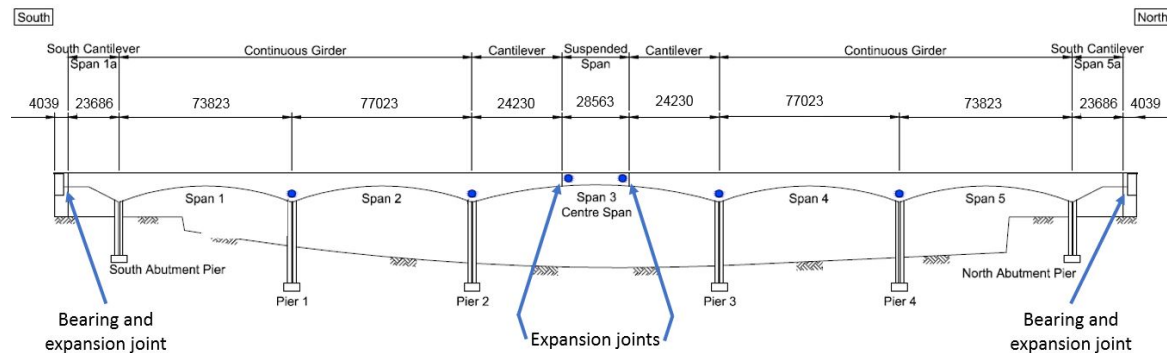


Fig. 5.1 Elevation of Waterloo Bridge, London. ATS prism and corner reflector locations are marked as red dots.

Waterloo Bridge is a 434m long concrete bridge carrying the A301 across the River Thames in London [114]. The bridge comprises two reinforced concrete, multi-cell box girders and a concrete deck. It has five main spans and is nominally symmetric about its centreline (Figure 5.1). The box girders and deck are continuous over two spans, with cantilever projections beyond the abutment piers and into the central span, where they support a central drop-in section. In 1981 the bridge was designated as a Grade II* Listed structure by Historic England.

The bridge responds to changes in temperature by expanding or contracting over its 434m length. This daily and seasonal change in length of the structure is accommodated through four expansion joints, one at each abutment either end of the bridge and one at each end of the central drop-in span. Recent inspections have revealed a number of concerns relating to the performance of the bridge's articulation, prompting further work to investigate the bridge's current condition and develop potential remedial solutions if necessary.

The roller bearings supporting the bridge's central drop-in span are unusual in design. The recent inspections highlighted significant deterioration, with parts of these bearings becoming detached. This prompted safety concerns for river traffic passing under the bridge. There were also concerns that the bearings and lateral restraint members across the joints may have locked up due to corrosion, silt build-up and dislodged components. If true, this would have the consequential effect of changing the bridge's articulation, introducing additional stresses into the structure's deck and piers when the bridge expands and contracts due to temperature

variations. There are approach slabs at both ends of the bridge which are supported by bearings on the ends of the approach viaducts. The original segmental roller bearings at the north and south abutments were replaced with elastomeric bearing pads in 2006 and 2010 respectively. However, some of the replacement bearings have themselves failed and displaced from their supports, suggesting that they were experiencing movement ranges greater than expected during their design. The bridge's approach viaducts also respond to temperature changes and may therefore have contributed to the failure of the elastomeric bearings.

5.3 Experimental set up

5.3.1 Traditional monitoring

An automated monitoring system made up of 48 temperature sensors (located at multiple points along the length as well as through the deck at top, middle and bottom of the concrete section), and 20 displacement transducers (at the bearing and expansion joint locations) was installed by a contractor within the bridge deck in December 2017. Measurements from these temperature and displacement gauges were taken simultaneously every 1 second.

In addition, two Automated Total Stations (ATS) were installed looking at either side of the bridge to monitor 12 reflective prisms. Six prisms were installed on each side of the structure (at each of the bridge's river piers, and one at each end of the central drop-in span, marked as red dots in Figure 5.1). Eight additional prisms were installed as reference points at positions which are not located on the bridge structure, but on adjacent sites on the River Thames embankment (Figure 5.2). ATS readings of the prisms were taken every 5 minutes.

Tidal data for the duration of the monitoring period was provided by the Port of London Authority. The river water levels provided were recorded by the London Bridge gauge.

5.3.2 Satellite data sets

TerraSAR-X 'Stripmap' mode images (approximately 3m by 3m ground resolution) were tasked for acquisitions every 11 days in both ascending and descending directions from December 2017 until November 2018 (as listed in Appendix A). 30 images in the ascending mode and 30 images in the descending mode were used to process the time series movement of the corner reflectors. An 11-day interval is the shortest repeat cycle available for this satellite. SAR satellite constellations all currently have revisit periods in the order of days, rather than hours.

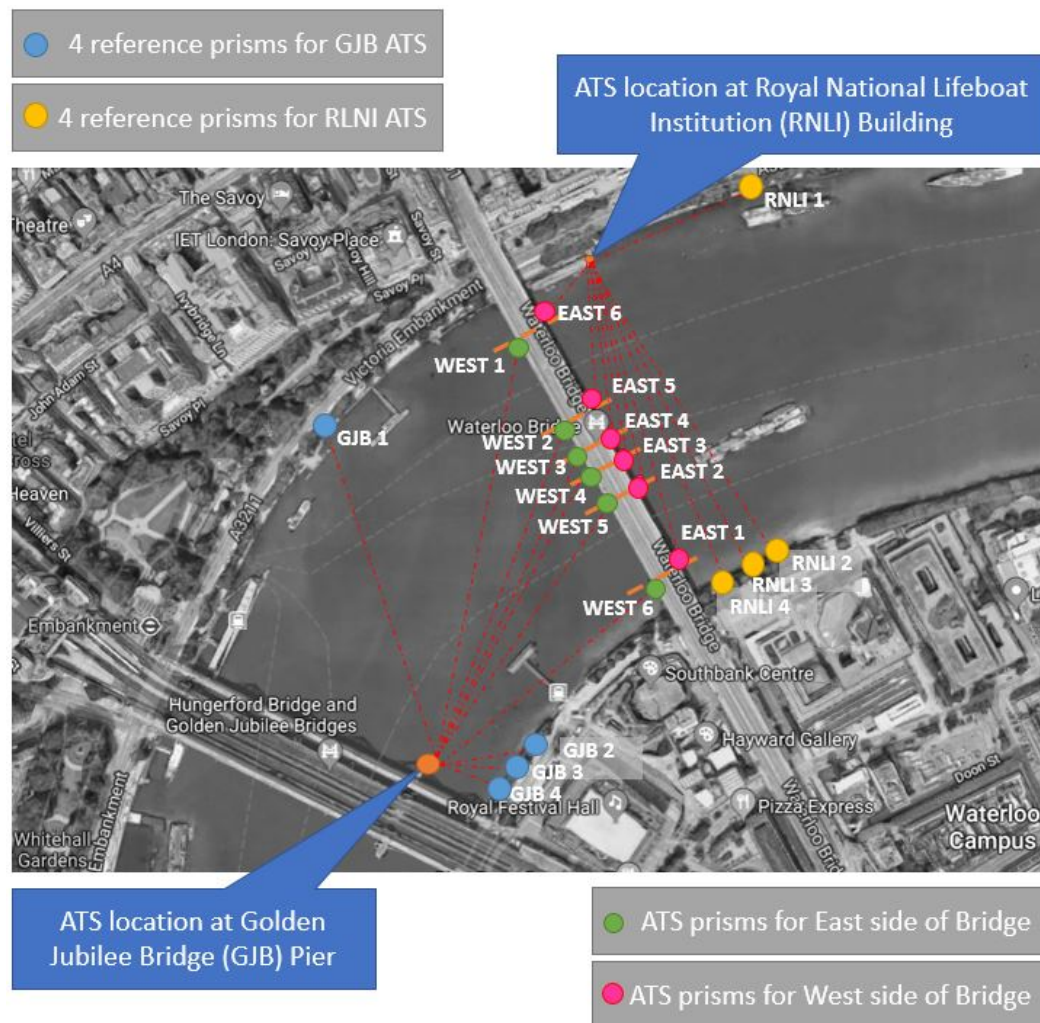


Fig. 5.2 Location of ATSs and target prisms on the bridge and reference prisms on the embankments (base optical imagery and map data provided by Google (2019)).

Shuttle Radar Topography Mission (SRTM) data with resolution of 3 arc-seconds (90m) was used as a Digital Elevation Model (DEM) during the interferometric processing. The data from this satellite was provided by NASA free of charge. This data was much coarser in resolution than the SAR data (the bridge is not represented within this image), but this is not a fundamental input in the processing of differential movement at discrete corner reflector locations (an ellipsoid representing Earth curvature could also have been used).

5.3.3 Corner reflectors

The SAR image of Waterloo Bridge was assessed prior to the installation of corner reflectors. It was noted that the concrete structure of the bridge provided few natural Persistent Scatterers



Fig. 5.3 Top image is a photo of the west side of Waterloo Bridge as taken from Golden Jubilee Bridge. Bottom image is a photo of East 6 aluminium corner reflector (circled) installed on bridge pier alongside ATS prism target.

(PSs), and the noise of the signal from other points on the bridge was relatively low. The corner reflector was sized in terms of its radar cross section (RCS), a measure of the reflectivity, such that the reflected signal would be significantly higher than the background clutter, but small enough to gain permission from the bridge owner so that it could be mounted on the bridge (Figure 5.3). The corner reflectors were the same size and material specification as those used for the NPL experiment. The corner reflectors had a corner length, l of 35cm,

where l is the length of the non-hypotenuse sides of the right-angled isosceles triangular plate (as defined in Figure 4.2 in Chapter 4).

The corner reflector material was again chosen to be aluminium, given that it is light weight and less susceptible to corrosion than steel. The pre-fabricated perforated sheeting was chosen to facilitate drainage, reduce wind load and reduce overall weight. In total, 12 corner reflectors were installed alongside each ATS prism location on the bridge (Figure 5.2). The reflectors were orientated such that the azimuth and elevation of each corner reflector was directed in the SAR satellite's line of sight (LOS) [100]. This was done to target the ascending pass on the west side of the bridge and the descending pass on the east. These corner reflectors were seen in the SAR imagery, and example of which is shown in Figure 5.4.

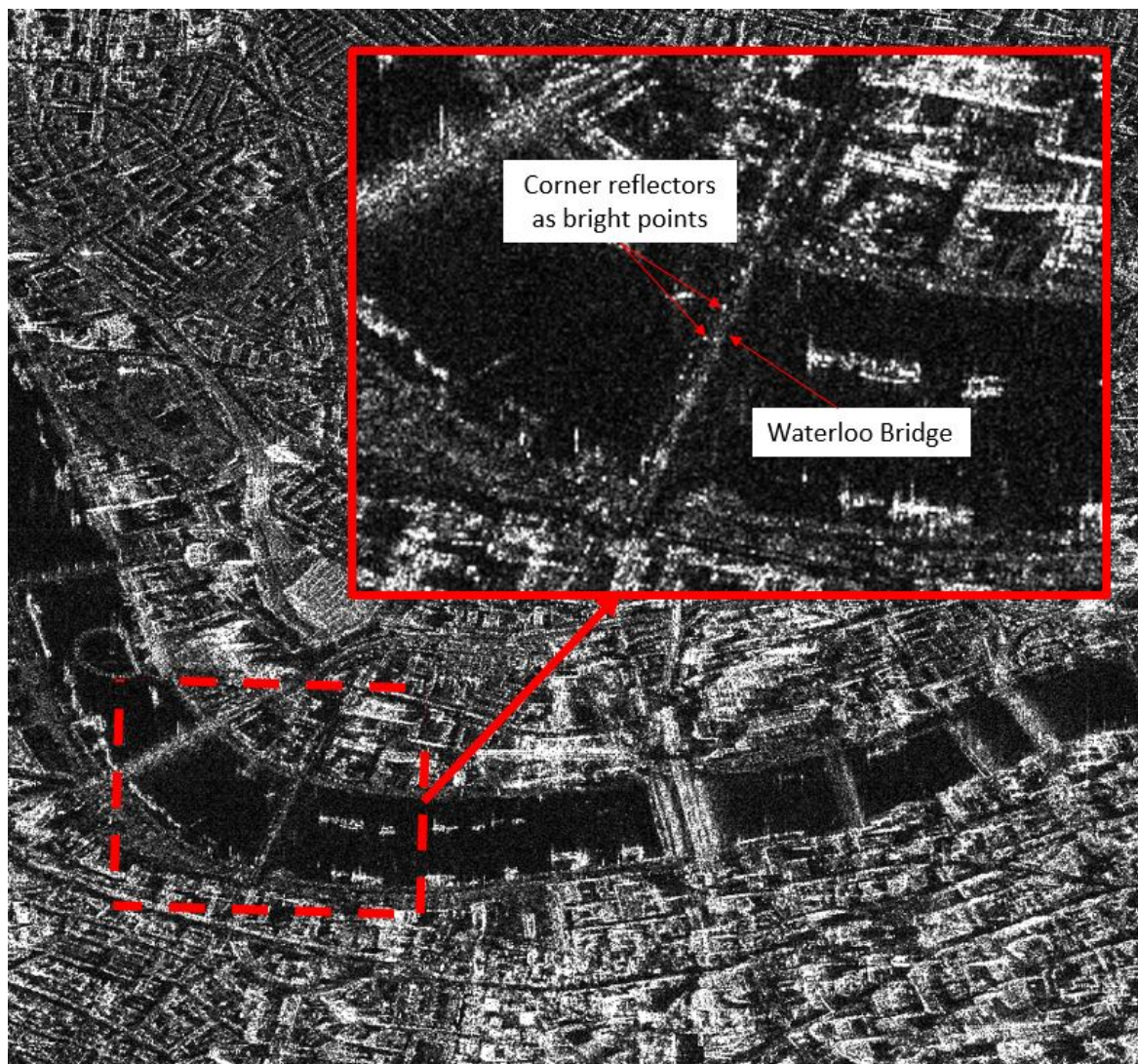


Fig. 5.4 Annotated SAR amplitude image with bridge marked and corner reflector installation appearing as bright points.

5.4 Method

5.4.1 Data processing of in-situ data

The ATS monitoring system was designed, by a contractor, to take line of sight distance and level readings to all bridge prisms, as well as to a number of points remote from the bridge (four points for each of the two ATS). The aim was to measure bridge movement, relative to stable reference points. This would enable bridge movements to be distinguished from any movements of the abutments or approach viaducts (which could be instrumented with displacement gauges). Raw data from the ATS monitoring system comprised angle and distance measurements from each of the ATS locations to the corresponding prisms. Every 2 hours each ATS observed each of its four reference prisms. Assuming that the coordinates of the reference prisms were fixed, the ATS calculated each prism's position at that moment. Due to measurement errors the angle and distance measurements from the four reference prisms did not all result in the same answer, so a Least Squares adjustment was carried out to select the most likely position. Every 5 minutes the ATS observed each of the bridge monitoring prisms and calculated their coordinates relative to its current location.

The reference prisms were installed on the river walls adjacent to the bridge. The river walls elsewhere in central London are known to be affected by the height of the tide. Figure 5.5 shows the variation with time of the measured distance between reference points on opposite sides of the river. Points RNLI 1 and RNLI 2 are to the East of the bridge, and points GJB 1 and GJB 2 are to the West of the structure (refer to Figure 5.2 for locations). The predicted tidal height is also shown on Figure 5.5. It can clearly be seen that the distance between the riverwalls varies and is strongly correlated with the height of the tide. Since movements of the river walls appear to be similar in magnitude to movements of some parts of the bridge it is not possible to remove the effects of this error from the data, hence the absolute coordinates of all ATS monitoring prisms cannot be relied upon.

The initial processing method proposed by the contractor for the ATS data assumed that the reference prisms are stationary, which is not true and would report false results. Thus, for interpretation of bridge movement, the reported coordinates for each set of readings from the ATS have first been shifted so that the origin of each coordinate system is located at the prism at the south end of the bridge. These prisms are East 1 for the ATS at the RNLI Building, and West 6 for the ATS at the GJB Pier. The reported coordinates have been rotated such that the relative movements of all points (including both monitoring and reference prisms) can be determined longitudinally and transversely to the bridge.

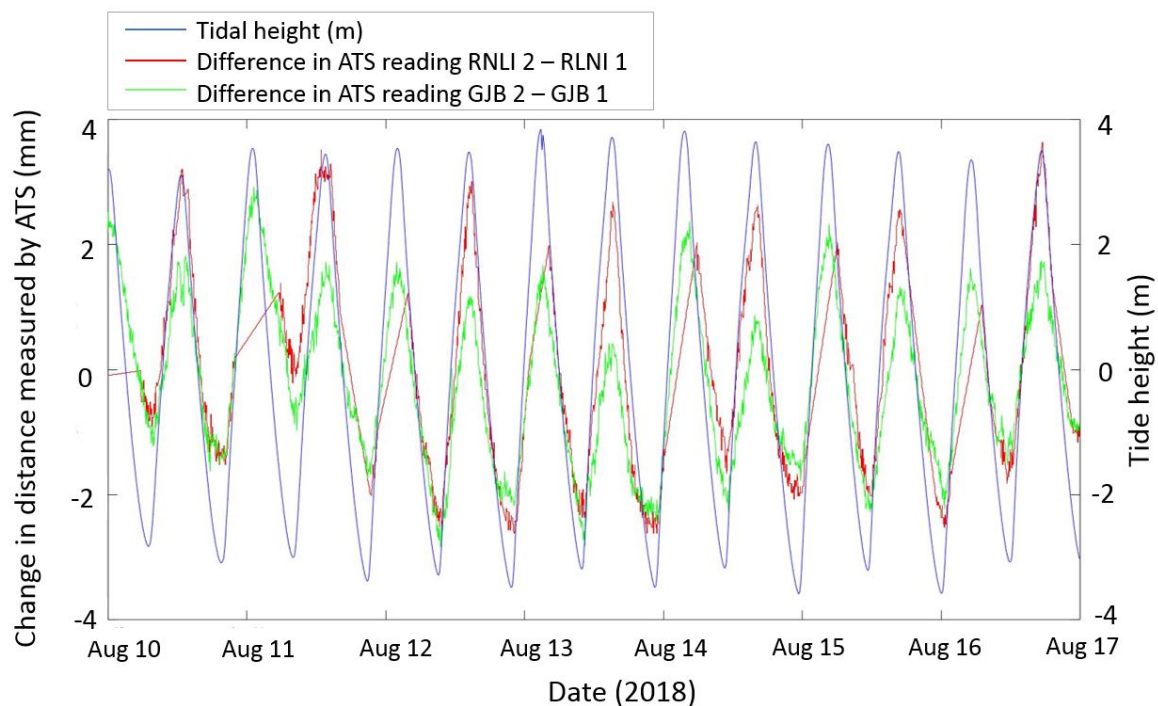


Fig. 5.5 Plot of distance across river between north and south river walls over time. River reference prism data plotted in red and green; Tide data (plotted in blue) provided by London Port Authority for gauge at London Bridge.

5.4.2 Data processing of SAR data

As outlined in Chapter 2, multi-temporal InSAR techniques come in a number of different commercial and openly available algorithms, which are broadly classified into Persistent Scatterer Interferometry (PSI) methods or Small Baseline Subset (SBAS) methods (or a combined approach). For this study on Waterloo Bridge, the points of interest were clearly identifiable point targets created by the installation of corner reflectors. As the corner reflectors created highly reflective point targets clearly visible above any clutter coming from reflections in the surrounding area, the PSI method as described by Ferretti et al. [24] was employed through use of the SARscape software package [115]. A stack of acquisitions was processed separately for each of the ascending and the descending pass directions.

5.5 Results

The processing of each stack of images (the ascending stack and the descending stack) collected after the installation of the corner reflectors identified some new persistent scatterers compared to images processed prior to installation, which can be attributed to the corner

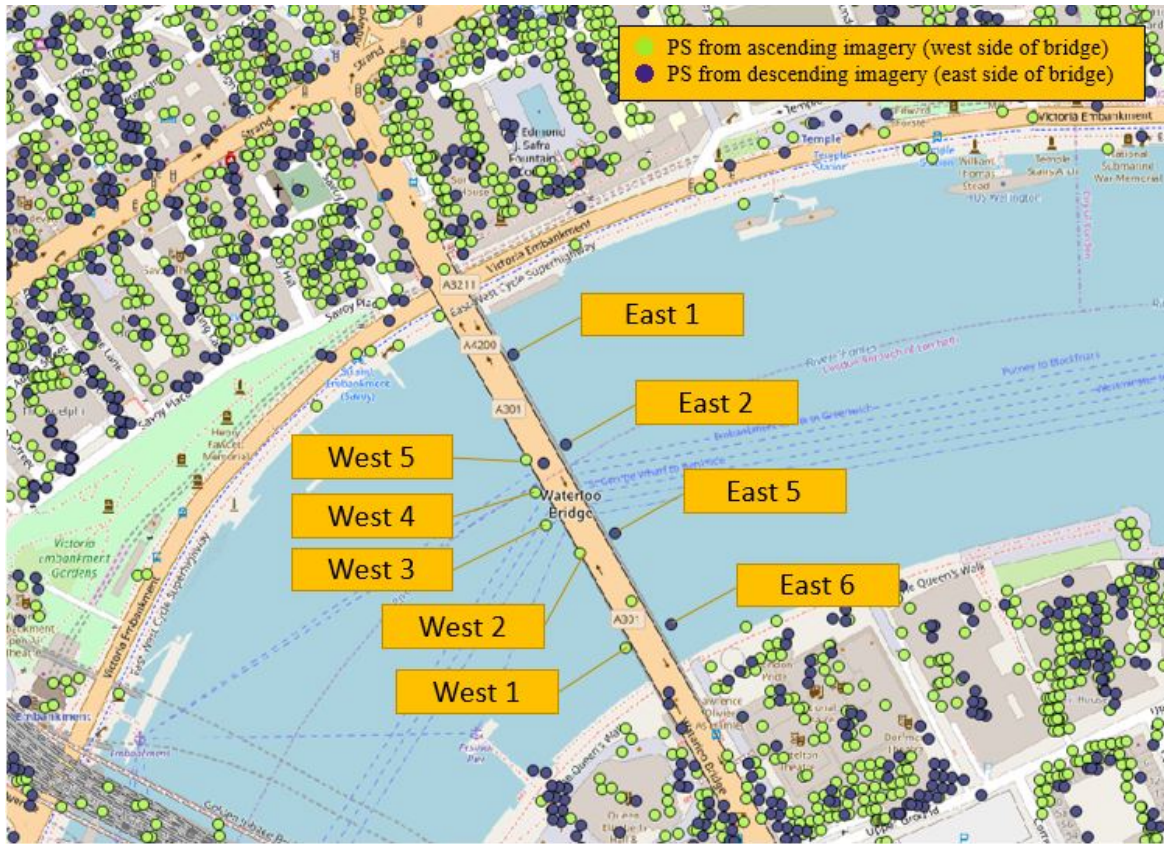


Fig. 5.6 Persistent scatterers monitored on Waterloo Bridge. Green dots indicate persistent scatterers derived from the TerraSAR-X data stack taken in an ‘ascending’ direction and blue dots indicate persistent scatterers derived from the TerraSAR-X data stack taken in a ‘descending’ direction.

reflectors. However, 3 of the 12 corner reflector locations do not show up as persistent scatterers. Possible reasons for this omission include a reflector becoming dirty or events such as a bird nesting in the corner reflector. Although the latter issue was not visible during on-site inspections, one reflector did have litter thrown into it. The PSI processing produced PSs (with in LOS displacements measured over time) for 4 out of 6 corner reflector locations on the East side and 5 out of 6 corner reflector locations on the West side of the bridge (Figure 5.6).

5.5.1 Resolving in one direction of movement

Measurements in the LOS direction are not a particularly useful quantity from a bridge engineering point of view. In terms of bridge movement, we are primarily concerned with

movements within the bridge's own reference system: longitudinal and transverse expansion, vertical movement, and any rotation.

Mathematically, the line of sight movement we have measured using SAR (d_{LOS}) can be considered as the equation below:

$$d_{LOS} = \underline{A} \underline{y}^T \quad (5.1)$$

where

$$\underline{A} = [(\cos\theta \quad \sin\theta\cos\alpha \quad \sin\theta\sin\alpha)] \quad (5.2)$$

$$\underline{y} = [(d_V \quad d_L \quad d_T)] \quad (5.3)$$

α is the heading angle relative to the bridge (angle of the SAR satellite flight path, Figure 5.7), θ is the incidence angle (angle between the SAR beam and the vertical, Figure 5.8), and d_V , d_L , and d_T refer to the vertical, longitudinal and transverse components of the displacement vector respectively.

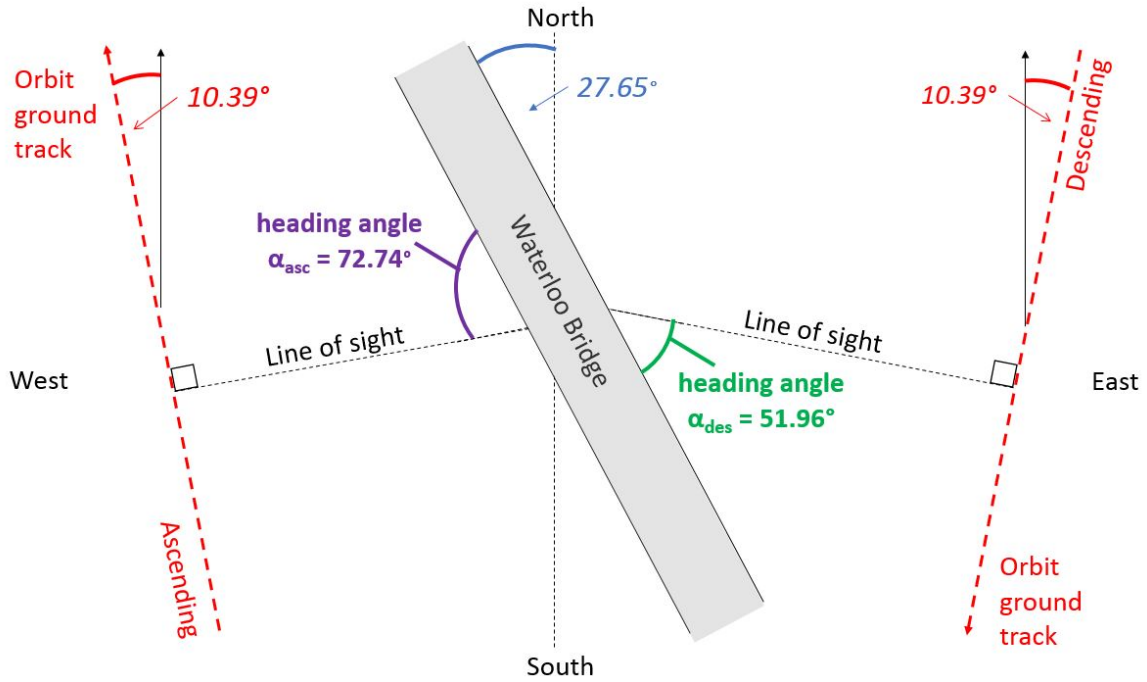


Fig. 5.7 Bridge orientation in relation to satellite imaging geometry.

In order to compare equivalent ATS and SAR datasets, it was initially assumed that all bridge movement only occurred in the longitudinal direction (the direction along the bridge from one river embankment to the other). By applying loading envelopes of various load

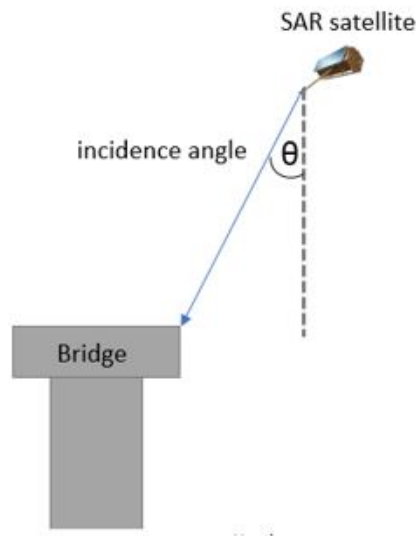


Fig. 5.8 Incidence angle in relation to bridge and satellite imaging geometry.

scenarios into a structural model of the bridge (created using the finite element package LUSAS) it was found that the predominant loading case would be in the longitudinal direction due to thermal expansion. With this initial assumption, the relationship between the line of sight (LOS) displacements and those in the bridge longitudinal direction was derived using the geometry in Figures 5.7 and 5.8.

The graph in Figure 5.9 plots the movement of the bridge when all line of sight of movement is assumed to be in the longitudinal direction. There is a notable anomalous point in April. As the images were not taken simultaneously, the SAR signal for each image can be affected differently by the atmosphere on a given day. The image in this instance was suspected to have been affected by a significant atmospheric artefact. This was confirmed through interrogation of the interferograms related to the date of this acquisition, and this measurement point was discarded from the readings in further analyses.

As explained in Section 5.4.1, only relative longitudinal movements measured by the ATS could be relied upon, and in this case these were taken relative to the southern end of the bridge (ATS prisms at West 6 and East 1 locations). For an equivalent comparison, the longitudinal components of the LOS movements were calculated, and the measurements at locations W6 and E1 were subtracted for the west and east readings respectively, to provide SAR measurements relative to the southern end of the bridge. The ATS and SAR measurements could then be plotted and studied in comparison.

When plotting the ATS- and SAR-derived relative longitudinal movements as well as temperature over time (such as the example in Figure 5.10), the seasonal variation seen in the SAR readings over the year matches the overall temperature profile and agrees with the

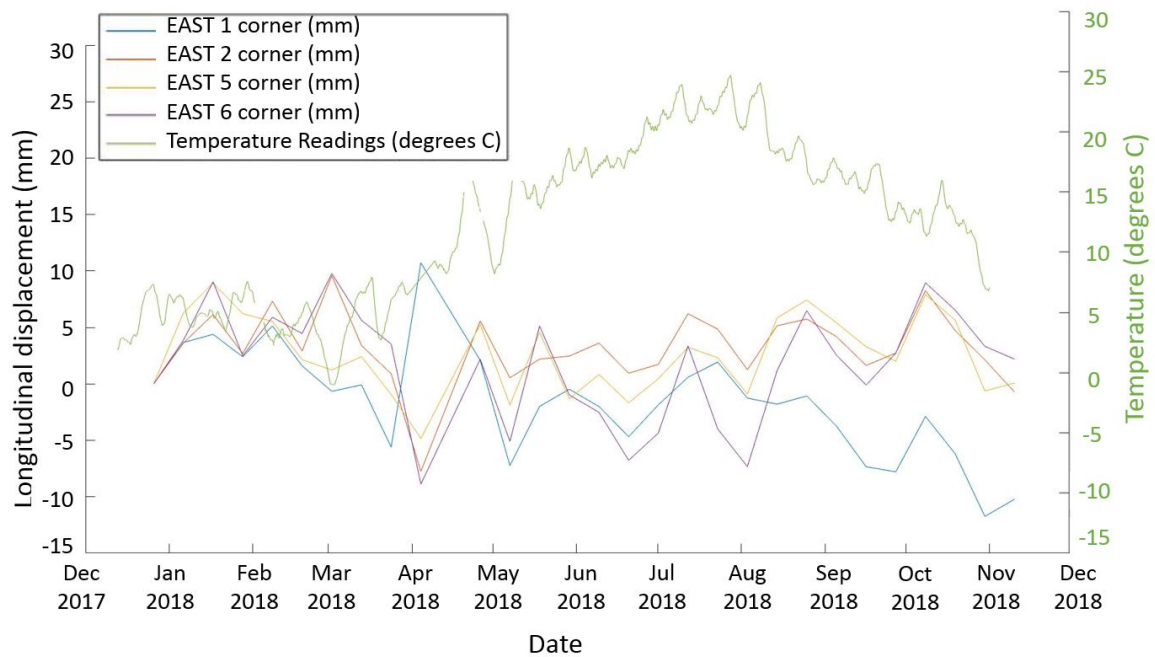


Fig. 5.9 Graph of average bridge deck temperature and InSAR-measured longitudinal movement of points along the eastern side of the bridge plotted against time.

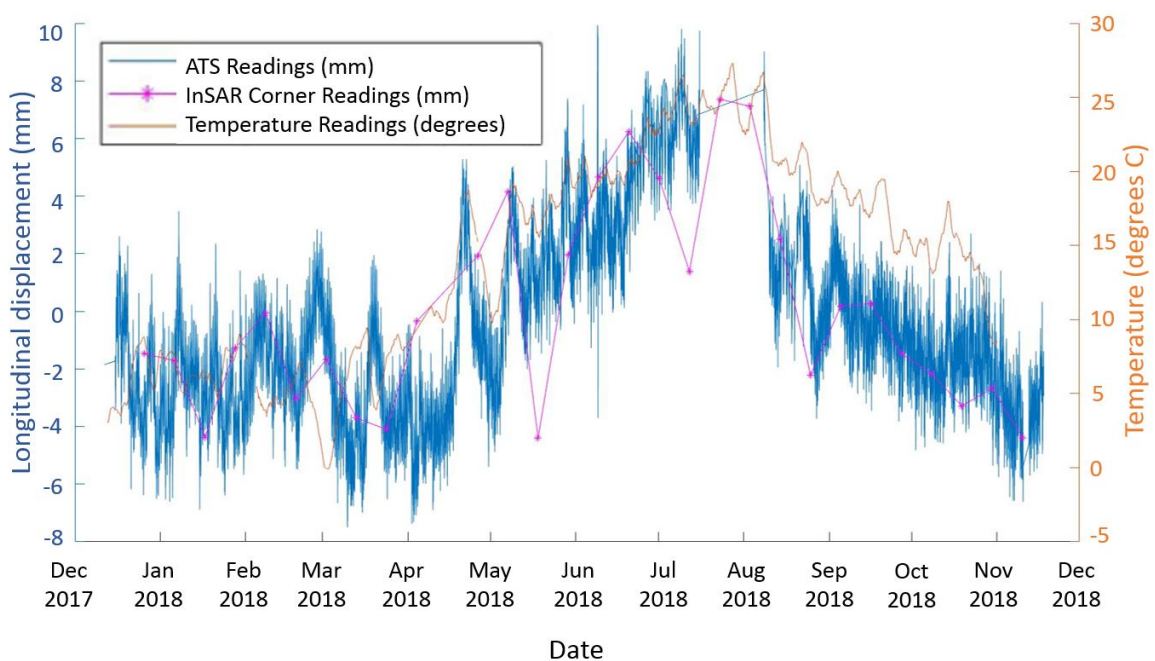


Fig. 5.10 Plot of relative ATS and SAR movements for Pier location 2 relative to Pier location 6 on the east side of the bridge.

ATS readings. However, on looking at the direct comparison of points (selecting the ATS readings at the time of SAR acquisition, such as the examples produced in Figure 5.11) there is variation between the two readings. The correlation coefficient of relative ATS measurement against relative SAR movement varies from 0.41 to 0.76. This does show that the readings are positively correlated.

Examining the plots in Figure 5.11 reveals that the profiles correlate well for the beginning part of the time period considered. However, the two sets of values begin deviating from each other in May and they begin converging again in October. The reason for the discrepancy in trend, visible from May 2018 onward, is difficult to assess. A plausible explanation might be a phase unwrapping error, i.e. a processing error occurring due phase aliasing which affects the trend of the measurements with a shift. Phase unwrapping errors are likely to occur for rapid motion and gaps in the data and can be corrected post-processing by an operator when independent measures are available. In the TerraSAR-X case, movements larger than 7.7mm between acquisitions may be subject of unwrapping errors.

This would suggest that this correlation coefficient as a simple measure of uncertainty is not ideally suited to understanding the complex data profile being considered. Therefore another means of assessing the fit between ATS and SAR measurements will be considered in Section 5.6.

5.5.2 Using multiple look directions

Several approaches have been developed in recent years to exploit the potential of InSAR to determine three-dimensional surface displacement [77]. The most straightforward approach is the combination of multiple InSAR LOS measurements from different SAR viewing geometries.

This approach of integrating multiple look directions has recently been extended into three-dimensional deformation monitoring of bridges [116], however, for direct comparison against ATS readings in a thermally responsive bridge, this approach has limitations since the observation period of the datasets are not exactly the same. If the acquisitions at different look angles are taken on different days or different times in the day, the bridge will be subjected to a different temperature, thus affecting the movement it experiences. As such, the measurement readings could not be combined to form the total movement, and this approach was therefore not suitable for monitoring of bridges such as Waterloo Bridge.

A first approximation of bridge movement in Section 5.5.1 assumed all movement was in one direction. Using a second line of sight direction would solve one further unknown. The concrete piers are each 35m long and 5m wide and span the transverse length of the deck. Using the reasonable assumption that the structure is rigid in the transverse direction,

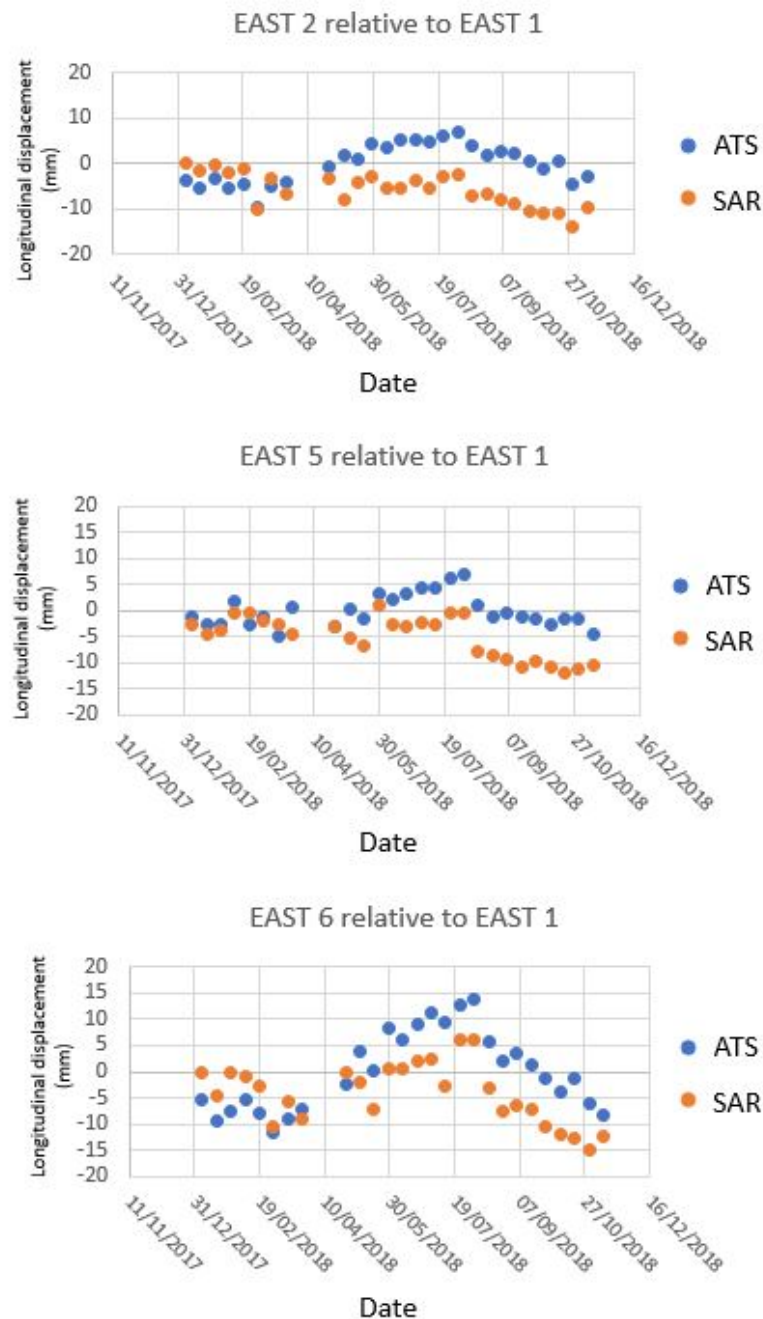


Fig. 5.11 Comparison between relative ATS and SAR longitudinal measurements at various locations on the bridge.

the LOS measurement in corresponding east and west sides of the bridge can be combined together, using acquisitions taken at the same temperature. This approach decomposes the LOS vector into longitudinal and vertical components (assuming zero transverse movement),

but reduces the number of readings down to 10 instances when the east and west side had readings at the same temperature instance. This approach does not, however, ensure that the tidal loading was the same at each instance, which lowers the number of viable readings further.

5.6 Multidimensional analysis

This experiment was set up primarily to compare InSAR measurements with traditional surveying measurements as collected by ATS readings. The approach for comparing the two measurement methods (ATS and SAR) has been to attempt to convert the SAR readings into a frame of reference that can be directly compared with the ATS readings. This has revealed that the readings do not match perfectly, but it is also difficult to quantify how well these two measurements agree, especially as they are each measuring different components of the bridge's deformation. In order to quantify the fit of the two datasets in capturing the bridge movement, multidimensional analysis was employed.

The time series of SAR signals associated with each corner reflector on the bridge identify a multidimensional signature of the linear transformations (e.g. translation, rotation) which the bridge may undergo as a result of various loading cases such as tidal movements, temperature expansion, live traffic load deformations and concrete shrinkage and creep. Point-by-point analysis involving first order statistical measures (e.g. average) and second order statistical measures (e.g. variance) may not be sufficient to investigate the accuracy of SAR signals being used to infer the same information as the measurements acquired by the ATS ground stations [117]. The approach of employing first and second order statistical measures might also be affected by issues such as sparsity of data and complex data structures that could strongly degrade the characterisation of the considered scenario. Furthermore, undesired phenomena such as over-fitting of data points and noise amplification induced by the nonlinear combination of the elements' scattering may not be efficiently tackled. As a result, the overall investigation results may be dramatically jeopardised and information loss might occur.

The following sections employ multidimensional analysis to compare the fit of SAR to ATS measurements, and map these two sets of measurements in an attempt to better understand the relationship between the two sets of measurement results. The goal of this mathematical approach was to quantify how suitable SAR could be for bridge monitoring purposes by investigating how well SAR-based estimates of movements are correlated to actual ground movements. Using this approach, an aggregate metric (η) can be produced which gives an overview of how reliable the whole set of SAR acquisitions is feasible to

describe the movements recorded in-situ. Furthermore, by means of the geometrical approach based on the analysis of the polytope characteristics, it is possible to track the nature of the relationship between SAR and ATS trends, so that the complexity of the impact of the environmental factor in the structural movements, as well as the complicated nature of the non-idealities that affect SAR acquisitions and analysis, can be addressed. It is worth noting that classic statistical approaches would not allow this deep investigation, as they would discard the actual impact of acquisitions that would not follow the standard trend, so to limit the ability to describe the way SAR and ATS could actually be linked.

5.6.1 Measure of fit

In order to provide a thorough investigation of the statistical and stochastic characteristics, a multidimensional approach exploring the manifold properties of the SAR and ATS measurements was considered. Specifically, it was possible to understand the relationship between these ATS and SAR measurements by taking into account the volume of the multidimensional subspace spanned by them. A set of R records characterised by N attributes can be identified as a N -dimensional polytope [118]. According to a vertex geometry description of multidimensional datasets, every point existing within the volume spanned by the R records in this subspace can be characterised as a function of these N -dimensional samples [119, 120]. Thus, the volume spanned in a multidimensional space by a dataset provides relevant information on the properties of its own records. Moreover, it can be used to infer useful characteristics on similarities and regularities when comparing datasets.

In the case of Waterloo Bridge, it was possible to understand how accurately the SAR measurements can track and characterise the ATS ground measurements by assessing the volumes spanned by their corresponding N -dimensional polytopes (where N is the number of acquisitions), and then computing their ratio. In other terms, let R be the number of corner reflectors (in the same position as the ATS targets) that are considered. Let $\underline{a}_r = [a_{r_n}]_{n=1,\dots,N}$ and $\underline{s}_r = [s_{r_n}]_{n=1,\dots,N}$ be the ATS and SAR displacement measurements, respectively, associated with the r -th corner reflector location (i.e., $r \in \{1, \dots, R\}$). Every element in these vectors lies within the real number space, \mathbb{R} .

Then, let us define two $R \times N$ matrices $\underline{\underline{A}} = \{\underline{a}_r\}_{r=1,\dots,R}$ and $\underline{\underline{S}} = \{\underline{s}_r\}_{r=1,\dots,R}$. Thus, the volume spanned by the ATS measurements $\underline{\underline{A}}$ and SAR measurements $\underline{\underline{S}}$ in the multidimensional space can be written as $V_A = \sqrt{|\det[\underline{\underline{A}}]|}$ and $V_S = \sqrt{|\det[\underline{\underline{S}}]|}$. Given the nature of the elements in $\underline{\underline{A}}$ and $\underline{\underline{S}}$, it is possible to prove that V_A and V_S are positive [118]. Furthermore, the aforementioned polytopes covers a subspace in the N -dimensional space along the same directions [118–121]. Therefore, it is possible to assume that the ratio $\eta = V_S/V_A$ would

provide useful insights on how representative the ATS ground measurements are in terms of the SAR signals. Specifically, as $\eta \rightarrow 1$, we can expect that the SAR records would be carrying the same information of the ground measurements. Moreover, if $\eta > 1$, it is possible to state that the ground displacements can be identified and mapped from SAR acquisitions. In the case considered here, the values of η for the vertical and longitudinal component of the bridge displacements were 1.24 and 1.13, respectively.

5.6.2 Mapping of SAR and ATS functions

Following this approach, we can understand how the SAR measurements could be used to describe the ground measurements, and quantify their effectiveness in this sense. To this aim, we can consider the SAR time series associated with each corner reflector as the extreme points of the aforesaid polytope that identify $\underline{\underline{S}}$. Hence, they represent a set of linear basis in the N -multidimensional space. Therefore, it is possible to write a generic N -dimensional vector ϕ as a combination of the SAR records. Specifically, it has been proven that a polynomial combination of the basis induced by the extreme points can be used to characterise the linear and nonlinear effects occurring within the polytope [122].

Thus, ϕ can be approximated as a polynomial combination of $\underline{\underline{S}}$, i.e., $\sum_{k=1}^p \sum_{r=1}^R \omega_{rk} \underline{\underline{S}}_r^k$, where $\underline{\underline{S}}_r^k = [s_{rn}^k]_{(r,k) \in \{1, \dots, R\} \times \{1, \dots, p\}}$, ω_{rk} is the coefficient that weights the contribution of $\underline{\underline{S}}_r$ for the k th order, and p is the order of power of the non-linear contribution. Furthermore, we can estimate the precision in characterizing the ϕ properties using the basis in $\underline{\underline{S}}$ by computing the Euclidean distance between ϕ and $\sum_{k=1}^p \sum_{r=1}^R \omega_{rk} \underline{\underline{S}}_r^k$. Then, it is possible to assume that the ability of SAR to understand and quantify the actual displacements of the corner reflectors (that generate linear and nonlinear effects onto the SAR records) can be assessed by computing the reconstruction error that is achieved when approximating the ground measurements by means of the SAR measurements associated with each corner reflector as per the aforementioned approach. The reconstruction error (RE) can be written as follows:

$$RE = \sqrt{\frac{1}{RN} \sum_{l=1}^R \left\| \underline{a}_l - \sum_{k=1}^p \sum_{r=1}^R \omega_{rk} \underline{\underline{S}}_r^k \right\|^2} \quad (5.4)$$

where

RE (Reconstruction Error) identifies the coefficient that drives the k -th order contribution based on the r -th SAR measurement when approximating the l -th ground measurement;

ω_{rk} is the weighting of the k -th order contribution of the signal associated with the r -th corner reflector SAR measurement.

As such, ω_{rkl} is estimated by solving a linear programming problem where the minimisation of RE is the objective function, with sum-to-one and non-negativity constraints applied to the ω factors, i.e., $\sum_{r,k} \omega_{rkl} = 1$ and $\omega_{rkl} \geq 0 \forall (r,k,l)$ [122]. This is plotted in Figure 5.12.

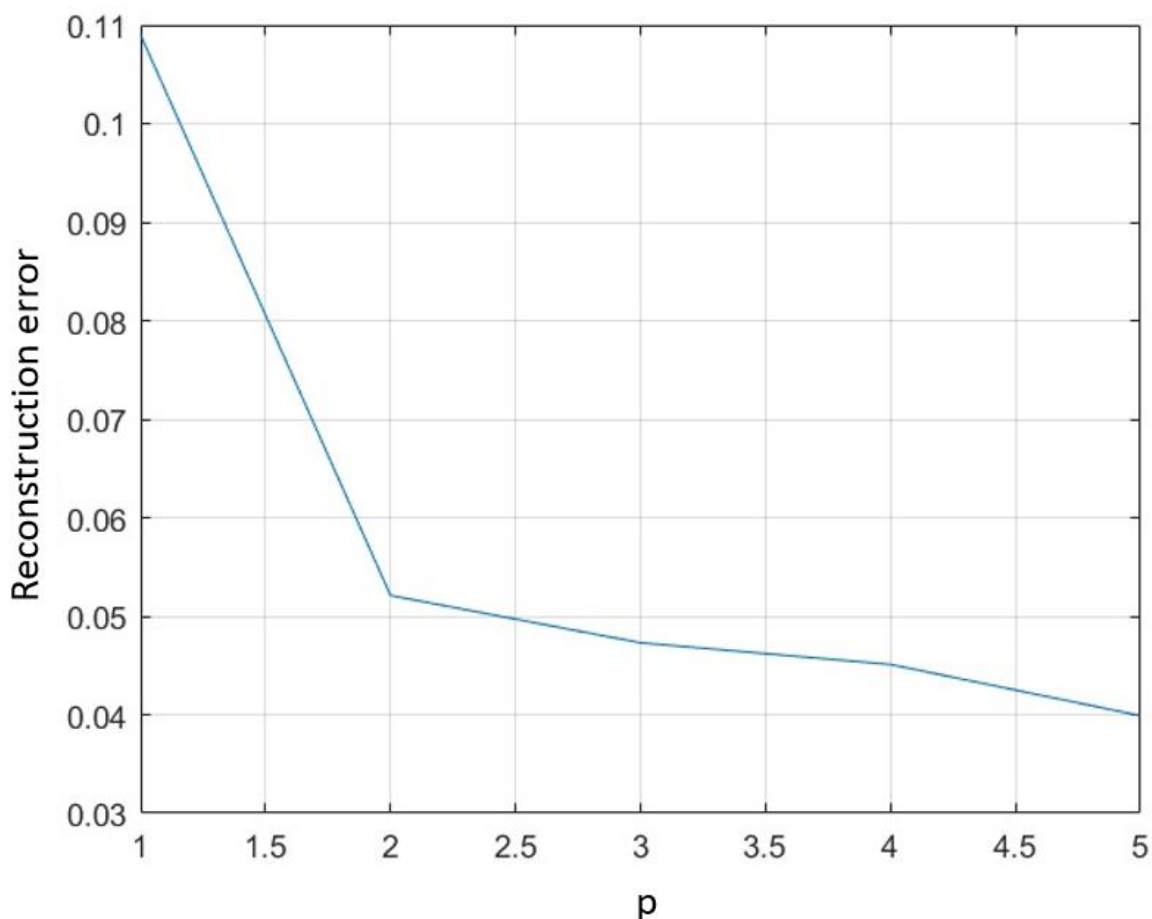


Fig. 5.12 Graph of possible Reconstruction Error (RE) values for different values of p (the order of power of the non-linear contribution).

The value of $p = 1$ would signify a linear relationship between the SAR and ATS readings, and higher values indicate higher order polynomial mapping between the two entities. The RE value decreases as we consider higher order non-linear combinations of the SAR signals to characterise what is shown by the ATS readings (Figure 5.12). This signifies the complicated relationship between the two entities, the SAR and ATS readings themselves, resulting from non-linear effects. This could include non-idealities associated with the non-perfect positioning of the ATS (i.e. the ATS is not fixed, which becomes a problem when the reference prisms cannot be relied upon). The next section explores this consideration and tries to quantify if and how the ATS position moves.

5.7 Method to combine terrestrial and SAR

In addition to considering the merits and disadvantages of each of the ATS and SAR systems, there existed an opportunity to consider how the satellite measurements could be used to supplement the ATS measurements. In doing so, the the unknown total station positions and other unknown quantities could be resolved, giving a better insight into the absolute movements of the bridge (rather than the relative measurements derived from the data). The premise of this analysis is that there was a misalignment of the ATS in (x, y, z) from one SAR acquisition to another (i.e. the ATS is not stationary as generally assumed with convetional surveying practice).

Let us consider the east readings for point i at time t and let us define its coordinates in a three dimensional space as Ex_i^t , Ey_i^t , and Ez_i^t . Then, it is possible to describe these quantities in terms of the corresponding ATS measurements (Figure 5.13) at each timestamp as follows:

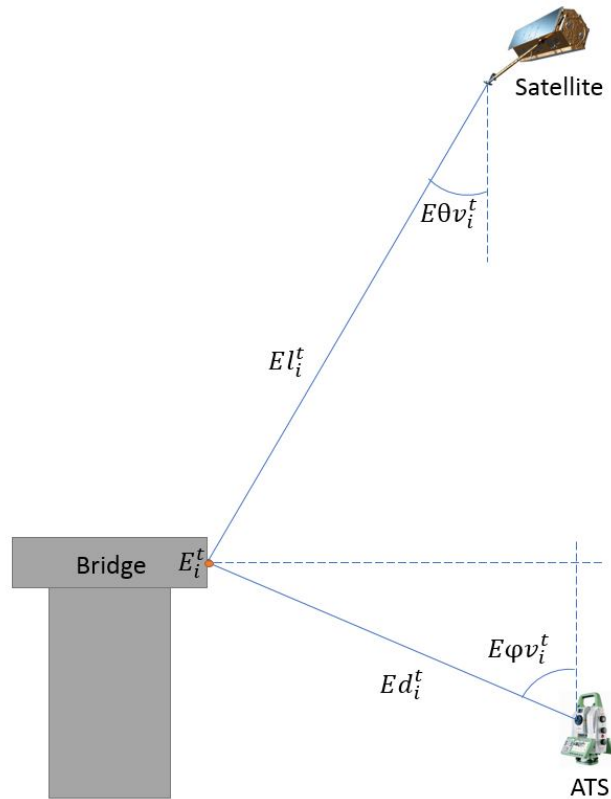


Fig. 5.13 ATS viewing geometry as used to define Equations 5.5 and 5.6. Diagrams are not drawn to scale.

$$\begin{aligned}
Ex_i^t &= Ax^t + Ed_i^t \sin(E\phi v_i^t) \cos(A\phi^t + E\phi h_i^t), \\
Ey_i^t &= Ay^t + Ed_i^t \sin(E\phi v_i^t) \sin(A\phi^t + E\phi h_i^t), \\
Ez_i^t &= Az^t + Ed_i^t \cos(E\phi v_i^t),
\end{aligned} \tag{5.5}$$

where:

- Ax^t , Ay^t , and Az^t identify the 3-D coordinates of the ATS position at time t ;
- $A\phi^t$ is the reference angle used to compute the ATS measurements at time t ;
- Ed_i^t represents the distance between the i -th east point and ATS at time t ;
- $E\phi v_i^t$ and $E\phi h_i^t$ are the vertical and horizontal angles measured from eastern point i to $A\phi^t$ at time t , respectively.

Analogously, it is possible to characterize Ex_i^t , Ey_i^t , and Ez_i^t as functions of the satellite measurements (Figure 5.13) as follows:

$$\begin{aligned}
Ex_i^t &= Sx^t + El_i^t \sin(E\theta v_i^t) \cos(E\theta h_i^t), \\
Ey_i^t &= Sy^t + El_i^t \sin(E\theta v_i^t) \sin(E\theta h_i^t), \\
Ez_i^t &= Sz^t - El_i^t \cos(E\theta v_i^t),
\end{aligned} \tag{5.6}$$

where:

- Sx^t , Sy^t , and Sz^t identify the 3-D coordinates of the satellite position at time t : given the satellite imaging geometry over 500km above earth, if the satellite position is considered to be the same for every coherent acquisition, and we can write $Sx^t = Sx$, $Sy^t = Sy$, and $Sz^t = Sz \forall t$;
- El_i^t represents the line-of-sight distance between satellite and the i -th east point at time t ;
- $E\theta v_i^t$ and $E\theta h_i^t$ are the vertical and horizontal angles measured from eastern point i to satellite line-of-sight at time t , respectively.

Hence, it was possible to extract information on the aforesaid unknown quantities in the system by considering the corresponding equations in (5.5) and (5.6). Thus, the following equations hold:

$$\begin{aligned}
Ax^t - Ax^{t-1} &= El_i^t \sin(E\theta v_i^t) \cos(E\theta h_i^t) \\
&\quad - El_i^{t-1} \sin(E\theta v_i^{t-1}) \cos(E\theta h_i^{t-1}) \\
&\quad + Ed_i^{t-1} \sin(E\phi v_i^{t-1}) \cos(A\phi^{t-1} + E\phi h_i^{t-1}) \\
&\quad - Ed_i^t \sin(E\phi v_i^t) \cos(A\phi^t + E\phi h_i^t), \\
Ay^t - Ay^{t-1} &= El_i^t \sin(E\theta v_i^t) \sin(E\theta h_i^t) \\
&\quad - El_i^{t-1} \sin(E\theta v_i^{t-1}) \sin(E\theta h_i^{t-1}) \\
&\quad + Ed_i^{t-1} \sin(E\phi v_i^{t-1}) \sin(A\phi^{t-1} + E\phi h_i^{t-1}) \\
&\quad - Ed_i^t \sin(E\phi v_i^t) \sin(A\phi^t + E\phi h_i^t), \\
Az^t - Az^{t-1} &= El_i^{t-1} \cos(E\theta v_i^{t-1}) - El_i^t \cos(E\theta v_i^t) \\
&\quad + Ed_i^{t-1} \cos(E\phi v_i^{t-1}) - Ed_i^t \cos(E\phi v_i^t)
\end{aligned} \tag{5.7}$$

The ATS could have been moving in three dimensions over time (x, y, z). Let us focus our attention on the vertical component of the ATS misplacement between two consecutive timestamps, i.e., $Az^t - Az^{t-1}$. Taking into account the readings obtained by considering two different points (two different ATS target or SAR corner reflector locations on the bridge), i and j , it is possible to write:

$$\begin{aligned}
&El_i^{t-1} \cos(E\theta v_i^{t-1}) - El_i^t \cos(E\theta v_i^t) \\
&+ Ed_i^{t-1} \cos(E\phi v_i^{t-1}) - Ed_i^t \cos(E\phi v_i^t) = \\
&El_j^{t-1} \cos(E\theta v_j^{t-1}) - El_j^t \cos(E\theta v_j^t) \\
&+ Ed_j^{t-1} \cos(E\phi v_j^{t-1}) - Ed_j^t \cos(E\phi v_j^t)
\end{aligned} \tag{5.8}$$

Thus, since $E\theta v_i^t = E\theta v^t \forall i$, it is possible to write:

$$\cos(E\theta v^{t-1}) = \alpha_{ij}^t \cos(E\theta v^t) + \beta_{ij}^t, \quad (5.9)$$

where

$$\alpha_{ij}^t = \frac{El_i^t - El_j^t}{El_i^{t-1} - El_j^{t-1}},$$

$$\beta_{ij}^t = \tilde{\beta}_{ij}^t / (El_i^{t-1} - El_j^{t-1}),$$

$$\text{and } \tilde{\beta}_{ij}^t = Ed_i^t \cos(E\phi v_i^t) - Ed_i^{t-1} \cos(E\phi v_i^{t-1}) + Ed_j^{t-1} \cos(E\phi v_j^{t-1}) - Ed_j^t \cos(E\phi v_j^t).$$

Figure 5.14 plots this relationship over a number of different values. This plot only serves to show the complex (trigonometrically derived) relationship of these viewing geometries based on looking at two different points on one side of the bridge. A further view point must be considered to narrow the ranges of values presented.

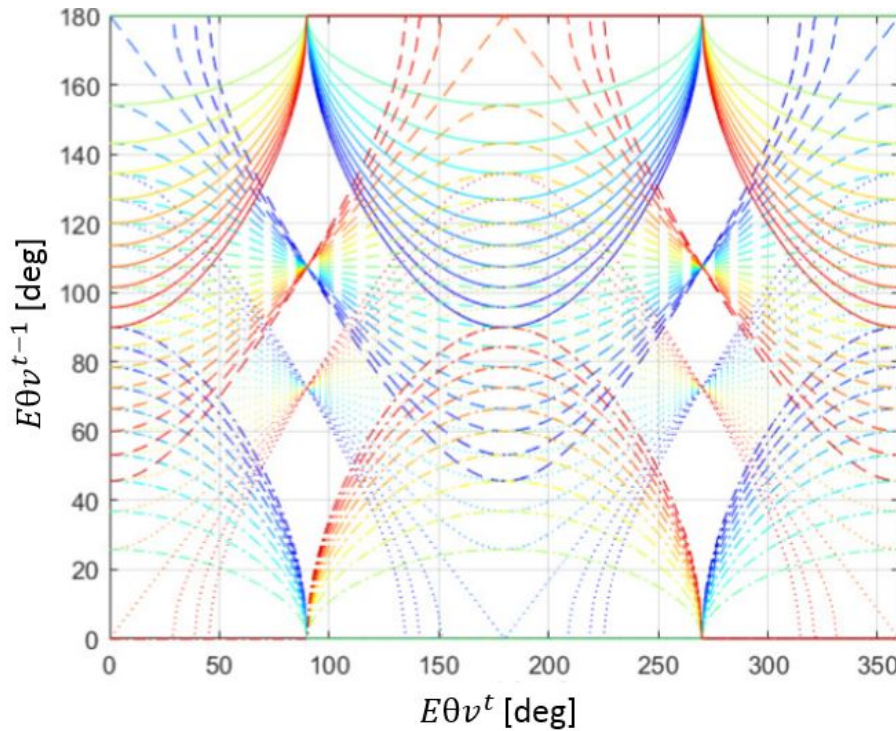


Fig. 5.14 $E\theta v^{t-1}$ as a function of $E\theta v^t$, α_{ij}^t , and β_{ij}^t as in (5.9). The different set-ups of α_{ij}^t and β_{ij}^t are represented in terms of different line colours and styles, respectively. Specifically, the colours from blue to red represent values of α_{ij}^t ranging from -1 to 1. Solid lines, dashed lines, point lines, and dash-point lines identify $\beta_{ij}^t = \{-1, -0.5, 0.5, 1\}$, respectively.

Then, the analytical expression of $\cos(E\theta v^t)$ can be derived by taking into account the reading from a third point from the bridge, k , so that it is possible to write:

$$\cos(E\theta v^t) = \frac{\beta_{ij}^t - \beta_{ik}^t}{\alpha_{ij}^t - \alpha_{ik}^t}. \quad (5.10)$$

Once the values described in Equation 5.9 and Equation 5.10 are placed in the $Az^t - Az^{t-1}$ equation, the vertical component of the actual movement of the ATS, Δz_{ATS} , can be retrieved. The Δz_{ATS} results are plotted in Figure 5.15 for the data collected on Waterloo bridge from January to December 2018, thus providing insight into the movement of the ATS device location itself during the period of measurement.

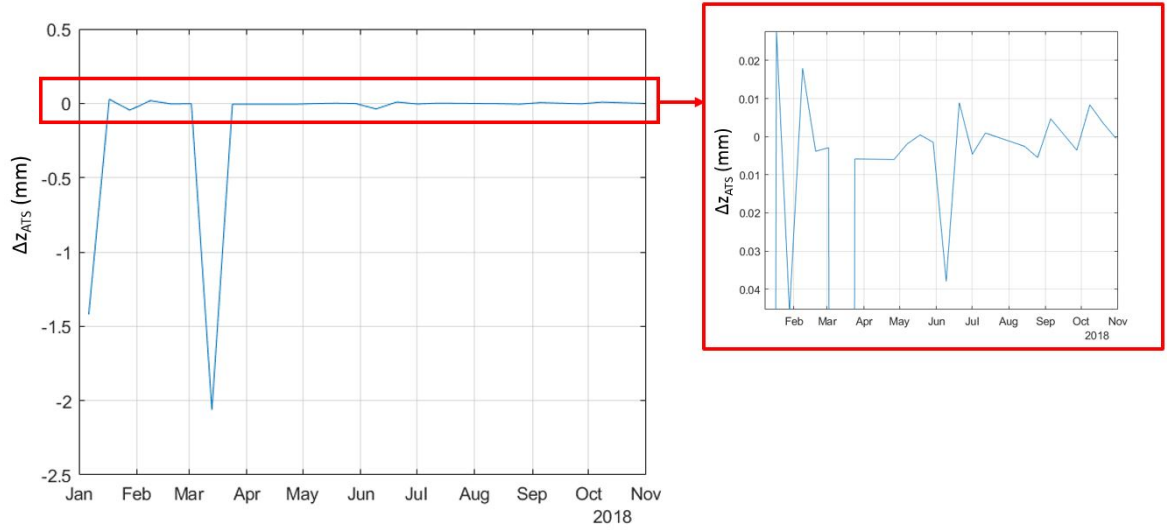


Fig. 5.15 Misplacement of ATS on the vertical direction $\Delta z_{ATS} = Az^t - Az^{t-1}$ computed according to Equations (5.8), (5.9), and (5.10).

So far, only the vertical component of the movement of the ATS device has been considered. Let us now take into account a horizontal component of movement, the $Ax^t - Ax^{t-1}$ difference. Assuming that $E\theta h_i^t = E\theta h^t \forall i$ and using standard trigonometric identities, it is possible to prove that the following equation holds:

$$\begin{aligned} (a_j^{t-1} - a_i^{t-1}) \cos(E\theta h^{t-1}) &= (a_j^t - a_i^t) \cos(E\theta h^t) \\ &\quad + (b_i^t - b_j^t) \cos(A\varphi^t) \\ &\quad + (c_j^t - c_i^t) \sin(A\varphi^t) \\ &\quad + (b_j^{t-1} - b_i^{t-1}) \cos(A\varphi^{t-1}) \\ &\quad + (c_i^{t-1} - c_j^{t-1}) \sin(A\varphi^{t-1}), \end{aligned} \quad (5.11)$$

where the a , b and c coefficients are defined as follows:

- $a_i^t = El_i^t \sin(E\theta v_i^t)$;
- $b_i^t = Ed_i^t \sin(E\phi v_i^t) \cos(E\phi h_i^t)$;
- $c_i^t = Ed_i^t \sin(E\phi v_i^t) \sin(E\phi h_i^t)$.

Then, we can define $\cos(E\theta h^t)$ as follows:

$$\begin{aligned} (A_{ij} - A_{ik}) \cos(E\theta h^t) = & (B'_{ik} - B'_{ij}) \cos(A\phi^t) \\ & + (C'_{ik} - C'_{ij}) \sin(A\phi^t) \\ & + (B''_{ik} - B''_{ij}) \cos(A\phi^{t-1}) \\ & + (C''_{ik} - C''_{ij}) \sin(A\phi^{t-1}), \end{aligned} \quad (5.12)$$

where

- $A_{ij} = (a_j^t - a_i^t) / (a_j^{t-1} - a_i^{t-1})$;
- $B'_{ij} = (b_i^t - b_j^t) / (a_j^{t-1} - a_i^{t-1})$;
- $B''_{ij} = (b_i^{t-1} - b_j^{t-1}) / (a_j^{t-1} - a_i^{t-1})$;
- $C'_{ij} = (c_i^t - c_j^t) / (a_j^{t-1} - a_i^{t-1})$;
- $C''_{ij} = (c_i^{t-1} - c_j^{t-1}) / (a_j^{t-1} - a_i^{t-1})$.

Finally, it is possible to write:

$$R'_{ijkm} \cos(A\phi^t - \Delta'_{ijkm}) = R''_{ijkm} \cos(A\phi^{t-1} - \Delta''_{ijkm}), \quad (5.13)$$

where the R' , R'' , Δ' and Δ'' parameters are defined as follows:

- $R'_{ijkm} = \sqrt{(D'_{ijk} - D'_{ijm})^2 + (E'_{ijk} - E'_{ijm})^2}$;
- $R''_{ijkm} = \sqrt{(D''_{ijk} - D''_{ijm})^2 + (E''_{ijk} - E''_{ijm})^2}$;
- $\Delta'_{ijkm} = \arctan[(E'_{ijm} - E'_{ijk}) / (D'_{ijk} - D'_{ijm})]$;
- $\Delta''_{ijkm} = \arctan[(E''_{ijm} - E''_{ijk}) / (D''_{ijk} - D''_{ijm})]$;
- $D'_{ijk} = (B'_{ik} - B'_{ij}) / (A_{ij} - A_{ik})$;

- $D''_{ijk} = (B''_{ik} - B''_{ij}) / (A_{ij} - A_{ik});$
- $E'_{ijk} = (C'_{ik} - C'_{ij}) / (A_{ij} - A_{ik});$
- $E''_{ijk} = (C''_{ik} - C''_{ij}) / (A_{ij} - A_{ik}).$

In order to solve for the unknown horizontal position of the ATS, the viewing geometry of the SAR and ATS from 5 different locations on one side of the bridge would need to be employed (two further sets of measurements than the 3 points required to understand vertical movement).

5.8 Discussion

This investigation on Waterloo Bridge addresses a number of topics related to the practicality of InSAR for bridge monitoring. To consider the relevance for bridge monitoring, the suitability of the measurement in terms of precision and reliability is first discussed (including reflections on improvement of the experiment). This is then followed by some considerations in terms of an asset owner practically implementing such techniques to monitor bridges similar to Waterloo.

5.8.1 Understanding InSAR quality

There are a number of measurement assumptions that affect the InSAR processing output. The differential InSAR technique measures line of sight (LOS) changes of the relative displacement of a point in the SAR image with respect to a reference point. Within the processing algorithm, there is an opportunity to input points that are known to be motionless or whose displacement is known, referred to as ‘Ground Control Points’ (GCPs, as mentioned in the theory in Chapter 2). Without user input of these GCPs, points are selected to act as the GCPs based on the imagery and assumed to be motionless. The reference point is selected based on it having a high coherence value (an indication that the point is stable over time) and on it not being subjected to local deformations. This means that the motion described by each of the points of interest on the bridge are affected by the actual motion of this point in a similar manner to the reference prisms for the ATS system influencing the reading of the ATS prisms on the bridge.

In this project the reference points were taken from large buildings within a couple of kilometres of the bridge site. These buildings appear to have little movement in the local area according to the SAR data supplied but could actually have some movement at the same

millimetre scale as the deformation we are trying to measure on the bridge. As the ‘absolute’ movements taken by the satellite are actually relative to another point that is assumed to be fixed (which in practice will never truly be stationary) there will always be an unknown error in the ‘absolute’ measurements.

Based on this premise, future work using a similar set up should include corner reflectors located at some distance away from the bridge, preferably fixed to the ground, that could be used as the local reference datum for any movements. Another improvement to this experimental set up would be to set up GNSS stations to control the reference system stability by using the known GNSS-measured points as reference points. However, it was not considered in this instance as GNSS receivers were not able to be set up and left in central London (GNSS receivers come at considerable cost and could not be left due to the risk of interference, theft, or malicious harm by pedestrian access as has previously occurred on projects in the area). There are Ordnance Survey GNSS stations at permanent locations around the wider London region (e.g. at Teddington, Stratford, etc.) but these are several kilometres away and therefore not close enough to the site to discount atmospheric effects when processing SAR data for comparison between the GNSS site and the Waterloo Bridge site.

Further work to consider the practical implementation of such a set up would be to consider the relative costs of installing corner reflectors on a bridge and on an adjacent reference datum points and monitoring using satellite data, in comparison with installing and operating a traditional ATS ground surveying monitoring system over a period of years.

A final point for consideration in terms of the data quality is the increase in measurement uncertainty when the different orbit SAR data combinations are used to obtain longitudinal components. As described in the NPL corner experiment, there is an increased measurement uncertainty introduced when considering a component of motion from the line-of-sight vector. In using different combinations to obtain a longitudinal component, the uncertainty of the measurement value is increased.

5.8.2 InSAR data sparsity

Future technological advances within the earth observation field may likely increase the sampling frequency of measurements. For example, putting more satellites in the same orbit enables shorter revisit times, which brings further opportunities for satellite monitoring. The current 11-day revisit period for the TerraSAR-X satellites used in this study are only frequent enough to pick up seasonal temperature trends within a season, and has a good chance of missing peak values or being affected by aliasing. If much shorter, say 3-hourly, readings were eventually possible with planned future satellite deployments, then the scope

of observable behaviours would be much greater as loading patterns from diurnal temperature cycles, tidal motion, etc. would be picked up.

5.8.3 Use of corner reflectors

This research demonstrated the potential for bridge structures to be retrofitted with corner reflector devices to monitor points of interest over time using InSAR. However, there are two key considerations that have to be made in deciding whether to do so. Firstly, as previously outlined, the bridge must exhibit a low enough level of clutter (evaluated by the Signal-to-Clutter Ratio, SCR) such that the radar reflection from the corner reflector is clearly distinguishable from other points on the bridge. Secondly, there must be a minimum spacing between the corner reflectors installed, such that the response from one corner reflector does not interfere with another. This spacing was dependent on the resolution of the satellite imaging being used. In this case, reflectors spaced at distances greater than 24m meant that 3m square resolution cells (which become larger than 3m during the processing due to various multilooking and filtering steps), would be clearly discernible from one another within the SAR radar imagery and interferometric processing.

5.9 Conclusions

Small scale corner reflectors were trialled for the use of InSAR to monitor points of interest on Waterloo Bridge. The displacements of these key points on the bridge were monitored over time using both InSAR and ATS measurements for comparison. The technique was able to measure displacements of one point on the bridge relative to another, but the limited frequency of satellite readings and noise within readings means that it is not a technique that could replace traditional monitoring methods. Seasonal thermal expansion could be tracked using InSAR measurements, and there is an opportunity to complement traditional visual inspection regimes with these additional measurement insights.

The relationship between SAR and ATS readings was explored using multidimensional analysis to understand how accurately the SAR measurements could be mapped to and characterise the ATS readings. It was found that the two readings were directly related such that they could be mapped, but the nature of the transformation was highly non-linear. The overall plots of relationship indicate that SAR data can be used as a reasonable indication of bridge movement, but some irregularities must be further explored for full confidence. Finally a combination of ATS and SAR readings can be used together to determine unknown

positions and uncertainties, however, in practice this would be a high cost financially and in terms of effort to be sufficient value to asset owners.

Chapter 6

Hammersmith Flyover

6.1 Introduction

This Chapter studied the use of InSAR measurements on monitoring the behaviour of Hammersmith Flyover, a road bridge spanning in an east-west direction within an urban environment in West London. Rather than monitoring controlled points of measurement, as in the case of Waterloo Bridge, the Hammersmith Flyover provided an example of a bridge without corner reflector or other retrofits, making use of ‘natural SAR reflections’ from the bridge for InSAR monitoring. Similar to the previous study, InSAR measurements of displacement were compared against traditional in-situ measurements, this time in the form of displacement sensors fitted onto the bridge rather than surveying methods.

This Chapter on the monitoring of Hammersmith Flyover using InSAR satellite methods has three parts. First, the challenges of interpreting InSAR data in relation to bridges in urban environments are presented. Secondly, a methodology for identifying relevant points of interest on the bridge is developed and tested. Finally, a comparison of InSAR data and in-situ monitoring data is undertaken, so to assess the ability of InSAR analysis to identify defects in bridge articulation.

6.2 Bridge structure

The Hammersmith Flyover in London, United Kingdom, was constructed in the 1960s as a strategic road asset carrying 4 lanes of traffic in and out of London from the west (Figure 6.1). It is a 622m long post-tensioned prestressed concrete segmental bridge. It was considered to be an innovative structure in its time, and is generally considered to be the first major segmental precast post-tensioned highway structure in the UK. It is made up of 16 spans

(typically 42m in length) forming a single, central spine beam with transverse cantilevers supporting the roadway. The bridge is articulated by roller bearings at the base of each of the 15 piers, and one expansion joint located in one of the centre spans separating the superstructure into two structurally independent sections. Longitudinal restraint is provided at the abutments at either end of the bridge.



Fig. 6.1 Photo of Hammersmith Flyover from below. Photo reproduced with the kind permission of Ramboll UK.

6.3 Background to monitoring work

In the last decade, the bridge has experienced a number of problems, leading to its closure during the Christmas period in 2011, causing severe disruption to traffic and the local economy (outline summary of event in Table 6.1). The reason for closure was primarily due to severe corrosion of the prestressing tendons within the flyover, accelerated by increased use of de-icing salts on the road. The flyover was not originally designed to be subjected to de-icing salt, as designers provided electric deck heating. However, this system became defective and stopped working at some point in the decades prior to the bridge's closure in 2011.

In addition, visual inspection of the bridge revealed concerns regarding bridge bearing performance at multiple locations. Bearings allow bridges to move under imposed loading,

and the seizing or restricted movement of bearings can lead to significant problems due to restraint against expansion. This restraint could cause additional bending moments in the deck and induce stresses that the bridge was not designed to withstand. For this reason, it is important to inspect bridge bearings during inspections and also ensure that they are able to move. If they are not able to move, further analysis should be undertaken to understand the level of damage imposed and identify whether replacement is needed.

InSAR provides the opportunity to collect readings related to bridge movement in an interval period of days. Thus, it may enhance bridge monitoring by detecting signs of unusual behaviour that develops in the periods between visual inspections or are not picked up visually. This study was undertaken primarily to investigate the following questions:

- a) Can InSAR be used to identify anomalous movement behaviour?
- b) Can InSAR monitoring be used in practical applications with existing and accepted civil engineering digital environments and tools (with a view towards creating an automated system that warns end-users of unusual or anomalous behaviour related to the bridge)?

Table 6.1 Timeline of events for Hammersmith Flyover

2010	Installation and start of structural health monitoring by Transport for London.
Dec 2011	Decision taken to close the Hammersmith Flyover to all traffic for almost three weeks over Christmas 2011.
Jan 2012	Hammersmith Flyover was reopened to traffic with one lane operational in each direction. Traffic was restricted to cars and vans only (7.5 tonne gross vehicle weight limit).
Jan to May 2012	Phase 1 strengthening designed and constructed to strengthen five critical piers (work taking place in the central reserve of the eastern half of the bridge).
May 2012	Hammersmith Flyover was re-opened in full to all traffic ahead of London 2012 summer Olympic Games in July.
2013	Phase 2 of the strengthening project started; One of the first activities was the break-out of the central reserve that was not affected by the work in 2012 (mainly western 2/3 of the structure)
Nov 2014 to Dec 2015	Bearing base pit strengthening, bearing jacking and bearing replacement.

6.4 Deployed monitoring systems

6.4.1 Deployed traditional monitoring systems

From 2010 to present, the bridge has been fitted with a number of different monitoring systems. These include a vast range of sensors counting approximately 300 acoustic emission sensors to detect wire breaks in the prestressing tendons, temperature sensors, inclinometers and strain gauges on the piers, and displacement transducers and automated total stations to detect and measure pier displacement. The bridge was also used to test a novel wireless sensor structural health monitoring (SHM) system to showcase the application of wireless sensor networks (WSNs) in parallel with wired monitoring solutions. The result is a patchwork of different data sources at various time periods between 2010 and 2018. More specific details regarding different aspects of these deployments on Hammersmith Flyover are described in Webb et al. (2014) [123].

For the purpose of this study, only those deployments providing information on thermal expansion of the bridge were considered. Systems such as acoustic emission monitoring to detect wire breakages within the prestressing tendons were not taken into account, as such defects cannot be picked up through the monitoring of displacements of the deck. Data from the following existing sensor systems were used:

- Temperature sensors embedded in the top, bottom and web of the deck at 4 midspan locations of the bridge - spans BC, FG, KL and OP (Figure 6.2)
- Displacement transducers (Linear Variable Differential Transformers, LVDTs) used for measuring linear displacement at bearing locations at the base of each pier (piers B to P) (Figure 6.3)

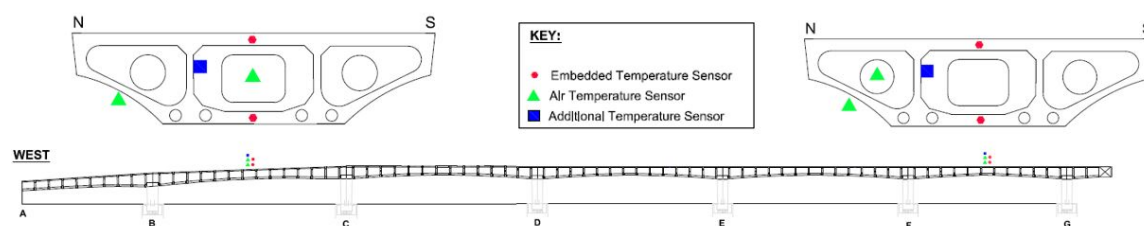


Fig. 6.2 Temperature sensor locations through the deck on the bridge. The span locations shown are BC and FG, but similar installations collected temperature readings at locations KL and OP.

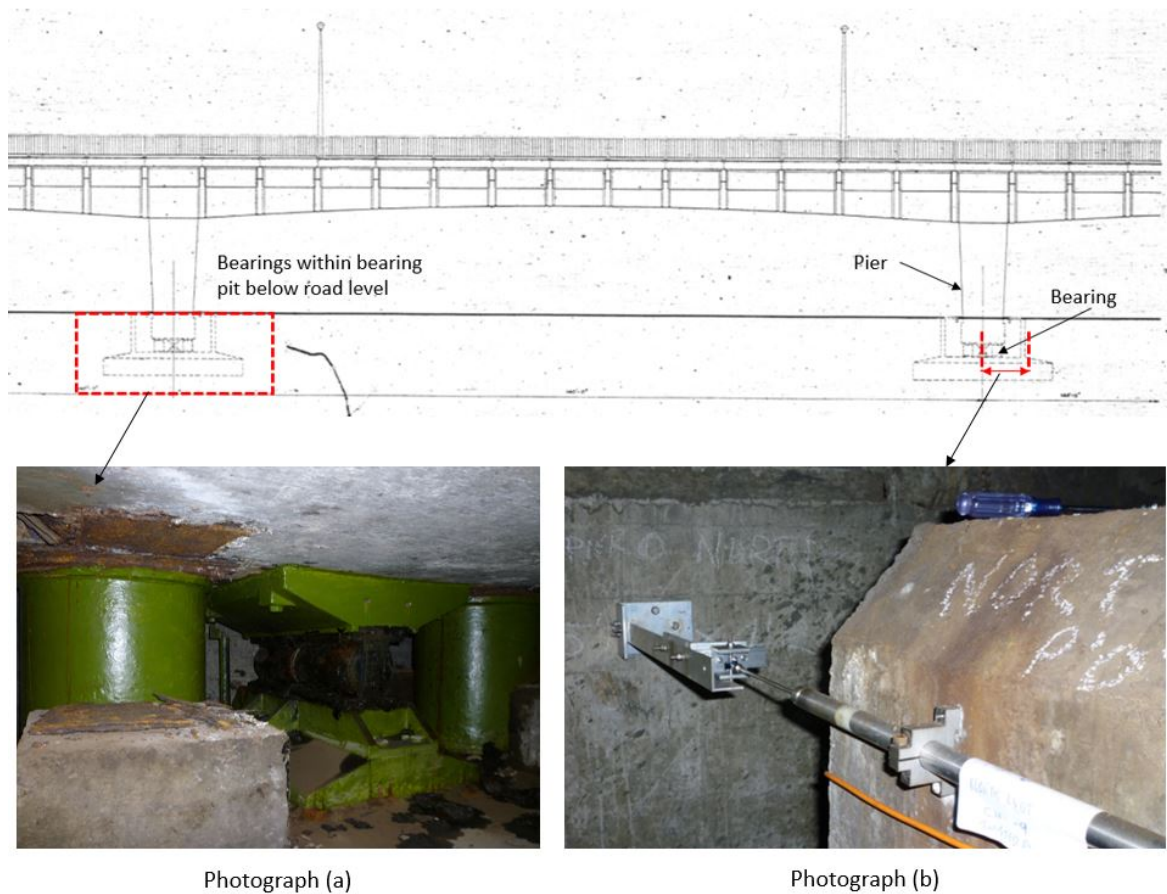


Fig. 6.3 LVDT installation for bearing movement measurement. Photograph (a) shows bearing within bearing pit and Photograph (b) shows LVDT installation between wall of bearing pit and base of pier. Photographs taken by and included with permission of Graham Webb.

During the period of this study, one of the existing SHM schemes was removed by a contractor and later replaced with another, intended for longer term installation and monitoring of the bridge. The earlier scheme provides data for the period from August 2010 to August 2015 and the later installation was intended to provide data uploaded from the bridge onto an online portal from September 2015 to November 2018.

6.4.2 InSAR data analysis

Archive Cosmo SkyMed-X SAR data together with Cosmo SkyMed-X acquisitions tasked specifically for this research (both of the same pixel resolution of approximately 3m by 3m) were collected to provide a stack of remotely sensed records collected from 2015 to 2018. Additionally, a preliminary dataset of processed Cosmo SkyMed-X SAR acquisitions taken

over the London region (including the Hammersmith area) for the period from 2011 to 2015 were provided by Telespazio VEGA (processed by an external party, the acquisition dates processed as outlined in Appendix B).

Unlike the TerraSAR-X acquisitions used in the previous studies at NPL and Waterloo Bridge, this stack has a large variation in revisit period (time between acquisitions) and the perpendicular baselines were much larger. The perpendicular baselines for satellite positions for the TerraSAR-X data used in this study (Figure 6.4) was controlled to be between $\pm 250\text{m}$, whilst the Cosmo SkyMed-X data was up to $\pm 1500\text{m}$. For the processing done by the author, a restricted baseline of $\pm 1000\text{m}$ was selected and acquisitions far outside of these range (two acquisitions in total) were discarded.

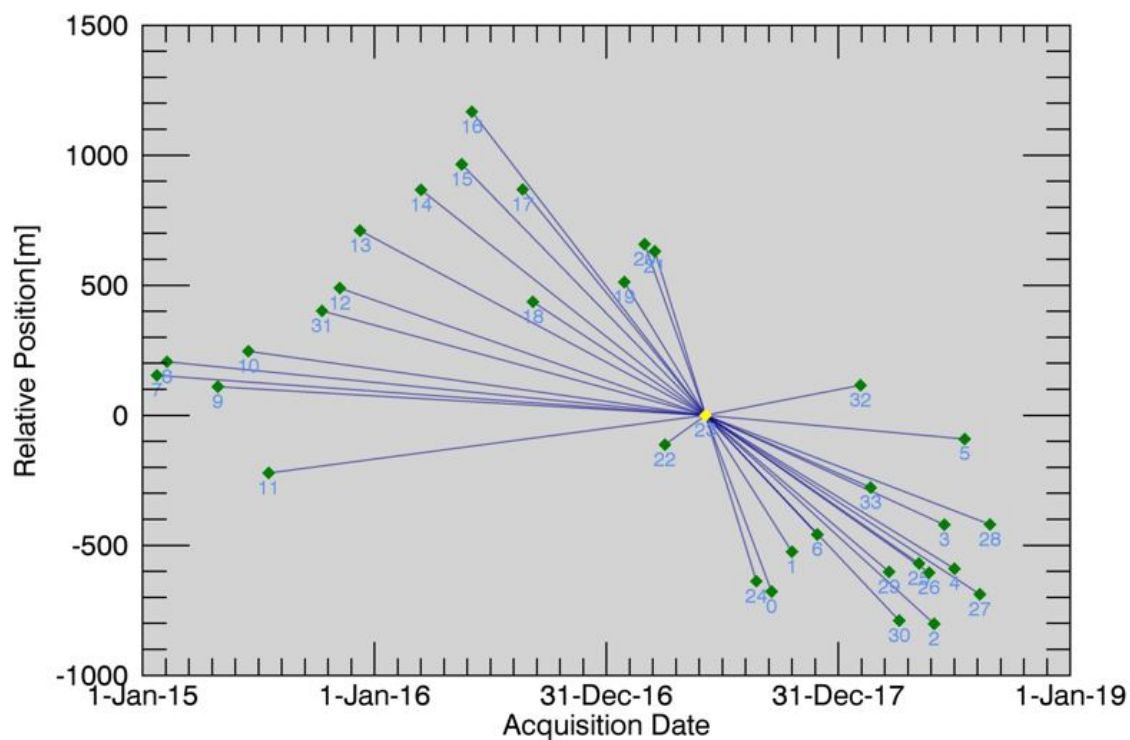


Fig. 6.4 Time-position plot for 2015 to 2018 images processed

Shuttle Radar Topography Mission (SRTM) data with resolution of 3 arc-second (90m) was used as a Digital Elevation Model (DEM) during the interferometric processing. The SAR data was processed by the author (2015-2018 acquisitions) using standard PSI algorithms as included in the SARscape software package. A modified development of the PSI algorithm developed by the company E-Geos (details of which were not made available) was employed for the dataset processed and provided by Telespazio VEGA. Thus, for this work

on Hammersmith Flyover, two sets of PSI results were produced, one for the 2011 to 2015 period, and a second for the 2015 to 2018 period (with different PS than those in the first set).

6.5 Results

The InSAR processing results were then interpreted to extract the relevant PS of interest for this study. Figure 6.5 shows a typical output from PSI processing in the format of a shape file (.shp file extension) where PSs are marked as points, the location of which is determined during the geocoding stage of InSAR processing, where the SAR coordinates are mapped onto geographical coordinates. In this case the results were mapped onto the World Geodetic System 84 (WGS84) coordinate system. The shape file of PS locations can be opened in Geographic Information Systems (GIS) software packages to display the Cartesian coordinates of the PS points. Each of this data points contains a profile of LOS movement over time, as well as characteristics describing the behaviour of the output products from the PSI processing (such as coherence value, or linear velocity in mm/year).

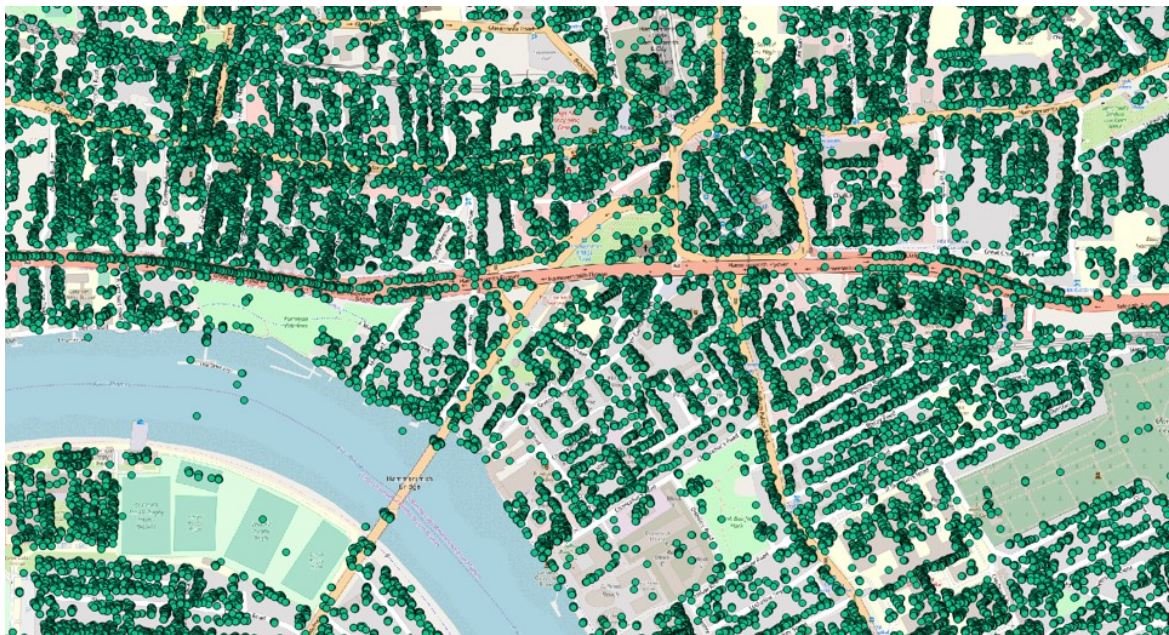


Fig. 6.5 PS points on Hammersmith Flyover and surrounding area overlaid onto Open Street Map base imagery.

The PS points can be overlaid onto an optical satellite image or map of the area (as in Figure 6.5) to manually interpret the locations of the PS points as attributed to objects on the ground, such as buildings or bridges. It is worth reminding that each ‘dot’ represents an approximate location of the resultant reflection from a multi-looked pixel area.

The PS points can then be attributed to corresponding man-made objects (such as facades of buildings, or metal parapets or edge beams of bridges) by user interpretation, but this might be challenging because of the particular imaging effects caused by SAR imaging geometry in urban areas. The literature also presents a method of simulating the reflections through ray tracing [124] to better interpret the imagery. In order to understand some of the InSAR processed PS location results, the following section reviews some of the SAR imaging effects that would affect bridges in urban scenarios, such as Hammersmith Flyover, which is surrounded by buildings and other structures.

6.6 Methods for interpreting InSAR outputs

It is clear from Figure 6.4 that there are a number of regions in the bridge missing PS points. The bridge has a consistent form and structure, which would suggest that each section should be equally suitable for PSI application. However, the viewing geometry of a SAR image results in certain geometric distortions on the resultant imagery (Figure 6.6). The side-view imaging in the slant-range direction causes such effects as foreshortening, layover and radar shadows, as described in the theory in Chapter 2, Section 2.2.3.

6.6.1 Digital modelling

Overlay of PSI results onto three-dimensional representations of buildings and other assets to aid interpretation has become common practice in recent years. This is done within visualisation tools for the specific task of visualising PS data points. Within traditional civil engineering and asset management practice, the management and exchange of monitoring data is addressed by the information technology approach known as building information modelling (BIM). Its main purpose is to manage digital representations of all information related to a built asset during its entire life cycle, to improve productivity and quality while reducing costs [125]. The concept of BIM is not simply to describe graphical representations of assets, but also to link other associated data sets (for example, material specifications, costs, component identification, etc.).

In the application of InSAR data into civil engineering environments, it is advantageous to make use of any existing data and model, as well as to integrate the satellite data within an established and existing systems. The processed InSAR data (PS point output) can be geocoded to specific geographical locations (based on selected mapping and projection information) and output files can be opened and interpreted within Geographic Information Systems (GIS) software. This allows for geometrical models of the bridge and surrounding

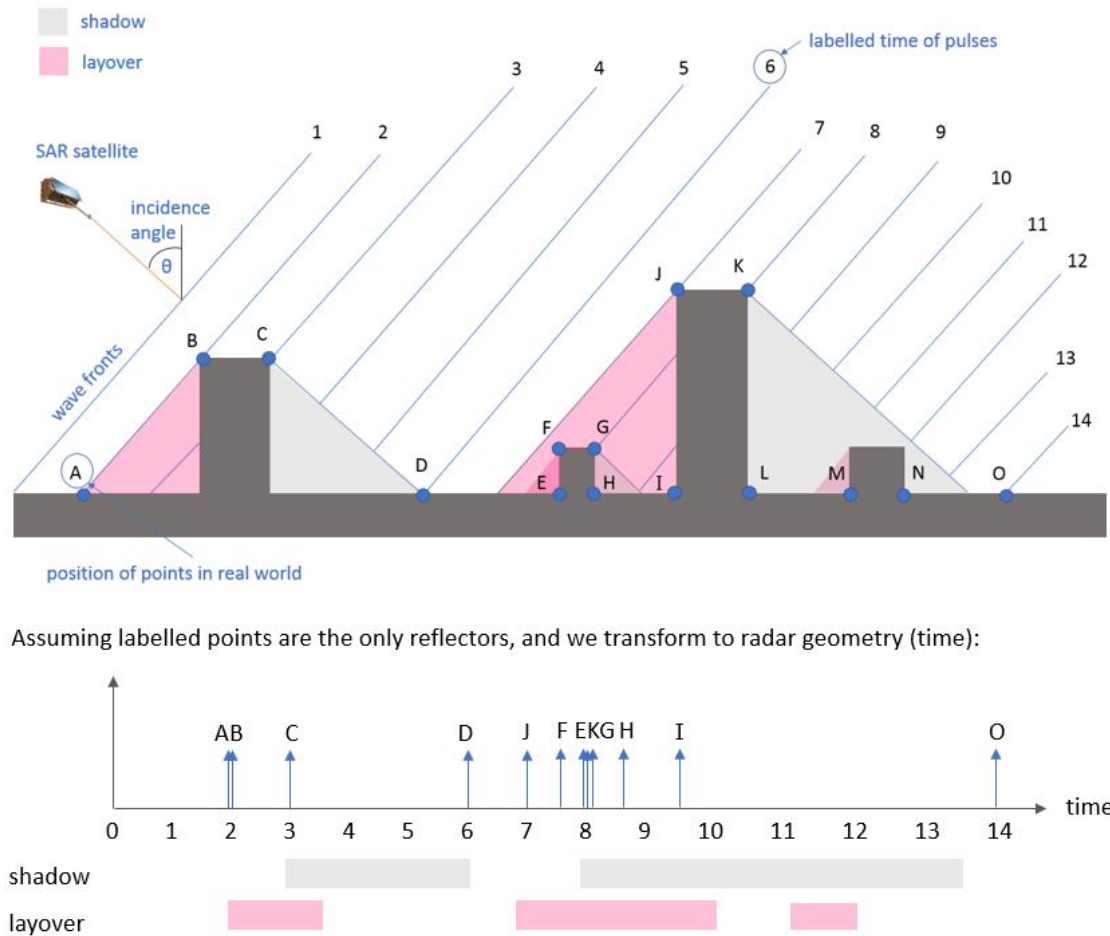


Fig. 6.6 Sketch to illustrate SAR imaging effects impacting Hammersmith imagery (urban landscape with tall buildings). Based on sketch developed by T. Wright.

buildings, as well as other environmental datasets (such as floodplains, planned construction activities such as excavation or dewatering, etc. in map layers) to be overlaid onto the asset in the GIS domain to get further insights about the context in which the asset is sitting and enhance the interpretation of the PS point cloud.

The primary issue with this approach is that the integration of BIM and GIS spaces is not a standard or automated process and requires specialists who are able to integrate the two systems together (even simple three-dimensional geometry and GIS spaces). Most three-dimensional models within civil engineering are built within a model space with an arbitrary origin assigned (Diagram A in Figure 6.7). An online software package called GeoBIM (by a company called Group BC) was used to import the geometric BIM model of Hammersmith Flyover into a GIS space. The PS point cloud was then imported and manually overlaid onto the GIS map. (Diagram B in Figure 6.7). Initially this was done using InSAR

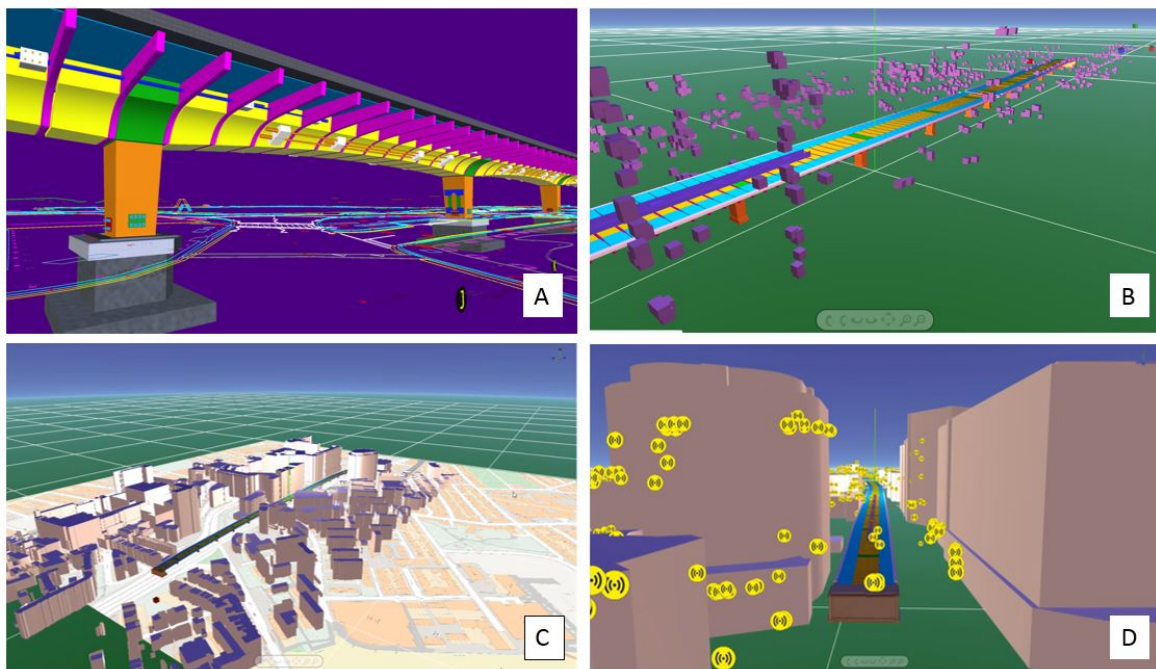


Fig. 6.7 Three-dimensional interpretation of PS points on Hammersmith Flyover: a) BIM model stripped to pure geometry; b) Bridge model imported into GIS space with PS points; c) Ordnance Survey building elevation information also imported into GIS space; d) Model and PS in GIS environment used to aid interpretation of PS points.

data processed by others an importing the point cloud of PS points based on the (x, y, z) coordinates specified within the PSI output data. The initial import of these two datasets within the same GIS space revealed that the point cloud was situated on a plane much higher than the bridge or surrounding buildings. The data appeared to align in (x, y) with the bridge but on a horizontal plane much higher up from the ground level. From an application point of view, it is important to understand that the cause of this misplacement is due to a error in the geocoding stage of the PSI processing. There are several sources and consequences of geocoding error [126]. The height error in this particular case would correspond to the reference DEM input during the PSI processing. The height accuracy of the PS point cloud depends on the DEM error of the reference point. The height error of this reference point results in an offset for all points, and has an effect of the resulting geocoded coordinates both in the horizontal as well as vertical components.

On working with suppliers of InSAR services it was noticed that PS datasets were manually aligned in plan $(x-y)$ as well as in height (z) . In the case of imperfect geocoding in this case, a manual adjustment of the InSAR point cloud was made by visually matching lines of PS points clearly aligned with various buildings and the bridge structure. This was

deemed sufficient for the purpose of this study as the option to reprocess the data for the trial set was not available, and the output required was only for interpretation purposes. Other works in the literature focus on correcting geocoding errors [126]. As previously explained in Chapter 2, these PS points are not actually representative of a point, but rather the representation of areas marked out by pixels in SAR imagery. It is therefore important to keep in mind that uncertainty of position must be addressed when considering the location of the points (and therefore need to be interpreted along with other inputs).

Finally, openly available Ordnance Survey building height data was imported along with the BIM geometry model of Hammersmith Flyover (Diagram C in Figure 6.7) to integrate built environment data with the PS point cloud to determine which of the PSs were coming from the bridge and which from the ground and surrounding buildings (example shown in Diagram D in Figure 6.7).

6.6.2 Method for the identification of target points

Using the 3D model identified which PS were likely to come from the bridge. For practical applications, it would be useful to understand which parts of the bridge the PS come from, in this case which PSs were most likely to be attributed to a particular pier and side of bridge. To this aim, a process to narrow down the selected points, and then a method developed as part of this research to select PSs of interest is outlined in this section.

The PSs for Hammersmith were located primarily on the outer top surface of either side of the bridge, suggesting that the SAR reflections might have come from the parapet or outer edge of the concrete deck. There were no points present on the central reservation or roadway. This is logical as cars, trucks and other vehicles constantly pass over the roadway, preventing the SAR waves from reaching a consistent point. The passing of vehicles could also block SAR reaching the central reservation which end up being in a radar shadow at these moments, therefore eliminating PS points in this region too.

For this study, the location of the points has been associated with each pier (the deck was divided in lines at each midspan and all PS points in between consecutive midspan lines were attributed to the pier in between either line). A number of points attributed to a particular pier (Pier N) are shown in yellow in Figure 6.8. In this diagram, any other persistent scatterers attributed to buildings and other objects have been already excluded.

Using structural modelling and understanding of the bridge behaviour, the primary cause of deformation of Hammersmith Flyover is thermal loading which causes expansion and contraction, with most movement occurring in the centre of the bridge and decreasing towards each span. A finite element model of Hammersmith Flyover (made using the software LUSAS) was used to model a series of different loading and temperature scenarios.

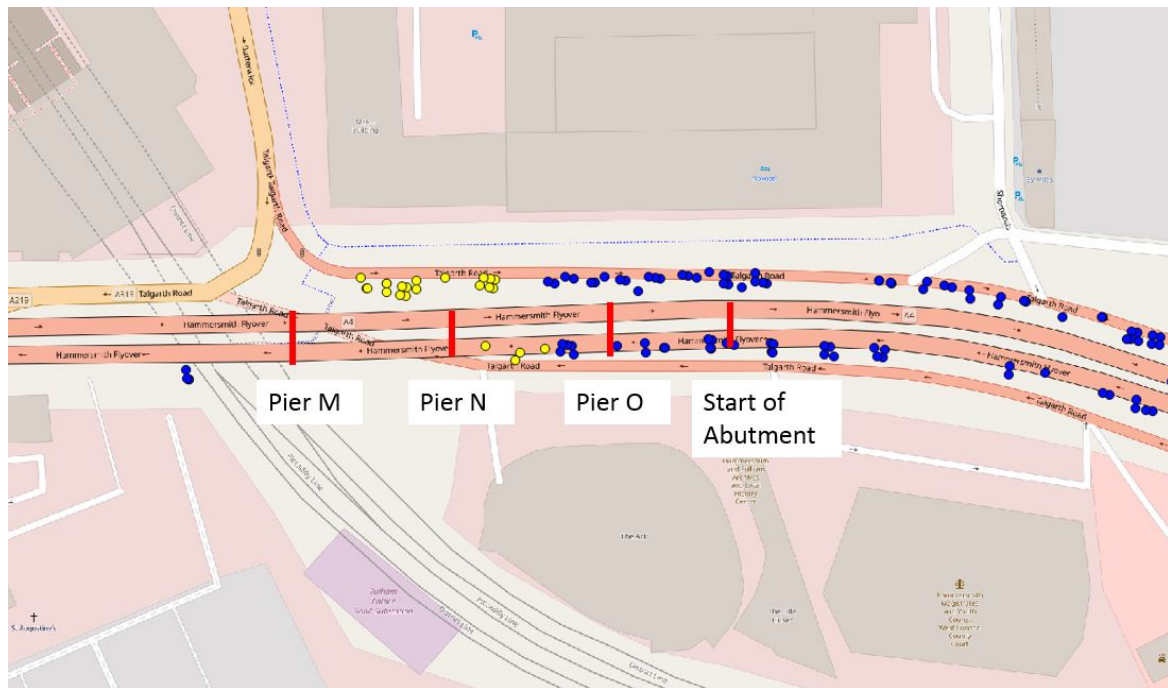


Fig. 6.8 Points representing persistent scatterers associated to the bridge overlaid onto a map of the bridge. The points in yellow highlight persistent scatters on the south side of the bridge that were attributed to Pier N. The points in blue are other persistent scatterers attributed to the bridge.

This was confirmed by displacement gauge data collected from the base of each pier which showed horizontal movement of the bearing in the form of a sinusoidal oscillation over a yearly period, reprising the basic trend of the temperature measured.

It is worth recalling that InSAR bridge studies in the literature remove the thermal component of bridge movement to understand remaining behaviours and settlement, as discussed in the literature review in Chapter 3. This would be useful in removing one dominant load response to look for other behaviours, such as settlement. Nonetheless, removing the displacements attributed to temperature would limit the analysis of the bridge bearings for each pier expand and contract primarily due to non-linear displacements induced by thermal loading. Therefore, the PSs of interest from the bridge (those that reflect the movement accommodated through the bearings) are those with a sinusoidal profile.

The method developed to identify the PS points of interest makes use of the Fast Fourier Transform (FFT). Fourier Transforms are used to decompose a function of time into the frequencies that it is comprised of, i.e. it is the frequency domain representation of the original signal. The time-dependent signal as an expansion of its frequency components, or the Fourier transform $F(\omega)$, is represented as follows:

$$F(\omega) = \int_{-\infty}^{+\infty} f(t)e^{-i\omega t} \quad (6.1)$$

The Discrete Fourier Transform (DFT) is version of the Fourier transform that deals with a finite discrete-time signal and a finite or discrete number of frequencies. The Fast Fourier Transform (FFT) is another method for calculating the DFT based on the size of the input data being a power of 2, and is computationally many times more efficient than the DFT. Passing the data through a DFT would reveal the number of different sine wave frequencies that sum together to form the considered signal. In the dataset considered here, there is one sine wave oscillation of movement in the PS points we are searching for. Therefore, a single spike at a low frequency should appear.

Take, for example, the measured temperature data for one of the bridge spans in Figure 6.9. This data shows a clear seasonal oscillation, with smaller oscillations on a daily basis. When passed through a FFT (Figure 6.10), this appears as two clear wave frequencies for each of the two sine oscillations (daily and seasonal), plus smaller spikes at other frequencies accounting for some noise.

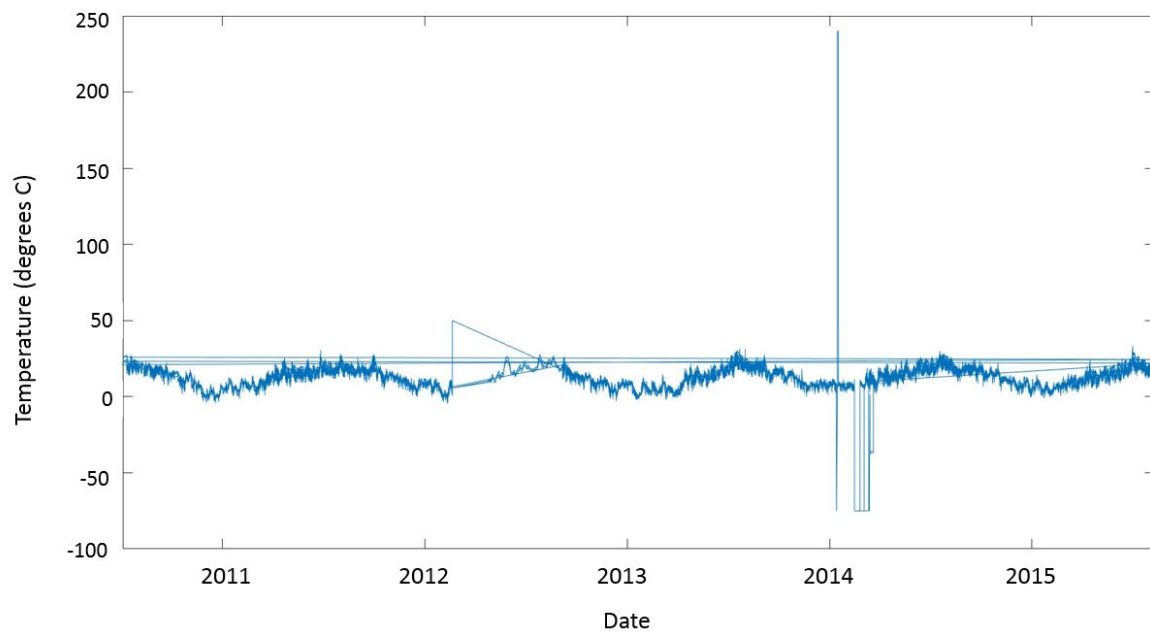


Fig. 6.9 Temperature data for span BC (as extracted from data portal, unfiltered and without obvious anomalous points removed).

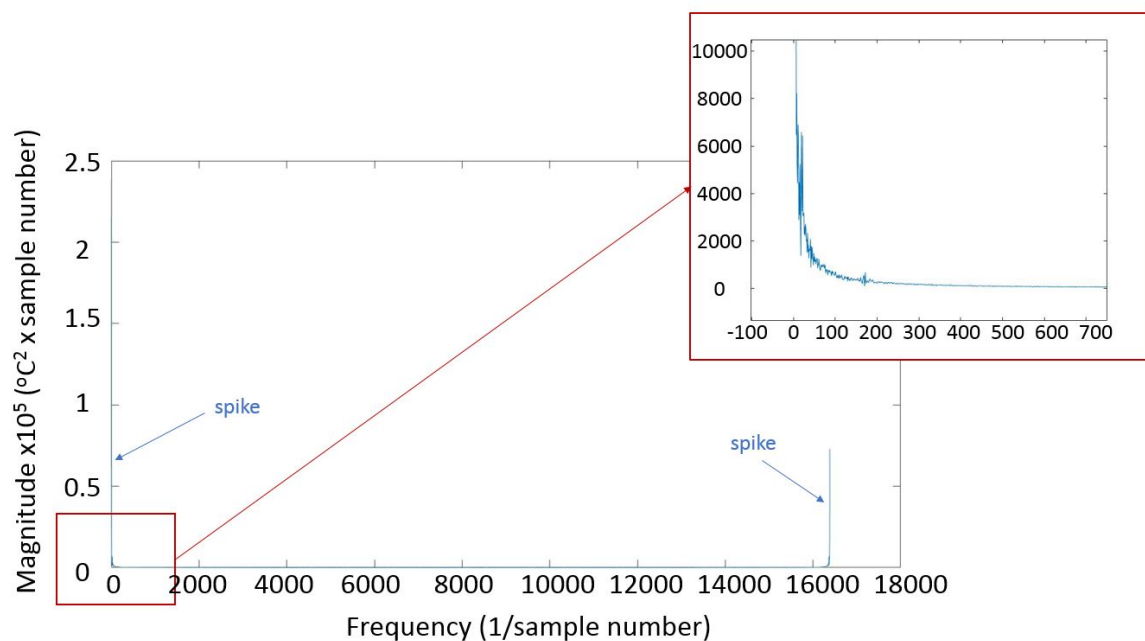


Fig. 6.10 Temperature data of span BC passed through a Fast Fourier Transform (FFT). The magnitude value is the power spectral density of the signal.

To select the PS points attributed to a particular pier, each of the PS displacement over time profiles were passed through an FFT to identify which exhibited the sinusoidal profile. Those which exhibit a sinusoidal profile display clear spikes in the frequency domain (either clearly or with some noise, Figure 6.11) whilst those that did not comprise of sinusoidal behaviour (such as the example in Figure 6.12) were discarded from the considered set.

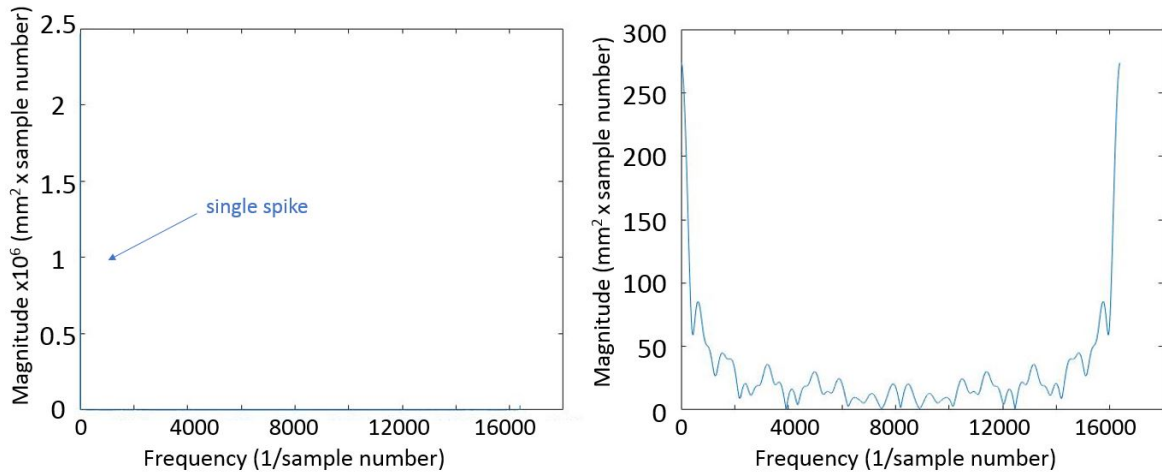


Fig. 6.11 Two examples of selected InSAR points which do exhibit oscillating behaviour passed through a FFT. The magnitude value is the power spectral density of the signal.

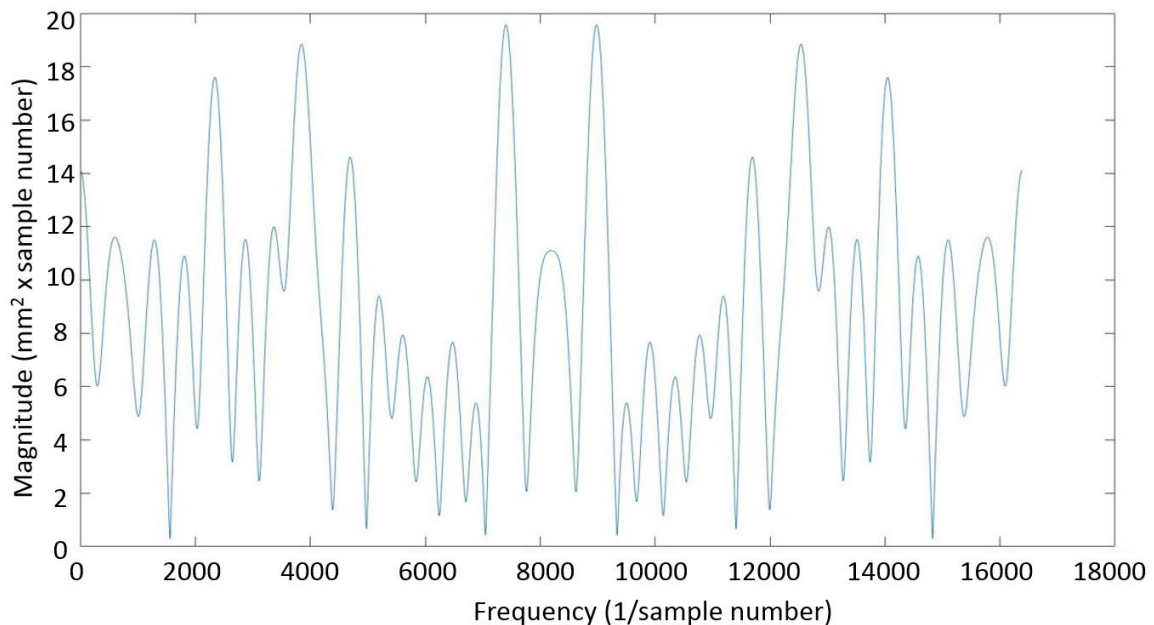


Fig. 6.12 Selected InSAR point which does not exhibit oscillating behaviour passed through a FFT. The magnitude value is the power spectral density of the signal.

These selected points were then plotted over time against the movement measured by traditional in-situ displacement gauges attached to the bearings and bearing pit. Figure 6.13 shows one of the PS points attributed to Pier B alongside the measured bearing displacement data and nearest temperature gauge (average deck temperature in span BC). The InSAR measurement plotted is the measured line of sight (LOS) displacement.

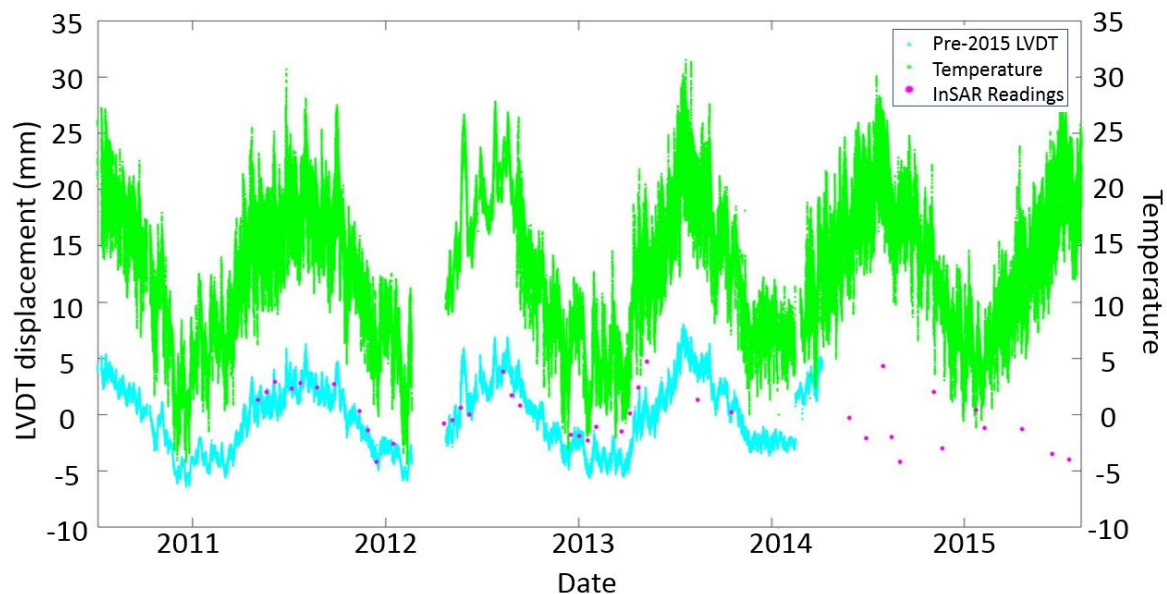


Fig. 6.13 Movement of Pier B as measured by LVDT and selected InSAR point, alongside temperature, over time.

6.7 Bridge behaviour anomaly detection

The method developed provides a means of selecting InSAR points that exhibit oscillating behaviour over time. Monitoring for changes in the nature of this oscillating behaviour can be used to spot signs of unusual behaviour in Hammersmith Flyover. The bridge owner found Hammersmith Flyover to have problems with some of the bearings in the bridge, and bearing replacement activities were carried out in 2014 and 2015. In particular, some of the bearings were found to have seized, severely restricting horizontal movement of the bridge at the pier locations of these seized bearings [123]. This was true in the case of Pier N, which was able to move to a larger extent after bearing replacement. The points attributed to Pier N (as described in Figure 6.8) are plotted in Figure 6.14. The method developed to select oscillating points of interest was then applied, giving rise to Figure 6.15, which plots just the selected points of interest.

The LVDT measurements in Figure 6.15 show that the Pier N bearing moves to a larger extent after bearing replacement. The motion of Pier N corresponds to the temperature, also plotted on this figure using readings taken on the OP span. There were no LVDT readings during the bearing installation as the first SHM system had been removed, but the second SHM system had not been installed or started collecting data. There was also a lack of LVDT data for all piers from the end of 2017. All SHM data from Hammersmith Flyover stopped being received during this research work, and was found to have been caused by a cut in electricity supply to the SHM system due to unpaid electricity bills. This stop in data collection was not noticed by the contractor who installed the system and provided access to the data, and the problem was not able to be rectified to continue data collection for this study.

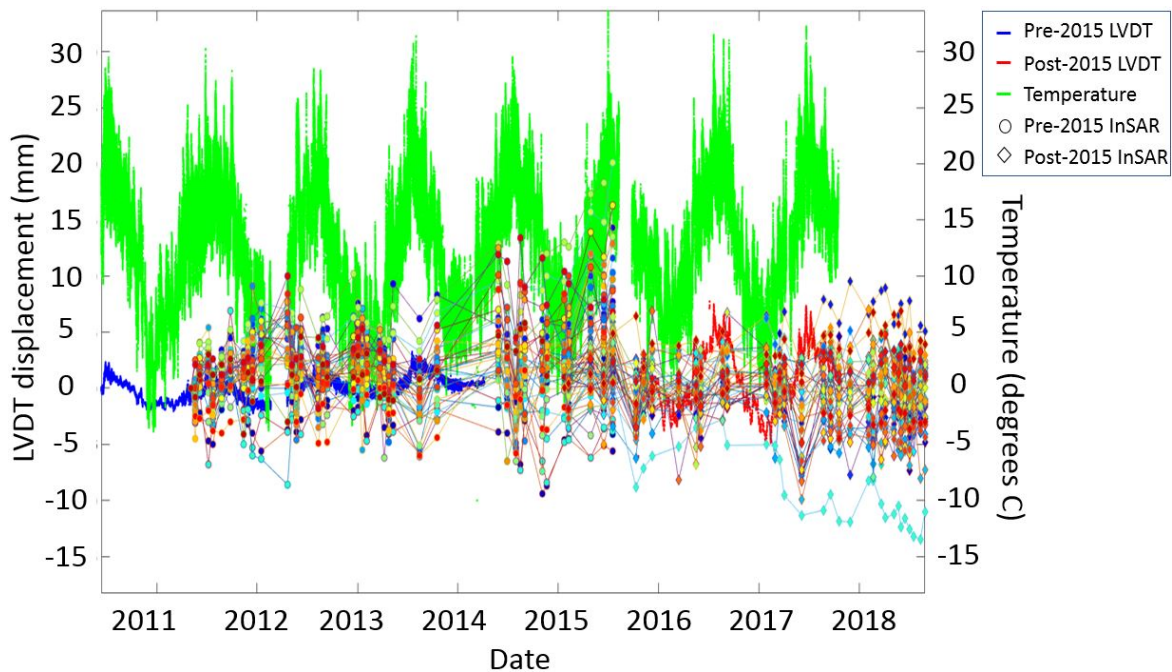


Fig. 6.14 Movement of Pier N as measured by LVDT (two different systems, pre- and post-2015) and all InSAR PS points attributed to Pier N (with 2011 to 2015 dataset and 2015 to 2018 dataset), alongside temperature, over time.

The InSAR-derived (LOS) measurements from the two SAR datasets were also plotted on Figure 6.15. The direction of horizontal displacement for Hammersmith Flyover is in the east-west direction. This is ideally orientated for SAR viewing geometry to pick up horizontal displacements between acquisitions. Given that the bridge is known to have negligible vertical displacement at the piers (from previous studies and monitoring data) the LOS measurement would primarily be picking up the horizontal thermal expansion, as so

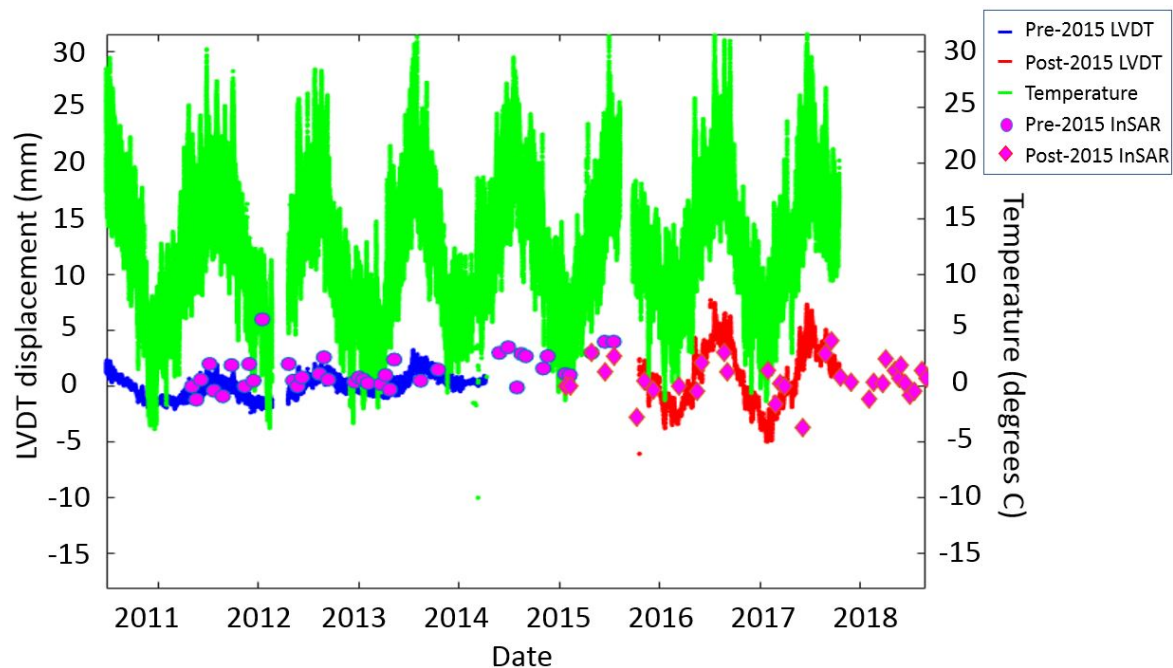


Fig. 6.15 Movement of Pier N as measured by LVDT (two different systems, pre- and post-2015) and two selected InSAR PS points (with 2011 to 2015 dataset and 2015 to 2018 dataset), alongside temperature, over time.

this was plotted instead of working out components of the LOS displacement as was done in the Chapter on Waterloo Bridge.

In this instance, the bridge movement is primarily due to thermal temperature, and the thermal-related displacement measurements highlighted the problems with the bearing. Removing this thermal component of displacement at the InSAR stage of processing and evaluating the data would have missed this problem. In Figure 6.15, the change in oscillations in the InSAR measurements can be seen before and after the bearing displacement. If this change in bearing behaviour can be seen from InSAR measurements, there exists an opportunity to use InSAR to identify signs of bearing failure. In practice this would be more difficult, as the measurements would not show a change from seized bearing to a bearing that is free to move, but rather a slower more ambiguous decrease in amplitude of oscillation.

Ideally, this study would have shown the InSAR and LVDT measurements before and after bearing replacement of a pier towards the centre of the bridge. The piers towards the centre of the bridge experienced much larger horizontal displacements (and therefore larger amplitude of oscillations). However, none of these piers had bearings that seized. Pier N was known to have had a bearing that seized and was replaced in 2014/2015, as it had much smaller amount of horizontal displacement than more central piers, it is less easy to see the difference in oscillation amplitude before and after the bearing replacement.

6.8 Discussion

In terms of the application of SAR to bridge monitoring in practical terms, SAR data can be used in the absence of other sensor measurements (in this instance to spot unusual or anomalous behaviours) but it can also be used to augment the information provided by a wider digital sensor network. However, these must be taken with an understanding that SAR measurements are not useful in all bridge monitoring cases, and will not provide measurements for all bridges. These considerations are presented in the discussion below.

6.8.1 Augmenting a wider digital network

More generally, the opportunities to take advantage of includes the SAR imagery having global coverage, more frequent revisit in comparison to traditional visual inspection regimes (but less frequent than traditional sensors), no power supply requirement on site and no on-site maintenance visits or costs. It provides the additional opportunity of wide area coverage, taking measurements not just from the asset of interest (which is what traditional monitoring would be limited to), but also of the ground and other assets in the surrounding region - metres or even kilometres away.

Despite these notable opportunities, the optimum use of InSAR methods is to consider them as a tool within the tool-belt of technologies available to bridge owners. It provides a wide area picture and collects low frequency measurements as part of the picture. This can augment the frame of view provided by sensors at single points at much higher frequencies. The growth of information modelling, three-dimensional modelling and digital environments in BIM provide opportunities to develop tools that can combine and leverage the information derived by these different tools.

One possible use of InSAR datasets is to provide information in the absence of other sources. InSAR monitoring offers a further advantage over traditional sensor monitoring in that it does not require an electrical connection or power source at site or closure and physical access to the bridge. Therefore, it would be possible to retrieve some information on the assets even if they are not properly equipped with sensor monitoring systems, or in case of loss of in-situ monitoring data. In this instance, monitoring data in 2018 was missing due to an unpaid electricity bill which was missed, and cut energy supply to the sensors. In other instances, such as the monitoring of Waterloo Bridge in the previous chapter, the SHM can have unforeseen limitations due to poor assumptions or unexpected loading and behaviour. InSAR has the opportunity to provide an additional measurement ‘perspective’.

6.8.2 Understanding the suitability of InSAR to a specific bridge

The SAR acquisition geometry imposes limitations on what bridges (or parts of bridges, as illustrated in this case study on Hammersmith Flyover) can be monitored using InSAR. The suitability of the bridge to SAR imaging can be assessed by opening radar images and point target analysis, but simulations can be used to understand what parts of the bridge would reflect, and whether there are any effects such as shadow preventing the use of InSAR for monitoring. Simulated reflectivity maps can be used to aid interpretation of SAR images, to predict backscattering effects in SAR images and to identify groups of strong PS points, and has been developed into software tools for simulating backscattering effects which occur in high resolution SAR images [127, 124]. This simulation concept is based on ray tracing techniques which simulate emission of radar from a virtual SAR through model space and illuminate three-dimensional models of the real-world scenario to be studied.

InSAR monitoring is used to monitor millimetre-scale movements of assets in the satellite line of sight, and understanding other bridge problems, such as acoustic emission sensors to monitor for corrosion of pre- or post-stressing tendons, strain gauges to derive stresses, and inclinometer readings monitoring small scale tilt cannot be superseded by InSAR. It is thus important to understand the appropriate failure mechanisms and bridge defects for which InSAR could provide additional insights, as well as limitations based on material, geometry and orientation of the bridge.

It is also worth remembering Hammersmith Flyover was optimally orientated for InSAR horizontal measurement as movement of the bridge was primarily due to thermal expansion, causing displacements of the bridge in the east-west direction. If the flyover was orientated in the direction of the satellite flight path (north-south), the displacement measurements collected by InSAR would hardly be able to accurately describe this longitudinal expansion due to thermal loading of the bridge.

6.8.3 Understanding InSAR data quality

The previous experiments have made use of TerraSAR-X SAR data and looked at the measurement reliability and uncertainty of measured results. This study has employed a stack Cosmo SkyMed-X SAR acquisitions, which has a different set of properties than the TerraSAR-X data used in the previous experiments. The impact of these properties on the data quality should be considered. Large temporal gaps in acquisitions of up to 3 months make the InSAR processing less robust than using the TerraSAR-X data which were acquired in a regular 11-day time interval. For using Cosmo SkyMed-X data in future similar monitoring regimes, a more regular acquisition strategy of SAR images should be employed.

Section 6.4.2 provided information on the spatial baselines of the SAR data acquired. In addition to long temporal baselines, long spatial baselines lead to decorrelation of differential InSAR data. Figure 6.4 provided an overview of the perpendicular baselines of the SAR satellites during each acquisition with respect to the central reference image. In addition to increasing noise and decorrelation in the data, the imprecise orbital tube means that the acquisitions are not perfectly aligned, and when coregistered into a stack to process, the edges of the image are less likely to align and overlapping data is lost. This means that bridges located closer to the edge of the SAR acquisition may not be captured.

The quality of the results presented in this case study were also impacted by geocoding errors, as outlined in the results. This impacts the interpretation of the PS points and how they are attributed to objects. Within the interpretation methods presented in this Chapter, this would mean a risk of either including points that should not be attributed to the bridge (or be attributed instead to a different section of the bridge) or missing points that should be considered.

6.8.4 InSAR data sparsity

In addition to limitations for InSAR to be employed in bridge monitoring caused by data quality and accuracy, there are limitations which arise from the use of a differential InSAR dataset that seems not to be fully adequate in terms of resolution. Not having SAR acquisitions at a sufficient pixel resolution or frequency limits the ability to investigate structural movements; as discussed in the previous Chapter, daily variations (or variations in smaller time period more generally) can be missed and having a pixel resolution that is not sufficiently small results in fewer PS after InSAR processing, with each PS covering a wider area and perhaps only picking up the more predominant of two distinct movements.

One outcome of this study was the development of a method to extract InSAR persistent scatterers that are likely to be linked to measurements of the bridge experiencing oscillating displacements over time. Using the InSAR data with this method was not generally as simple and clear as distinguishing the two cases shown in Figures 6.11 and 6.12. It was difficult to discriminate between the points exhibiting the oscillating behaviour and the remaining points that were identified by the InSAR. The selection of the oscillating points was made by making use of the periodicity of the InSAR time series record of a particular point. The sinusoidal oscillation sought in this example has periodicity that is typically annual (due to seasonal temperature variation). To grasp this periodicity through the FFT method outlined, there must be a sufficient number of points to cover the periodicity and define the behaviour.

The periodic behaviour of the InSAR time series would have been better captured if there was a regular sampling of measurement points (SAR acquisitions) for the time considered.

The Cosmo SkyMed-X acquisitions processed (as listed in Appendix B) were not well spaced. There were several acquisitions in some months, and then large gaps without an acquisition for several months afterwards. The FFT method proposed was still able to be used to identify the points of interest, but the accuracy and the practical use of this method might be jeopardised if there is insufficient coverage of SAR acquisitions in the time period being studied.

6.9 Conclusions

This study highlights a number of SAR viewing geometry considerations when using InSAR to monitor bridges in urban scenarios. Within this study a possible method to identify InSAR persistent scatterers pertaining to the bridge (rather than buildings or other objects in the surroundings) is suggested, making use of models and data commonly available within civil engineering and urban planning practice. Finally a method to identify InSAR persistent scatterers exhibiting oscillating behaviour due to thermal loading of the bridge is developed by employing Fast Fourier Transforms. This approach looks promising but it is worth noting that the accuracy of the outcomes of this analysis is directly related to the ability of the SAR acquisition to uniformly cover the time period under investigation. If SAR acquisitions are available to form regular and uniform coverage, it would be possible to detect and more reliably quantify the oscillation and periodicity of the SAR records that can be directly linked to the thermal expansion displacements. The FFT approach can also then be developed to monitor signs of bearing or other movement problems in similar types of bridges which are optimally aligned for InSAR measurement.

Chapter 7

Tadcaster Bridge

7.1 Introduction

Within this research, it has been established that InSAR measurement technologies are able to provide displacement measurements at a scale that is relevant to the bridge-monitoring community. These movements may be due to a number of different loading factors, or deformation scenarios. One of the potential opportunities InSAR satellite measurement technology is to be used to identify signs or precursors of failure in bridge assets. As InSAR can only measure displacements at a measurement interval of multiple days, this limits the application of InSAR to identifying signs of problems expressed through slow moving displacements over long time periods, such as settlement or the seasonal thermal responses investigated in the previous Chapters. Another failure mechanism which may show movements indicating unusual behaviour prior to failure is scour failure.

In this Chapter a bridge which partially collapsed due to scour failure is investigated using SAR imagery collected prior to the collapse to see whether measurements of bridge settlement prior to collapse can be picked up using InSAR. Material from this chapter has previously been published in a paper by Selvakumaran et al. [128].

7.2 Scour failure in bridges

Scour has caused the failure of hundreds of bridges globally in recent decades and is the primary cause of bridge failure in the United States [129]. In the United Kingdom, the increase in rainfall and flooding events in recent years has exacerbated this problem and contributed to the collapse of multiple bridge structures. Of notable concern from these failures is the loss of human life, or ‘near misses’ which could have resulted in a larger tragedy.

Notable examples include the Malahide Viaduct and RDG1 48 River Crane Bridge collapses in 2009, which each occurred moments after the passing of passenger trains [130, 131].

Scour is a natural phenomenon. It can be defined as the excavation and removal of material from the bed and banks of streams as a result of the erosive action of flowing water [132]. This erosive action in the vicinity of bridge piers can lead to the removal of ground material on which bridges are founded, increasing the risk of undermining bridge piers and resulting in collapse (Figure 7.1). Changes in water flow rates during flooding can make bridge piers particularly susceptible to scour. The collapse of bridges and other structures in or adjacent to water bodies highlights the essential importance in finding new methods to undertake inspection and structural health monitoring (SHM) of bridges to identify precursors indicating signs of impending failure.

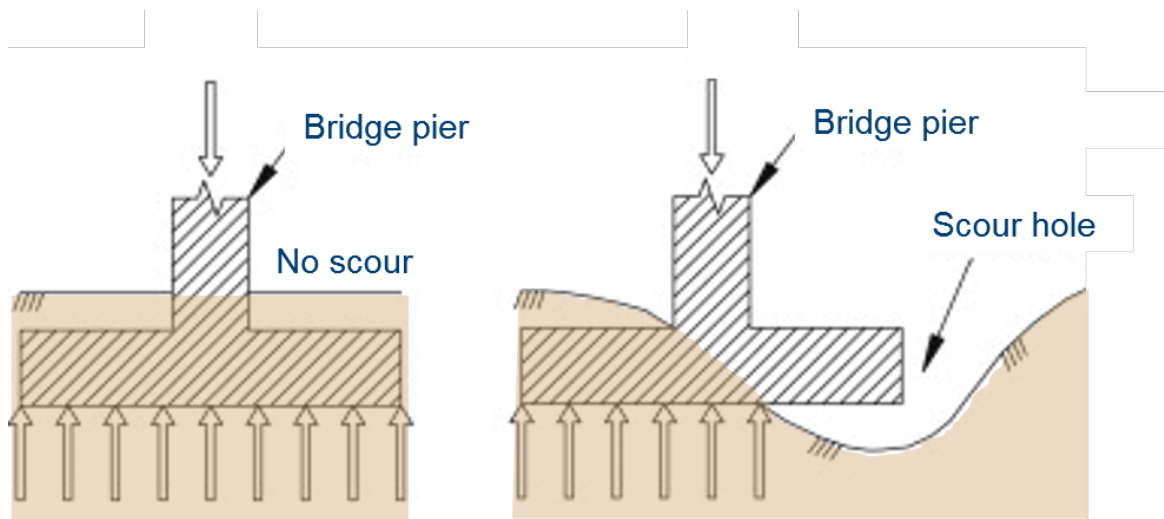


Fig. 7.1 Illustration of how scour might affect a bridge pier.

With regards to bridges that have piers founded within water bodies, such that they are not able to be seen below the water surface, an additional challenge is presented in inspecting foundations to detect scour or other damage. Standard practice is to conduct initial scour assessments at a minimum prescribed time interval (e.g. once every three years for UK rail structures), with those highlighted as being at risk having a special maintenance plan put in place, including inspections after major flood events. The traditional method of conducting such inspections is to send divers to visually assess damage. This procedure has several limitations. Diver inspections cannot be undertaken during flood events or during the recession of the flood (due to flow velocity, turbulence or debris accumulation at a structure) when bridges are especially vulnerable [133]. Diver safety is put at risk when working in hazardous water environments to look under foundations that could collapse on top of them,

and even when a diver or other recording device is sent underwater, it may not be apparent that there is a problem (for example, when loose backfill material hides a scour hole) [134].

Other endeavours in the field of scour monitoring include the development of instrumentation to provide early warning of scour problems. The advantage of fixed equipment over divers is that sensors can provide more frequent readings and thus a more timely warning. Such instruments include single-use devices, pulse or radar devices, buried or driven rod systems, sound-wave devices, fibre-Bragg grating (FBG) devices and electrical conductivity devices, and are described and evaluated in the literature [135–137]. However, traditional scour monitoring instrumentation often requires expensive installation, maintenance and presence of an external power supply, and can also be susceptible to debris damage during flooding. Often, the interpretation of data from these instruments can be time-consuming and difficult [134, 137].

7.3 Using InSAR for monitoring deformations due to scour

Remote sensing through InSAR could overcome many of these issues by providing a remote monitoring system for measuring deformations at the bridge deck, above the water line. InSAR provides a means of complementing visual inspections with more objective data, collected over wide areas, and more frequently than visual inspections (SAR satellite acquisitions are taken in a frequency of days, rather than years). As SAR is an active imaging system, and can be used both day and night and through cloud cover, it provides more frequent readings during flooding periods when bridges over water bodies are more susceptible to failure and inaccessible. The large area footprint of each satellite acquisition means that eventually a number of structures could be tracked per frame, rather than installing individual terrestrial monitoring systems on each bridge location. Employing InSAR remote sensing techniques can provide asset owners with supplementary data which would not otherwise be captured through traditional visual inspections or in the period between inspections, such as millimetre-scale deformations undetectable by eye or the deformation of the ground in the region around the bridge, which may be moving due to unforeseen effects. Studies have shown that InSAR can be applied to monitor anthropogenic effects on infrastructure such as water extraction or mining [138, 139] and unforeseen ground movements affecting bridge piers could also be picked up (e.g. due to ground water level changes or earthquakes).

The potential of InSAR to be used as part of early warning systems to identify precursors to bridge failure has been highlighted by Sousa and Bastos [91] who examined the steady linear deformation of points on a bridge in the years preceding its collapse. The work presented below is based on a new bridge failure case study at Tadcaster (UK), in which

non-linear deformation in a localised area of a masonry arch bridge was observed over a short period of time immediately prior to the partial collapse of the bridge at this section. Observations and insights of localised areas across the transverse section of the relatively small Tadcaster Bridge (only 10m wide) are made possible using higher resolution X-band SAR data in the Tadcaster study (from TerraSAR-X rather than C-band Envisat data used in the previous bridge failure study by Sousa and Bastos [91]). A methodology is presented for the automatic identification through InSAR of uncharacteristic behaviour in the months prior to collapse, which is primarily small millimetre deformation not visible by eye. The application of InSAR data in such a manner provides a means of early warning prior to collapse.

7.4 Study area

On the evening of December 29th, 2015, following a period of severe rainfall and flooding, the upstream section of the fifth pier of Tadcaster Bridge collapsed into the River Wharfe, resulting in a partial collapse and closure of the bridge (Figure 7.2). This closure cut the town in two, resulting in vehicles being required to take a long detour to the next major road bridge and the installation of a temporary footbridge which was installed for the reconstruction period of the collapsed bridge. It also resulted in serious issues concerning utilities, communications and power services (which used bridges as a conduit to cross the river). A gas main was fractured in the collapse, resulting in the evacuation of hundreds of residents.

Tadcaster Bridge is a historic nine-arch masonry bridge over the River Wharfe in Tadcaster, United Kingdom. It is approximately 100m long and 10m wide, carrying a single lane of vehicular traffic in each direction and a pedestrian walkway on each side. The bridge (prior to collapse) comprised two structures of different dates, built side by side to expand the width of the original structure. Documentary evidence [140] suggested it was built from 1698 to 1699 replacing an earlier bridge on the same site that had been swept away by flood. The deck of the 1698 bridge was then raised and its west end widened slightly (probably in 1736 and 1753 respectively), before a second bridge was built alongside it upstream from 1791 to 1792, effectively doubling the width of the river crossing.

Tadcaster Bridge carries a main road so there is a requirement that it undergoes a 'General Inspection' every two years, and a 'Principal Inspection' every six years. Flooding events in recent years prior to the collapse meant that the bridge was inspected by divers to detect movement of the river bed that may have resulted in scour.



Fig. 7.2 Bridge schematic showing location of bridge and extent of collapse. Photo of collapse site taken after flooding receded. Imagery provided courtesy of North Yorkshire County Council and annotated by the author.

The failure of Tadcaster Bridge was captured on video as it collapsed [141]. A pronounced dip in the masonry can be seen immediately prior to the pier below giving way (Figure 7.3).

7.5 Method

7.5.1 Data sets

To analyse the deformation behaviour in the period preceding collapse, 48 TerraSAR-X ‘Stripmap’ mode images (3m by 3m ground resolution) taken prior to the collapse in the 20-month period from 9th March 2014 to 26th November 2015 were analysed (image acquisition list given in Appendix A). The final acquisition in November was the last image available prior to the bridge collapse on 29th December 2015. These image acquisitions were taken at 11-day intervals where possible. LIDAR data produced by the UK Environment Agency was then used in subsequent processing work as a Digital Elevation Model of 2m resolution.

7.5.2 Processing Methods

The Chapters on Waterloo Bridge and Hammersmith Flyover employed Persistent Scatterer Interferometry (PSI) as these studies made use of point targets which were stable and coherent over time. Small Baseline Subset (SBAS) techniques (as described in Chapter 2) provide a methodology which can be employed over areas which have more distributed SAR reflections within a pixel (rather than single dominant reflector source). In contrast to PSI techniques, SBAS techniques impose constraints on the maximum temporal and spatial baselines, and allow the analysis of distributed targets [31, 29]. The basis of the SBAS technique uses pairs of low-pass filtered (multilooked) differential InSAR interferograms. The data pairs involved in the generation of the interferograms are selected in order to minimize the spatial, temporal and Doppler separation (baseline) between the acquisition orbits, thus limiting the decorrelation phenomena.

Both PSI and SBAS techniques were considered for this study to investigate whether a deformation signal in the area of failure could be observed over the bridge prior to its failure. Suitability and application of InSAR stacking techniques to bridges is heavily influenced by the form and geometry of the structure. For example, for larger multi-span cable-stayed or suspension bridges, it can sometimes be to understand where scatterers (where SAR reflections) are coming from. As another example, the metal parapet of concrete bridges can provide good persistent scatterers, but a masonry bridge provides less stable reflectors for PSI techniques in comparison with other bridges studied in the literature. In this example, there was one metal lamp post which would likely act as a reflector, which was blocked from



Fig. 7.3 Stages before scour collapse of Tadcaster Bridge. Top image is of the bridge in the summer before collapse (photograph provided by North Yorkshire County Council). The middle image and bottom image are taken from a video capturing the actual bridge collapse (video source: Press Association [142]).

the line of sight of the satellite by tree foliage. Thus, no persistent scatterers were derived on the bridge from PSI processing. In contrast, the SBAS technique was found to be more appropriate for this case, and 8 different distributed scatterer locations across the bridge have been detected.

7.6 Results

The standard SBAS processing chain [31] was implemented within the SARscape software package [115]. The temporal and geometrical configuration of the TerraSAR-X acquisitions relative to the ‘Super Master Image’ is shown in Figure 7.4. The Super Master Image is the reference acquisition for the processing and the interferogram pairs will be co-registered on this reference geometry. It is usually in the middle of the time period being studied and the perpendicular baselines calculated. For this study, the software selected this image based on creating a maximum number of interferogram pair connections.

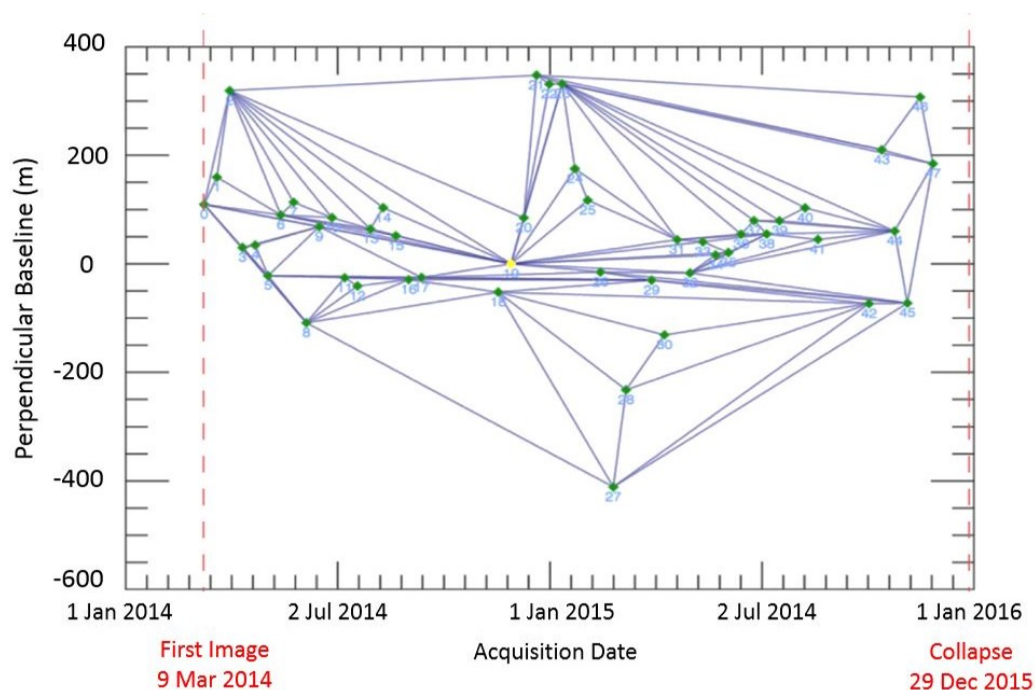


Fig. 7.4 Temporal - perpendicular baseline for the interferometric stack used in this study. Each acquisition is marked by the green points, with the super master image used being identified as the yellow point.

The connection graph (similar to those generated for PSI analysis) is useful to help understand if the network of differential interferograms is well connected (the network should be homogeneous and every acquisition should be connected with others with an high

redundancy). Figure 7.4 is an additional plot to the connection graph generated as part of SBAS processing which is obtained through a Delaunay triangulation. Images were collected over a period of just over 20 months between March 2014 and November 2015. The points represent the acquisitions used in the SBAS analysis, and a connection graph is also used to define pairs of interferograms. The interferometric processing generated 925 interferograms to identify stable distributed scatterers.

7.6.1 Deformation map

The SBAS results in the form of scatterers overlaid onto the mean SAR amplitude image is presented in Figure 7.5. A challenge for end users in the application of InSAR stacking techniques for structural monitoring is the interpretation of what the scatterers physically represent on the asset. Water bodies are often quite easy to identify in SAR amplitude imagery as they feature darker pixels and are incoherent and not picked up by interferometry methods. Conversely, man-made objects with hard (reflective) surfaces are more easily picked up by various InSAR stacking techniques.

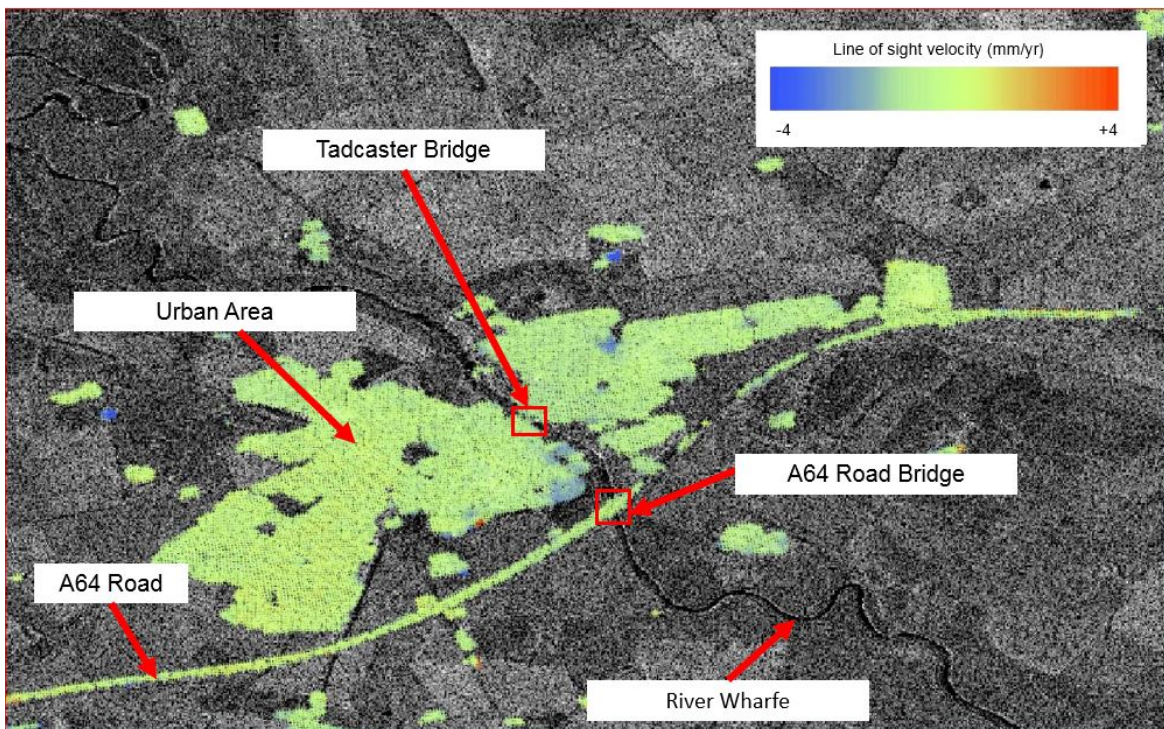


Fig. 7.5 SBAS results over Tadcaster visualised over the mean SAR amplitude image of the site.

In results processed for this study, the scatterers pertaining to bridges are identified as the only points crossing the River Wharfe (seen in the dark pixels on the SAR mean amplitude image, and by the absence of pixels outlining the profile of the river and embankment in the SBAS results). This occurs at two locations in the image in Figure 7.5: once at the geographical location of Tadcaster Bridge, and the other where the A64 motorway is seen to cross the image, including over the river (at the location of a larger road bridge). The section of the SBAS results attributed Tadcaster Bridge has been enlarged and overlaid onto an optical image in bottom right and top right images of Figure 7.6. The overlay of SBAS results onto an optical image can be helpful in interpretation, but it should be remembered that the InSAR results do not correspond directly to features within an optical image.

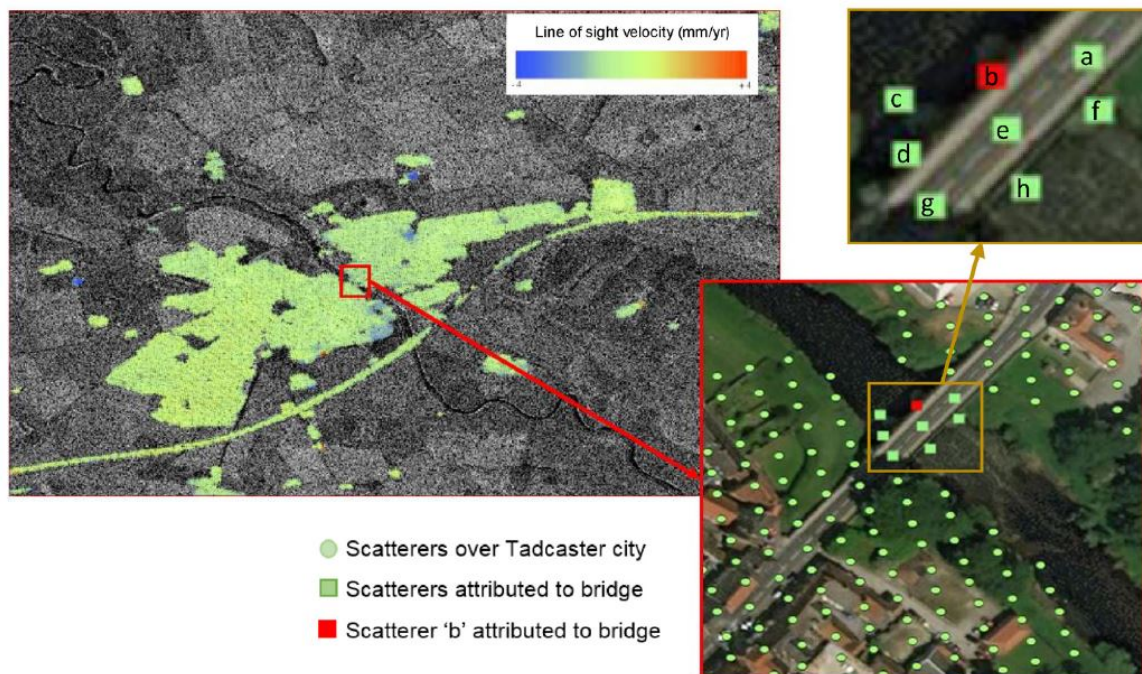


Fig. 7.6 (Top left) SBAS results over Tadcaster visualised over the mean SAR amplitude image of the site; (Top right and bottom right) SBAS results superimposed over optical image of the bridge area, noting points attributed to the bridge for this study.

Deformation maps are commonly plotted as outputs of InSAR analysis to show deformation over time (line of sight displacements as mm per year). This is useful for effects such as the study of deformation in cities after tunnelling or in the steady settlement of structures over time [60, 143, 144], but in the case of bridge movements resulting from scour such with Tadcaster Bridge, this representation is misleading. The scatterers on the bridge using this form of plotting are all marked as “steady” (indicated by a line of sight velocity of close to 0mm/year) with no general trend of rising or falling, due to the assumption that

points on the ground will move in a linear trend over time. Simply viewing the deformation map would suggest that there is little to no movement occurring on the bridge. Depending on the structural form and layout, bridges could oscillate in response to a number of load conditions (such as temperature or vehicular loading) or remain largely steady over years with a sudden change in deformation (say in the case of flooding causing localised scour around a bridge pier). It would be more relevant to consider the plot of the scatterers in terms of their movement over time.

The plot of the eight points attributed to Tadcaster Bridge (top right image of Figure 7.6) are shown in Figure 7.7. The movement detected was the displacement in the line of sight (LOS) of the SAR satellite over time, and was plotted as movement relative to the position of the bridge at the first acquisition, taken on 9th March 2014. The general variation in movement can be attributed to a combination of some real movement of parts of the bridge, and uncertainty within measurement (as previously evaluated in the NPL experiment in Chapter 4). As discussed below in section 7.7.2, broadly speaking, a masonry arch bridge of this kind is expected to remain roughly over time.

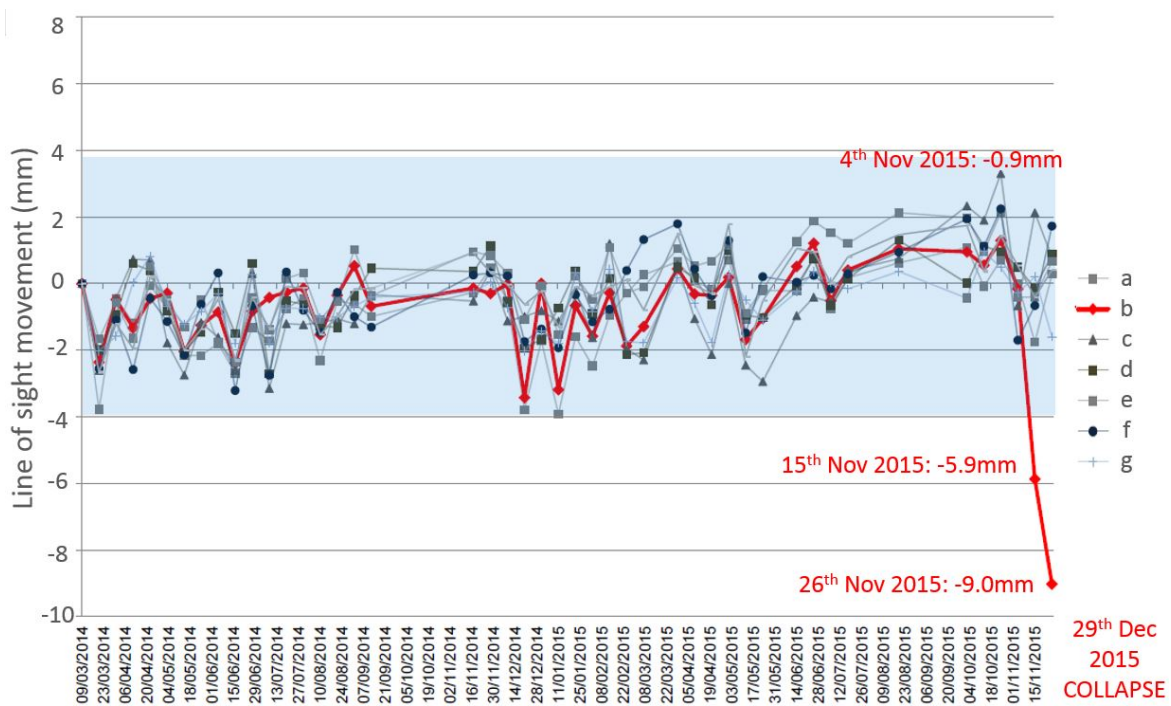


Fig. 7.7 Movement of scatterers attributed to the bridge plotted over time. The collection of 8 points plotted at a specific time on the x-axis corresponds to a SAR image acquired over the site. The y-axis marks movement in the line of sight of the SAR satellite.

7.7 Discussion

The practical application of the results presented in this case study would be to consider how such InSAR monitoring procedures could be developed into a system that would be able to identify unusual behaviour and warn asset owners that precursors to failure are occurring in their asset. The following sections discuss how the results can be interpreted to identify a precursor to scour failure (and the limitations of doing so in practice) before developing an adaptive threshold level to set a potential trigger level and then discussing further developments required for promoting the use of this method and considerations for end users to be aware of.

7.7.1 Precursors to failure

As seen in the graph plotted in Figure 7.7, the scatterers attributed to Tadcaster Bridge generally, apart from some measurement ‘noise’, remained steady within +2mm and -4mm per year for a period of almost two years prior to the collapse. Even after this period, only one region of the bridge (scatterer ‘b’) diverged from this ‘normal’ behaviour at 15th November 2015 and 26th November 2015 and was interpreted as exhibiting unusual behaviour of potential concern. Although it was not possible to discern which exact area of the bridge this scatterer area is coming from, in the cluster of scatterers attributed to the bridge, scatterer ‘b’ was positioned on the upstream side of the bridge deck in the middle region of the length of the bridge (Figure 7.6). This directly correlated with the region of the failed pier, which collapsed only on the upstream side of the bridge (the downstream side remaining intact). The point on 17th July 2015 was marked as anomalous and removed. The interferograms were studied at this point and it was identified that these points could be discounted due to being impacted excessively by atmospheric artefacts.

The final two movement measurements plotted for scatterer ‘b’ on the 15th November 2015 and the 26th November 2015 were considered as outliers to all other measured bridge behaviour. These dates are the final measurements collected prior to the collapse on 29th December 2015. The significance of these results is that movement suggesting a precursor to failure could be seen in the data one month prior to collapse. As the abnormal movements identified are only less than 1cm, they would have been virtually impossible to detect visually in a bridge during any visual inspection undertaken on the same dates.

As previously noted, the final acquisition was taken in the month prior to the collapse, with no further acquisitions available between November 26th 2015 and the collapse on 29th December 2015, where the majority of deformation would have occurred. As such, only a couple of acquisitions identified the localised deformation. The reliability would be

improved if further images during this period were available to confirm the deformation trend. Unfortunately there were no further images available in the archive for this period prior to collapse.

The theory in Chapter 2 highlights the the rate of displacement that can be measured using InSAR is limited due to the 2π ambiguity of the measurement technique. TerraSAR-X has a wavelength of 31mm, which limits the magnitude of maximum observable movement of a scatterer between two observations to 15mm, and the direction of movement becomes difficult to distinguish when movement between two consecutive acquisitions is above 7.5mm ($\lambda/4$). In this example, the movements were less than this value, but an alternative assessment would be required to pick up values that fell outside this range.

In most applications of this technique, deformation detected only on one scatterer would raise questions regarding the reliability of that scatterer. However, the form of bridge failure mechanism must be taken into account. Tadcaster Bridge is a masonry arch which partially collapsed due to scour at the base of the pier. The bridge deformed only very locally at one point-like geographic location which is approximated by one individual scatterer, with the rest of the bridge remaining intact (without deformation). The correlation between the geographical location of the point and the actual failure demonstrated the reliability of that specific measurement point.

The primary advantages of using InSAR for bridge monitoring of scour susceptible structures is that the method can provide a means of collecting movement measurements in regular intervals, especially during periods when it is not possible to send divers or use more traditional inspection means. As bridges are not able to be inspected every few days or weeks, InSAR provides a tool to gain more information about potential risks. This must however, be considered in line with disadvantages and limitations. The size, location and natural reflectivity of the bridge will determine whether InSAR can be used and limit the bridges for which this technique would be suitable. Changes in vegetation, such as trees overgrowing and obscuring line of sight of the satellite will limit the effectiveness of its use. The basis of using InSAR as a tool for scour monitoring relies on the bridge deck itself deforming, inferring pier displacement due to lack of support at the foundations of the piers; it does not identify the presence of a scour hole around the foundations in all cases where there might be one present.

7.7.2 Identification of outliers

To automatically identify outliers for a potential early warning system using SAR data as it is collected and re-processed over time, an approach was required to analyse the processed InSAR time series as it evolved over time. The scatterers in this instance represented a time

series which remained fairly stationary in movement, as is expected for masonry arch bridges with a structure such as Tadcaster Bridge. However, some other bridge types such as large steel and concrete multi-span bridges may have systematic variations that are associated with daily and seasonal temperature change, or other loading effects. Furthermore, for establishing a fully automatic system there are no data points labelled as ‘normal’ or ‘outlier’ available before or during the collection and processing of the SAR data itself. Consequently, the movement behaviour of the bridge must be interpreted specifically for each bridge in an unsupervised and adaptive way.

Figure 7.8 shows a development of Figure 7.7 which incorporates this adaptive threshold. The green lines either side of the plotted movements mark the boundary for outliers (the method for which this outlier threshold is identified is detailed in below). Points outside of the region defined by the green line are considered as unusual bridge behaviour to investigate.

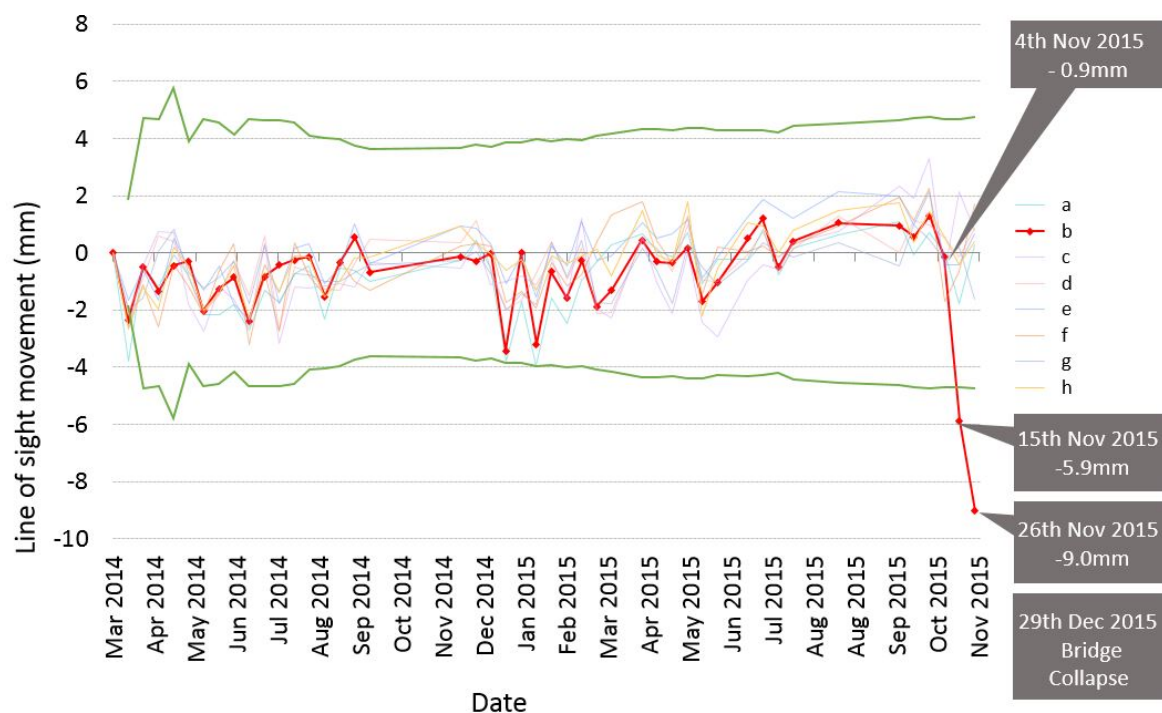


Fig. 7.8 Movement of scatterers attributed to the bridge plotted over time with adaptive threshold. The collection of 8 points (a-h) plotted at a specific time on the x-axis corresponds to a SAR image acquired over the site. The y-axis marks movement in the line of sight of the SAR satellite. The green line marks the boundary for outliers and points outside of this bounded region are flagged as unusual bridge behaviour.

For the detection of outliers a non-parametric method based on the interquartile range has been developed. The interquartile range considers the central 50% of data measurement values (i.e., the values between the first and third quartile) and is related to the median, rather

than mean. Considering 1.5 times the interquartile range either side of the interquartile range would identify outliers, with 3 times the interquartile range identifying “extreme outliers” [145]. At each time interval, the interquartile range based on the current and all previous measurements on the bridge, is calculated in a cumulative way and multiplied by three to produce the threshold for “extreme outliers”.

Consequently, data was classified as outlier/non-outlier based on whether they fall outside this threshold. The level outside which “outliers” lie (considering all values measured up to the date considered) is marked of on Figure 7.8 in green. The final two measurements from scatterer ‘b’ prior to the collapse of the pier lie significantly outside the range of any threshold of ‘normal’ behaviour, and were successfully identified by the outlier detection process. If this was being considered during monitoring, rather than a retrospective analysis of failure, the identification of the point on the 15th November 2015 would flag that further behaviour should be carefully monitored. This, plus the second data point collected on 26th November 2015, would signal that the asset owner should consider an immediate, more detailed inspection, based on the interpretation of the data. Ideally further points would have been tracked in the period between 26th November 2015 and the collapse to monitor the progression of the failure, but unfortunately no further acquisitions were available until after the collapse date for this example.

Data availability looks more promising as time passes, and more frequent acquisitions are becoming available from multiple satellites within the same orbit. The PAZ radar satellite launched in February 2018 in the same constellation as TerraSAR-X, will double the acquisition capacity and halve the revisit time for interferometric applications. More frequent satellite revisit times greatly aids such monitoring applications of critical infrastructure.

A very simple measure to define a range of ‘normal’ behaviour is to consider all points of the processed data set and declaring all instances more than plus or minus three standard deviations from the mean ‘outlier’. Three standard deviations either side of the mean contains 99.7% of data instances in a data set [146]. This approach reveals a threshold of $\pm 3.88\text{mm}$, and marks the two final points of scatterer ‘b’ as outliers.

7.7.3 Application to early warning systems

The identification of precursors to failure would make this method of InSAR measurement technically feasible for use as an early warning system. If movements outside a threshold range of ‘normal’ behaviour could be notified to asset owners, there would be the opportunity to send bridge inspectors to investigate if there was indeed a problem with the bridge and, if so, identify the nature of the defect.

InSAR stacking techniques through various methods, such as PSI, SBAS and others as discussed earlier in this paper, would then be applied to all acquisitions acquired to date. The points that relate to the bridge and its movement would then be tracked over time, using anomaly detection methodologies, such as that presented here, to identify outliers.

Work in combining optical and InSAR satellite imagery for feature extraction including specific consideration of bridges over water bodies [63, 147], as well as research into interpretation of SAR data as specifically applicable to the identification of specific bridge features and behaviours [62, 147], will hopefully enable better identification of bridge structures within SAR data, and provide clearer attribution of scatterers to specific areas of a bridge.

7.7.4 Mapping movement behaviour against environmental data

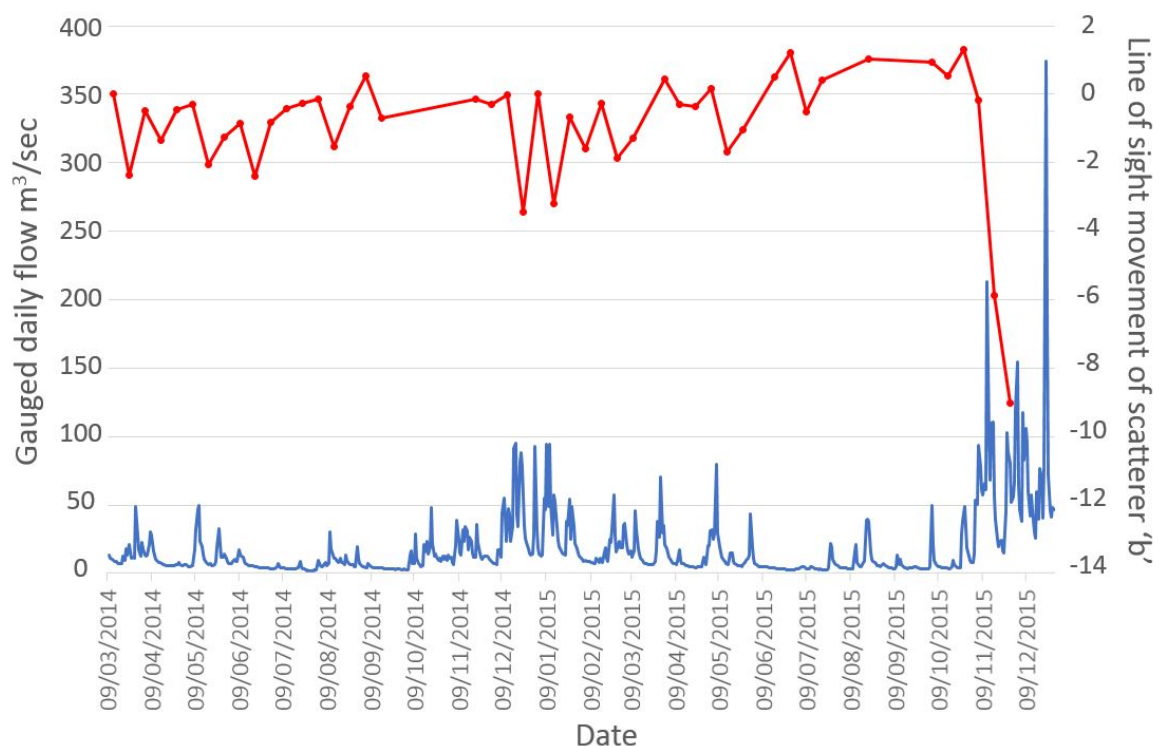


Fig. 7.9 UK National River Flow Archive data plotting the daily flow rate (blue) measured by a flow gauge in the River Wharfe stationed upstream of Tadcaster Bridge plotted in alongside the progression of scatterer 'b' (red) on Tadcaster Bridge over time.

Scour effects around bridge piers is caused by changing river flow, as was visible in case of Tadcaster Bridge. The River Wharfe had been swollen in the months preceding the collapse, with heavy rainfall starting in late October, continuing through November and

December. Data from the UK National River Flow Archive from a site 1.4 km upstream from the bridge (Figure 7.9) shows larger river volumes in the winter of 2015, just prior to the collapse. This river gauging station at Tadcaster recorded a peak flow rate of $547\text{m}^3/\text{s}$ during this winter which was the highest ever recorded flow in the period since records began 25 years previously. The severe conditions of persistent high flow would have accelerated scour behaviour, with final collapse on 29th December 2015 occurring after a large flooding event.

Scour is one of the main causes of bridge failures, but is difficult to monitor or predict. There are, however, several different known precursors to scour failure. These include:

- Debris/blockage between spans
- Change in water profile of water passing through the bridge
- Change in level at bridge deck (signifying pier displacement)
- Pier displacement and change in behaviour (vibration)
- Monitoring for scour holes themselves and identifying loose backfill

InSAR monitoring is not able to look at below surface measures dealing with identifying loose backfill concerns. The remainder of the potential signs can be addressed through different options combining satellite and in-situ measurement. It is worth considering that InSAR technologies provide one perspective on identifying precursors to scour failure. The ability to combine this with a wider sensor network and map environmental changes either on the ground or from other satellite sources (such as optical data which, for example, could potentially be used to identify blockages in the bridge arches) would provide asset owners with more valuable insights than InSAR monitoring on its own.

7.7.5 InSAR processing considerations

The primary conclusion of this Chapter is highlighting the opportunity to use InSAR monitoring to identify a precursor to failure. One limitation of the study conducted is that it was produced by one author given a particular set of data and processing assumptions and parameters. As noted in previous chapters, the quality of the data is impacted with the temporal and spatial baselines of the SAR acquisitions, and having a different stack of images might impact the results. However, further work could be undertaken in taking the same SAR stack of acquisitions and considering the effect of different users processing the same SAR stack to quantify the sensitivity of the results. In principle, this would generate similar output data that would have raised the alarm on 15th of November as show in Figures 7.7 and 7.8

as there is significant variation from the other points monitored, well outside what could be interpreted as noise. If another user were to process the data, the variations that could arise would most like come from the earlier variations in the SBAS processing chain, where the sample is multi-looked to reduced noise. The parameters selected in this stage could impact the number and location of measurement points generated. Furthermore, any thresholds set with regards to allowable noise or coherence could also impact the number and location of measurements points. One further problem would be the end user only applying PSI algorithms and not SBAS algorithms (which did not generate suitable PS points to monitor). As outlined in the chapter on InSAR theory, there are a number of different processing algorithms and parameters that could be applied. If the choices made result in measurement of several points on the bridge, including the area of interest, they may not result in the same points being monitored, but the point over the area that resulted in collapse should result in a large deviation relative to the other points on the bridge which would trigger a warning event.

7.8 Conclusions

The results demonstrate the potential of InSAR X-band data to detect unusual deformations in masonry arch bridge structures. This, together with the development of suitable outlier identification methodologies, provides the potential capability to give early warning of scour failure. To achieve this, InSAR stacking techniques were applied to a stack of 48 X-band SAR images taken over Tadcaster Bridge for a two-year period preceding its partial collapse in December 2015 due to scour failure. Scatterers which could be attributed to the bridge were identified and the movement of these points over time were analysed using outlier detection to identify a region of the bridge that exhibited unusual deformation behaviour. This region matches the region which collapsed one month after this behaviour was identified from the data, and correlates with the flooding period and collapse timeline and mechanism of the bridge due to scour. The prior identification of localised collapse in a bridge structure suggests a promising application in early warning systems, and there would be merit in working to identify further failure case studies and relevant SAR data for study.

The method presented outlines a promising method for detecting precursors to scour failure of bridges, but more case studies and examples should be investigated. One of the key problems with studying failure cases using data is the availability of a suitable quantity of SAR data to enable the processing of a stack over a sufficiently long period prior to collapse. Images must be taken at the same incidence angle and direction, and a minimum number of acquisitions are required for InSAR stacking techniques. In order to track behaviour that deviates from ‘normal’ bridge movement, a sufficient number of data points are needed to

determine what the ‘normal’ behaviour of the bridge is. Although there are many examples of scour failure, there is difficulty in finding a suitable stack of images to process that meets these criteria, and considered acquisition planning must be made for infrastructure at risk.

Chapter 8

InSAR for Bridge Structural Monitoring: Conclusions

The motivation for this research stems from the need to support the field of bridge monitoring, by providing asset owners with insights to inform maintenance and asset management decisions. This is carried out with the broad goal of preventing excessive deterioration and collapse of key transport infrastructure. Interferometric Synthetic Aperture Radar (InSAR) monitoring is a rapidly growing field that provides the opportunity to assist asset owners in the monitoring of bridges that are difficult to access and not inspected as frequently as would otherwise be desired. Rather than focusing on on-site monitoring of a single asset, InSAR can provide a means of global remote monitoring with each satellite image covering large geographical regions. This means that multiple structures, as well as the region surrounding the bridge asset, can be monitored by InSAR with displacement measurement readings at regular intervals.

Standard bridge inspection processes can be supported through the provision of measured displacement of points on a bridge during the periods between scheduled visual inspections. Based on review of current structural health monitoring practices, the research was designed to go beyond understanding whether satellite SAR sensors could be deployed for bridge monitoring. Instead, it was designed to better determine how InSAR sits within existing monitoring technologies and practices, and how to provide demonstrable value to asset owners. With this in mind, the research objectives were developed to address the following questions:

- 1. Can InSAR satellite measurement technology provide remote measurement at the necessary level of accuracy, reliability and resolution such that it is able to replace or complement traditional forms of physical measurement and monitoring of bridge assets?*
- 2. Can InSAR satellite measurement technology be used to identify signs or precursors of failure in bridge assets?*

Within the current literature there exists a number of validation studies that show that InSAR measurements can measure displacement to millimetre and sub-millimetre scale. However, there are also many studies which highlight that within applied contexts, rather than carefully controlled experiments, the accuracy is less precise but still within millimetre scale precision. This measurement precision depends on a number of variables such as location, number of acquisitions, atmospheric effects, chosen parameters and processing algorithms, etc. The experiment conducted at NPL verified that the measurement uncertainty within the data processed for the bridge case studies considered in this research could be considered as $\pm 2\text{mm}$, with up to 0.7mm of measurement uncertainty when considering a vertical component of the measured displacement. This experiment additionally served to verify that corner reflectors, of a smaller scale than those used in tests in the literature, were suitable for the experiment on Waterloo Bridge.

The validation of suitable accuracy and reliability of measurement set the scene for conducting measurements on live bridge test sites. The experiment to study Waterloo Bridge demonstrated the limitations of using one-dimensional line of sight measurements. Despite a number of methods presented in the literature on using different viewing geometries to work out horizontal and vertical components of the line of sight displacement measurement, the practicalities of viewing geometry mean that multiple viewing directions may not "see" the same point, and therefore do not facilitate use of such methods. Employing structural engineering knowledge, some assumptions were made to consider displacements in particular directions as negligible and work out a component of the line of sight measurement in the longitudinal direction of the bridge (the direction of interest).

Using the measurements derived from these assumptions, the profile of longitudinal displacement over time followed the same trend as that measured using conventional displacement sensors. Current SAR satellites take repeat acquisitions over a particular location in a time frequency of days, meaning that these measurements can be used to monitor long term behaviour, such as seasonal temperature changes observed in Waterloo Bridge, but nothing close to the frequency of conventional measurements from sensors and total stations (which would pick up the change in temperature over a day). Furthermore, effects such as tidal loading seen on bridges such as Waterloo are not picked up due to their repeat loading

cycle occurring multiple times between SAR acquisitions. The measurements produced by InSAR did not precisely match the readings taken by the automated total stations (ATS), and multidimensional analysis was used to map the difference between the two sets of readings. This revealed that the difference in InSAR and ATS readings from the point of view of overall three-dimensional bridge motion could be considered small. The difference in readings (mapping SAR displacements to ATS) was not a systematic or simple offset, but instead mapped from one to another using a complex polynomial function. This is attributed to the non-linearity of SAR measurements, and the various non-linear adjustments made and parameters used during the InSAR processing.

The limited frequency of satellite readings and satellite viewing geometry means that it is not a technique that could replace traditional monitoring methods, but can be used more for tracking seasonal trends, and there is an opportunity to complement traditional inspection regimes with additional information, such as monitoring any deformation of the ground region surrounding the bridge. It can also be used together with other measurement forms to provide additional insights, as shown by combining InSAR measurements with automated total station readings to determine the movement of the total station itself. However, in viewing this in practice within the perspective of ‘value for the asset owner’, it would not be worth the financial cost or effort required to install corner reflectors and purchase commercial-grade SAR imagery to work out whether the total station was in a location that was moving.

From having controlled points of measurement on the Waterloo Bridge, the Hammersmith Flyover provided an example of a bridge without retrofits, making use of natural SAR reflections for InSAR monitoring. This study revealed several further challenges to overcome for the practical and operational deployment of InSAR monitoring of bridges. The Hammersmith Flyover study included considerations of SAR viewing geometry and limitations on what the SAR satellite is and is not “able to see”. It is not immediately clear what components of the bridge that the reflections are coming from, and as detailed in the current literature, the three-dimensional location positioning of SAR persistent scatterers is not particularly accurate (at best in the 10s of centimetres [68]). This research proposed new methods of using existing civil engineering modelling tools, together with InSAR processed results, to narrow down the relevant persistent scatterer points. This selection of points initially was based on bridge geometry, and then further narrowed by making use of structure knowledge related to the bridge behaviour (derived using finite element structural models and bridge engineering knowledge) to filter for points which had movement over time that matched the desired profile.

The experiments on Waterloo Bridge and Hammersmith Flyover highlighted a number of practical considerations when working with InSAR data, and it is worth reflecting on the nature of InSAR monitoring in comparison with the approach of a bridge engineer using structural monitoring solutions to address a concern. Each bridge has its own structure, material, orientation, articulation and required functionality (e.g. expansion due to temperature). Once a problem has been identified, the perspective of the bridge engineer or asset owner tends to be focused on a local basis, addressing a specific concern. As previously outlined in the literature, large-scale SHM schemes looking for data-driven insights rather than addressing a call to a specific concern are not always perceived as value for asset owners [40]. Engineering monitoring solutions are usually developed in direct response to visible or suspected problems, procuring instrumentation and monitoring to a specified technical specification as defined in the terms of reference of the specific asset (such as longitudinal, transverse and vertical displacement of a bridge deck).

InSAR monitoring, on the other hand, is dependent on the local circumstances, such as the bridge orientation relative to the satellite orbit path, the bridge position and environmental surroundings, and the expected magnitude and direction of displacement. It also works on a more ‘opportunistic’ basis. The parts of the bridge or area of study are not selected, but rather are based on surfaces that reflect well (which depends on material, geometry, etc.). As in the case of the NPL and Waterloo experiments, specific known points that reflect the SAR signal can be created using corner reflectors, providing an option of retrofitting existing bridges to monitor key points of interest. However, this is limited to certain scenarios where the signal-to-clutter ratio around the corner reflector is sufficiently low as to be able to clearly identify the corner reflector’s response above other reflections. Furthermore, the reflectors would have to be spaced sufficiently far so as not to overlap with other reflectors within the same pixel (or group of pixels in multi-looked results).

Having determined that InSAR is of sufficient measurement scale, accuracy and precision for bridge engineering contexts, the second research question was targeted at finding specific examples and contexts for which InSAR monitoring could be applied to spot signs of problems, or precursors to failure. One example was highlighted in the Hammersmith Flyover study, where a method was developed to identify InSAR persistent scatterers on the bridge that showed oscillations of movement with seasonal temperature changes, and could potentially be used to spot signs of bearing or other bridge articulation problems. The study on Tadcaster Bridge highlighted a distinct movement in the region of the Tadcaster Bridge prior to the actual event of collapse. This precursor to failure, observed in the data over a month before the actual collapse, suggests the possible use of InSAR as a means of an early warning system in structural health monitoring of bridges at risk of scour. A method for

creating a warning system using an adaptive threshold was then developed. However, it is worth noting again that the bridge material and geometry limit the list of bridges suitable for using such measures. Furthermore, the study should be extended to other test cases to confirm the results through repeat studies. In this case the movement was able to be measured as it was slow moving over time, and primarily in a vertical direction (rather than a horizontal displacement in a north-south direction that the satellite would be unable to pick up).

This topic of measurement limitation is a key drawback to InSAR measurement that should be clearly outlined to any bridge engineer considering this measurement method. As outlined in the theory, the limit of π on the differential phases corresponds to a maximum differential deformation of $\lambda/4$ over two consecutive SAR acquisitions (where λ is the SAR wavelength). This therefore limits the size of measurement that can be measured without ambiguity.

The interpretation of SAR images (taken in radar geometry), the choice of processing parameters and algorithms for InSAR processing, as well as the interpretation of line of sight (LOS) displacement measurements require a substantial level of specialist knowledge. Further to this, the availability, accessibility, resolution, frequency and viewing geometries of different satellite sources and product specifications can create a barrier between the earth observation and civil engineering communities in understanding the potential opportunities and limitations. To gain the most benefit from such measurement techniques, it is important for civil engineering end users to properly understand the limitations and subtleties of this form of measurement. They should also consider some of the additional benefits not traditionally monitored at present. The bridge design process involves a number of assumptions: the loads to be applied onto the bridge or to which structure will be subjected through environmental conditions must be estimated, material strengths must be estimated, and design criteria must be selected. These assumptions are rarely verified upon completion (though factors of safety in the design account for this uncertainty). Furthermore, it should be considered that impact of changing environmental conditions due to climate change and anthropogenic effects (for example, dewatering in construction or mining) can cause unforeseen loading conditions and these effects themselves can sometimes be picked up through InSAR monitoring.

The space sector is advancing, with more SAR satellites planned for launch in coming years. It is expected that the number of satellites within a given orbit will increase, and that the frequency of readings over time will increase. These expectations, together with different angles and viewing geometries, bring improved potential for the use of satellites in bridge monitoring. As more and more SAR satellites and datasets become available, there is a need to develop advanced methodologies and products with algorithms developed and

tuned towards the application of bridge monitoring. As discussed in the literature, there are a number of different PSI, SBAS and combination processing algorithms, many of which have assumed components such as thermal estimation and assumed deformation models. Future work could include adapting such algorithms to better suit bridge movement patterns and behaviours.

One other consideration is that this research was conducted with the understanding of what bridge behaviours and failures were expected. A different set of results would be achieved if the problem was unknown, and data was simply processed without this expectation, as different parameters and assumptions might have been selected. This bias in parameter selection should be considered, but it could also be said that making use of bridge engineering knowledge could help filter data to find the most relevant behaviours. Future work in bridge monitoring should consider the type of displacements a bridge undergoes, and possible failure mechanisms and understanding how the processing assumptions, and therefore end output, would reflect each of these scenarios. This may in turn require the same set of data to be processed in different ways.

Further work considering the sparsity of available data measurements is needed, which could consider advanced signal processing methods to extract relevant structural monitoring information from multiple features and data sources (for example, combining different SAR resolutions or incorporating optical imagery information). To develop automated bridge monitoring solutions or employ machine learning methods to analyse the data, it is important to guarantee physical interpretability of the data. The approach will need to be multidisciplinary – no one single data source or one single discipline of engineering will be able to undertake this task.

Taking the above considerations into account, a short summary of 'best practice' for use of InSAR in bridge monitoring could be presented as follows:

1. Understanding whether InSAR is suitable and what the imaging or measurement requirements are.
 - Consider whether the bridge of interest reflect SAR such that measurement points will be available at points of interest (and if not can/should corner reflectors be installed to augment the reflection response) - this could be done with radar simulations to better understand SAR viewing geometry.
 - Understand what kind of bridge movements are expected, including direction and maximum movements - what can the satellite realistically capture given its wavelength, spatial resolution and pixel size).

- Understand what other in-situ datasets are available - whether the SAR data be used to augment an existing sensor network and whether there is data to tie the relative SAR movements into real world grids (e.g. GNSS measurements).
 - Understand the number and resolution of images required (and which constellation(s) of satellites would achieve that, along with an understanding of how to weigh the benefits and limitations, e.g. better controlled orbits or shorter revisit periods); these can be tasked as new acquisitions, taken from the archive or a combination of both.
2. Processing of SAR data should be undertaken by an InSAR processing specialist. The equivalent analogy of SAR processing in a civil engineering context would be to consider creating structural Finite Element Models (FEM) to understand bridge behaviour. Despite a number of simple to use software packages being developed in recent years, there is a risk in allowing users to plug in parameters without understanding impact; similar to someone creating a bridge model without understanding structural behaviour and the assumptions built within FEM packages.
 3. Understanding SAR viewing geometry, line-of-sight measurements, etc. to understand what is being measured (along with the nuances in signal processing that mean that the location of the persistent scatterer "point" may not be where it appears to be projected on a map).
 4. Understanding the precision and uncertainty of the measurements taken, especially when trying to convert line-of-sight measurements into directions and coordinate frames as desired by bridge engineers (e.g. converting to longitudinal displacement in a bridge has limitations, adds measurement uncertainty and has less accuracy in directions along the path of the satellite orbit).
 5. Application of InSAR to bridge and civil engineering applications more generally should be a multidisciplinary endeavour. Civil engineers and InSAR specialists should not work in silos. The best use of such tools going forward would be for InSAR specialists to work with educated and informed civil engineering end users, to apply the current state-of-the-art and develop new methods and automated tools for asset owners (ideally leveraging advancements in digital engineering and bridge engineering to inform the InSAR processing).

For successful implementation of InSAR in the monitoring of bridges, it is important to understand the limitations and opportunities of InSAR. The use of InSAR for bridge

monitoring could potentially be improved as SAR data and processing specifications (resolution, frequency, processing assumptions) improve. At the current stage of technological development, it should be considered as a tool for specific bridges and failure mechanisms rather than a full bridge monitoring solution. In summary, InSAR monitoring does have the scale and precision of measurements to support bridge monitoring activities, but only for specific bridge cases, and for monitoring particular types of bridge deformation and behaviour.

References

- [1] RAC Foundation, “Bridge maintenance backlog grows,” tech. rep., RAC Foundation, London, UK, 2019.
- [2] American Society Of Civil Engineers (ASCE), “Bridge Infrastructure | Structurally Deficient Bridges | ASCE’s 2017 Infrastructure Report Card,” 2017.
- [3] M. Moore, B. Phares, B. Graybeal, R. Dennis, and G. Washer, “Reliability of Visual Inspection for Highway Bridges , Volume I : Final Report,” Tech. Rep. FHWA-RD-01-020, U.S. Department of Transport, McLean, VA, 2001.
- [4] F. Lea and C. R. Middleton, “Reliability of Visual Inspection for Highway Bridges,” Tech. Rep. CUED/D-STRUCT/TR. 201, Department of Engineering, University of Cambridge, Cambridge, 2002.
- [5] W. G. The Highways Agency, Transport Scotland and T. D. for Regional Development Northern Ireland, “Inspection of Highway Structures,” tech. rep., The Highways Agency, Transport Scotland, Welsh Government and The Department for Regional Development Northern Ireland, 2007.
- [6] S. McRobbie, M. Wright, and A. Chan, “Can technology improve routine visual bridge inspections ?,” *Proceedings of the ICE - Bridge Engineering*, vol. 168, no. BE3, pp. 197–207, 2015.
- [7] J. Bennetts, P. Vardanega, C. Taylor, and S. Denton, “Bridge data - What do we collect and how do we use it?,” in *Proceedings of the International Conference on Smart Infrastructure and Construction*, (Cambridge, UK), pp. 531–536, ICE Publishing, 2016.
- [8] R. Bamler and P. Hartl, “Synthetic aperture radar interferometry,” *Inverse Problems*, vol. 14, no. 4, pp. 1–54, 1998.
- [9] A. Ferretti, C. Prati, and F. Rocca, “Permanent Scatters in SAR Interferometry,” *IEEE Transactions on Geoscience and Remote Sensing*, vol. 39, no. 1, pp. 8–20, 2001.
- [10] C. R. Middleton, D. Ph, C. Eng, P. J. Vardanega, D. Ph, M. Asce, G. T. Webb, D. Ph, and P. R. A. Fiddler, “SMART Infrastructure - Are We Delivering on the Promise?,” in *6th Australian Small Bridges Conference*, (Sydney, Australia), 2014.
- [11] L. Cohen, *Research Methods in Education*. London, UK: Routledge, 5th ed., 2002.
- [12] T. C. Powell, “Competitive advantage: Logical and philosophical considerations,” *Strategic Management Journal*, vol. 22, no. 9, pp. 875–888, 2001.

- [13] R. K. Yin, *Case study research: Design and methods*. Los Angeles, CA: Sage, 5th ed., 2014.
- [14] X. Zhou, N. B. Chang, and S. Li, "Applications of SAR interferometry in earth and environmental science research," *Sensors*, vol. 9, no. 3, pp. 1876–1912, 2009.
- [15] R. Bamler and B. Schättler, "SAR data aquisition and image formation," in *SAR geocoding: data and systems* (G. Schreier, ed.), pp. 53–102, Karlsruhe, Germany: Wichmann, 1993.
- [16] I. Cumming and F. Wong, *Digital Processing of Synthetic Aperture Radar Data: Algorithms and Implementation*. Norwood, United States: Artech House Publishers, 2005.
- [17] R. F. Hanssen, *Radar Interferometry: Data Interpretation and Error Analysis*. Springer Netherlands, 1st ed., 2001.
- [18] A. Ferretti, A. Monti-Guarnieri, and C. Prati, "InSAR Principles-Guidelines for SAR Interferometry Processing and Interpretation (TM-19)," *ESA*, no. February, p. 48, 2007.
- [19] A. Ferretti, A. Monti-Guarnieri, and C. Prati, "InSAR Principles: Guidelines for SAR Interferometry Processing and Interpretation (TM-19), Part C," *ESA*, 2007.
- [20] A. Ferretti, A. Monti-guarnieri, C. Prati, and F. Rocca, "InSAR Principles: Guidelines for SAR Interferometry Processing and Interpretation (TM-19), Part B," *ESA*, p. 71, 2007.
- [21] A. Moreira, P. Prats-Iraola, M. Younis, G. Krieger, I. Hajnsek, and K. P. Papathanassiou, "A Tutorial on Synthetic Aperture Radar," *IEEE Geoscience and Remote Sensing Magazine*, pp. 6–43, 2013.
- [22] S. Huang and D. Liu, "Some uncertain factor analysis and improvement in spaceborne synthetic aperture radar imaging," *Signal Processing*, vol. 87, p. 3202–3217, 2007.
- [23] M. R. de Leeuw and L. M. T. de Carvalho, "Performance evaluation of several adaptive speckle filters for SAR imaging," in *Anais XV Simpósio Brasileiro de Sensoriamento Remoto - SBSR*, pp. 7299–7305, 2009.
- [24] A. Ferretti, C. Prati, and F. Rocca, "Nonlinear subsidence rate estimation using permanent scatterers in differential SAR interferometry," *IEEE Transactions on Geoscience and Remote Sensing*, vol. 38, no. 5, pp. 2202–2212, 2000.
- [25] P. A. Rosen, S. Hensley, I. R. Joughin, F. K. Li, S. N. Madsen, E. Rodríguez, and R. M. Goldstein, "Synthetic Aperture Radar Interferometry," *Proceedings of the IEEE*, vol. 88, no. 3, pp. 334–382, 2000.
- [26] A. K. Gabriel, R. M. Goldstein, and H. A. Zebker, "Mapping small elevation changes over large areas - Differential radar interferometry," *Journal of Geophysical Research*, vol. 94, no. B7, pp. 9183–9191, 1989.

- [27] M. Crosetto, O. Monserrat, M. Cuevas-González, N. Devanthery, and B. Crippa, "Persistent Scatterer Interferometry: A review," *ISPRS Journal of Photogrammetry and Remote Sensing*, vol. 115, pp. 78–89, 2016.
- [28] F. Bovenga, A. Belmonte, A. Refice, G. Pasquariello, R. Nutricato, D. O. Nitti, and M. T. Chiaradia, "Performance analysis of satellite missions for multi-temporal SAR interferometry," *Sensors (Switzerland)*, vol. 18, no. 5, pp. 1–16, 2018.
- [29] A. Hooper, H. Zebker, P. Segall, and B. Kampes, "A new method for measuring deformation on volcanoes and other natural terrains using InSAR persistent scatterers," *Geophysical Research Letters*, vol. 31, no. 23, pp. 1–5, 2004.
- [30] A. Ferretti, G. Savio, R. Barzaghi, A. Borghi, S. Musazzi, F. Novali, C. Prati, and F. Rocca, "Submillimeter accuracy of InSAR time series: Experimental validation," *IEEE Transactions on Geoscience and Remote Sensing*, vol. 45, no. 5, pp. 1142–1153, 2007.
- [31] P. Berardino, G. Fornaro, R. Lanari, and E. Sansosti, "A new algorithm for surface deformation monitoring based on small baseline differential SAR interferograms," *IEEE Transactions on Geoscience and Remote Sensing*, vol. 40, pp. 2375–2383, 11 2002.
- [32] E. Rodriguez and J. Martin, "Theory and design of interferometric synthetic aperture radars," *IEEE Proceedings of Radar and Signal Processing*, vol. 139, no. 2, pp. 147–159, 1992.
- [33] M. Simons and P. A. Rosen, "Interferometric Synthetic Aperture Radar Geodesy," *Treatise on Geophysics*, vol. 3, pp. 391–446, 2007.
- [34] R. Scheiber and A. Moreira, "Coregistration of interferometric SAR images using spectral diversity," *IEEE Transactions on Geoscience and Remote Sensing*, vol. 38, no. 5, pp. 2179–2191, 2000.
- [35] A. K. Gabriel and R. M. Goldstein, "Crossed orbit interferometry: theory and experimental results from SIR-B," *International Journal of Remote Sensing*, vol. 9, no. 5, pp. 857–872, 1988.
- [36] Z. Li and J. Bethel, "Image coregistration in SAR interferometry," in *Proc. Int. Arch. Photogramm., Remote Sens. Spatial Inf. . . .*, vol. XXXVII, (Beijing), pp. 433–438, ISPRS, 2008.
- [37] M. Schwäbisch, "Fast and efficient technique for SAR interferogram geocoding," in *International Geoscience and Remote Sensing Symposium (IGARSS)*, vol. 2, (Seattle, WA, USA), pp. 1100–1102, IEEE, 1998.
- [38] K. Bowers, V. Buscher, R. Dentten, M. Edwards, J. England, M. Enzer, A. K. Parlikad, and J. Schooling, "Smart Infrastructure: Getting more from strategic assets," tech. rep., Centre for Smart Infrastructure and Construction, Cambridge, UK, 2018.
- [39] I. F. C. Smith, "Grand Challenges of Structural Sensing," *Frontiers in Built Environment*, vol. 1, pp. 1–3, 2015.

- [40] G. T. Webb, P. J. Vardanega, and C. R. Middleton, "Categories of SHM Deployments: Technologies and Capabilities," *Journal of bridge engineering (ASCE)*, vol. 20, no. 11, pp. 1–15, 2015.
- [41] K. Wong, "Design of a structural health monitoring system for long-span bridges," *Structure and Infrastructure Engineering*, vol. 3, no. 2, pp. 169–185, 2007.
- [42] D. Massonnet, K. Feigl, M. Rossi, and F. Adragna, "Radar interferometric mapping of deformation in the year after the Landers earthquake," *Nature*, vol. 369, no. 6477, pp. 227–230, 1994.
- [43] H. A. Zebker, P. A. Rosen, R. M. Goldstein, A. Gabriel, and C. L. Werner, "On the derivation of coseismic displacement fields using differential radar interferometry: The Landers earthquake," in *Journal of Geophysical Research*, vol. 99, pp. 19617–19634, 1994.
- [44] A. Tronin, "Remote sensing and earthquakes: A review," *Physics and Chemistry of the Earth, Parts A/B/C*, vol. 31, no. 4, pp. 138–142, 2006.
- [45] R. Bürgmann, P. Segall, M. Lisowski, and J. Svarc, "Postseismic strain following the 1989 Loma Prieta earthquake from GPS and leveling measurements," *Journal of Geophysical Research: Solid Earth*, vol. 102, no. B3, pp. 4933–4955, 1997.
- [46] H. A. Zebker, F. Amelung, and S. Jonsson, "Remote sensing of volcano surface and internal processes using radar interferometry," *Remote Sensing of Active Volcanism*, vol. 116, pp. 179–205, 2000.
- [47] B. Osmanoglu, T. H. Dixon, S. Wdowinski, E. Cabral-Cano, and Y. Jiang, "Mexico City subsidence observed with persistent scatterer InSAR," *International Journal of Applied Earth Observation and Geoinformation*, vol. 13, no. 1, pp. 1–12, 2011.
- [48] D. L. Galloway, K. W. Hudnut, S. E. Ingebritsen, S. P. Phillips, G. Peltzer, F. Rogez, and P. A. Rosen, "Detection of aquifer system compaction and land subsidence using interferometric synthetic aperture radar, Antelope Valley, Mojave Desert, California," *Water Resources Research*, vol. 34, no. 10, pp. 2573–2585, 1998.
- [49] Z. Perski, R. Hanssen, A. Wojcik, and T. Wojciechowski, "InSAR analyses of terrain deformation near the Wieliczka Salt Mine, Poland," *Engineering Geology*, vol. 106, no. 1, pp. 58–67, 2009.
- [50] J. Rutqvist, D. W. Vasco, and L. Myer, "Coupled reservoir-geomechanical analysis of CO₂ injection and ground deformations at In Salah, Algeria," *International Journal of Greenhouse Gas Control*, vol. 4, no. 2, pp. 225–230, 2010.
- [51] T. R. Lauknes, J. Dehls, Y. Larsen, K. A. Høgda, and D. J. Weydahl, "A comparison of SBAS and PS ERS InSAR for subsidence monitoring in Oslo, Norway," in *European Space Agency, (Special Publication) Fringe 2005*, (Frascati, Italy), European Space Agency, 2006.
- [52] J. R. Elliott, R. J. Walters, and T. J. Wright, "The role of space-based observation in understanding and responding to active tectonics and earthquakes," *Nature Communications*, vol. 7, 2016.

- [53] M. Crosetto, O. Monserrat, R. Iglesias, and B. Crippa, “Persistent Scatterer Interferometry: Potential, Limits and Initial C-and X-band comparison,” *Photogrammetric Engineering and Remote Sensing*, vol. 76, no. 9, pp. 1061–1069, 2010.
- [54] E. Sansosti, P. Berardino, M. Bonano, F. Calò, R. Castaldo, F. Casu, M. Manunta, M. Manzo, A. Pepe, S. Pepe, G. Solaro, P. Tizzani, G. Zeni, and R. Lanari, “How second generation SAR systems are impacting the analysis of ground deformation,” *International Journal of Applied Earth Observation and Geoinformation*, vol. 28, pp. 1–11, 2014.
- [55] L. Chang, R. P. Dollevoet, and R. F. Hanssen, “Nationwide Railway Monitoring Using Satellite SAR Interferometry,” *IEEE Journal of Selected Topics in Applied Earth Observations and Remote Sensing*, vol. 10, no. 2, pp. 596–604, 2017.
- [56] D. Tarchi, H. Rudolf, G. Luzi, L. Chiarantini, P. Coppo, and A. J. Sieber, “SAR Interferometry for Structural Changes Detection: a Demonstration Test on a Dam,” in *International Geoscience and Remote Sensing Symposium. (IGARSS)*, (Hamburg, Germany), pp. 1522–1524, IEEE, 1999.
- [57] P. Milillo, D. Perissin, J. T. Salzer, P. Lundgren, G. Lacava, G. Milillo, and C. Serio, “Monitoring dam structural health from space: Insights from novel InSAR techniques and multi-parametric modeling applied to the Pertusillo dam Basilicata, Italy,” *International Journal of Applied Earth Observation and Geoinformation*, vol. 52, pp. 221–229, 2016.
- [58] J. J. Sousa, I. Hlaváčová, M. Bakoň, M. Lazecký, G. Patrício, P. Guimarães, A. M. Ruiz, L. Bastos, A. Sousa, and R. Bento, “Potential of Multi-temporal InSAR Techniques for Bridges and Dams Monitoring,” *Procedia Technology*, vol. 16, pp. 834–841, 2014.
- [59] G. Barla, A. Tamburini, S. Del Conte, and C. Giannico, “InSAR monitoring of tunnel induced ground movements,” *Geomechanik und Tunnelbau*, vol. 9, no. 1, pp. 15–22, 2016.
- [60] D. Perissin, Z. Wang, and H. Lin, “Shanghai subway tunnels and highways monitoring through Cosmo-SkyMed Persistent Scatterers,” *ISPRS Journal of Photogrammetry and Remote Sensing*, vol. 73, pp. 58–67, 2012.
- [61] P. Milillo, R. Bürgmann, P. Lundgren, J. Salzer, D. Perissin, E. Fielding, F. Biondi, and G. Milillo, “Space geodetic monitoring of engineered structures: The ongoing destabilization of the Mosul dam, Iraq,” *Scientific Reports*, vol. 6, pp. 1–7, 2016.
- [62] X. Qin, M. Liao, M. Yang, and L. Zhang, “Monitoring structure health of urban bridges with advanced multi-temporal InSAR analysis,” *Annals of GIS*, vol. 23, no. 4, pp. 293–302, 2017.
- [63] U. Soergel, H. Gross, A. Thiele, and U. Thoennessen, “Extraction of bridges over water in high-resolution InSAR data,” *Photogrammetric Computer Vision*, vol. 36, 2006.

- [64] U. Soergel, E. Cadario, A. Thiele, and U. Thoennessen, "Feature extraction and visualization of bridges over water from high-resolution InSAR data and one orthophoto," *IEEE Journal of Selected Topics in Applied Earth Observations and Remote Sensing*, vol. 1, no. 2, pp. 147–153, 2008.
- [65] M. Eineder, C. Minet, P. Steigenberger, X. Cong, and T. Fritz, "Imaging geodesy - Toward centimeter-level ranging accuracy with TerraSAR-X," *IEEE Transactions on Geoscience and Remote Sensing*, vol. 49, no. 2, pp. 661–671, 2011.
- [66] P. Dheenathayalan and R. F. Hanssen, "Radar Target Type Classification and Validation," in *International Geoscience and Remote Sensing Symposium (IGARSS)*, (Melbourne, Australia), pp. 923–926, IEEE, 2013.
- [67] P. Dheenathayalan, D. Small, A. Schubert, and R. F. Hanssen, "High precision positioning of radar scatterers," *Journal of Geodesy*, vol. 90, no. 5, pp. 403–422, 2016.
- [68] P. Dheenathayalan, D. Small, and R. F. Hanssen, "3-D Positioning and target association for medium-resolution SAR sensors," *IEEE Transactions on Geoscience and Remote Sensing*, vol. 56, no. 11, pp. 6841–6853, 2018.
- [69] X. X. Zhu, S. Member, S. Montazeri, C. Gisinger, R. F. Hanssen, and R. Bamler, "Geodetic SAR Tomography," *IEEE Transactions on Geoscience and Remote Sensing*, vol. 54, no. 1, pp. 1–18, 2015.
- [70] C. Gisinger, U. Balss, R. Pail, X. X. Zhu, S. Montazeri, S. Gernhardt, and M. Eineder, "Precise three-dimensional stereo localization of corner reflectors and persistent scatterers with TerraSAR-X," *IEEE Transactions on Geoscience and Remote Sensing*, vol. 53, no. 4, pp. 1782–1802, 2015.
- [71] S. Auer, S. Gernhardt, S. Hinz, N. Adam, and R. Bamler, "Simulation of Radar Reflection at Man-Made Objects and its Benefits for Persistent Scatterer Interferometry," in *European Conference on Synthetic Aperture Radar (EUSAR)*, (Friedrichshafen, Germany), pp. 1–4, 2008.
- [72] P. Marinkovic, G. Ketelaar, F. Van Leijen, and R. Hanssen, "InSAR quality control: Analysis of five years of corner reflector time series," in *European Space Agency, (Special Publication) Fringe*, (Frascati, Italy), European Space Agency, 2008.
- [73] G. Quin and P. Loreaux, "Submillimeter accuracy of multipass corner reflector monitoring by PS technique," *IEEE Transactions on Geoscience and Remote Sensing*, vol. 51, no. 3, pp. 1775–1783, 2013.
- [74] D. Raucoules, B. Bourguine, M. de Michele, G. Le Cozannet, L. Closset, C. Bremmer, H. Veldkamp, D. Tragheim, L. Bateson, M. Crosetto, M. Agudo, and M. Engdahl, "Validation and intercomparison of Persistent Scatterers Interferometry: PSIC4 project results," *Journal of Applied Geophysics*, vol. 68, no. 3, pp. 335–347, 2009.
- [75] M. Crosetto, O. Monserrat, C. Bremmer, R. Hanssen, R. Capes, and S. Marsh, "Ground Motion Monitoring Using SAR Interferometry: Quality Assessment," *European Geologist Magazine*, No. 26, no. January, pp. 12–15, 2008.

- [76] N. Adam, A. Parizzi, M. Eineder, and M. Crosetto, "Practical persistent scatterer processing validation in the course of the Terrafirma project," *Journal of Applied Geophysics*, 2009.
- [77] J. Hu, Z. W. Li, X. L. Ding, J. J. Zhu, L. Zhang, and Q. Sun, "Resolving three-dimensional surface displacements from InSAR measurements: A review," *Earth-Science Reviews*, vol. 133, pp. 1–17, 2014.
- [78] N. B. Bechor and H. A. Zebker, "Measuring two-dimensional movements using a single InSAR pair," *Geophysical Research Letters*, vol. 33, no. 16, pp. 1–5, 2006.
- [79] F. Casu, A. Manconi, A. Pepe, and R. Lanari, "Deformation time-series generation in areas characterized by large displacement dynamics: The SAR amplitude pixel-offset SBAS technique," *IEEE Transactions on Geoscience and Remote Sensing*, vol. 49, no. 7, pp. 2752–2763, 2011.
- [80] S. Gudmundsson, F. Sigmundsson, and J. M. Carstensen, "Three-dimensional surface motion maps estimated from combined interferometric synthetic aperture radar and GPS data," *Journal of Geophysical Research: Solid Earth*, vol. 107, no. B10, pp. 13–1, 2002.
- [81] T. J. Wright, B. E. Parsons, and Z. Lu, "Toward mapping surface deformation in three dimensions using InSAR," *Geophysical Research Letters*, vol. 31, no. 1, pp. 1–5, 2004.
- [82] K. Goel, F. Rodriguez Gonzalez, N. Adam, J. Duro, and M. Gaset, "Thermal dilation monitoring of complex urban infrastructure using high resolution SAR data," in *IEEE Geoscience and Remote Sensing Symposium (IGARSS)*, no. 1, (Quebec City, Canada), pp. 954–957, IEEE, 2014.
- [83] M. Lazecky, D. Perissin, M. Bakon, J. M. De Sousa, I. Hlavacova, and N. Real, "Potential of satellite InSAR techniques for monitoring of bridge deformations," in *2015 Joint Urban Remote Sensing Event (JURSE)*, (Lausanne, Switzerland), pp. 4–7, 2015.
- [84] M. Lazecky, I. Hlavacova, M. Bakon, J. J. Sousa, D. Perissin, and G. Patricio, "Bridge Displacements Monitoring Using Space-Borne X-Band SAR Interferometry," *IEEE Journal of Selected Topics in Applied Earth Observations and Remote Sensing*, vol. 10, no. 1, pp. 205–210, 2017.
- [85] O. Monserrat, M. Crosetto, M. Cuevas, and B. Crippa, "The thermal expansion component of persistent scatterer interferometry observations," *IEEE Geoscience and Remote Sensing Letters*, vol. 8, no. 5, pp. 864–868, 2011.
- [86] M. Crosetto, O. Monserrat, M. Cuevas-González, N. Devanthéry, G. Luzi, and B. Crippa, "Measuring thermal expansion using X-band persistent scatterer interferometry," *ISPRS Journal of Photogrammetry and Remote Sensing*, vol. 100, pp. 84–91, 2015.
- [87] G. Fornaro, D. Reale, and S. Verde, "Bridge thermal dilation monitoring with millimeter sensitivity via multidimensional SAR imaging," *IEEE Geoscience and Remote Sensing Letters*, vol. 10, no. 4, pp. 677–681, 2013.

- [88] M. Bakon, D. Perissin, M. Lazecky, and J. Papco, "Infrastructure Non-linear Deformation Monitoring Via Satellite Radar Interferometry," *Procedia Technology*, vol. 16, pp. 294–300, 2014.
- [89] D. Cusson, P. Ghuman, M. Gara, and A. Mccardle, "Remote Monitoring of Bridges From Space," in *Anais do 54º Congresso Brasileiro do Concreto*, no. 1, (Maceió, Brazil), 2012.
- [90] M. Del Soldato, R. Tomás, J. Pont, G. Herrera, J. C. G. Lopez-Davalillos, and O. Mora, "A multi-sensor approach for monitoring a road bridge in the Valencia harbor (SE Spain) by SAR Interferometry (InSAR)," *Rendiconti Online Societa Geologica Italiana*, vol. 41, no. June, pp. 235–238, 2016.
- [91] J. J. Sousa and L. Bastos, "Multi-temporal SAR interferometry reveals acceleration of bridge sinking before collapse," *Natural Hazards and Earth System Science*, vol. 13, no. 3, pp. 659–667, 2013.
- [92] P. Milillo, G. Giardina, D. Perissin, G. Milillo, A. Coletta, and C. Terranova, "Pre-Collapse Space Geodetic Observations of Critical Infrastructure: The Morandi Bridge, Genoa, Italy," *Remote Sensing*, vol. 11, no. 12, pp. 1–14, 2019.
- [93] D. Cusson, K. Trischuk, G. Hewus, M. Gara, and P. Ghuman, "Satellite-Based Monitoring of a Highway Bridge in Canada - Challenges , Solutions and Value," in *ISHMII 2017*, no. December, 2017.
- [94] C. Gentile and G. Bernardini, "Output-only modal identification of a reinforced concrete bridge from radar-based measurements," *NDT and E International*, vol. 41, no. 7, pp. 544–553, 2008.
- [95] A. W. Doerry, "Reflectors for SAR Performance Testing," Tech. Rep. January, Sandia National Laboratories, Albuquerque, 2008.
- [96] M. Crosetto, J. A. Gili, O. Monserrat, M. Cuevas-González, J. Corominas, and D. Serral, "Interferometric SAR monitoring of the Vallcebre landslide (Spain) using corner reflectors," *Natural Hazards and Earth System Science*, vol. 13, no. 4, pp. 923–933, 2013.
- [97] A. W. Doerry and B. C. Brock, "SANDIA REPORT Radar Cross Section of Triangular Trihedral Reflector with Extended Bottom Plate," tech. rep., Sandia National Laboratories, Springfield, U.S., 2009.
- [98] M. C. Garthwaite, "Correction: On the Design of radar corner reflectors for deformation monitoring in multi-frequency InSAR [Remote Sens., 9, (2017), (648)] DOI: 10.3390/rs9070648," *Remote Sensing*, vol. 10, no. 1, 2018.
- [99] J. Norris, P. W. Vachon, D. Schlingmeier, R. English, L. Gallop, D. R&d, and C. ttawa, "Expendable Trihedral Corner Reflectors for Target Enhancement and Position Control in RADARSAT-1 Fine Beam Mode SAR Imagery: Results from an Exercise Narwhal Pre-Trial Deployment," tech. rep., Defence R&D Canada, Ottawa, Canada, 2004.

- [100] K. Sarabandi and T. C. Chiu, "Optimum corner reflectors for calibration of imaging radars," *IEEE Transactions on Antennas and Propagation*, vol. 44, no. 10, pp. 1348–1361, 1996.
- [101] G. Ruck and C. Krichbaum, "Radar Cross Section Handbook Supplement," tech. rep., Advanced Research Projects Agency, Washington D.C., U.S., 1968.
- [102] M. C. Garthwaite, S. Nancarrow, A. Hislop, M. Thankappan, J. H. Dawson, and S. Lawrie, *The Design of Radar Corner Reflectors for the Australian Geophysical Observing System*. 2015.
- [103] Y. Qin, D. Perissin, and L. Lei, "The design and experiments on corner reflectors for urban ground deformation monitoring in Hong Kong," *International Journal of Antennas and Propagation*, vol. 2013, pp. 1–8, 2013.
- [104] T. Ootshi, "A Study of Microwave Leakage through Perforated Flat Plates," *IEEE Transactions on Microwave Theory and Techniques*, vol. 20, no. 3, pp. 235–236, 1972.
- [105] M. Crosetto, C. C. Tscherning, B. Crippa, and M. Castillo, "Subsidence monitoring using SAR interferometry: Reduction of the atmospheric effects using stochastic filtering," *Geophysical Research Letters*, vol. 29, no. 9, pp. 26–1, 2002.
- [106] Analytical Graphics Inc. (AGI), "Systems Tool Kit," 2018.
- [107] A. Johnson, *Plane and Geodetic Surveying*. Boca Raton: CRC Press (Taylor & Francis Group), 2nd ed., 2014.
- [108] Ordnance Survey, "A Guide to Coordinate Systems in Great Britain," tech. rep., Southampton, 2018.
- [109] F. Onn and H. A. Zebker, "Correction for interferometric synthetic aperture radar atmospheric phase artifacts using time series of zenith wet delay observations from a GPS network," *Journal of Geophysical Research: Solid Earth*, vol. 111, no. 9, pp. 1–16, 2006.
- [110] Ordnance Survey, "Benchmark locator (available at: <https://www.ordnancesurvey.co.uk/benchmarks/>)," 2018.
- [111] F. Kruse, A. Lefkoff, J. Boardman, K. Heidebrecht, A. Shapiro, P. Barloon, and A. Goetz, "The Spectral Image Processing System (SIPS)- Interactive Visualization and Analysis of Imaging Spectrometer Data," *Remote Sensing of Environment*, vol. 44, pp. 145–163, 1993.
- [112] BIPM, IEC, IFCC, ILAC, ISO, IUPAC, IUPAP, and OIML, "JCGM 104. Evaluation of measurement data — An introduction to the "Guide to the expression of uncertainty in measurement" and related documents," Tech. Rep. July, Joint Committee for Guides in Metrology, Sèvres, France, 2009.
- [113] B. Taylor and C. Kuyatt, "Guidelines for Evaluating and Expressing the Uncertainty of NIST Measurement Results," tech. rep., Gaithersburg, MD, 1993.

- [114] E. Buckton and J. Cuerel, “The New Waterloo Bridge,” *Journal of the Institution of Civil Engineers*, vol. 20 (7), no. June, pp. 145–178, 1943.
- [115] sarmap SA, “SARscape®,” 2014.
- [116] X. Qin, X. Ding, and M. Liao, “Three-Dimensional Deformation Monitoring and Structural Risk Assessment of Bridges by Integrating Observations from Multiple SAR Sensors,” in *IEEE International Geoscience and Remote Sensing Symposium (IGARSS)*, (Valencia, Spain), pp. 1384–1387, IEEE, 2018.
- [117] S. Boyd and L. Vandenberghe, *Convex Optimization*. Cambridge, UK: Cambridge University Press, 2004.
- [118] V. Kaibel and A. Schwartz, “On the complexity of polytope isomorphism problems,” *Graphs and Combinatorics*, vol. 19, no. 2, p. 215–230, 2003.
- [119] V. Prasolov, *Problems and Theorems in Linear Algebra*. Providence, U.S.: American Mathematical Society, 1st ed., 1994.
- [120] G. E. Bredon, *Topology and Geometry*, vol. 91. New York, U.S.: Springer, 2017.
- [121] G. H. Golub and C. F. V. Loan, “Matrix Computations,” *The Mathematical Gazette*, vol. 74, no. 469, p. 322, 1990.
- [122] A. Marinoni and P. Gamba, “A novel approach for efficient P-Linear hyperspectral unmixing,” *IEEE Journal on Selected Topics in Signal Processing*, vol. 9, no. 6, pp. 1156–1168, 2015.
- [123] G. T. Webb, P. J. Vardanega, P. R. A. Fidler, and C. R. Middleton, “Analysis of Structural Health Monitoring Data from Hammersmith Flyover,” *Journal of bridge engineering (ASCE)*, vol. 19, no. 6, pp. 1–11, 2014.
- [124] S. Auer, S. Hinz, and R. Bamler, “Ray Tracing Simulation Techniques for Understanding High Resolution SAR Images,” *IEEE Transactions on Geoscience and Remote Sensing*, vol. 48, no. 3, pp. 1445–1456, 2010.
- [125] M. Davila, L. J. Butler, N. Gibbons, I. Brilakis, M. Z. E. B. Elshafie, and C. Middleton, “Management of structural monitoring data of bridges using BIM,” *ICE Proceedings: Bridge Engineering*, no. November, pp. 1–15, 2016.
- [126] S. Montazeri, F. R. González, and X. X. Zhu, “Geocoding error correction for InSAR point clouds,” *Remote Sensing*, vol. 10, no. 10, pp. 1–22, 2018.
- [127] S. Gernhardt and S. Hinz, “Advanced displacement estimation for PSI using high resolution SAR data,” *International Geoscience and Remote Sensing Symposium (IGARSS)*, vol. 3, no. 1, pp. 1276–1279, 2008.
- [128] S. Selvakumaran, S. Plank, C. Geiß, C. Rossi, and C. Middleton, “Remote monitoring to predict bridge scour failure using Interferometric Synthetic Aperture Radar (InSAR) stacking techniques,” *International Journal of Applied Earth Observation and Geoinformation*, vol. 73, no. April, pp. 463–470, 2018.

- [129] B. E. Hunt, *Monitoring Scour Critical Bridges*. Washington, D.C.: National Academies of Sciences, Engineering, and Medicine, 2009.
- [130] RAIB, “Rail Accident Report: Failure of Bridge RDG1 48 between Whitton and Feltham,” Tech. Rep. November 2009, 2010.
- [131] RAIU, “Malahide Viaduct Collapse on the Dublin to Belfast Line, on the 21 st August 2009,” tech. rep., RAIU, 2010.
- [132] L. Hamill, *Bridge Hydraulics*. London: CRC Press (Taylor & Francis Group), 1st ed., 1998.
- [133] A. Kirby, A. Kitchen, M. Escameia, and O. Chesterton, *Manual on scour at bridges and other hydraulic structures (C742)*. London: CIRIA, 2nd ed., 2015.
- [134] Highways Agency, “The Assessment of Scour and Other Hydraulic Actions at Highway Structures (BD97/12),” tech. rep., The Highways Agency, Transport Scotland, Welsh Government and The Department for Regional Development Northern Ireland, 2012.
- [135] J.-Y. Lu, J.-H. Hong, C.-C. Su, C.-Y. Wang, and J.-S. Lai, “Field Measurements and Simulation of Bridge Scour Depth Variations during Floods,” *Journal of Hydraulic Engineering*, vol. 134, no. 6, pp. 810–821, 2008.
- [136] M. Fisher, M. N. Chowdhury, A. A. Khan, and S. Atamturktur, “An evaluation of scour measurement devices,” *Flow Measurement and Instrumentation*, vol. 33, pp. 55–67, 2013.
- [137] L. J. Prendergast and K. Gavin, “A review of bridge scour monitoring techniques,” *Journal of Rock Mechanics and Geotechnical Engineering*, vol. 6, no. 2, pp. 138–149, 2014.
- [138] L. Bateson, F. Cigna, D. Boon, and A. Sowter, “The application of the Intermittent SBAS (ISBAS) InSAR method to the South Wales Coalfield, UK,” *International Journal of Applied Earth Observation and Geoinformation*, vol. 34, pp. 249–257, 2014.
- [139] M. D. Farago, G. Cooksley, M. Costantini, F. Minati, F. Trillo, L. Paglia, and J. Gates, “Understanding the advantages of satellite Earth Observation as surveying tool for infrastructure monitoring,” in *Proceedings of the International Conference on Smart Infrastructure and Construction*, (Cambridge, UK), pp. 257–263, ICE Publishing, 2016.
- [140] M. Jecock and L. Jessop, “Tadcaster Bridge, Tadcaster, North Yorkshire : Assessment of Significance Assessment of Significance,” Tech. Rep. 27, Historic England, Portsmouth, United Kingdom, 2016.
- [141] P. Association, “Tadcaster bridge over river Wharfe collapses during flooding – video,” 2015.

- [142] Press_Association, “Tadcaster bridge over river Wharfe collapses during flooding – video (available at: <https://www.theguardian.com/environment/video/2015/dec/30/tadcaster-bridge-river-wharfe-collapses-flooding-video>),” 2015.
- [143] E. Erten, A. Reigber, and O. Hellwich, “Generation of three-dimensional deformation maps from InSAR data using spectral diversity techniques,” *ISPRS Journal of Photogrammetry and Remote Sensing*, vol. 65, no. 4, pp. 388–394, 2010.
- [144] B. Osmanoglu, F. Sunar, S. Wdowinski, and E. Cabral-Cano, “Time series analysis of InSAR data: Methods and trends,” 2016.
- [145] J. W. Tukey, *Exploratory Data Analysis*. Reading, MA: Addison-Wesley Publishing, 1977.
- [146] V. Chandola, A. Banerjee, and V. Kumar, “Anomaly Detection: A Survey,” *ACM Computer Survey*, vol. 41, no. 3, pp. 1–58, 2009.
- [147] J. Zhao, J. Wu, X. Ding, and M. Wang, “Elevation extraction and deformation monitoring by multitemporal InSAR of Lupu Bridge in Shanghai,” *Remote Sensing*, vol. 9, no. 9, pp. 1–13, 2017.

Appendix A

TerraSAR-X London SAR acquisitions

Refer to Table A.1. All acquisitions have an incidence angle range of 36.11 - 38.5 degrees. Ascending acquisitions were taken at 17:44 and descending acquisitions were taken at 06:17.

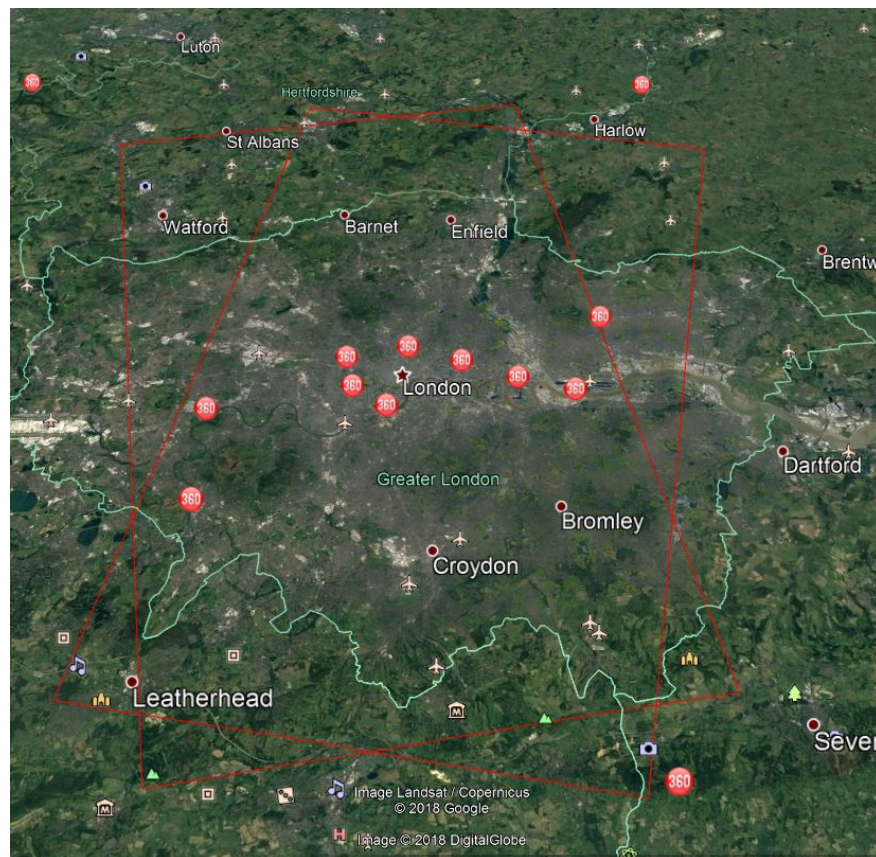


Fig. A.1 Footprint of TerraSAR-X imagery overlaid onto Google Earth imagery (optical satellite imagery from Landsat/Copernicus).

Table A.1 TerraSAR-X acquisition list for Waterloo Bridge study

Ascending Acquisition Dates	Descending Acquisition Dates
18-DEC-2017	15-DEC-2017
29-DEC-2017	26-DEC-2017
09-JAN-2018	06-JAN-2018
20-JAN-2018	17-JAN-2018
31-JAN-2018	28-JAN-2018
11-FEB-2018	08-FEB-2018
22-FEB-2018	19-FEB-2018
05-MAR-2018	02-MAR-2018
16-MAR-2018	13-MAR-2018
27-MAR-2018	24-MAR-2018
07-APR-2018	04-APR-2018
18-APR-2018	26-APR-2018
29-APR-2018	07-MAY-2018
10-MAY-2018	18-MAY-2018
21-MAY-2018	29-MAY-2018
01-JUN-2018	09-JUN-2018
12-JUN-2018	20-JUN-2018
23-JUN-2018	01-JUL-2018
04-JUL-2018	12-JUL-2018
15-JUL-2018	23-JUL-2018
26-JUL-2018	03-AUG-2018
06-AUG-2018	14-AUG-2018
17-AUG-2018	25-AUG-2018
28-AUG-2018	05-SEP-2018
08-SEP-2018	16-SEP-2018
19-SEP-2018	27-SEP-2018
30-SEP-2018	08-OCT-2018
11-OCT-2018	19-OCT-2018
22-OCT-2018	30-OCT-2018
02-NOV-2018	10-NOV-2018

Appendix B

Cosmo SkyMed-X London SAR acquisitions

The acquisitions processed by e-geos and provided by Telespazio VEGA UK for this research are listed in Table B.1. These acquisitions were in Stripmap mode. The acquisitions tasked for this research and archive images provided for this research and processed by the author are listed in Table B.2. The acquisition processed by the author were taken in Stripmap mode with an incidence angle range of 25.0 - 27.9 degrees.

Table B.1 Cosmo SkyMed-X acquisition list provided by Telespazio

Acquisition Dates	Acquisition Dates	Acquisition Dates	Acquisition Dates
05-MAY-2011	16-JAN-2011	18-JAN-2013	31-JUL-2014
21-MAY-2011	21-APR-2012	03-FEB-2013	16-AUG-2014
06-JUN-2011	07-MAY-2012	23-MAR-2013	01-SEP-2014
08-JUL-2011	23-MAY-2012	08-APR-2013	04-NOV-2014
24-JUL-2011	08-JUN-2012	24-APR-2013	20-NOV-2014
25-AUG-2011	11-AUG-2012	10-MAY-2013	23-JAN-2015
26-SEP-2011	27-AUG-2012	14-AUG-2013	08-FEB-2015
13-NOV-2011	12-SEP-2012	17-OCT-2013	29-APR-2015
29-NOV-2011	17-DEC-2012	28-MAY-2014	16-JUN-2015
15-DEC-2011	02-JAN-2013	29-JUN-2014	18-JUL-2015

Table B.2 Cosmo SkyMed-X acquisition list processed by author

Acquisition Dates	Acquisition Dates	Acquisition Dates	Acquisition Dates
23-JAN-2015	17-MAY-2016	24-AUG-2017	23-MAY-2018
08-FEB-2015	02-JUN-2016	17-SEP-2017	31-MAY-2018
29-MAR-2015	21-AUG-2016	19-OCT-2017	16-JUN-2018
16-JUN-2015	06-SEP-2016	28-NOV-2017	02-JUL-2018
18-JUL-2015	28-JAN-2017	04-FEB-2018	18-JUL-2018
10-OCT-2015	01-MAR-2017	20-FEB-2018	11-AUG-2018
07-NOV-2015	17-MAR-2017	21-MAR-2018	27-AUG-2018
09-DEC-2015	02-APR-2017	06-APR-2018	
14-MAR-2016	05-JUN-2017	07-MAY-2018	



Fig. B.1 Footprint of Cosmo SkyMed-X imagery overlaid onto Google Earth imagery (optical satellite imagery from Landsat/Copernicus).

Appendix C

Tadcaster site SAR acquisitions

Refer to Table C.1. All acquisitions are in the ascending pass, taken in StripMap mode, and have an incidence angle range of 19.7 - 23.2 degrees. Acquisitions were taken at 17:36.



Fig. C.1 Footprint of TerraSAR-X imagery overlaid onto Google Earth imagery (optical satellite imagery provided by Landsat/Copernicus).

Table C.1 TerraSAR-X acquisition list for Tadcaster Bridge study

Acquisition Date	Acquisition Date
09-MAR-2014	22-JAN-2015
20-MAR-2014	02-FEB-2015
31-MAR-2014	13-FEB-2015
11-APR-2014	24-FEB-2015
22-APR-2014	07-MAR-2015
03-MAY-2014	29-MAR-2015
14-MAY-2014	09-APR-2015
25-MAY-2014	20-APR-2015
05-JUN-2014	01-MAY-2015
16-JUN-2014	12-MAY-2015
27-JUN-2014	23-MAY-2015
08-JUL-2014	03-JUN-2015
19-JUL-2014	14-JUN-2015
30-JUL-2014	25-JUN-2015
10-AUG-2014	06-JUL-2015
21-AUG-2014	17-JUL-2015
01-SEP-2014	08-AUG-2015
12-SEP-2014	19-AUG-2015
17-NOV-2014	02-OCT-2015
28-NOV-2014	13-OCT-2015
09-DEC-2014	24-OCT-2015
20-DEC-2014	04-NOV-2015
31-DEC-2014	15-NOV-2015
11-JAN-2015	26-NOV-2015